Assessing Greenland and Antarctic firn processes from multi-source satellite data

Li, W.

DOI
10.4233/uuid:14936805-90ef-4800-a464-6734d0b9c048

Publication date
2025

Document Version
Final published version

Citation (APA)
Li, W. (2025). *Assessing Greenland and Antarctic firn processes from multi-source satellite data*. [Dissertation (TU Delft), Delft University of Technology]. https://doi.org/10.4233/uuid:14936805-90ef-4800-a464-6734d0b9c048

Important note
To cite this publication, please use the final published version (if applicable).
Please check the document version above.

Assessing Greenland and Antarctic firn processes from multi-source satellite data

Weiran Li

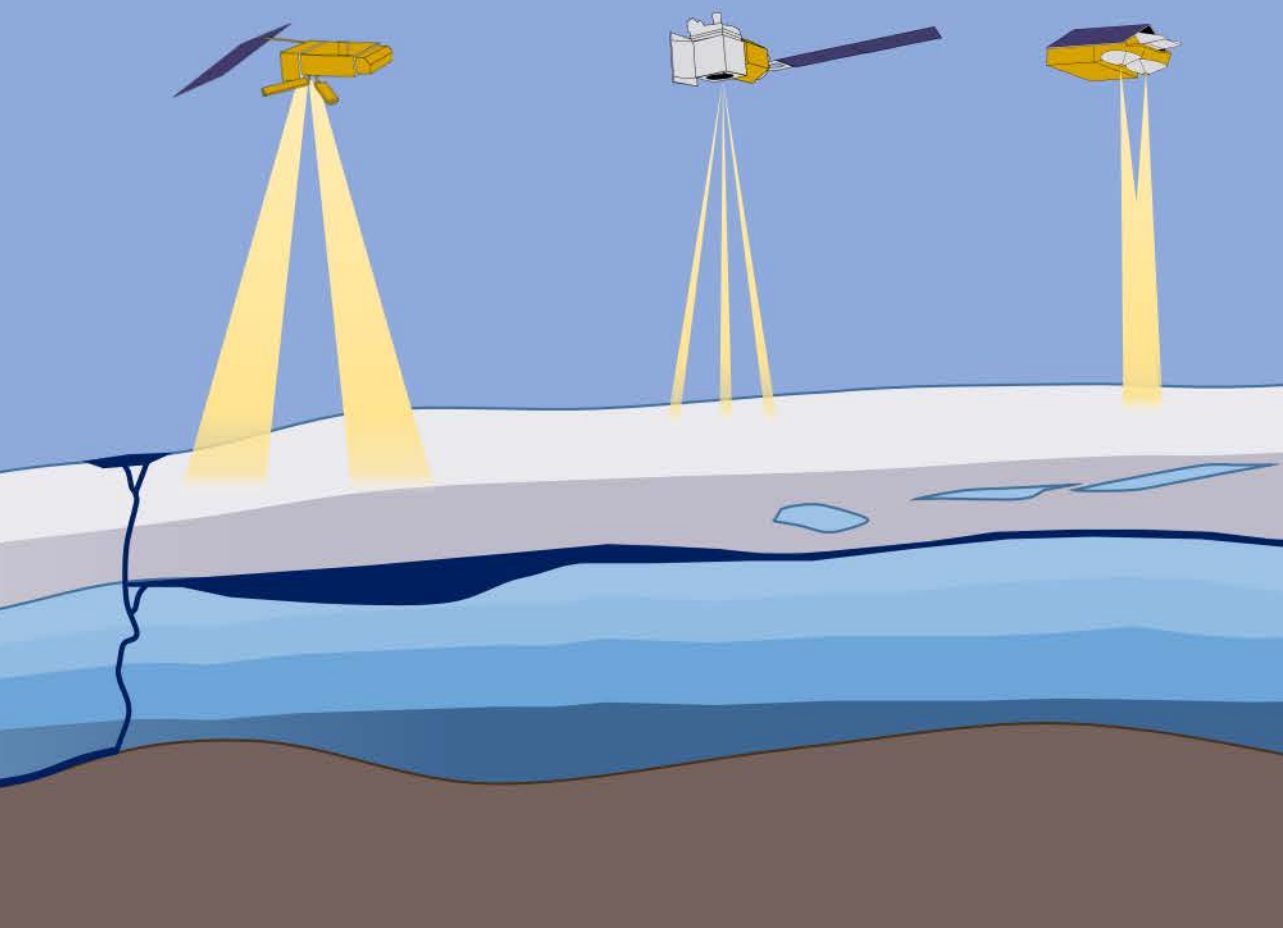

ASSESSING GREENLAND AND ANTARCTIC FIRN PROCESSES FROM MULTI-SOURCE SATELLITE DATA

ASSESSING GREENLAND AND ANTARCTIC FIRN PROCESSES FROM MULTI-SOURCE SATELLITE DATA

Dissertation

for the purpose of obtaining the degree of doctor
at Delft University of Technology
by the authority of the Rector Magnificus, Prof.dr.ir. T.H.J.J. van der Hagen,
chair of the Board for Doctorates
to be defended publicly on
Tuesday 15, April 2025 at 10:00 o'clock

by

Weiran LI

Master of Science in Geomatics,
Delft University of Technology, Delft, the Netherlands,
born in Beijing, China.

This dissertation has been approved by the promotors.

Promotor: Prof. dr. ir. R.F. Hanssen
Promotor: Dr. S.L.M. Lhermitte

Composition of the doctoral committee:

Rector Magnificus,	chairperson
Prof. dr. ir. R.F. Hanssen,	Technische Universiteit Delft, promotor
Dr. S.L.M. Lhermitte,	Technische Universiteit Delft & KU Leuven, promotor
Onafhankelijke leden:	
Prof. dr.-Ing. habil R. Klees,	Technische Universiteit Delft
Prof. dr. ir. F. Lopez Dekker,	Technische Universiteit Delft
Dr. S.B. Simonsen,	Danmarks Tekniske Universitet
Dr. R.C. Lindenbergh,	Technische Universiteit Delft
Dr. ir. D.C. Slobbe,	Technische Universiteit Delft
Prof. dr. ir. S.C. Steele-Dunne,	Technische Universiteit Delft, reserved

Dr. ir. D.C. Slobbe of Delft University of Technology has contributed greatly to the preparation of this dissertation.

This research was financially supported by the Dutch Research Council (NWO) through the ALWGO.2017.033 project.

Keywords: firn processes, Greenland, Antarctica, satellite radiometer, satellite scatterometer, satellite altimeter

Printed by: Ipskamp Printing, proefschriften.net

Cover: designed by Lorenzo Iannini.

ISBN 978-94-6473-772-1

An electronic version of this dissertation is available at
`http://repository.tudelft.nl/`.

博观而约取，厚积而薄发

苏轼

Study extensively and absorb selectively,
so you can then apply your knowledge effectively.

SU Shi

CONTENTS

SUMMARY

Assessing firn processes within Greenland and Antarctica is important in recent decades, as melt–refreezing processes can result in accelerated meltwater runoff and land-ice discharge. Meanwhile, surface and depth hoar crystal formation have an impact on the surface warming and surface mass balance (SMB) of the ice sheets. Typically, these processes are monitored using in situ firn core measurements, or estimated using climate models. However, the in situ measurements are sparse due to the harsh conditions of the polar regions, while the climate models are based on simplified assumptions which introduce various uncertainties. The recent advancements of satellite remote sensing techniques provide the opportunity to monitor the firn processes over the ice sheets, due to a vast spatial coverage and a frequent revisit time.

This thesis explores the capability of satellite radiometers, scatterometers and altimeters to assess firn processes, including firn density variation and melt–refreezing processes. Conventionally, satellite radiometers and scatterometers are used in detecting melt events over the ice sheets, based on the principle that melt events change the dielectric constant within the firn layer, while the satellite altimeter is typically used for estimating surface elevation changes over ice sheets. This thesis, on the contrary, explores the feasibility of using radiometers and scatterometers to assess the dry-firn density; meanwhile, it assesses the potential of using the altimeters to observe the melt–refreezing events of firn. The rationale behind this thesis is that the long-term variations in satellite radiometer and scatterometer observations depend on the changing scattering properties due to variations in near-surface firn densities, which provides the opportunity for using satellite radiometer and scatterometer observations to estimate long-term changes in firn densities. Meanwhile, the shape of the waveform obtained by a satellite radar altimeter can be influenced by volume and surface scattering of firn. By assessing the variation of firn scattering properties using the waveform information, the occurrence and impact of melt–refreezing processes within the firn layer can be assessed. Therefore, more potentials lie in the application and interpretation of remote sensing data in the studies of the cryosphere.

To study the aforementioned application and performance of different satellite remote sensing techniques, this thesis consists of two main aspects which are further divided into three studies. The first aspect as well as the first study (Chapter 2) uses a combination of satellite radiometer and scatterometer observations (brightness temperature T_B and normalised backscatter intensity σ^0_A, respectively) time series to estimate the long-term firn density over Antarctic dry snow zone. First, the dry snow zone is distinguished from melt zones by identifying long-term anomalies in T_B and σ^0_A time series using a clustering approach. Within the identified dry snow zone, we estimate the firn density using a random forest (RF) regression approach with the combination of T_B and σ^0_A time series as the input. Due to the sparsity of the in situ density measurements, densities from a firn densification model (FDM) are used as the “true" densities. 10 %

of the FDM densities are used to train the RF regressor, while all the FDM densities are used for the validation to assess the performance of the method. The estimated densities using RF correspond well with the FDM densities spatially, when averaged over the long time period. However, the temporal correspondence between the RF-estimated and the FDM densities is compromised. The discrepancy is primarily due to the simple assumption that T_B and σ^0_A variations are purely driven by variations in the firn density and are therefore sufficient to be directly used as the input to the RF regressor. Another major reason for the discrepancy is that T_B and σ^0_A variations can be driven by varying firn grain sizes as a results of changing wind velocity and direction, while the wind pattern has a simplified linear relationship with firn density within the FDM, which causes inaccuracy in the FDM density. This study therefore provides indications and potentials for further studies to incorporate in situ density measurements and better parametrisations of climate parameters.

The second aspect of this thesis, which is composed of two studies, focuses on the application of satellite altimeters to studying the melt–refreezing within Greenland firn. The melt–refreezing events introduce the formation of high-density ice lenses, which alters the scattering properties of Greenland firn. The altered scattering properties can be typically represented by the difference between laser and radar altimeter height estimates, as radar wavelengths have a larger penetration depth than laser. This difference is usually at a sub-metre level. However, a complex topography can result in multi-metre slope-induced errors in height estimates. Therefore, to accurately derive the laser–radar height difference, we first put forward an (leading edge point-based; LEPTA) approach (Chapter 3) to correct for the slope-induced errors with an improved accuracy compared to the existing approaches. The principle of this approach is to identify which points on the terrain contribute to the rise of the leading edge of the radar altimeter waveform by utilising a high-resolution digital elevation model (DEM). We apply the approach on the CryoSat-2 Low Resolution Mode (LRM) Level-1b (L1b) data. When validated with height estimates obtained from a laser altimeter (ICESat-2), LEPTA outperforms the existing correction approaches as well as the height estimates provided by European Space Agency (ESA) CryoSat-2 Level-2I (L2I) data. The study also demonstrates that the LEPTA approach is sensitive to the definition of the leading edge width (LeW) and the bias and resolution of the DEM. Finally, by increasing the retracking threshold from 20 % to 70 %, the height difference between ICESat-2 and CryoSat-2 indicates that the height estimates from CryoSat-2 transits from surface height to height within the firn layer.

Finally, we present the spatio-temporal variations of CryoSat-2 LeW (Chapter 4), in order to assess the spatio-temporal variations of volume scattering of the Greenland firn, especially under the condition of the recent recurrent melt–refreezing processes. This P first distinguishes the regions where volume scattering dominates the LeW variations from the regions where surface scattering dominates with an existing surface roughness dataset as well as the DEM that indicates the complexity of topography. In addition, this study will derive the height difference between ICESat-2 and CryoSat-2 as an indicator of Ku-band radar penetration bias hence volume scattering. Following the results of Chapter 3, a 50 % retracking threshold and the LEPTA method are used to derive the height estimates from CryoSat-2 LRM L1b data. By comparing the LeW variation with external datasets and the in-house derived height differences, this study successfully delineates

the regions where volume scattering dominates LeW variations. Subsequently, we qualitatively compare the LeW variations with firn densities, firn air content (FAC), melt, refreeze and snow height change variations from an FDM model and a climate model. The comparison shows that the LeW is most capable of indicating volume scattering changes caused by melt–refreezing processes in the central dry snow zones of Greenland. This study demonstrates the long-lived impact of the 2012 melt over Greenland on the volume scattering of Greenland's firn, as well as the effect of the temporary yet increasing frequent melt events in the recent years.

Overall, this thesis is an extensive research on the approaches to utilise and analyse various sources of satellite remote sensing data for observing firn processes in polar regions. At the same time, it also provides insights into the limitations and potential improvements of using satellite remote sensing data for a quantitative measurement of Greenland and Antarctic firn evolutions, such as estimating firn densities and assessing the timing and the extent of melt events and the subsequent ice-lens formations. This thesis also provides indications for improving the current firn models, including better parametrisation of wind patterns and ice-lens formations. Such improvements are expected to increase the accuracy of estimating meltwater storage and surface mass balance over the Greenland and Antarctic ice sheets. In addition, this thesis provides a method to correct for slope-induced errors in radar altimetry, which provides insights into how the accuracy of height estimations from radar altimeters can be improved by utilising the leading edge information from radar altimetry waveforms.

SAMENVATTING

De beoordeling van firnprocessen in Groenland en Antarctica is de afgelopen decennia steeds belangrijker geworden. Smeltprocessen kunnen leiden tot versnelde afvoer van smeltwater en landijs, wat directe gevolgen heeft voor de massabalans van de ijskappen. Daarnaast beïnvloedt de vorming van rijpijskristallen, zowel aan het oppervlak als in diepere lagen, de opwarming en massabalans (SMB) van de ijskappen. Deze processen worden doorgaans gevolgd met in-situ metingen van firnkernen of geschat met klimaatmodellen. In-situ metingen zijn echter schaars vanwege de extreme omstandigheden in de poolgebieden, terwijl klimaatmodellen vereenvoudigde aannames hanteren die onzekerheden met zich meebrengen. De recente vooruitgang in satellietmeettechnieken biedt nieuwe mogelijkheden om firnprocessen te monitoren. Dankzij hun brede ruimtelijke dekking en frequente herhalingstijd kunnen satellieten bijdragen aan een beter begrip van firndichtheidsvariaties en smelt-herbevriezingsprocessen.

Dit proefschrift onderzoekt het potentieel van satellietradiometers, -scatterometers en -altimeters bij de beoordeling van firnprocessen, waaronder variaties in firndichtheid en de herbevriezing van smeltwater. Satellietradiometers en -scatterometers worden doorgaans gebruikt om de aanwezigheid van smelt boven ijskappen te detecteren, omdat smeltwater de diëlektrische eigenschappen van de firnlaag verandert. Satellietaltimeters worden vooral ingezet voor het schatten van hoogteveranderingen. Deze studie richt zich echter op het gebruik van radiometers en scatterometers om de dichtheid van droge firn te bepalen en onderzoekt het potentieel van altimeters bij de detectie van smelt- en herbevriezingsprocessen binnen de firnlaag. De achterliggende gedachte is dat langetermijnvariaties in satelliet-radiometer- en scatterometerwaarnemingen worden beïnvloed door dezelfde klimaatparameters (zoals temperatuur, wind en neerslag) die ook firndichtheid bepalen. Hierdoor kunnen deze waarnemingen worden ingezet voor het schatten van langetermijnveranderingen in firndichtheid. Daarnaast kan de vorm van de golfvorm die door een satellietradaraltimeter wordt waargenomen, worden beïnvloed door volume- en oppervlakteverstrooiing in firn. Door deze variaties in verstrooiingseigenschappen te analyseren, kunnen smelt- en herbevriezingsprocessen beter worden gekarakteriseerd. Dit onderzoek benadrukt daarom de mogelijkheden van satellietdata bij het bestuderen van de cryosfeer.

Om deze toepassingen en de prestaties van verschillende aardobservatietechnieken te evalueren, bestaat dit proefschrift uit twee hoofdaspecten, onderverdeeld in drie studies. Het eerste aspect richt zich op de schatting van firndichtheid met behulp van satellietradiometer- en scatterometerwaarnemingen. In Hoofdstuk 2 wordt een clusteranalyse toegepast op langetermijnanomalieën in de helderheidstemperatuur (T_B) en genormaliseerde backscatterintensiteit (σ^0_A) om de droge sneeuwzone in Antarctica te onderscheiden van smeltzones. Binnen deze zone wordt firndichtheid geschat met een

The Summary is translated into Dutch on DeepL.com (free version) and proofread by Koen Haakman and Stef Lhermitte.

random forest (RF)-regressiemethode, waarbij T_B- en σ^0_A-tijdreeksen als input dienen. Omdat in-situ dichtheidsmetingen beperkt beschikbaar zijn, worden dichtheden uit een firnverdichtingsmodel (FDM) gebruikt als referentie. De resultaten tonen een sterke ruimtelijke overeenkomst tussen de RF-geschatte dichtheden en FDM-dichtheden op lange termijn. De temporele overeenkomst is echter minder nauwkeurig, voornamelijk door de vereenvoudigde aanname dat T_B en σ^0_A direct worden beïnvloed door dezelfde klimaatparameters als firndichtheid. Daarnaast spelen windsnelheid en -richting een grotere rol in de variatie van T_B en σ^0_A dan het firnverdichtingsmodel momenteel aanneemt. Deze studie benadrukt daarom de noodzaak om in-situ metingen en verbeterde parametrisaties van klimaatfactoren te integreren in toekomstige onderzoeken.

Het tweede aspect van dit proefschrift, bestaande uit twee studies, richt zich op de toepassing van satellietaltimeters bij het bestuderen van smeltprocessen in de Groenlandse firn. Smelten en herbevriezen leidt tot de vorming van ijslenzen met een hoge dichtheid, wat de verstrooiingseigenschappen van firn verandert. Dit heeft invloed op het hoogteverschil tussen laser- en radaraltimeters, omdat radiogolven dieper in firn doordringen dan laserstraling. Dit hoogteverschil is doorgaans minder dan een meter, maar complexe topografieën kunnen fouten in hoogteschattingen van meerdere meters veroorzaken. Om deze fouten te corrigeren, introduceert Hoofdstuk 3 een nieuwe methode, de Leading Edge Point Tracking Approach (LEPTA), die hellingseffecten in CryoSat-2-radaraltimetrie corrigeert door gebruik te maken van een hoogresolutie digitaal hoogtemodel (DEM). Validatie met laseraltimetergegevens van ICESat-2 toont aan dat LEPTA nauwkeurigere hoogteschattingen oplevert dan bestaande correctiemethoden en de Level-2I-gegevens van de European Space Agency (ESA). De studie toont tevens aan dat de prestaties van LEPTA afhangen van de definitie van de leading edge width (LeW) en de resolutie van het DEM. Bovendien bevestigt een verhoogde retrackingdrempel (van 20 % naar 70 %) dat CryoSat-2-hoogteschattingen kunnen verschuiven van oppervlaktehoogte naar een grotere diepte binnen de firnlaag.

Tot slot presenteren we de spatio-temporele variaties van CryoSat-2 LeW (Hoofdstuk 4), om de spatio-temporele variaties van de volumeverstrooiing van de Groenlandse firn te beoordelen, vooral tijdens van de recente terugkerende smelt- en herbevriezingsprocessen. Deze studie onderscheidt eerst de regio's waar volumeverstrooiing de LeW-variaties domineert van de regio's waar oppervlakteverstrooiing domineert, met een bestaande dataset voor oppervlakteruwheid en het DEM die de complexiteit van de topografie aangeeft. Daarnaast leidt deze studie het hoogteverschil tussen ICESat-2 en CryoSat-2 af als indicator voor de vertekening van de Ku-band radarpenetratie en dus van de volumeverstrooiing. Op basis van de resultaten van Hoofdstuk 3 worden een retrackingdrempel van 50 % en de LEPTA-methode gebruikt om hoogteschattingen af te leiden uit CryoSat-2 LRM L1b-data. Door de LeW-variatie te vergelijken met externe datasets en onze intern afgeleide hoogteverschillen, bakent deze studie met succes de regio's af waar volumeverstrooiing de LeW-variaties domineert. Vervolgens vergelijken we de LeW variaties kwalitatief met firn dichtheden, firn air content (FAC), smelt, herbevriezing en sneeuwhoogteveranderingen uit een FDM model en een klimaatmodel. De vergelijking laat zien dat de LeW het best in staat is om veranderingen in de volumeverstrooiing aan te geven die worden veroorzaakt door smelt- en herbevriezingsprocessen in de centrale droge sneeuwzones van Groenland. Deze studie toont de langdurige in-

vloed aan van de smelt op Groenland in 2012 op de volumeverstrooiing van de Groenlandse firn, evenals het effect van de tijdelijke maar in frequentie toenemende smeltgebeurtenissen in de afgelopen jaren.

Over het geheel genomen is dit proefschrift een uitgebreid onderzoek naar de benaderingen voor het gebruik en de analyse van verschillende bronnen van satellietmetingen voor het observeren van firnprocessen in poolgebieden. Tegelijkertijd geeft het ook inzicht in de beperkingen en mogelijke verbeteringen van het gebruik van satellietdata voor een kwantitatieve meting van de evolutie van de ijskap op Groenland en Antarctica, zoals het schatten van de dichtheid van de ijskap en het beoordelen van de timing en de omvang van smeltgebeurtenissen en de daaropvolgende vorming van ijslagen. Dit proefschrift geeft ook aanwijzingen voor het verbeteren van de huidige firnmodellen, waaronder een betere parametrisering van windpatronen en ijslensformaties. Dergelijke verbeteringen zullen naar verwachting de nauwkeurigheid van de schatting van de smeltwateropslag en de massabalans aan het oppervlak van de Groenlandse en Antarctische ijskappen vergroten. Daarnaast biedt dit proefschrift een methode om te corrigeren voor fouten in radarhoogtemetingen die door hellingen worden veroorzaakt, wat inzicht geeft in hoe de nauwkeurigheid van hoogteschattingen van radarhoogtemeters kan worden verbeterd door gebruik te maken van de leading edge-informatie van de golfvormen van radarhoogtemetingen.

LIST OF ABBREVIATIONS

AIS	Antarctic ice sheet
AMSR2	Advanced Microwave Scanning Radiometer2
AMSR-E	Advanced Microwave Scanning Radiometer - Earth Observing System Sensor
AMSR-U	Advanced Microwave Scanning Radiometer Unified
AMSU-B	Advanced Microwave Sounding Unit B
ASCAT	The Advanced Scatterometer
ATLAS	Advanced Topographic Laser Altimeter System
ATM	Airborne Topographic Mapper
C3S	Copernicus Climate Change Service
CDS	Climate Data Store
CIMR	Copernicus Imaging Microwave Radiometer
CRISTAL	Copernicus Polar Ice and Snow Topography Altimeter
DEM	Digital elevation model
DMRT	Dense-medium radiative theory
DMSP	Defense Meteorological Satellite Program
EGIG	Expédition Glaciologique Internationale Au Groenland
ERA5	ECMWF Reanalysis v5
ERS	European Remote Sensing
ESA	European Space Agency
EUMETSAT	European Organisation for the Exploitation of Meteorological Satellites
FAC	Firn air content
FDM	Firn Densification Model
FR	Frequency ratio
GrIS	Greenland ice sheet
IMAU	Institute for Marine and Atmospheric research Utrecht
JAXA	Japan Aerospace Exploration Agency
LEPTA	Leading edge point-based
LeW	Leading edge width
LR	Linear regression
LRM	Low Resolution Mode
MAR	Modèle Atmosphérique Régional (Regional Atmospheric Model)
MCoRDS	Multichannel Coherent Radar Depth Sounder
MEMLS	Microwave emission model of layered snowpacks
MIRAS	Microwave Imaging Radiometer using Aperture Synthesis
MWC	Melt water content

NASA	National Aeronautics and Space Administration
NOAA	National Oceanic and Atmospheric Administration
NSIDC	National Snow and Ice Data Center
OCOG	Offset centre of gravity
OIB	Operation IceBridge
PR	Polarisation ratio
QuikSCAT	Quick Scatterometer
RACMO	Regional Atmospheric Climate Model
RCM	Regional climate model
RF	Random forest
RMSE	Root mean square error
ROSE-L	Radar Observing System for Europe operating in L-band
RSR	Radar Statistical Reconnaissance
SAR	Synthetic aperture radar
SARIn	Synthetic Aperture Radar Interferometry
SIR	Scatterometer image reconstruction
SMB	Surface mass balance
SMRT	Snow Microwave Radiative Transfer
SSM/I	Special Sensor Microwave/Imager
SSMIS	Special Sensor Microwave Imager/Sounder
SUMup	Surface Mass Balance and Snow Depth on Sea Ice Working Group
T_B	Brightness temperature
TeS	Trailing edge slope
TKK	Helsinki University of Technology
XPGR	Cross polarization gradient ratio

1

INTRODUCTION

1.1. FIRN PROCESSES AND RESEARCH MOTIVATION

Greenland and Antarctic ice sheets have attracted increasing attention in recent decades due to observed climate change impacts and their crucial role in regulating the global climate system by influencing sea levels (van den Broeke et al., 2016; Frederikse et al., 2020), ocean circulation (Schmittner et al., 2011), and ecosystems (Constable et al., 2022). Over both ice sheets, the changes in recent decades are characterised by mass loss due to ice discharge and runoff typically originating from the firn layer (Vandecrux et al., 2019).

Firn is the intermediate state between snow and glacial ice (van den Broeke, 2008), which is formed as fresh snow accumulates on the ice sheets and undergoes metamorphism, a process where the density, grain size, grain shape, impurity of snow, and the volume of pore space change over time and depth (Obbard et al., 2011). The firn layer consists of interconnected pore spaces which, when surface melt occurs over the ice sheets, are capable of accommodating meltwater in liquid or refrozen form (Harper et al., 2012). With this feature, the firn layer acts as a buffer against the contribution of surface melt to sea-level rise (Forster et al., 2013; Machguth et al., 2016). However, when the surface melt increases due to atmospheric warming (van Angelen et al., 2013; Vandecrux et al., 2018) and to the darkening of the ice sheets (van As et al., 2013), an increased amount of meltwater refreezes in the porous firn (Harper et al., 2012; van Angelen et al., 2013); the refreezing releases latent heat in this process, subsequently increasing firn compaction and reducing the space of firn pores and their capacity to store more meltwater (van den Broeke et al., 2016; Machguth et al., 2016; Vandecrux et al., 2019). The reduction of firn pore spaces is referred to as firn air depletion, and can be parametrised by a decrease in firn air content (FAC; Vandecrux et al., 2019), a parameter defined as the vertical distance over which the firn layer can be compressed until its density reaches that of the glacial ice (917 kg m^{-3}). The increased firn compaction can be parametrised by an increase in firn density (Vandecrux et al., 2018).

In addition, an increased grain size can cause the darkening of the ice sheets, which is parametrised by a decreased surface albedo (Tedesco et al., 2016). In the snow–firn metamorphism process, the structure of firn is affected by the temperature gradient in the firn layer. A small temperature gradient allows the formation of small, well-bonded grains, while a high temperature gradient contributes to the increase of grain size (Obbard et al., 2011). In particular, surface and depth hoar crystals, typically characterised

by a decreased firn density and an increased grain size, are formed under a high temperature gradient (Fukuzawa and Akitaya, 1993). Therefore, their formation can result in a decrease in surface albedo (Flanner and Zender, 2006), which contributes to surface warming (Picard et al., 2012; van Angelen et al., 2012), the subsequent increase in meltwater production, and finally the mass loss from the ice sheets (Arthern et al., 2006).

In Greenland, melting across higher elevations and runoff across the margins can be observed (Trusel et al., 2018). The surface melt and runoff have been a main contributor of Greenland mass loss since the early 2000s (Enderlin et al., 2014), which contributes to the global sea-level rise by approximately 0.7 mm a^{-1} (van den Broeke et al., 2016). Over the entire Greenland ice sheet (GrIS), the aforementioned melt–refreezing process within the firn layer occurs. When this process reoccurs, the ability of firn to retain meltwater decreases due to firn air depletion, hence the further produced meltwater penetrates the ice layer of the ice sheet, creating a lubricating effect and resulting in an increased runoff and mass loss (Joughin et al., 2008).

Similar yet distinct processes and impacts of firn can also be observed over the Antarctic ice sheet (AIS), where the main source of mass loss is the ice loss from the land. Under normal circumstances, the ice loss is modulated by the buttressing effect of the ice shelves fringing the continent (Dupont and Alley, 2005). However, when the stability of ice shelves is disrupted by increased surface melt or instability, it can lead to increased mass loss from the land (Pritchard et al., 2012). The melt–refreeze process originating from the firn layer is a precursor of the ice-shelf collapse, as surface melt has been observed over the Antarctic ice shelves (Kingslake et al., 2017; Dunmire et al., 2020; Spergel et al., 2021; Li et al., 2021) due to climate forcing such as turbulent heat fluxes, foehn winds (Lenaerts et al., 2016; Wille et al., 2019) and regional climate warming (Scambos et al., 2000). Firn air depletion and repeated compression and uplift following melt–refreeze cycles can result in ice shelf instability, hydrofracture and collapse (van den Broeke, 2005; Banwell et al., 2013; Munneke et al., 2014; Bell et al., 2017). The collapse of Antarctic ice shelves leads to accelerated ice discharge from the land (Rignot, 2004; Scambos, 2004; Pritchard et al., 2012). For example, the West Antarctic ice sheet has shown increasing ice loss as well as instabilities (Joughin and Alley, 2011). Modelled results also depicted potential vulnerabilities of the East Antarctic ice sheet under a warming climate (Mengel and Levermann, 2014; Golledge et al., 2017; Garbe et al., 2020). Finally, the formation of depth hoar crystals can be occasionally observed over both ice sheets, which has the potential to increase surface warming (Picard et al., 2012).

To sum up, the firn over the GrIS and the AIS acts as a buffer for meltwater runoff with its pore spaces. As firn pore spaces deplete and albedo decreases, both of which contribute to ice mass loss, the resulting sea-level rise becomes a significant global concern (van den Broeke et al., 2016; Bamber et al., 2019; Frederikse et al., 2020). Given that mass loss from both the Greenland and Antarctic ice sheets often originates in the firn layer, continuous monitoring and assessment of firn conditions are essential for understanding future sea-level rise projections.

1.2. ASSESSMENT OF FIRN PROCESSES USING IN SITU AND MODELLED DATA

In this PhD thesis, the melt–refreeze process and variations in firn properties (such as firn density and grain size) are referred to as firn processes. In the aforementioned firn processes, for example, the melt–refreeze process can be usually characterised by an increase in firn density and a decrease in FAC (Nilsson et al., 2015; Otosaka et al., 2019; Vandecrux et al., 2019); the hoar crystal formation can be characterised by a decreased firn density and an increased grain size (Fukuzawa and Akitaya, 1993; Champollion et al., 2013). Typical approaches to study firn processes include field measurements (Harper et al., 2012) and firn models (Reijmer et al., 2012; Brils et al., 2022; Veldhuijsen et al., 2023).

In situ measurements generally refers to firn core measurements. By using the mass and geometry of the firn cores, the firn density can be estimated (Schaller et al., 2016; Graeter et al., 2018). Using the density, furthermore, the firn air content can be estimated with (Vandecrux et al., 2019)

$$\mathrm{FAC}_z = \sum_{k=1}^{N} m_k \left(\frac{1}{\rho_k} - \frac{1}{\rho_{\mathrm{ice}}} \right) \tag{1.1}$$

where z is the depth of the retrieved firn core, N is the number of sections composing the firn core, ρ_k and m_k are the firn density and mass at the k-th depth interval, and ρ_{ice} is the ice density conventionally assumed to be 917 kg m^{-3}. Chemical components of the firn core can also be obtained, which are an important indicator of firn processes (Capron et al., 2013; Graeter et al., 2018). The most up-to-date and standardised dataset of in situ measurements of firn properties is the Surface Mass Balance and Snow on Sea Ice Working Group (SUMup) dataset (Montgomery et al., 2018; Vandecrux et al., 2024). The dataset contains measurements of firn density, temperature and accumulation over the ice sheets collected between 1989 and 2024. Although the in situ measurements are expected to have high resolution and reliability, as they show the real firn condition at specific locations (Montgomery et al., 2018), the availability are restricted by the spatial and temporal sparsity of measurements (Brucker et al., 2011; Johnson et al., 2020).

To simulate the firn properties on a large and continuous spatial and temporal scale, as well as to complement the sparse in situ data, regional climate models (RCMs) and firn models are commonly used. In the models, a large variety of firn processes such as densification, metamorphism, retention and refreezing of meltwater have been parameterised. MAR (Modèle Atmosphérique Régional) is a widely used RCM, combining an atmospheric modelling (Gallée and Schayes, 1994) and the Soil Ice Snow Vegetation Atmosphere Transfer (SISVAT) scheme (Gallée et al., 2001). The SISVAT scheme employs a multilayered snowpack model which simulates melting, percolation, refreezing and albedo changes as a result of snow metamorphism (Brun et al., 1989, 1992; Fettweis, 2022). The IMAU Firn Densification Model (IMAU-FDM) is on the other hand a semi-empirical firn model which uses physics-based densification equations combined with parameters calibrated with observed firn density profiles (Ligtenberg et al., 2011; Veldhuijsen et al., 2023). The model can provide information on firn temperature, firn density, liquid-water content, FAC and surface height changes due to firn and surface mass

balance (SMB) processes (Veldhuijsen et al., 2023). In this model, fresh snow density and firn densification rate are expressed as a function of climate parameters, such as snow accumulation, surface temperature and wind velocity. The coefficients within the function are determined by fitting the measured firn densities to climate parameters. In Greenland, the most up-to-date version (IMAU-FDM v1.2G) defines the fresh snow density ρ_s as (Brils et al., 2022)

$$\rho_s = A_{\mathrm{GRE}} + B_{\mathrm{GRE}} \cdot T_a \tag{1.2}$$

where $\bar{T}_a$ is the annual mean near-surface (usually 2 m) air temperature, and A_{GRE} and B_{GRE} are the fit coefficients; whereas in Antarctica, ρ_s is defined by IMAU-FDM v1.2A as (Veldhuijsen et al., 2023)

$$\rho_s = A_{\mathrm{ANT}} + B_{\mathrm{ANT}} \cdot T_s + C_{\mathrm{ANT}} \cdot V_{10} \tag{1.3}$$

where T_s is the instantaneous surface temperature, V_{10} is the 10 m wind velocity, and A_{ANT}, B_{ANT} and C_{ANT} are the fit coefficients. Over time, the dry-firn densification rate is defined as (Arthern et al., 2010)

$$\frac{d\rho}{dt} = D\dot{b}g(\rho_{\mathrm{ice}} - \rho)e^{-\frac{E_C}{RT} + \frac{E_g}{RT_{ave}}} \tag{1.4}$$

where $\dot{b}$ is the long-term average accumulation rate, g is the gravitational acceleration, ρ is the density of the layer, E_c and E_g are the activation energies for creep and grain growth, respectively, R is the gas constant, T is the instantaneous layer temperature, T_{ave} is the long-term average surface skin temperature, and D is a constant determined empirically, which can be 0.03 or 0.07 depending on ρ. The FAC is also available in IMAU-FDM, calculated as (Brils et al., 2022)

$$\mathrm{FAC} = \sum_{j}^{n_z} \frac{\rho_{\mathrm{ice}} - \rho_j}{\rho_{\mathrm{ice}}} \Delta z_j \tag{1.5}$$

where n_z is the number of layers in the modelled firn profile, and ρ_j and Δz_j are the firn density and thickness of the j-th layer, respectively.

Despite the high availability of the models, inter-comparisons between different models as well as between models and available field measurements show discrepancies, which means that not all the processes or local climate phenomena are described adequately (Reijmer et al., 2012; Keenan et al., 2021). For example, MAR does not include drifting snow transport fluxes, which can result in a bias in modelled SMB (Agosta et al., 2019; Kittel et al., 2021); a simplification of accumulation can cause a bias in the modelled surface elevation in IMAU-FDM (Veldhuijsen et al., 2023); in IMAU-FDM v1.2G, the effect of wind velocity on fresh snow has not been parametrised due to insufficient wind measurements over Greenland, while in IMAU-FDM v1.2A, the linear relationship between fresh snow and wind velocity can be an over simplification (Veldhuijsen et al., 2023). Furthermore, the coarse spatial resolution of models cannot capture the small-scale, local climate phenomena (Dethinne et al., 2023). Therefore, new methods are necessary to assess and monitor firn processes.

1.3. SATELLITE REMOTE SENSING FOR ICE SHEETS

The recent developments in satellite remote sensing techniques have demonstrated potential for assessing firn processes as they can overcome spatial and temporal restrictions. However, how physical phenomena over GrIS and AIS influence signals acquired from remote sensing instruments remains to be better explored. Efforts have been made to simulate satellite signals through radiative transfer modelling. The inputs of the models typically include firn properties such as firn density, temperature, grain size (or correlation length) and microstructure. The developments of the microwave emission model of layered snowpacks (MEMLS; Mätzler and Wiesmann, 1999; Wiesmann and Mätzler, 1999), the Helsinki University of Technology (HUT, now referred to as TKK; Pulliainen et al., 1999) model, and the dense-medium radiative theory (DMRT; Tsang et al., 2000) enable the modelling of passive satellite signals, among which DMRT and MEMLS can also simulate active satellite signals (Tsang et al., 2007; Proksch et al., 2015). In addition, multiple radiative transfer modelling theories have been integrated into the Snow Microwave Radiative Transfer (SMRT) thermal emission and backscatter model (Picard et al., 2018; Larue et al., 2021). Despite these advancements, however, all models exhibit uncertainties compared to real satellite signals due to various assumptions on layering and characterisations of scatterers (Tedesco and Kim, 2006). The surface roughness is also under-represented in modelling active signals (Larue et al., 2021; Shukla et al., 2024). As such, the interpretation of satellite signals in relation to firn processes remains a significant challenge. This PhD therefore aims to address this gap by leveraging datasets from multiple satellite missions covering Greenland and Antarctica over a long period. This PhD will be data-driven, where the focus is to interpret the combination of long-term satellite data time series, with the help of radiative transfer modelling as well as the firn models. Using the satellite missions with different measurement principles and operating in different frequencies, this PhD will offer a more integrated understanding of firn processes across the Greenland and Antarctic ice sheets.

Various studies have been conducted using satellite remote sensing techniques to study different aspects (e.g. elevation change, ice velocity) and geophysical phenomena (e.g. melt and refreezing, precipitation) of the cryosphere, especially over GrIS and AIS. This thesis focuses on the use of satellite radiometers, scatterometers and altimeters to assess the long-term firn processes. The major advantage of satellite radiometers, scatterometers and radar altimeters is that their measurements are not hindered by the varying weather conditions, such as cloud and rain (Brucker et al., 2010; Picard et al., 2012; Ridley and Partington, 1988). Their ability of penetrating into the firn layer by decimetres to metres (Surdyk, 2002; Michel et al., 2014; Nilsson et al., 2015) also facilitates the monitoring of firn processes, such as the variations in firn density (Nilsson et al., 2015) and grain size (Brucker et al., 2010). In addition, although the operating frequency is comparable between a satellite scatterometer and a synthetic aperture radar (SAR), the satellite scatterometer has the advantage of a higher data availability both spatially and temporally over both Greenland and Antarctica, allowing a more continuous monitoring of firn processes. Finally, the high accuracy and little penetration ability of satellite laser altimeters make them a reliable reference for the surface height of the firn layer. This feature is especially beneficial, when the derivation of penetration bias of radar signals is required. Typically, satellite radiometers and scatterometers are used for melt detec-

tion, while satellite altimeters are used for estimating elevation changes of the ice sheets. However, due to the impact of firn processes on radar scattering, these satellite sensors all have the potential of revealing firn processes including melt–refreezing process, and variations in firn density and grain size. For a general understanding of the state of the art, the typical instruments, applications and potentials of satellite remote sensing missions on GrIS and AIS are elucidated in the following sub-sections.

1.3.1. MICROWAVE RADIOMETERS

The microwave radiometer is a calibrated passive microwave receiver that measures thermally-emitted electromagnetic radiation. The amount of radiation a microwave radiometer receives is expressed as the equivalent blackbody temperature or brightness temperature (Le Vine and Skou, 2006). According to Planck's Law, for a blackbody, the specific intensity is given by (Lubin and Massom, 2006):

$$B_\lambda(T) = \frac{2hc^2\lambda^{-5}}{\exp(hc/\lambda kT) - 1} \tag{1.6}$$

where c is the speed of light in a vacuum, h is Planck's constant, k is Boltzmann's constant, λ is the wavelength and T is the absolute temperature. In the microwave (centimetre) wavelengths, $hc/\lambda kT \ll 1$, therefore Eq. 1.6 reduces to the Rayleigh-Jeans approximation (Lubin and Massom, 2006):

$$B_\lambda(T) = \frac{2ckT}{\lambda^4} \tag{1.7}$$

The measured radiation intensity $B_\lambda(T)$ divided by $\frac{2ck}{\lambda^4}$ is therefore referred to as brightness temperature (T_B). Depending on the configuration and utilisation of different satellite microwave radiometers, the sensors measure T_B at a range of frequencies and in horizontal or vertical polarisation. The most recent available satellite sensors providing T_B datasets are summarised in Table 1.1; the AMSR-U instruments are from Japan Aerospace Exploration Agency (JAXA); AMSU-B was from National Oceanic and Atmospheric Administration (NOAA); MIRAS onboard Soil Moisture and Ocean Salinity (SMOS) is from European Space Agency (ESA); and SSM/I and SSMIS are from the Defense Meteorological Satellite Program (DMSP). An example of the T_B data from SSMIS over Antarctica and Greenland is shown in Figure 1.1, where the T_B is acquired from the vertically and horizontally polarised channels of 19 GHz, and averaged over the entire period between 2011 and 2020. Over both ice sheets, high T_B values (> 240 K) are generally observed in coastal areas where atmospheric warming and recurrent melting occur (Kingslake et al., 2017; Tedesco and Fettweis, 2020). However, T_B values decrease in regions where an increasing heterogeneity of the firn–ice transition occurs due to occasional melting (Nicolas et al., 2017; Tedesco and Fettweis, 2020), causing an increasing scattering (Houtz et al., 2021), such as in West Antarctica close to the Ross Sea, and the percolation zone of Greenland. Overall, T_B values from the vertical polarisation are approximately 20 K higher than those from the horizontal polarisation.

The typical applications of satellite microwave radiometers for studying ice sheets include snow melt detection and snow metamorphism observation.

Table 1.1: Available satellite microwave radiometry sensors that provide recent brightness temperature measurements. For polarisation, H represents horizontal and V represents vertical. The Advanced Microwave Scanning Radiometer Unified (AMSR-U) observations incorporate observations from the Advanced Microwave Scanning Radiometer - Earth Observing System Sensor (AMSR-E) and the Advanced Microwave Scanning Radiometer2 (AMSR2) sensor.

Sensor name	Frequency	Polarisation	Incidence angle	Available spatial resolution
Advanced Microwave Scanning Radiometer Unified (AMSR-U)	18.7 GHz 23.8 GHz 36.5 GHz 89.0 GHz	H & V H & V H & V H & V	55 °	12.5 km or 25 km 12.5 km or 25 km 12.5 km or 25 km 6.25 km or 12.5 km
Advanced Microwave Sounding Unit B (AMSU-B)	89 GHz 150 GHz	V V	48 °	16 km 16 km
Microwave Imaging Radiometer using Aperture Synthesis (MIRAS)	L-band (1.4 GHz)	H & V	42.5 °	30–50 km
Special Sensor Microwave/Imager (SSM/I)	19 GHz 22 GHz 37 GHz 85 GHz	H & V V H & V H & V	53 °	25 km 25 km 25 km 12.5 km
Special Sensor Microwave Imager/Sounder (SSMIS)	19 GHz 22 GHz 37 GHz 91 GHz	H & V V H & V H & V	53 °	25 km 25 km 25 km 12.5 km

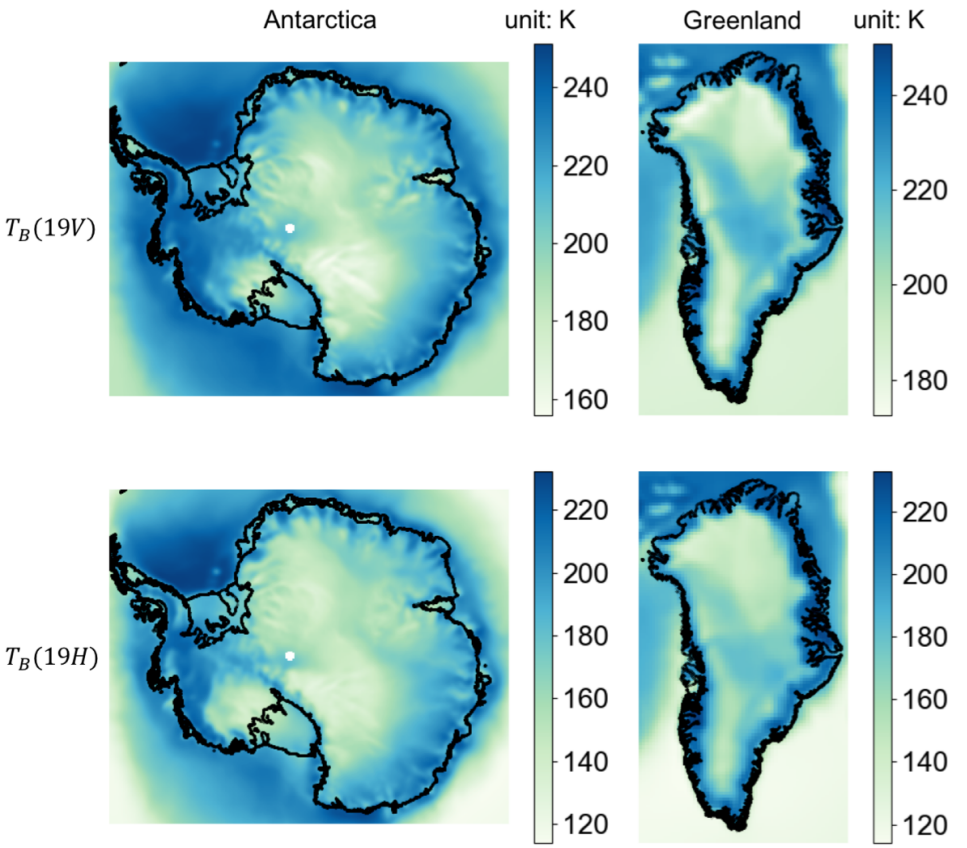

Figure 1.1: SSMIS brightness temperatures (T_B) from 19 GHz, both vertical and horizontal channels over AIS and GrIS, temporally averaged between 2011 and 2020. The T_B data are acquired from the National Snow and Ice Data Center (NSIDC; Meier et al., 2021); the coastline of AIS is from Depoorter et al. (2013) and the coastline of GrIS is from Gerrish (2020).

MELT DETECTION USING SATELLITE RADIOMETERS

A variety of methods have been developed to detect melt events based on the considerably increasing T_B as a consequence of an increase in liquid water content and hence an increase in the imaginary part of snow permittivity (Ulaby et al., 1986; Tedesco, 2007). Melt detection is usually performed on time series of T_B (19 GHz or 37 GHz) or parameters derived from multiple channels of T_B.

Using a single channel of T_B time series, Mote et al. (1993) and Zwally and Fiegles (1994) detect melt in Greenland and the Antarctic Peninsula, respectively, when T_B exceeds a threshold over the winter average. Such a threshold varies depending on the exact location of pixel, and is re-calculated every year. Based on the Zwally and Fiegles (1994) study, Torinesi et al. (2003) adopted T_B time series acquired with the 19 GHz horizontal polarisation channel to detect melt on AIS with a two-fold detection method. T_B values that are 30 K above the T_B values averaged over the entire studied time and region

are first masked out as strong melt signals. After masking out the strong melt, the mean and standard deviation of T_B are computed, and T_B values deviating from the mean by 3 times of the standard deviation are identified as melt.

Another typical method to detect melt is a clustering approach. Johnson et al. (2020) proposed a K-means approach, where T_B time series are divided into two clusters using K-means clustering method. However, comparison of different methods shows large differences in detecting melt, and the performances of all methods vary spatially; ice lenses and firn stratigraphy can also bias the detection results (Johnson et al., 2020).

The combination of different channels, furthermore, can facilitate melt detection as meltwater has a larger impact on emissions at a higher frequency. Abdalati and Steffen (1995) proposed a T_B-derived parameter, cross polarisation gradient ratio (XPGR), defined as

$$\mathrm{XPGR} = \frac{T_B(19\mathrm{H}) - T_B(37\mathrm{V})}{T_B(19\mathrm{H}) + T_B(37\mathrm{V})} \tag{1.8}$$

where $T_B(19\mathrm{H})$ is the T_B from the 19 GHz horizontal polarisation channel, and $T_B(37\mathrm{V})$ is the T_B from the 37 GHz vertical polarisation channel. The threshold of XPGR, above which melt is detected, is dependent on the instrument; for SSM/I and SSMIS, the threshold for XPGR is -0.0158 (Abdalati and Steffen, 1997; Johnson et al., 2020).

OBSERVATION OF VARIATIONS IN FIRN PROPERTIES USING SATELLITE RADIOMETERS

The observation of snow metamorphism using satellite microwave radiometers is focused on temporal variations of snow grain sizes on AIS, which have an impact on snow albedo (Flanner and Zender, 2006; Picard et al., 2012). Due to the insufficient data on AIS snow albedo, Picard et al. (2012) used satellite radiometry (AMSU-B) to obtain information on snow grain size which can then be used to estimate snow albedo. The study defined snow grain index (GI) as

$$\mathrm{GI} = 1 - T_B(150\mathrm{GHz}) / T_B(89\mathrm{GHz}) \tag{1.9}$$

which increases as grain size increases.

Champollion et al. (2013) conducted a study utilising the 18.7 GHz and 36.5 GHz channels of AMSR-E to observe hoar-crystal formation and disappearance at Dome C, Antarctica. For both frequencies, the study defined a polarisation ratio (PR) as

$$\mathrm{PR}(f) = T_B(f, \mathrm{H}) / T_B(f, \mathrm{V}) \tag{1.10}$$

where f represents the frequency, and H and V refer to horizontal and vertical polarisation channel, respectively. The hoar-crystal formation is characterised by a decrease in snow density and an increase in snow grain size, which is linked to an increase in PR (Champollion et al., 2013). Using ESA's SMOS satellite data, Leduc-Leballeur et al. (2017) correlated the increase of H-polarisation T_B to low-density hoar crystal formation, and the decrease of the T_B to a storm that removed or compacted the layer of the surface light snow. However, the aforementioned studies are conducted at Dome C, within a temporal period when field measurements were available; whether the methods can be valid in a wider range of locations and temporal periods remains to be assessed.

1

1.3.2. SCATTEROMETERS

Scatterometers are side-looking, active instruments that emit microwave signals and receive the reflected signals from the objects in the line-of-sight (Hanssen, 2001). For an illuminated surface, the received power (P_r) is expressed as (Ulaby et al., 2019):

$$P_r(\theta_a, \phi_a) = \frac{P_t G^2(\theta_a, \phi_a)\lambda^2}{(4\pi)^3 R^4}\sigma \tag{1.11}$$

where P_t is the transmitted power, G is the antenna gain, (θ_a, ϕ_a) is the direction from the radar to the target, R is the range between the surface and the sensor, λ is the wavelength, and σ is the radar cross section (RCS) of the observed surface. The observation is usually referred to as sigma-nought (σ^0), which is defined as the RCS normalised with respect to the surface area A (Ulaby et al., 2019):

$$\sigma^0 = \sigma / A \tag{1.12}$$

and is expressed in the unit of decibel (dB). The most recent satellite scatterometers include the Ku-band (13.4 GHz) Quick Scatterometer (QuikSCAT) from National Aeronautics and Space Administration (NASA) and the C-band (5.255 GHz) Advanced Scatterometer (ASCAT) from European Organisation for the Exploitation of Meteorological Satellites (EUMETSAT). The available spatial resolutions of σ^0 are originally approximately 25 km, and are enhanced to 4.45 km using the scatterometer image reconstruction (SIR) algorithm (Long et al., 1993; Early and Long, 2001; Trusel et al., 2012). Both instruments can provide data from daily polar overpasses. In addition, the SIR algorithm provides ASCAT σ^0 normalised to a reference incidence angle, conventionally defined as 40 ° (Lindsley and Long, 2010). An example of the normalised σ^0 data from ASCAT over Antarctica and Greenland is provided in Figure 1.2. Over Antarctica, higher σ^0 (between −15 dB and −5 dB) can be observed mainly over the high-elevation regions with megadunes and regions with undulating topography (Fahnestock et al., 2000; Fraser et al., 2016). Towards the coastal regions, low σ^0 (< −15 dB) can be observed. Fraser et al. (2016) attributed the low σ^0 primarily to a high precipitation, as a higher thickness of the firn layer cased by the high precipitation increases the on-way loss of the radar signal (Drinkwater, 1989). Over Greenland, the highest σ^0 values (> −5 dB) are observed in the percolation zone, where the occasional melt–refreezing processes produce ice lenses that are characterised by a high ice grain and act as a strong scatterer (Long and Drinkwater, 1994). The low σ^0 (between −15 dB and −10 dB) in central Greenland is due to the weak volume scattering of the fine-grained firn, while the comparably low σ^0 in the Greenland ablation zone is due to the lack of volume scattering caused by a uniform refrozen layer (Joughin et al., 2016).

Scatterometers are typically used to detect melt and interpret the surface or near-surface snow or firn properties in the dry snow zone of ice sheets.

MELT DETECTION USING SATELLITE SCATTEROMETERS

The common practice of using backscatter intensity information for melt detection involves thresholding, as σ^0 is greatly reduced by the high dielectric constant of liquid water due to a reduced volume scattering and an increased microwave absorption (Stiles and Ulaby, 1980). The melt detection approaches over both GrIS and Antarctic ice shelves

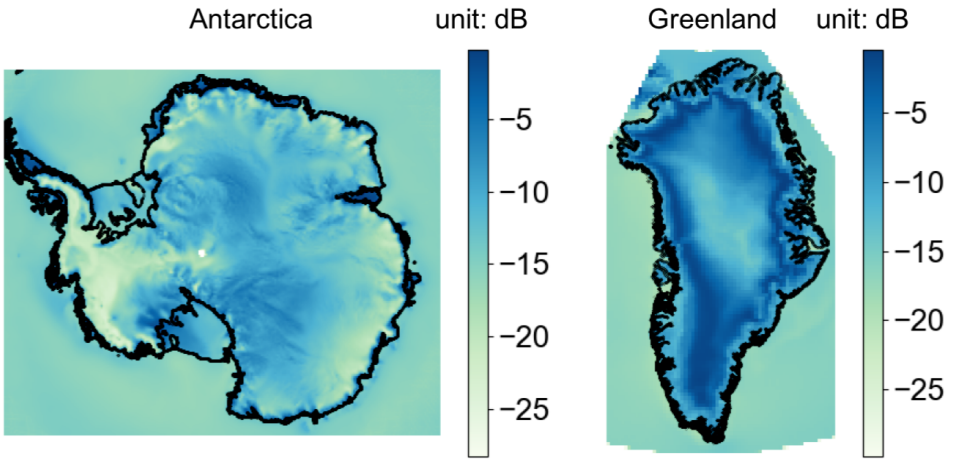

Figure 1.2: ASCAT backscatter intensity (σ^0) normalised to 40° incidence angle over AIS and GrIS, temporally averaged between 2011 and 2020. The σ^0 data are acquired from Brigham Young University (BYU) Microwave Earth Remote Sensing (MERS) laboratory (2010), and down-sampled to the same spatial resolution of NSIDC's Polar Stereographic Projection; the coastline of AIS is from Depoorter et al. (2013) and the coastline of GrIS is from Gerrish (2020).

usually use a reduction in σ^0 compared with its winter mean; for each pixel, melting day (MD) is defined as

$$\mathrm{MD} = \begin{cases} 1, & \text{if } \sigma_i^0 < \overline{\sigma_w^0} - b \\ 0, & \text{if } \sigma_i^0 \geq \overline{\sigma_w^0} - b \end{cases} \tag{1.13}$$

where σ_i^0 is the ith daily backscatter value for a pixel, $\overline{\sigma_w^0}$ is the mean austral winter backscatter per pixel before the melting season, and b is an empirically determined threshold. Common choices of b can vary between 2 dB using Ku-band QuikSCAT (Trusel et al., 2012) and 3 dB using C-band scatterometer and SAR (Nagler and Rott, 2000; Wismann, 2000; Luckman et al., 2014; Johnson et al., 2020).

ASSESSMENT OF FIRN PROPERTIES USING SATELLITE SCATTEROMETERS

Apart from melt events, various studies have tried to explore the relationship between σ^0 and other firn properties, however such relationship is not straightforward and can be driven by multiple surface processes simultaneously. A comparison between snow accumulation and σ^0 from C-band and Ku-band scatterometer in dry-snow zones of GrIS was performed by Drinkwater et al. (2001). The study cannot derive an explicit relationship between snow accumulation and C-band σ^0, but can establish a relatively more direct negative correlation between snow accumulation and Ku-band σ^0. Rotschky et al. (2006) assessed snow accumulation as a linear function of C-band and Ku-band σ^0. While a negative correlation between σ^0 and accumulation is valid along certain (sub-)transects over AIS, the correlation established by the study is restricted to low-accumulation dry snow zone areas. The conclusion is especially compromised with the presence of small-scale surface roughness features or scattering layers, such as ice lenses and depth hoar.

Fraser et al. (2016) explored the relationship between normalised ASCAT σ^0 and parameters from atmospheric and firn models, such as slope aspect, precipitation, surface temperature, wind speed and persistence, upper 1 m grain size, and upper 1 m firn density, between July 2007 and January 2012. The study manages to reconstruct the long-term mean σ^0 using the modelled atmospheric and firn parameters, and establishes a correlation between σ^0 and precipitation on long timescales in dry snow zones of AIS. On average, the upper 1 m grain size has a positive correlation with σ^0. The upper 1 m density shows a reasonably negative correlation with σ^0. However, both density and grain size are not as highly correlated with σ^0 as precipitation. The correlation between the seasonal cycle of both parameters and the σ^0 cycle also cannot be established. Finally, the study shows strong links between σ^0 and temperature anomalies.

The aforementioned studies show that using the σ^0 information from scatterometer and SAR is promising in assessing certain firn processes, i.e. melt and accumulation. It is important to note that the relationship between σ^0 and snow accumulation is not applicable to areas with melting, as subsurface meltwater retention and refrozen layer can bias σ^0 (Fraser et al., 2016). Furthermore, while dry snow grain size and density can be drivers of σ^0 variation, they are driven by firn temperature, surface precipitation and wind which are also divers of variations in multiple satellite signals. Therefore, a multi-source remote sensing data assimilation method is expected to improve the assessment in this aspect (Fraser et al., 2016).

1.3.3. ALTIMETERS

The altimeter is an active, nadir-looking instrument that emits pulses and receives the reflected pulses from the Earth surface. Depending on the measurement principles, satellite altimeters can be categorised into radar altimeter, which sends microwave pulses to the ground and receives the echos as waveforms (Chelton et al., 2001; Quartly et al., 2021), and laser altimeter, which sends laser pulses to the ground and receives the reflected photons and their travel times (Smith et al., 2019). The most recent and available satellite missions with radar altimeters include European Remote Sensing (ERS) satellites ERS-1, ERS-2, Envisat, CryoSat-2 and Sentinel-3 from ESA, operating in Ku-band; Envisat also operates in S-band in addition. The most recent satellite missions with laser altimeters are Ice Cloud and land Elevation Satellite (ICESat) and ICESat-2 from NASA; the laser of both altimeters is at 532 nm.

Among the satellite radar altimeter missions, CryoSat-2 has the advantage of being operated in different modes: the Low Resolution Mode (LRM) is a conventional pulse-limited altimeter which illuminates the measured surface with a 1.65 km diameter pulse-limited footprint (Schneider et al., 2018); the Synthetic Aperture Radar (SAR) transmits a burst of pulses and reduces the along-track footprint to 300 m with Delay-Doppler processing (Schneider et al., 2018; Abdalla et al., 2018); and the Synthetic Aperture Radar Interferometry (SARIn) mode uses two antennas to derive the across-track angle by calculating the difference between the measurements from different antennas (Jensen, 1999; Wingham et al., 2004; Schneider et al., 2018; Aublanc et al., 2021). To derive height estimates from radar altimetry operated in all modes, a retracking process which identifies the location of the surface echo in the waveform needs to be performed (Otosaka et al., 2019). For the polar regions, LRM is operated over ice-sheet interiors, SAR mode is

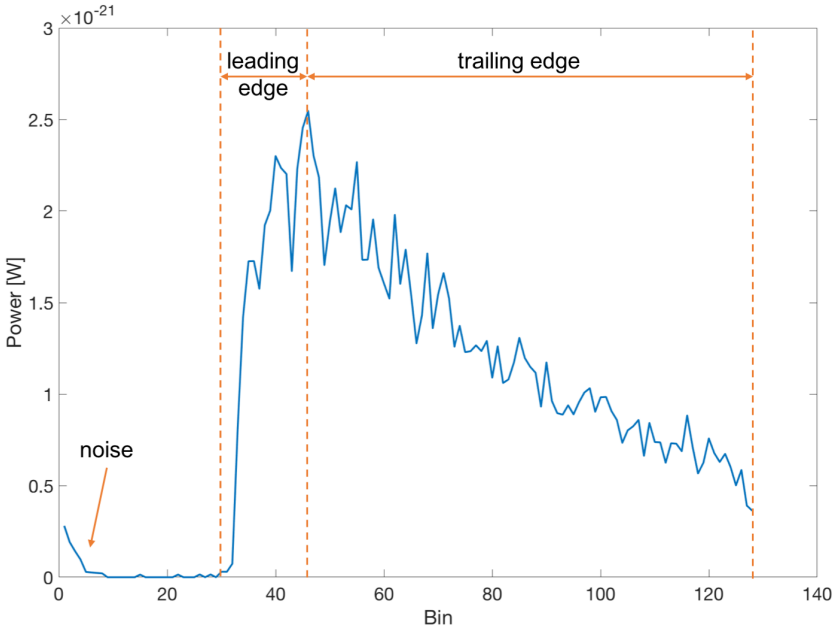

Figure 1.3: An example of a radar altimeter waveform from CryoSat-2 Low Resolution Mode (LRM) over Greenland. Leading edge and trailing edge are key features used for various studies.

operated over the oceans, and SARIn mode is operated over ice-sheet margins (Calafat et al., 2017). An example of a LRM waveform is illustrated in Figure 1.3, with key features labelled. The backscatter intensity can also be calculated from the waveform and expressed as σ^0; the method of σ^0 calculation depends on the retracking method (Gommenginger et al., 2010).

Pulse-limited radar altimeters and laser altimeters are primarily used in deriving ice-sheet elevation or SMB changes. Various studies have been conducted over both Greenland and Antarctica over different time periods and, different satellite radar altimeters have been employed accordingly, including ERS-1, ERS-2, Envisat, and CryoSat-2 (Davis and Ferguson, 2004; Zwally et al., 2005; Khvorostovsky, 2012; Flament and Rémy, 2012; Liu et al., 2023). When deriving elevation changes from radar altimeters, uncertainties can be introduced due to radar penetration into snow and the impact of near-surface snow properties on radar signals (Rémy and Parouty, 2009). Different processing methods for radar altimetry data and for correction of waveform parameters can also introduce biases in such estimations (Simonsen and Sørensen, 2017). Laser altimeters, on the other hand, reduces the uncertainties introduced by radar waveform processing and snow penetration effects. By comparing heights derived from ERS-2 and obtained from ICESat, Thomas et al. (2008) demonstrated that the radar altimeter has a lower height estimate than the laser altimeter due to the penetration effect when snowfall occurs, while a lifted height from radar altimeter can be observed due to the melt events.

Although the radar penetration acts as an error source in the study of ice-sheet el-

evation changes, it facilitates the study of firn properties. Brenner et al. (2007) compared Envisat elevation measurements with ICESat measurements over GrIS and AIS, and showed that when the surface slope is below 0.1 °, the difference between Envisat and ICESat was 9 cm over GrIS and −40 cm over AIS. Michel et al. (2014) calculated the difference between Envisat and ICESat, and showed that the difference varied between −1 m and −0.5 m over AIS. Although the results can be retracker-dependent (Brenner et al., 2007), both studies indicated the penetration depth of Ku-band radar into snow. Tran et al. (2008) combined the dual-frequency σ^0 from Envisat and the T_B and T_B ratio from ERS satellites to classify the snow types over GrIS and AIS, and managed to distinguish melt zones in GrIS. Following the intensive melt event over GrIS in 2012, Nilsson et al. (2015) studied the time series of several parameters derived from radar altimeter waveforms: the backscatter intensity σ^0, the leading edge width (LeW), the trailing edge slope (TeS), the waveform peakiness, and the elevation difference between CryoSat-2 elevations and a reference DEM. The study showed that the intensive melt event can be observed in the time series as an increase in σ^0, peakiness and elevation difference, and as a drop in LeW and TeS. This indicates that the formation of ice lenses following the meltwater refreezing results in a specular surface and a reduction of penetration depth. Adodo et al. (2018) assessed the spatial and temporal variations of Ku-band σ^0 in Antarctica with an electromagnetic model, and showed that the σ^0 variation over the interior or flat regions is dominated by volume scattering, and in the other regions dominated by surface scattering. Larue et al. (2021) translated field measurements of firn properties in Antarctica into waveforms using a radiative transfer model. Using CryoSat-2 σ^0, Scanlan et al. (2023) derived an inverted backscattering model to estimate surface roughness and density over GrIS between 2013 and 2019.

Finally, while Michel et al. (2014) and Nilsson et al. (2015) derived and demonstrated the Ku-band penetration depths, their application of such depths is mainly focused on the flat regions of AIS and GrIS. Over terrains with more complex topography, slope-induced errors should be better corrected for, as Ku-band penetration depths are usually at the centimetre and decimetre level, whilst the slope-induced errors are at the metre level (Levinsen et al., 2016). Conventional correction methods show compromised performances over both AIS and GrIS (Roemer et al., 2007; Levinsen et al., 2016), therefore improvements are required in this aspect.

1.4. RESEARCH OBJECTIVES

The aforementioned studies demonstrate overall well-established methods for satellite radiometers and scatterometers to detect surface melt, and for altimeters to estimate elevation changes over ice sheets. However, studies that explored how variations in firn properties can affect satellite observations usually lack the discussion on whether one can deduce the firn property variations from satellite observations. For instance, the correlation of radiometer and scatterometer observations with temperature, precipitation and wind (Champollion et al., 2013; Fraser et al., 2016) shows the theoretical potential of these observations in assessing firn properties over dry snow zones (mainly located in AIS). On the other hand, due to radar's penetration into firn, the waveform information from radar altimeter can indicate sub-surface firn property variations, which are most influenced by melt and subsequent ice-lens formation (Nilsson et al., 2015). In

particular, the height difference between laser and radar altimeters can be an indicator of penetration depth (Michel et al., 2014; Nilsson et al., 2015), and the variations in leading edge width (LeW) can be indicative of variations in volume scattering. Currently, a long-term and ice-sheet-wide study of the aforementioned potentials has not yet been performed. Furthermore, the slope-induced error in radar altimeter has a major influence on studying the radar penetration depth in firn, hence should be better accounted for before studying the penetration effect of radar altimetry.

Therefore, this PhD aims to explore the possibility of using the spatio-temporal variations in satellite observations to interpret variations in firn properties. Specifically, we explore the novel methods to utilise and interpret radiometer, scatterometer and altimeter observations with respect to firn processes. This PhD exploits the impact of varying firn densities on radiometer and scatterometer data, and the impact of melt–refreezing cycles on altimeter data. In this PhD, decadal, ice-sheet wide time series of satellite measurements will be processed, and interpreted with the help of the most advanced firn models as well as radiative transfer models. Within this process, a method to improve the correction of slope-induced errors in radar altimeter height estimates will be proposed and assessed. The detailed research objectives are hence formulated into the following research questions:

- **What is the added value of combining radiometer and scatterometer data in estimating firn density in the Antarctic dry-snow zone?**

  Firn density is one of the most indicative parameters of firn status, as their variation can contribute to the varying estimation of SMB and the subsequent sea-level change. While many climate and snow models are created to estimate firn density profiles over AIS, discrepancies may occur between the modelled densities and the real densities. Previous studies showed that the precise mechanisms underlying the impact of firn density on either T_B from radiometers or σ^0 from scatterometers were not always fully understood, as a linear relationship between firn densities and satellite observations could not be established. However, as firn densities theoretically have an impact on microwave scattering properties, we aim to propose and assess a method to estimate firn densities using satellite microwave data and a non-linear model. Furthermore, melt events and subsequent refreezing can also introduce anomalous microwave signals which hinder the interpretation and quantification. As a simple thresholding method for melt detection can also be associated with uncertainties, depending on the particular threshold used to define melts, we propose a melt-detection method where we exploit the long-term time series of T_B and σ^0. The study is two-fold: firstly, we use a combination of T_B and σ^0 time series anomalies to identify dry regions using an unsupervised approach. Secondly, a combination of T_B and σ^0 time series is used as input to a random forest (RF) regressor to estimate firn densities in dry regions. Due to the sparsity of field measurements, we use modelled densities from IMAU-FDM as a priori density data. A part of the modelled densities is used for training the RF regressor, and the IMAU-FDM densities are also used to assess the performance of RF.

- **How can radar altimeter waveform information be used to improve the correction for slope-induced errors in height estimation?**

Assessments of the volume scattering properties of radar altimeter signals within the firn layer often require deriving variations in the penetration ability of radar. The penetration ability is assessed by comparing the radar altimeter height estimates with a reference surface height. However, errors can be introduced in the interior of Greenland where conventional pulse-limited radar altimeters are operated due to certain undulations of topography and the large pulse-limited footprint of radar altimeters. Since the leading edge of radar can be affected by surface scattering, we propose a method adopting leading edge information of the radar altimeter waveform to correct for slope-induced errors by identifying potential points on the ground that have an impact on the leading edge. The method will be compared with standard ESA products and methods from previous studies. Factors that can potentially affect the performance of our method will be identified and sensitivity analyses will be performed.

- **To what extent can a long-term analysis of radar altimeter data improve the understanding of firn processes over Greenland?**

  Previous studies have shown that the waveform information from radar altimeters can be affected by variations in firn processes through varying surface and volume scattering. Among all the parameters derived from radar altimeter waveform, the leading edge width (LeW) is a parameter sensitive to the reduction of penetration depth following a melt event, showing a simultaneous reduction. The subsequent long-term LeW variation should also be indicative of the new-snow deposition: the new snow is characterised by fine grain with low densities, contrary to the high-density, subsurface reflective ice lenses. As new snow deposits, it forms a firn layer with regular volume scatterers, increases the penetration ability of radar altimeter signal, and hence the LeW increases. However, surface scattering, mainly due to topography and surface roughness, can also affect LeW variations. Therefore, this study explores the spatial and temporal variations of LeW, and compares the variations with external datasets indicating both surface and volume scattering to assess the potential and limitations of using long-term time series of LeW to indicate the variations in Greenland firn volume scattering. In addition, this study also tries to derive the penetration depth of Ku-band radar altimeter by computing the height difference between laser and radar altimeters. In deriving the height with the radar altimeter, the novel approach to correct for slope-induced errors proposed in this study is adopted. The penetration depth is also used to support the interpretation of LeW variations and to provide indications for future studies. Based on the analysis of the long-term LeW variations, finally, we aim to provide an assessment of the firn conditions over Greenland.

The first research question aims to develop a machine-learning method that estimates the firn density in dry-firn zones. The second research question serves as a preliminary research to the third research question: by improving the accuracy of height estimation using pulse-limited radar altimeter, the penetration ability of the radar altimeter signal into firn can be reliably estimated. The third research question focuses on the melt–refreezing patterns over Greenland, where the abrupt high-density ice layers form within the firn instead of the conventional firn densification process (e.g. over

Antarctic dry zones). By investigating these research questions, this PhD will cover the study of both dry and melt firn conditions over the ice sheets using long-term satellite data. It will also provide indications for future studies to effectively integrate the satellite data into models that could potentially monitor firn processes over Greenland, Antarctica and small ice caps worldwide.

The satellite data utilised in this PhD are listed as follows:

- Radiometer data: SSMIS, 19 GHz and 37 GHz, both vertical and horizontal polarisation;
- Scatterometer data: ASCAT;
- Radar altimeter data: CryoSat-2 operating in LRM, Level-1b (L1b) and Level-2I (L2I);
- Laser altimeter: ICESat-2 L3A Land Ice Height (ATL06) product.

1.5. THESIS ROAD-MAP

Based on the aforementioned motivation, the state of the art and the objectives, this PhD thesis is unfolded as follows.

Research question 1 is addressed in Chapter 2 by combining SSMIS T_B and ASCAT σ^0 to identify non-melt zones in AIS with a clustering approach and to estimate the firn densities over these zones using a random forest approach. This chapter aims to provide insights into the possibility of using a combined satellite dataset and a machine learning method to estimate unknown firn densities from the known ones. It is important to note that due to the limited availability of continuous field measurements, our "known densities" are modelled densities from a firn densification model (FDM). The performance of our method will be assessed and the potentials and limitations will be analysed.

Chapter 3 focuses on research question 2, where we compare our novel method to correct for slope-induced errors in pulse-limited radar altimeters with previous methods. The region of interest is the interior of GrIS. Data from CryoSat-2 LRM L1b will be used to obtain height assessments from a "slope" method, a "point-based" method and our novel method. CryoSat-2 LRM L2I heights will also be used as comparison. Our results are validated using height measurements from ICESat-2 ATL06 product, as we assume the heights obtained by laser altimeters to be a proxy of the surface height. We also perform a sensitivity analysis by tuning several parameters that can affect the performance of our method, such as the definition of LeW, the retracker threshold, the DEM bias and the DEM resolution.

Chapter 4 aims to answer research question 3. In this chapter, we use CryoSat-2 LRM L1b data to derive LeW and heights. The heights are then subtracted by ICESat-2 ATL06 heights to obtain a proxy of radar penetration ability. By analysing the time series of the obtained parameters, we can identify the formation of ice lenses from a melt–refreeze process over GrIS and assess the subsequent snow deposition and firn status. The density profiles from a regional atmospheric model (MAR) and an FDM, the available field measurements of densities, and available airborne radar data will be used as reference.

Chapter 5 lists the conclusions of this PhD, summarises the answers to the research questions, and provides analyses and recommendations for further works.

1

BIBLIOGRAPHY

Abdalati, W. and Steffen, K.: Passive microwave-derived snow melt regions on the Greenland Ice Sheet, Geophysical Research Letters, 22, 787–790, https://doi.org/https://doi.org/10.1029/95GL00433, 1995.

Abdalati, W. and Steffen, K.: Snowmelt on the Greenland Ice Sheet as Derived from Passive Microwave Satellite Data, Journal of Climate, 10, 165–175, https://doi.org/10.1175/1520-0442(1997)010<0165:sotgis>2.0.co;2, 1997.

Abdalla, S., Dinardo, S., Benveniste, J., and Janssen, P. A.: Assessment of CryoSat-2 SAR mode wind and wave data, Advances in Space Research, 62, 1421–1433, https://doi.org/10.1016/j.asr.2018.01.044, 2018.

Adodo, F. I., Remy, F., and Picard, G.: Seasonal variations of the backscattering coefficient measured by radar altimeters over the Antarctic Ice Sheet, The Cryosphere, 12, 1767–1778, https://doi.org/10.5194/tc-12-1767-2018, 2018.

Agosta, C., Amory, C., Kittel, C., Orsi, A., Favier, V., Gallée, H., van den Broeke, M. R., Lenaerts, J. T. M., van Wessem, J. M., van de Berg, W. J., and Fettweis, X.: Estimation of the Antarctic surface mass balance using the regional climate model MAR (1979–2015) and identification of dominant processes, The Cryosphere, 13, 281–296, https://doi.org/10.5194/tc-13-281-2019, 2019.

Arthern, R. J., Winebrenner, D. P., and Vaughan, D. G.: Antarctic snow accumulation mapped using polarization of 4.3-cm wavelength microwave emission, Journal of Geophysical Research: Atmospheres, 111, https://doi.org/10.1029/2004jd005667, 2006.

Arthern, R. J., Vaughan, D. G., Rankin, A. M., Mulvaney, R., and Thomas, E. R.: In situ measurements of Antarctic snow compaction compared with predictions of models, Journal of Geophysical Research: Earth Surface, 115, https://doi.org/10.1029/2009jf001306, 2010.

Aublanc, J., Thibaut, P., Guillot, A., Boy, F., and Picot, N.: Ice Sheet Topography from a New CryoSat-2 SARIn Processing Chain, and Assessment by Comparison to ICESat-2 over Antarctica, Remote Sensing, 13, 4508, https://doi.org/10.3390/rs13224508, 2021.

Bamber, J. L., Oppenheimer, M., Kopp, R. E., Aspinall, W. P., and Cooke, R. M.: Ice sheet contributions to future sea-level rise from structured expert judgment, Proceedings of the National Academy of Sciences, 116, 11 195–11 200, https://doi.org/10.1073/pnas.1817205116, 2019.

Banwell, A. F., MacAyeal, D. R., and Sergienko, O. V.: Breakup of the Larsen B Ice Shelf triggered by chain reaction drainage of supraglacial lakes, Geophysical Research Letters, 40, 5872–5876, https://doi.org/10.1002/2013gl057694, 2013.

Bell, R. E., Chu, W., Kingslake, J., Das, I., Tedesco, M., Tinto, K. J., Zappa, C. J., Frezzotti, M., Boghosian, A., and Lee, W. S.: Antarctic ice shelf potentially stabilized by export of meltwater in surface river, Nature, 544, 344–348, https://doi.org/10.1038/nature22048, 2017.

Brenner, A. C., DiMarzio, J. P., and Zwally, H. J.: Precision and Accuracy of Satellite Radar and Laser Altimeter Data Over the Continental Ice Sheets, IEEE Transactions on Geoscience and Remote Sensing, 45, 321–331, https://doi.org/10.1109/tgrs.2006.887172, 2007.

Brigham Young University (BYU) Microwave Earth Remote Sensing (MERS) laboratory: Standard BYU ASCAT Land/Ice Image Products, URL `https://www.scp.byu.edu/data/Ascat/SIR/Ascat_sir.html`, (Date accessed: 6 February 2021), 2010.

Brils, M., Kuipers Munneke, P., van de Berg, W. J., and van den Broeke, M.: Improved representation of the contemporary Greenland ice sheet firn layer by IMAU-FDM v1.2G, Geoscientific Model Development, 15, 7121–7138, https://doi.org/10.5194/gmd-15-7121-2022, 2022.

Brucker, L., Picard, G., and Fily, M.: Snow grain-size profiles deduced from microwave snow emissivities in Antarctica, Journal of Glaciology, 56, 514–526, https://doi.org/10.3189/002214310792447806, 2010.

Brucker, L., Picard, G., Arnaud, L., Barnola, J.-M., Schneebeli, M., Brunjail, H., Lefebvre, E., and Fily, M.: Modeling time series of microwave brightness temperature at Dome C, Antarctica, using vertically resolved snow temperature and microstructure measurements, Journal of Glaciology, 57, 171–182, https://doi.org/10.3189/002214311795306736, 2011.

Brun, E., Martin, E., Simon, V., Gendre, C., and Coleou, C.: An Energy and Mass Model of Snow Cover Suitable for Operational Avalanche Forecasting, Journal of Glaciology, 35, 333–342, https://doi.org/10.3189/s0022143000009254, 1989.

Brun, E., David, P., Sudul, M., and Brunot, G.: A numerical model to simulate snow-cover stratigraphy for operational avalanche forecasting, Journal of Glaciology, 38, 13–22, https://doi.org/10.3189/s0022143000009552, 1992.

Calafat, F., Cipollini, P., Bouffard, J., Snaith, H., and Féménias, P.: Evaluation of new CryoSat-2 products over the ocean, Remote Sensing of Environment, 191, 131–144, https://doi.org/10.1016/j.rse.2017.01.009, 2017.

Capron, E., Landais, A., Buiron, D., Cauquoin, A., Chappellaz, J., Debret, M., Jouzel, J., Leuenberger, M., Martinerie, P., Masson-Delmotte, V., Mulvaney, R., Parrenin, F., and Prié, F.: Glacial–interglacial dynamics of Antarctic firn columns: comparison between simulations and ice core air-δ^{15}N measurements, Climate of the Past, 9, 983–999, https://doi.org/10.5194/cp-9-983-2013, 2013.

Champollion, N., Picard, G., Arnaud, L., Lefebvre, E., and Fily, M.: Hoar crystal development and disappearance at Dome C, Antarctica: observation by near-infrared photography and passive microwave satellite, The Cryosphere, 7, 1247–1262, https://doi.org/10.5194/tc-7-1247-2013, 2013.

Chelton, D. B., Ries, J. C., Haines, B. J., Fu, L.-L., and Callahan, P. S.: Satellite Altimetry and Earth Sciences, chap. Satellite Altimetry, pp. 1–132, Academic Press: San Diego, 2001.

Constable, A., Harper, S., Dawson, J., Holsman, K., Mustonen, T., Piepenburg, D., and Rost, B.: Climate Change 2022: Impacts, Adaptation and Vulnerability. Contribution of Working Group II to the Sixth Assessment Report of the Intergovernmental Panel on Climate Change, Cambridge University Press, Cambridge, UK and New York, NY, USA, https://doi.org/10.1017/9781009325844.023, 2022.

Davis, C. and Ferguson, A.: Elevation change of the Antarctic ice sheet, 1995-2000, from ERS-2 satellite radar altimetry, IEEE Transactions on Geoscience and Remote Sensing, 42, 2437–2445, https://doi.org/10.1109/tgrs.2004.836789, 2004.

Depoorter, M. A., Bamber, J. L., Griggs, J., Lenaerts, J. T. M., Ligtenberg, S. R. M., van den Broeke, M. R., and Moholdt, G.: Synthesized grounding line and ice shelf mask for Antarctica, https://doi.org/10.1594/PANGAEA.819151, supplement to: Depoorter, MA et al. (2013): Calving fluxes and basal melt rates of Antarctic ice shelves. Nature, 502, 89-92, https://doi.org/10.1038/nature12567, 2013.

Dethinne, T., Glaude, Q., Picard, G., Kittel, C., Alexander, P., Orban, A., and Fettweis, X.: Sensitivity of the MAR regional climate model snowpack to the parameterization of the assimilation of satellite-derived wet-snow masks on the Antarctic Peninsula, The Cryosphere, 17, 4267–4288, https://doi.org/10.5194/tc-17-4267-2023, 2023.

Drinkwater, M.: LIMEX '87 ice surface characteristics: implications for C-band SAR backscatter signatures, IEEE Transactions on Geoscience and Remote Sensing, 27, 501–513, https://doi.org/10.1109/tgrs.1989.35933, 1989.

Drinkwater, M. R., Long, D. G., and Bingham, A. W.: Greenland snow accumulation estimates from satellite radar scatterometer data, Journal of Geophysical Research: Atmospheres, 106, 33 935–33 950, https://doi.org/10.1029/2001jd900107, 2001.

Dunmire, D., Lenaerts, J. T. M., Banwell, A. F., Wever, N., Shragge, J., Lhermitte, S., Drews, R., Pattyn, F., Hansen, J. S. S., Willis, I. C., Miller, J., and Keenan, E.: Observations of Buried Lake Drainage on the Antarctic Ice Sheet, Geophysical Research Letters, 47, e2020GL087 970, https://doi.org/10.1029/2020GL087970, 2020.

Dupont, T. K. and Alley, R. B.: Assessment of the importance of ice-shelf buttressing to ice-sheet flow, Geophysical Research Letters, 32, n/a–n/a, https://doi.org/10.1029/2004gl022024, 2005.

Early, D. and Long, D.: Image reconstruction and enhanced resolution imaging from irregular samples, IEEE Transactions on Geoscience and Remote Sensing, 39, 291–302, https://doi.org/10.1109/36.905237, 2001.

Enderlin, E. M., Howat, I. M., Jeong, S., Noh, M., van Angelen, J. H., and van den Broeke, M. R.: An improved mass budget for the Greenland ice sheet, Geophysical Research Letters, 41, 866–872, https://doi.org/10.1002/2013gl059010, 2014.

Fahnestock, M. A., Scambos, T. A., Shuman, C. A., Arthern, R. J., Winebrenner, D. P., and Kwok, R.: Snow megadune fields on the East Antarctic Plateau: Extreme atmosphere-ice interaction, Geophysical Research Letters, 27, 3719–3722, https://doi.org/10.1029/1999gl011248, 2000.

Fettweis, X.: Modèle Atmosphérique Régional (MAR) version 3.11 regional climate model output, 1979-2019, Greenland domain, 10 kilometer (km) horizontal resolution, https://doi.org/10.18739/A28G8FJ7F, 2022.

Flament, T. and Rémy, F.: Dynamic thinning of Antarctic glaciers from along-track repeat radar altimetry, Journal of Glaciology, 58, 830–840, https://doi.org/10.3189/2012jog11j118, 2012.

Flanner, M. G. and Zender, C. S.: Linking snowpack microphysics and albedo evolution, Journal of Geophysical Research, 111, https://doi.org/10.1029/2005jd006834, 2006.

Forster, R. R., Box, J. E., van den Broeke, M. R., Miège, C., Burgess, E. W., van Angelen, J. H., Lenaerts, J. T. M., Koenig, L. S., Paden, J., Lewis, C., Gogineni, S. P., Leuschen, C., and McConnell, J. R.: Extensive liquid meltwater storage in firn within the Greenland ice sheet, Nature Geoscience, 7, 95–98, https://doi.org/10.1038/ngeo2043, 2013.

Fraser, A. D., Nigro, M. A., Ligtenberg, S. R. M., Legrésy, B., Inoue, M., Cassano, J. J., Munneke, P. K., Lenaerts, J. T. M., Young, N. W., Treverrow, A., van den Broeke, M., and Enomoto, H.: Drivers of ASCAT C band backscatter variability in the dry snow zone of Antarctica, Journal of Glaciology, 62, 170–184, https://doi.org/10.1017/jog.2016.29, 2016.

Frederikse, T., Landerer, F., Caron, L., Adhikari, S., Parkes, D., Humphrey, V. W., Dangendorf, S., Hogarth, P., Zanna, L., Cheng, L., and Wu, Y.-H.: The causes of sea-level rise since 1900, Nature, 584, 393–397, https://doi.org/10.1038/s41586-020-2591-3, 2020.

Fukuzawa, T. and Akitaya, E.: Depth-hoar crystal growth in the surface layer under high temperature gradient, Annals of Glaciology, 18, 39–45, https://doi.org/10.3189/s02603055000112 3x, 1993.

Gallée, H. and Schayes, G.: Development of a Three-Dimensional Meso-γ Primitive Equation Model: Katabatic Winds Simulation in the Area of Terra Nova Bay, Antarctica, Monthly Weather Review, 122, 671–685, https://doi.org/10.1175/1520-0493(1994)122<0671:doatdm>2.0.co;2, 1994.

Gallée, H., Guyomarc'h, G., and Brun, E.: Impact Of Snow Drift On The Antarctic Ice Sheet Surface Mass Balance: Possible Sensitivity To Snow-Surface Properties, Boundary-Layer Meteorology, 99, 1–19, https://doi.org/10.1023/a:1018776422809, 2001.

Garbe, J., Albrecht, T., Levermann, A., Donges, J. F., and Winkelmann, R.: The hysteresis of the Antarctic Ice Sheet, Nature, 585, 538–544, https://doi.org/10.1038/s41586-020-2727-5, 2020.

Gerrish, L.: The coastline of Kalaallit Nunaat/ Greenland available as a shapefile and geopackage, covering the main land and islands, with glacier fronts updated as of 2017., https://doi.org/10.5285/8CECDE06-8474-4B58-A9CB-B820FA4C9429, 2020.

Golledge, N. R., Levy, R. H., McKay, R. M., and Naish, T. R.: East Antarctic ice sheet most vulnerable to Weddell Sea warming, Geophysical Research Letters, 44, 2343–2351, https://doi.org/10.1002/2016gl072422, 2017.

Gommenginger, C., Thibaut, P., Fenoglio-Marc, L., Quartly, G., Deng, X., Gómez-Enri, J., Challenor, P., and Gao, Y.: Retracking Altimeter Waveforms Near the Coasts, in: Coastal Altimetry, pp. 61–101, Springer Berlin Heidelberg, https://doi.org/10.1007/978-3-642-12796-0_4, 2010.

Graeter, K. A., Osterberg, E. C., Ferris, D. G., Hawley, R. L., Marshall, H. P., Lewis, G., Meehan, T., McCarthy, F., Overly, T., and Birkel, S. D.: Ice Core Records of West Greenland Melt and Climate Forcing, Geophysical Research Letters, 45, 3164–3172, https://doi.org/10.1002/2017gl076641, 2018.

Hanssen, R. F.: Radar Interferometry, Springer Netherlands, https://doi.org/10.1007/0-306-47633-9, 2001.

Harper, J., Humphrey, N., Pfeffer, W. T., Brown, J., and Fettweis, X.: Greenland ice-sheet contribution to sea-level rise buffered by meltwater storage in firn, Nature, 491, 240–243, https://doi.org/10.1038/nature11566, 2012.

Houtz, D., Mätzler, C., Naderpour, R., Schwank, M., and Steffen, K.: Quantifying Surface Melt and Liquid Water on the Greenland Ice Sheet using L-band Radiometry, Remote Sensing of Environment, 256, 112 341, https://doi.org/10.1016/j.rse.2021.112341, 2021.

Jensen, J.: Angle measurement with a phase monopulse radar altimeter, IEEE Transactions on Antennas and Propagation, 47, 715–724, https://doi.org/10.1109/8.768812, 1999.

Johnson, A., Fahnestock, M., and Hock, R.: Evaluation of passive microwave melt detection methods on Antarctic Peninsula ice shelves using time series of Sentinel-1 SAR, Remote Sensing of Environment, 250, 112 044, https://doi.org/https://doi.org/10.1016/j.rse.2020.112044, 2020.

Joughin, I. and Alley, R. B.: Stability of the West Antarctic ice sheet in a warming world, Nature Geoscience, 4, 506–513, https://doi.org/10.1038/ngeo1194, 2011.

Joughin, I., Das, S. B., King, M. A., Smith, B. E., Howat, I. M., and Moon, T.: Seasonal Speedup Along the Western Flank of the Greenland Ice Sheet, Science, 320, 781–783, https://doi.org/10.1126/science.1153288, 2008.

Joughin, I., Smith, B. E., Howat, I. M., Moon, T., and Scambos, T. A.: A SAR record of early 21st century change in Greenland, Journal of Glaciology, 62, 62–71, https://doi.org/10.1017/jog.2016.10, 2016.

Keenan, E., Wever, N., Dattler, M., Lenaerts, J. T. M., Medley, B., Munneke, P. K., and Reijmer, C.: Physics-based SNOWPACK model improves representation of near-surface Antarctic snow and firn density, The Cryosphere, 15, 1065–1085, https://doi.org/10.5194/tc-15-1065-2021, 2021.

Khvorostovsky, K. S.: Merging and Analysis of Elevation Time Series Over Greenland Ice Sheet From Satellite Radar Altimetry, IEEE Transactions on Geoscience and Remote Sensing, 50, 23–36, https://doi.org/10.1109/tgrs.2011.2160071, 2012.

Kingslake, J., Ely, J. C., Das, I., and Bell, R. E.: Widespread movement of meltwater onto and across Antarctic ice shelves, Nature, 544, 349–352, https://doi.org/10.1038/nature22049, 2017.

Kittel, C., Amory, C., Agosta, C., Jourdain, N. C., Hofer, S., Delhasse, A., Doutreloup, S., Huot, P.-V., Lang, C., Fichefet, T., and Fettweis, X.: Diverging future surface mass balance between the Antarctic ice shelves and grounded ice sheet, The Cryosphere, 15, 1215–1236, https://doi.org/10.5194/tc-15-1215-2021, 2021.

Larue, F., Picard, G., Aublanc, J., Arnaud, L., Robledano-Perez, A., Meur, E. L., Favier, V., Jourdain, B., Savarino, J., and Thibaut, P.: Radar altimeter waveform simulations in Antarctica with the Snow Microwave Radiative Transfer Model (SMRT), Remote Sensing of Environment, 263, 112 534, https://doi.org/10.1016/j.rse.2021.112534, 2021.

Le Vine, D. and Skou, N.: Microwave Radiometer Systems: Design and Analysis, Second Edition, Artech, 2006.

Leduc-Leballeur, M., Picard, G., Macelloni, G., Arnaud, L., Brogioni, M., Mialon, A., and Kerr, Y.: Influence of snow surface properties on L-band brightness temperature at Dome C, Antarctica, Remote Sensing of Environment, 199, 427–436, https://doi.org/10.1016/j.rse.2017.07.035, 2017.

Lenaerts, J. T. M., Lhermitte, S., Drews, R., Ligtenberg, S. R. M., Berger, S., Helm, V., Smeets, C. J. P. P., van den Broeke, M. R., van de Berg, W. J., van Meijgaard, E., Eijkelboom, M., Eisen, O., and Pattyn, F.: Meltwater produced by wind–albedo interaction stored in an East Antarctic ice shelf, Nature Climate Change, 7, 58–62, https://doi.org/10.1038/nclimate3180, 2016.

Levinsen, J. F., Simonsen, S. B., Sorensen, L. S., and Forsberg, R.: The Impact of DEM Resolution on Relocating Radar Altimetry Data Over Ice Sheets, IEEE Journal of Selected Topics in Applied Earth Observations and Remote Sensing, 9, 3158–3163, https://doi.org/10.1109/jstars.2016.2587684, 2016.

Li, W., Lhermitte, S., and López-Dekker, P.: The potential of synthetic aperture radar interferometry for assessing meltwater lake dynamics on Antarctic ice shelves, The Cryosphere, 15, 5309–5322, https://doi.org/10.5194/tc-15-5309-2021, 2021.

Ligtenberg, S. R. M., Helsen, M. M., and van den Broeke, M. R.: An improved semi-empirical model for the densification of Antarctic firn, The Cryosphere, 5, 809–819, https://doi.org/10.5194/tc-5-809-2011, 2011.

Lindsley, R. D. and Long, D. G.: Standard BYU ASCAT Land/Ice Image Products, Tech. rep., Brigham Young University Microwave Earth Remote Sensing (MERS) Laboratory, URL `https://www.scp.byu.edu/docs/pdf/MERS1002.pdf`, (Date accessed: 20 June 2022), 2010.

Liu, S., Jiang, J., Sun, Q., Wan, J., and Sheng, H.: Assessment of the Greenland ice sheet change (2011–2021) derived from CryoSat-2, Polar Science, 36, 100 940, https://doi.org/10.1016/j.polar.2023.100940, 2023.

Long, D., Hardin, P., and Whiting, P.: Resolution enhancement of spaceborne scatterometer data, IEEE Transactions on Geoscience and Remote Sensing, 31, 700–715, https://doi.org/10.1109/36.225536, 1993.

Long, D. G. and Drinkwater, M. R.: Greenland ice-sheet surface properties observed by the Seasat-A scatterometer at enhanced resolution, Journal of Glaciology, 40, 213–230, https://doi.org/10.3189/s0022143000007310, 1994.

Lubin, D. and Massom, R.: Polar Remote Sensing Volume I: Atmosphere and Oceans, Springer Berlin Heidelberg, https://doi.org/10.1007/3-540-30785-0, 2006.

Luckman, A., Elvidge, A., Jansen, D., Kulessa, B., Munneke, P. K., King, J., and Barrand, N. E.: Surface melt and ponding on Larsen C Ice Shelf and the impact of föhn winds, Antarctic Science, 26, 625–635, https://doi.org/10.1017/s0954102014000339, 2014.

Machguth, H., MacFerrin, M., van As, D., Box, J. E., Charalampidis, C., Colgan, W., Fausto, R. S., Meijer, H. A. J., Mosley-Thompson, E., and van de Wal, R. S. W.: Greenland meltwater storage in firn limited by near-surface ice formation, Nature Climate Change, 6, 390–393, https://doi.org/10.1038/nclimate2899, 2016.

Meier, W. N., Stewart, J. S., Wilcox, H., Scott, D. J., and Hardman, M. A.: DMSP SSM/I-SSMIS Daily Polar Gridded Brightness Temperatures, Boulder, Colorado USA. NASA National Snow and Ice Data Center Distributed Active Archive Center, https://doi.org/10.5067/MXJL42WSXTS1, (Date Accessed: 15 March 2021), 2021.

Mengel, M. and Levermann, A.: Ice plug prevents irreversible discharge from East Antarctica, Nature Climate Change, 4, 451–455, https://doi.org/10.1038/nclimate2226, 2014.

Michel, A., Flament, T., and Rémy, F.: Study of the Penetration Bias of ENVISAT Altimeter Observations over Antarctica in Comparison to ICESat Observations, Remote Sensing, 6, 9412–9434, https://doi.org/10.3390/rs6109412, 2014.

Montgomery, L., Koenig, L., and Alexander, P.: The SUMup dataset: compiled measurements of surface mass balance components over ice sheets and sea ice with analysis over Greenland, Earth System Science Data, 10, 1959–1985, https://doi.org/10.5194/essd-10-1959-2018, 2018.

Mote, T. L., Anderson, M. R., Kuivinen, K. C., and Rowe, C. M.: Passive microwave-derived spatial and temporal variations of summer melt on the Greenland ice sheet, Annals of Glaciology, 17, 233–238, https://doi.org/10.3189/s0260305500012891, 1993.

Munneke, P. K., Ligtenberg, S. R., Broeke, M. R. V. D., and Vaughan, D. G.: Firn air depletion as a precursor of Antarctic ice-shelf collapse, Journal of Glaciology, 60, 205–214, https://doi.org/10.3189/2014jog13j183, 2014.

Mätzler, C. and Wiesmann, A.: Extension of the Microwave Emission Model of Layered Snowpacks to Coarse-Grained Snow, Remote Sensing of Environment, 70, 317–325, https://doi.org/10.1016/s0034-4257(99)00047-4, 1999.

Nagler, T. and Rott, H.: Retrieval of wet snow by means of multitemporal SAR data, IEEE Transactions on Geoscience and Remote Sensing, 38, 754–765, https://doi.org/10.1109/36.842004, 2000.

Nicolas, J. P., Vogelmann, A. M., Scott, R. C., Wilson, A. B., Cadeddu, M. P., Bromwich, D. H., Verlinde, J., Lubin, D., Russell, L. M., Jenkinson, C., Powers, H. H., Ryczek, M., Stone, G., and Wille, J. D.: January 2016 extensive summer melt in West Antarctica favoured by strong El Niño, Nature Communications, 8, https://doi.org/10.1038/ncomms15799, 2017.

Nilsson, J., Vallelonga, P., Simonsen, S. B., Sørensen, L. S., Forsberg, R., Dahl-Jensen, D., Hirabayashi, M., Goto-Azuma, K., Hvidberg, C. S., Kjaer, H. A., and Satow, K.: Greenland 2012 melt event effects on CryoSat-2 radar altimetry, Geophysical Research Letters, 42, 3919–3926, https://doi.org/10.1002/2015gl063296, 2015.

Obbard, R. W., Baker, I., and Lomonaco, R. W.: Firn, pp. 290–293, Springer Netherlands, https://doi.org/10.1007/978-90-481-2642-2_661, 2011.

Otosaka, I., Shepherd, A., and McMillan, M.: Ice Sheet Elevation Change in West Antarctica From Ka-Band Satellite Radar Altimetry, Geophysical Research Letters, 46, 13 135–13 143, https://doi.org/10.1029/2019gl084271, 2019.

Picard, G., Domine, F., Krinner, G., Arnaud, L., and Lefebvre, E.: Inhibition of the positive snow-albedo feedback by precipitation in interior Antarctica, Nature Climate Change, 2, 795–798, https://doi.org/10.1038/nclimate1590, 2012.

Picard, G., Sandells, M., and Löwe, H.: SMRT: an active–passive microwave radiative transfer model for snow with multiple microstructure and scattering formulations (v1.0), Geoscientific Model Development, 11, 2763–2788, https://doi.org/10.5194/gmd-11-2763-2018, 2018.

Pritchard, H. D., Ligtenberg, S. R. M., Fricker, H. A., Vaughan, D. G., van den Broeke, M. R., and Padman, L.: Antarctic ice-sheet loss driven by basal melting of ice shelves, Nature, 484, 502–505, https://doi.org/10.1038/nature10968, 2012.

Proksch, M., Mätzler, C., Wiesmann, A., Lemmetyinen, J., Schwank, M., Löwe, H., and Schneebeli, M.: MEMLS3&a: Microwave Emission Model of Layered Snowpacks adapted to include backscattering, Geoscientific Model Development, 8, 2611–2626, https://doi.org/10.5194/gmd-8-2611-2015, 2015.

Pulliainen, J., Grandell, J., and Hallikainen, M.: HUT snow emission model and its applicability to snow water equivalent retrieval, IEEE Transactions on Geoscience and Remote Sensing, 37, 1378–1390, https://doi.org/10.1109/36.763302, 1999.

Quartly, G. D., Chen, G., Nencioli, F., Morrow, R., and Picot, N.: An Overview of Requirements, Procedures and Current Advances in the Calibration/Validation of Radar Altimeters, Remote Sensing, 13, 125, https://doi.org/10.3390/rs13010125, 2021.

Reijmer, C. H., van den Broeke, M. R., Fettweis, X., Ettema, J., and Stap, L. B.: Refreezing on the Greenland ice sheet: a comparison of parameterizations, The Cryosphere, 6, 743–762, https://doi.org/10.5194/tc-6-743-2012, 2012.

Ridley, J. K. and Partington, K. C.: A model of satellite radar altimeter return from ice sheets, International Journal of Remote Sensing, 9, 601–624, https://doi.org/10.1080/01431168808954881, 1988.

Rignot, E.: Accelerated ice discharge from the Antarctic Peninsula following the collapse of Larsen B ice shelf, Geophysical Research Letters, 31, https://doi.org/10.1029/2004gl020697, 2004.

Roemer, S., Legrésy, B., Horwath, M., and Dietrich, R.: Refined analysis of radar altimetry data applied to the region of the subglacial Lake Vostok/Antarctica, Remote Sensing of Environment, 106, 269–284, https://doi.org/10.1016/j.rse.2006.02.026, 2007.

Rotschky, G., Rack, W., Dierking, W., and Oerter, H.: Retrieving snowpack properties and accumulation estimates from a combination of SAR and scatterometer measurements, IEEE Transactions on Geoscience and Remote Sensing, 44, 943–956, https://doi.org/10.1109/tgrs.2005.862524, 2006.

Rémy, F. and Parouty, S.: Antarctic Ice Sheet and Radar Altimetry: A Review, Remote Sensing, 1, 1212–1239, https://doi.org/10.3390/rs1041212, 2009.

Scambos, T. A.: Glacier acceleration and thinning after ice shelf collapse in the Larsen B embayment, Antarctica, Geophysical Research Letters, 31, https://doi.org/10.1029/2004gl020670, 2004.

Scambos, T. A., Hulbe, C., Fahnestock, M., and Bohlander, J.: The link between climate warming and break-up of ice shelves in the Antarctic Peninsula, Journal of Glaciology, 46, 516–530, https://doi.org/10.3189/172756500781833043, 2000.

Scanlan, K. M., Rutishauser, A., and Simonsen, S. B.: Observing the Near-Surface Properties of the Greenland Ice Sheet, Geophysical Research Letters, 50, https://doi.org/10.1029/2022gl101702, 2023.

Schaller, C. F., Freitag, J., Kipfstuhl, S., Laepple, T., Steen-Larsen, H. C., and Eisen, O.: A representative density profile of the North Greenland snowpack, The Cryosphere, 10, 1991–2002, https://doi.org/10.5194/tc-10-1991-2016, 2016.

Schmittner, A., Silva, T. A. M., Fraedrich, K., Kirk, E., and Lunkeit, F.: Effects of Mountains and Ice Sheets on Global Ocean Circulation, Journal of Climate, 24, 2814–2829, https://doi.org/10.1175/2010jcli3982.1, 2011.

Schneider, R., Tarpanelli, A., Nielsen, K., Madsen, H., and Bauer-Gottwein, P.: Evaluation of multi-mode CryoSat-2 altimetry data over the Po River against in situ data and a hydrodynamic model, Advances in Water Resources, 112, 17–26, https://doi.org/10.1016/j.advwatres.2017.11.027, 2018.

Shukla, S., Wouters, B., Picard, G., Wever, N., Izeboud, M., Husman, S. d. R., Kausch, T., Veldhuijsen, S., Mätzler, C., and Lhermitte, S.: Large Variability in Dominant Scattering From Sentinel-1 SAR in East Antarctica: Challenges and Opportunities, IEEE Journal of Selected Topics in Applied Earth Observations and Remote Sensing, 17, 14 380–14 393, https://doi.org/10.1109/jstars.2024.3438233, 2024.

Simonsen, S. B. and Sørensen, L. S.: Implications of changing scattering properties on Greenland ice sheet volume change from Cryosat-2 altimetry, Remote Sensing of Environment, 190, 207–216, https://doi.org/10.1016/j.rse.2016.12.012, 2017.

Smith, B., Fricker, H. A., Holschuh, N., Gardner, A. S., Adusumilli, S., Brunt, K. M., Csatho, B., Harbeck, K., Huth, A., Neumann, T., Nilsson, J., and Siegfried, M. R.: Land ice height-retrieval algorithm for NASA's ICESat-2 photon-counting laser altimeter, Remote Sensing of Environment, 233, 111 352, https://doi.org/10.1016/j.rse.2019.111352, 2019.

Spergel, J. J., Kingslake, J., Creyts, T., van Wessem, M., and Fricker, H. A.: Surface meltwater drainage and ponding on Amery Ice Shelf, East Antarctica, 1973–2019, Journal of Glaciology, p. 1–14, https://doi.org/10.1017/jog.2021.46, 2021.

Stiles, W. H. and Ulaby, F. T.: The active and passive microwave response to snow parameters: 1. Wetness, Journal of Geophysical Research: Oceans, 85, 1037–1044, https://doi.org/10.1029/jc085ic02p01037, 1980.

Surdyk, S.: Using microwave brightness temperature to detect short-term surface air temperature changes in Antarctica: An analytical approach, Remote Sensing of Environment, 80, 256–271, https://doi.org/10.1016/s0034-4257(01)00308-x, 2002.

Tedesco, M.: Snowmelt detection over the Greenland ice sheet from SSM/I brightness temperature daily variations, Geophysical Research Letters, 34, https://doi.org/10.1029/2006gl028466, 2007.

Tedesco, M. and Fettweis, X.: Unprecedented atmospheric conditions (1948–2019) drive the 2019 exceptional melting season over the Greenland ice sheet, The Cryosphere, 14, 1209–1223, https://doi.org/10.5194/tc-14-1209-2020, 2020.

Tedesco, M. and Kim, E.: Intercomparison of Electromagnetic Models for Passive Microwave Remote Sensing of Snow, IEEE Transactions on Geoscience and Remote Sensing, 44, 2654–2666, https://doi.org/10.1109/tgrs.2006.873182, 2006.

Tedesco, M., Doherty, S., Fettweis, X., Alexander, P., Jeyaratnam, J., and Stroeve, J.: The darkening of the Greenland ice sheet: trends, drivers, and projections (1981–2100), The Cryosphere, 10, 477–496, https://doi.org/10.5194/tc-10-477-2016, 2016.

Thomas, R., Davis, C., Frederick, E., Krabill, W., Li, Y., Manizade, S., and Martin, C.: A comparison of Greenland ice-sheet volume changes derived from altimetry measurements, Journal of Glaciology, 54, 203–212, https://doi.org/10.3189/002214308784886225, 2008.

Torinesi, O., Fily, M., and Genthon, C.: Variability and Trends of the Summer Melt Period of Antarctic Ice Margins since 1980 from Microwave Sensors, Journal of Climate, 16, 1047–1060, https://doi.org/10.1175/1520-0442(2003)016<1047:vatots>2.0.co;2, 2003.

Tran, N., Remy, F., Feng, H., and Femenias, P.: Snow Facies Over Ice Sheets Derived From Envisat Active and Passive Observations, IEEE Transactions on Geoscience and Remote Sensing, 46, 3694–3708, https://doi.org/10.1109/tgrs.2008.2000818, 2008.

Trusel, L. D., Frey, K. E., and Das, S. B.: Antarctic surface melting dynamics: Enhanced perspectives from radar scatterometer data, Journal of Geophysical Research: Earth Surface, 117, https://doi.org/10.1029/2011jf002126, 2012.

Trusel, L. D., Das, S. B., Osman, M. B., Evans, M. J., Smith, B. E., Fettweis, X., McConnell, J. R., Noël, B. P. Y., and van den Broeke, M. R.: Nonlinear rise in Greenland runoff in response to post-industrial Arctic warming, Nature, 564, 104–108, https://doi.org/10.1038/s41586-018-0752-4, 2018.

Tsang, L., Chen, C.-T., Chang, A. T. C., Guo, J., and Ding, K.-H.: Dense media radiative transfer theory based on quasicrystalline approximation with applications to passive microwave remote sensing of snow, Radio Science, 35, 731–749, https://doi.org/10.1029/1999rs002270, 2000.

Tsang, L., Pan, J., Liang, D., Li, Z., Cline, D. W., and Tan, Y.: Modeling Active Microwave Remote Sensing of Snow Using Dense Media Radiative Transfer (DMRT) Theory With Multiple-Scattering Effects, IEEE Transactions on Geoscience and Remote Sensing, 45, 990–1004, https://doi.org/10.1109/tgrs.2006.888854, 2007.

Ulaby, F., Dobson, M. C., and Álvarez Pérez, J. L.: Handbook of Radar Scattering Statistics for Terrain, Norwood, MA: Artech House, 2019.

Ulaby, F. T., Moore, R. K., and Fung, A. K.: Microwave Remote Sensing: Active and Passive, Vol. 3, From Theory to Applications, Artech House, 1986.

van Angelen, J. H., Lenaerts, J. T. M., Lhermitte, S., Fettweis, X., Kuipers Munneke, P., van den Broeke, M. R., van Meijgaard, E., and Smeets, C. J. P. P.: Sensitivity of Greenland Ice Sheet surface mass balance to surface albedo parameterization: a study with a regional climate model, The Cryosphere, 6, 1175–1186, https://doi.org/10.5194/tc-6-1175-2012, 2012.

van Angelen, J. H., Lenaerts, J. T. M., van den Broeke, M. R., Fettweis, X., and van Meijgaard, E.: Rapid loss of firn pore space accelerates 21st century Greenland mass loss, Geophysical Research Letters, 40, 2109–2113, https://doi.org/10.1002/grl.50490, 2013.

van As, D., Fausto, R. S., Colgan, W. T., Box, J. E., and et al: Darkening of the Greenland ice sheet due to the melt-albedo feedback observed at PROMICE weather stations, https://doi.org/10.5167/UZH-131201, 2013.

van den Broeke, M.: Strong surface melting preceded collapse of Antarctic Peninsula ice shelf, Geophysical Research Letters, 32, n/a–n/a, https://doi.org/10.1029/2005gl023247, 2005.

van den Broeke, M.: Depth and Density of the Antarctic Firn Layer, Arctic, Antarctic, and Alpine Research, 40, 432–438, https://doi.org/10.1657/1523-0430(07-021)[broeke]2.0.co;2, 2008.

van den Broeke, M. R., Enderlin, E. M., Howat, I. M., Munneke, P. K., Noël, B. P. Y., van de Berg, W. J., van Meijgaard, E., and Wouters, B.: On the recent contribution of the Greenland ice sheet to sea level change, The Cryosphere, 10, 1933–1946, https://doi.org/10.5194/tc-10-1933-2016, 2016.

Vandecrux, B., Fausto, R. S., Langen, P. L., van As, D., MacFerrin, M., Colgan, W. T., Ingeman-Nielsen, T., Steffen, K., Jensen, N. S., Møller, M. T., and Box, J. E.: Drivers of Firn Density on the Greenland Ice Sheet Revealed by Weather Station Observations and Modeling, Journal of Geophysical Research: Earth Surface, 123, 2563–2576, https://doi.org/10.1029/2017jf004597, 2018.

Vandecrux, B., MacFerrin, M., Machguth, H., Colgan, W. T., van As, D., Heilig, A., Stevens, C. M., Charalampidis, C., Fausto, R. S., Morris, E. M., Mosley-Thompson, E., Koenig, L., Montgomery, L. N., Miège, C., Simonsen, S. B., Ingeman-Nielsen, T., and Box, J. E.: Firn data compilation reveals widespread decrease of firn air content in western Greenland, The Cryosphere, 13, 845–859, https://doi.org/10.5194/tc-13-845-2019, 2019.

Vandecrux, B., Amory, C., Ahlstrøm, A. P., Akers, P. D., Albert, M., Alley, R. B., Alves De Castro, M., Arnaud, L., Baker, I., Bales, R., Benson, C., Box, J. E., Brucker, L., Buizert, C., Chandler, D., Charalampidis, C., Cherblanc, C., Clerx, N., Colgan, W., Covi, F., Dattler, M., Denis, G., Derksen, C., Dibb, J. E., Ding, M., Dixon, D., Eisen, O., Fahrner, D., Fausto, R., Favier, V., Fernandoy, F., Freitag, J., Gerland, S., Harper, J., Hawley, R. L., Heuer, J., Hock, R., Hou, S., How, P., Humphrey, N., Hubbard, B., Iizuka, Y., Isaksson, E., Kameda, T., Karlsson, N. B., Kawakami, K., Kjær, H. A., Kreutz, K., Kuipers Munneke, P., Lazzara, M., Lemeur, E., Lenaerts, J. T. M., Lewis, G., Lindau, F. G. L., Lindsey-Clark, J., MacFerrin, M., Machguth, H., Magand, O., Mankoff, K. D., Marquetto, L., Martinerie, P., McConnell, J. R., Medley, B., Miège, C., Miles, K. E., Miller, O., Miller, H., Montgomery, L., Morris, E., Mosley-Thompson, E., Mulvaney, R., Niwano, M., Oerter, H., Osterberg, E., Otosaka, I., Picard, G., Polashenski, C., Reijmer, C., Rennermalm, A., Rutishauser, A., Scanlan, K., Simoes, J. C., Simonsen, S. B., Smeets, P. C., Smith, A., Solgaard, A., Spencer, M., Steen-Larsen, H. C., Stevens, C. M., Sugiyama, S., Svensson, J., Tedesco, M., Thomas, E., Thompson-Munson, M., Tsutaki, S., Van As, D., Van Den Broeke, M. R., Van Tiggelen, M., Wang, Y., Wilhelms, F., Winstrup, M., Xiao, J., and Xiao, C.: The SUMup collaborative database: Surface mass balance, subsurface temperature and density measurements from the Greenland and Antarctic ice sheets (2024 release), https://doi.org/10.18739/A2M61BR5M, 2024.

Veldhuijsen, S. B. M., van de Berg, W. J., Brils, M., Munneke, P. K., and van den Broeke, M. R.: Characteristics of the 1979–2020 Antarctic firn layer simulated with IMAU-FDM v1.2A, The Cryosphere, 17, 1675–1696, https://doi.org/10.5194/tc-17-1675-2023, 2023.

Wiesmann, A. and Mätzler, C.: Microwave Emission Model of Layered Snowpacks, Remote Sensing of Environment, 70, 307–316, https://doi.org/10.1016/s0034-4257(99)00046-2, 1999.

Wille, J. D., Favier, V., Dufour, A., Gorodetskaya, I. V., Turner, J., Agosta, C., and Codron, F.: West Antarctic surface melt triggered by atmospheric rivers, Nature Geoscience, 12, 911–916, https://doi.org/10.1038/s41561-019-0460-1, 2019.

Wingham, D., Phalippou, L., Mavrocordatos, C., and Wallis, D.: The mean echo and echo cross product from a beamforming interferometric altimeter and their application to elevation measurement, IEEE Transactions on Geoscience and Remote Sensing, 42, 2305–2323, https://doi.org/10.1109/tgrs.2004.834352, 2004.

Wismann, V.: Monitoring of seasonal snowmelt on Greenland with ERS scatterometer data, IEEE Transactions on Geoscience and Remote Sensing, 38, 1821–1826, https://doi.org/10.1109/36.851766, 2000.

Zwally, H. J. and Fiegles, S.: Extent and duration of Antarctic surface melting, Journal of Glaciology, 40, 463–475, https://doi.org/10.3189/s0022143000012338, 1994.

Zwally, H. J., Giovinetto, M. B., Li, J., Cornejo, H. G., Beckley, M. A., Brenner, A. C., Saba, J. L., and Yi, D.: Mass changes of the Greenland and Antarctic ice sheets and shelves and contributions to sea-level rise: 1992–2002, Journal of Glaciology, 51, 509–527, https://doi.org/10.3189/172756505781829007, 2005.

2

ESTIMATING ANTARCTIC FIRN DENSITY BY COMBINING RADIOMETER AND SCATTEROMETER DATA

The understanding of the spatial and temporal variations in Antarctic firn density is limited due to i) spatial and temporal limitations of in situ measurements, ii) potential modelling uncertainties, and iii) lack of firn density products driven by satellite remote-sensing data. To address this gap, this chapter explores the potential of satellite microwave radiometer (SMISS) and scatterometer (ASCAT) observations for assessing spatial and temporal dynamics of dry-firn density over the Antarctic ice sheet. Since a linear relationship with individual satellite observations is insufficient to explain the spatial and temporal variation in snow density, we investigate the potential of a non-linear random forest (RF) machine learning approach trained on radiometer and scatterometer data to derive the spatial and temporal variations in dry-firn density. In the estimation process, 10 years of SSMIS observations (T_B) and ASCAT observations (σ^0_A) is used as input features to a random forest (RF) regressor. The regressor is first trained on time series of modelled density and satellite observations at randomly sampled pixels and then applied to estimate densities in dry-firn areas across Antarctica. The RF results reveal a strong agreement between the spatial patterns estimated by the RF regressor and the modelled densities. However, the temporal patterns show some discrepancies, as the RF regressor tends to overestimate summer densities, except for high-elevation regions in East Antarctica and specific areas in West Antarctica. These errors may be attributed to underestimations of short-term or seasonal variations in the modelled density and the limitations of RF in extrapolating values outside the training data. Overall, our study presents a potential method for estimating unknown Antarctic firn densities using known densities and satellite parameters.

2.1. INTRODUCTION

The accelerated loss of mass from the Antarctic ice sheet, a trend anticipated to persist in the coming decades and centuries, underscores Antarctica's pivotal role as a major

This chapter has been published as Li, W., Veldhuijsen, S. B. M., and Lhermitte, S.: Machine learning of Antarctic firn density by combining radiometer and scatterometer remote-sensing data, The Cryosphere, 19, 37–61, https://doi.org/10.5194/tc-19-37-2025, 2025.

source of future sea level rise (Pattyn and Morlighem, 2020). Recognising the critical contribution to sea level rise uncertainty highlights the urgency of comprehending Antarctica's surface mass balance (SMB). A typical method to estimate the SMB of the Antarctic ice sheet is to convert satellite altimetry height measurements into SMB (Zwally et al., 2005; Kuipers Munneke et al., 2015; Schröder et al., 2019) with the help of firn (an intermediate state between snow and glacial ice; van den Broeke, 2008; Amory et al., 2024) density. In Antarctica, firn density is highly variable in space and time due to the varying surface climate conditions (Craven and Allison, 1998; Li and Zwally, 2004; van den Broeke, 2008; Fujita et al., 2016). Therefore, it is necessary to continuously monitor firn density in Antarctica.

A variety of methods have been developed to assess firn density. In situ measurements from firn cores, snow pits, and local near-infrared pictures are valuable for accurately understanding firn densities; however, these measurements are sparse in both space and time due to cost efficiency considerations, making them insufficient for comprehensive monitoring requirements (Macelloni et al., 2007; Picard et al., 2012; Champollion et al., 2013). In the absence of in situ data, firn densification models (FDMs), such as the semi-empirical IMAU-FDM (Ligtenberg et al., 2011; Veldhuijsen et al., 2023) are commonly utilised to estimate firn density and subsequent elevation changes (Schröder et al., 2019). Nonetheless, FDMs suffer from significant uncertainties (Verjans et al., 2020). For instance, the relationship between wind velocity and density, as derived by Sugiyama et al. (2012) and van den Broeke et al. (1999) exhibits notable discrepancies, introducing uncertainties when parametrising the effects of wind. Therefore, to obtain spatially and temporally continuous assessments of changes in firn densities, satellite remote sensing serves as an important complementary method (Picard et al., 2007; Brucker et al., 2014; Meredith et al., 2019). While numerous studies have investigated these assessments, they have identified intricate relationships between remote-sensing observations and firn density, making it challenging to implement remote-sensing models. Consequently, a satellite-based firn density product remains elusive.

Among satellite remote-sensing techniques, radiometers are a primary tool used for studying firn properties, offering various frequencies and polarisations that facilitate assessments of different firn properties at different depths (Picard et al., 2007, 2012; Champollion et al., 2013; Brucker et al., 2014; Amory et al., 2024). Radiometers measure the thermal radiation emitted by the ground surface and subsurface within the range of microwave penetration (Picard et al., 2007) and typically have a spatial resolution of ~ 25 km. The observed parameter is referred to as the brightness temperature (T_B), which has typically been used to derive Antarctic surface melting extent by detecting the sharp increase in emissivity and hence T_B (Picard et al., 2007; Tedesco, 2009; Nicolas et al., 2017; de Roda Husman et al., 2022). However, studies show that T_B can also be used to assess firn densities. For example, Champollion et al. (2013) used the temporal variation in the polarisation ratio of T_B at 19 GHz and 37 GHz to evaluate the density changes in firn induced by hoar crystal formation and disappearance at Dome C (75.06° S, 123.21° E; indicated in Figure 2.2a). Alternatively, Tran et al. (2008) classified seven firn facies over Antarctica using a combination of T_B, a specific ratio defined by T_B at 23.8 GHz and 36.5 GHz, and information from Ku- and S-band altimeters acquired in 2004. They attributed the different facies to varying surface roughness or firn grain size

driven by differences in climate parameters such as wind patterns, firn accumulation, and temperature, which are known to influence firn density (Lehning et al., 2002; Champollion et al., 2013).

Alternatively, active microwave observations, specifically radar scatterometer and synthetic aperture radar (SAR), with spatial resolutions of ~ 25 km and up to ~ 5 m, respectively, have been used to assess firn properties. The backscatter intensity (σ^0) is a common parameter measured by both scatterometer and SAR. Numerous studies have been performed to link the spatial or temporal variation in σ^0 to variations in certain firn properties. Fraser et al. (2016) analysed the drivers of spatial variation in C-band scatterometer σ^0 acquired between 2007 and 2012 in dry-firn zones of Antarctica. Their study concluded that (i) the seasonal variation in σ^0 is primarily driven by precipitation and firn temperature cycles and that (ii) σ^0 exhibits a high correlation with long-term precipitation, which also affects long-term densities. On the other hand, Rizzoli et al. (2017) exploited interferometric acquisitions of X-band SAR σ^0 from TanDEM-X, using the combination of σ^0 and a volume correlation factor to classify Greenland into four firn facies with an unsupervised machine learning method. The firn facies classified by this study can be attributed to different melt extents.

The aforementioned studies indicate the capability of various passive and active satellite observations, either individually or in combination, to evaluate spatial and temporal patterns of firn density. However, the precise mechanisms underlying the impact of firn density on satellite observations cannot always be fully understood (Champollion et al., 2013; Fraser et al., 2016; Rizzoli et al., 2017). In addition, previous studies using satellite observations to assess firn properties are restricted either to a specific location where in situ measurements are available (Champollion et al., 2013) or to a specific time period (Tran et al., 2008). Implementation of these aforementioned approaches to other areas or time periods therefore requires further assessment. Hence, it is crucial to identify suitable combinations of satellite observations and data fusion methods that enable the assessment of firn density across extensive regions and multiple seasons.

Consequently, the objective of this study is to propose and assess a methodology to derive firn density and its spatial and temporal variations over the Antarctic ice sheet based on daily satellite observations. To achieve this, we conduct a 3-fold experiment involving the comparison of time series data from the Special Sensor Microwave Imager/Sounder (SSMIS) and Advanced Scatterometer (ASCAT) satellites with the output of a semi-empirical firn densification model (IMAU-FDM). In the first experiment, we juxtapose the satellite time series with the output of IMAU-FDM to evaluate the potential of individual satellite parameters in linearly explaining density variations. The second experiment involves cluster analysis on the combined SSMIS and ASCAT satellite data to identify spatial and temporal patterns of satellite observations and compare them with IMAU-FDM density patterns. Then, we assess the potential of a non-linear random forest (RF) machine learning approach (Breiman, 1996, 2001) trained on SSMIS and ASCAT data to derive spatial and temporal variations in dry-firn density. More specifically, assuming firn densities in certain regions are known, this experiment aims to estimate firn densities of the unknown regions in space and time using a combination of satellite observations. Due to the currently limited availability of in situ density measurements, however, our study uses part of the modelled IMAU-FDM densities as "known" densities

to train the RF regressor. Finally, we evaluate our RF predictions with external reference data, i.e. available in situ firn density measurements (Surface Mass Balance and Snow on Sea Ice Working Group (SUMup)) and ERA5 climate parameters.

2.2. DATA

In this study, we evaluate the potential of satellite microwave radiometer (SSMIS) and scatterometer (ASCAT) observations in assessing the spatial and temporal dynamics of dry-firn density across the Antarctic ice sheet. We focus on the grounded Antarctic ice sheet only, where wet firn and melting that potentially affect the satellite microwave observations are less pronounced (Lenaerts et al., 2016; Kingslake et al., 2017; Spergel et al., 2021; Li et al., 2021; de Roda Husman et al., 2022). To account for this, we mask out all satellite observations over the ice shelves using the grounding line defined by Depoorter et al. (2013).

2.2.1. RADIOMETER DATA

Time series of brightness temperature (T_B) from the SSMIS are used in this study, as they are widely used to assess variations in firn properties (Tedesco and Kim, 2006; Tran et al., 2008; Brucker et al., 2010). The available measurement channels include vertically and horizontally polarised 19 GHz, 37 GHz and 91.655 GHz, and vertically polarised 22 GHz (Kunkee et al., 2008). However, for the purposes of this study, our focus is solely on the 19 GHz and 37 GHz channels, since the atmospheric influence is negligible at these frequencies (Picard et al., 2009; Brucker et al., 2011; Champollion et al., 2013). Theoretically, the penetration depths are 1–7 m (at 19 GHz) and 0.1–2 m (at 37 GHz) in dry-snow zones of Antarctica (Surdyk, 2002; Brucker et al., 2010). With the presence of liquid water, the imaginary part of snow permittivity increases, therefore T_B increases (Tedesco, 2007). However, the actual penetration depths can still vary per region (Picard et al., 2009). These characteristics ensure the possibility for SSMIS at 19 GHz and 37 GHz to monitor the changes in firn properties at a variety of depths. The daily polar-gridded T_B data are acquired from the National Snow and Ice Data Center (NSIDC) with a spatial resolution of 25 km for both the 19 GHz and 37 GHz channels (Meier et al., 2021). All data are acquired by the F17 sensor, as it provides continuous daily data acquisition in the period between January 1, 2011 and December 31, 2020.

2.2.2. SCATTEROMETER DATA

Backscatter intensity (σ^0) from synthetic aperture radar (SAR) was also previously used to assess density variations due to the melting–refreezing process of certain firn types (Rizzoli et al., 2017) and to examine variations in firn facies (Fahnestock et al., 1993). In this study, we employ time series of backscatter intensity from the Advanced Scatterometer (ASCAT) satellite sensor as an alternative to SAR σ^0, primarily due to its high temporal resolution (daily) and its coverage over the entire Antarctica. ASCAT is an operational C-band (5.255 GHz) fan-beam scatterometer (Figa-Saldaña et al., 2002; Fraser et al., 2016) that has been in operation on MetOp satellites since 2006. It operates in V polarisation and covers multiple incidence angles. For dry firn, the penetration depth of C-band ASCAT is approximately 20 m (Rignot, 2002). Following Larue et al. (2021),

we also performed a simulation using the Snow Microwave Radiative Transfer (SMRT) model (Picard et al., 2018), where firn properties at different depths of the firn layer are altered, and the impacts on both backscattering and brightness temperature are presented (Appendix 2.A). However, the top 1 m is most exposed to atmospheric drivers, which also affect the variability in C-band microwaves (Fraser et al., 2016). The ASCAT products used in this study are obtained from the Brigham Young University (BYU) Microwave Earth Remote Sensing (MERS) laboratory (2010) (Long et al., 1993; Early and Long, 2001; Lindsley and Long, 2010). The data are processed using the scatterometer image reconstruction (SIR) algorithm, which enhances the spatial resolution of images from 25 km to 4.45 km. The backscattering product adopted in our study is referred to as the A product in Long and Drinkwater (2000):

$$\sigma^0(\theta) = A + B(\theta - 40^\circ) \tag{2.1}$$

where A (in dB) is the originally measured σ^0 normalised to 40° and B (in dB per degree) is a parameter describing the dependence of the original σ^0 on θ. The processing of Long and Drinkwater (2000) accounts for the incidence angle dependence of the originally measured σ^0, as the measurements are made over multiple incidence angles (between 20° and 55°). In this study, we only use the isotropic normalised A parameter (hereafter σ^0_A), as it has been shown to better correlate with various climate parameters and with the long-term firn density (Fraser et al., 2016). In addition, the presence of liquid water can reduce the volume scattering and increase the microwave absorption (Stiles and Ulaby, 1980); this should be taken care of and will be elaborated in Section 2.3. To ensure consistent analysis between T_B and σ^0_A, the BYU σ^0_A products are interpolated to the same polar grids as the SSMIS T_B products using bi-linear interpolation. The data acquisition time is the same as that of the radiometer data.

2.2.3. DENSITIES FROM IMAU-FDM

To understand the spatio-temporal variation in satellite data, we compare the SSMIS and ASCAT satellite data to the output of a semi-empirical firn densification model. Therefore, we use output from the latest version of the IMAU firn densification model (IMAU-FDM v1.2A; Veldhuijsen et al., 2023). IMAU-FDM simulates the transient evolution of the Antarctic firn column, and is forced at the upper boundary by outputs of the Regional Atmospheric Climate Model (RACMO2.3p2) at a 27 km horizontal resolution (van Wessem et al., 2018) and with a temporal resolution of 10 days. The model employs up to 300 layers in thicknesses of 3 to 15 cm, which represent the firn properties in a Lagrangian way. The output is resampled to a regular grid with layers of 4 cm. The density of the freshly fallen snow is a function of instantaneous wind speed and temperature in IMAU-FDM. Over time, the simulated firn layers become denser due to dry-snow densification and meltwater refreezing.

To estimate at which depth the firn density has an impact on satellite microwaves, we perform a correlation estimation between satellite observation time series and IMAU-FDM density at different depths, as elaborated in Section 2.3.1. The unrealistically large values in IMAU-FDM densities (more than 917 kg m^{-3}) are treated as invalid. To facilitate comparison with the satellite products, the firn density data from IMAU-FDM are reprojected using bi-linear interpolation to the same polar grids as the satellite data, where

valid data are restricted to pixels within the Antarctic coastline provided by Depoorter et al. (2013).

2.2.4. REFERENCE IN SITU DENSITY MEASUREMENTS

Furthermore, we employ in situ density measurements obtained from the SUMup dataset (Koenig and Montgomery, 2018; Montgomery et al., 2018) as a reference for spatial evaluation of the satellite data and the RF regressor. SUMup provides information on the start point, end point and mid-point of measurements. We use the mid-point here to define the depth of the reference data. For each date of measurement at each location, if multiple measurements are available, only the density measurements at the shallowest mid-point depths are used. Such depths are also restricted to < 1 m. The measurements within the depth restriction were taken between January 22, 1984 and January 23, 2017 and consist of 67 valid points. The SUMup dataset does not contain time series but only single measurements on specific irregular dates throughout the time period between 1984 and 2017. Therefore, we use the SUMup dataset only for spatial evaluation of the potential uncertainties from both the IMAU-FDM densities and the densities estimated by the RF regressor.

2.2.5. ERA5 CLIMATE PARAMETERS

As mentioned in Section 2.1, IMAU-FDM can introduce discrepancies due to simplified parametrisation (Verjans et al., 2020), which can be propagated in the estimation process with the RF regressor. Therefore, to interpret the difference between the measured (SUMup or Leduc-Leballeur et al. (2017) data), modelled (IMAU-FDM) and estimated (RF) densities, it is important to understand the effects of climate conditions. Therefore, we use ERA5 wind speed estimated at midday (Muñoz-Sabater, 2019; Muñoz-Sabater et al., 2021) as an approximation of the daily wind conditions. By incorporating this information, we aim to better understand the discrepancies between the observed and IMAU-FDM densities and the source of discrepancies between the IMAU-FDM densities and the densities estimated from satellite observations with the RF regressor. The ERA5 wind speed data have a horizontal resolution of 9 km. Similarly to the IMAU-FDM data, we interpolate these climate variables to the same polar grids as the SSMIS data using bi-linear interpolation to ensure consistency in the analysis.

2.3. METHODS

We assess the potential of SSMIS and ASCAT satellite observations to assess dry-firn density in a 3-fold experiment. Firstly, we compare the satellite time series with the output of IMAU-FDM to evaluate the potential of individual satellite parameters to linearly explain density variations (Section 2.3.1). Secondly, we perform a cluster analysis on the combined SSMIS and ASCAT observations to identify spatio-temporal patterns in satellite observations. These patterns are then compared with the density patterns obtained from IMAU-FDM, and dry-snow zones are determined (Section 2.3.2). Finally, we quantify the potential of a non-linear random forest (RF) machine learning approach trained on SSMIS and ASCAT observations to derive the spatial and temporal variations in dry-firn density (Section 2.3.3). For clarity, the content of Section 2.3.2 and Section 2.3.3 is

summarised and visualised as a flowchart in Figure 2.1.

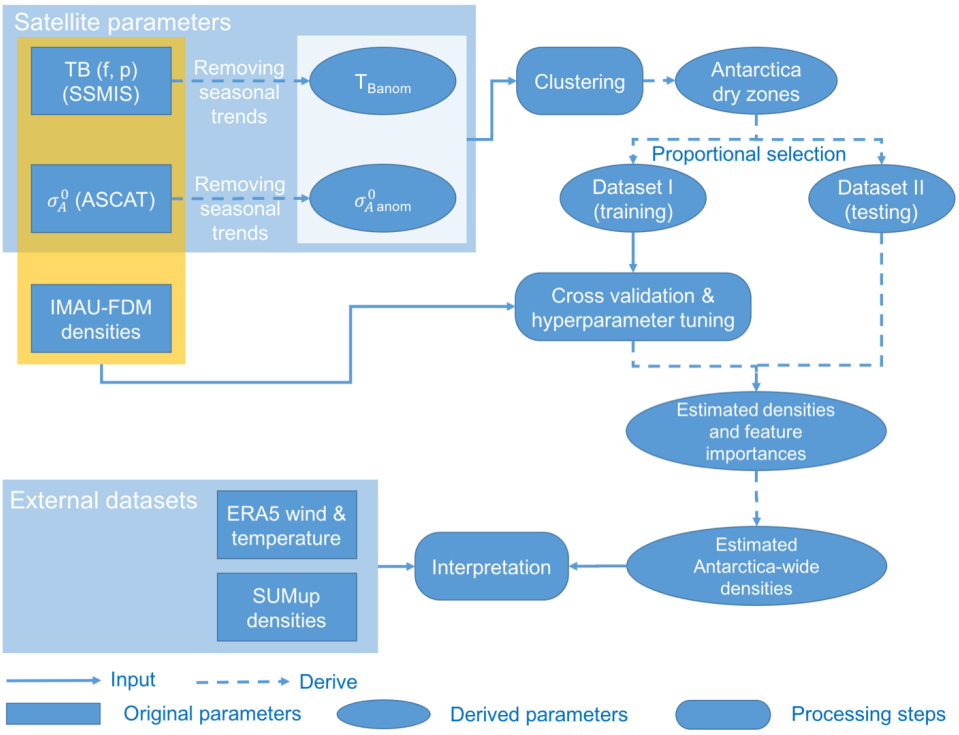

Figure 2.1: Overview flowchart of the data and method used in this study. The clustering process uses $T_{B_{anom}}$ and $\sigma^0_{A_{anom}}$ as input to derive dry snow zones over the Antarctic ice sheet. Then, pixels clustered as dry snow are included to estimate firn density with the RF regressor. Parameters used as features of the RF regressor are further elaborated in Section 2.3.3. Among the derived parameters, Antarctica dry zones, Dataset I and Dataset II are selected proportionally based on the number of pixels per cluster.

2.3.1. CALCULATION OF CORRELATION BETWEEN SATELLITE PARAMETERS AND FIRN DENSITY

To gain a general understanding of the spatial patterns of the satellite parameters and densities from IMAU-FDM, we calculate and visualise the map of T_B and σ^0_A and the IMAU-FDM firn density at a selected depth averaged between January 1 2011 and December 31 2020 (shown in Appendix 2.B). Then, to observe the temporal correlation between the satellite parameters and the IMAU-FDM densities, for each pixel, the correlation coefficient between different satellite parameters and the firn density over time is calculated and visualised. To ensure consistent temporal resolution for the analysis, the satellite parameters are downsampled from daily resolution to 10-day resolution to match the temporal resolution of the IMAU-FDM densities. Since the scattering properties of microwaves are affected by firn properties along the penetration depth (Ulaby et al., 1996; Bingham and Drinkwater, 2000; Arndt and Haas, 2019; Cartwright et al.,

2022), this analysis utilises densities from a range of depths, including 12 cm, 40 cm, 1 m, 2 m, 5 m and 10 m. The density of each depth is defined not as the specific density at a single depth but as the average density from the surface to this depth. The reason for this comparison is that, although the theoretical penetration depth can be larger than 20 m for the C-band in Antarctic dry firn (Rott et al., 1993), the surface conditions, such as temperature, wind, and precipitation have more impact on the shallow depth of the firn layer and on the satellite parameters (Tran et al., 2008; Picard et al., 2012; Champollion et al., 2013; Fraser et al., 2016). By calculating the correlation coefficients between IMAU-FDM densities and satellite parameters, we need to understand at which depth the densities cannot be affected by the surface conditions. We also need to estimate a depth threshold from which 37 GHz cannot penetrate the firn layers and hence cannot provide information on spatial and temporal variation in firn in this experiment, as the penetration ability reduces with an increasing frequency (Rott et al., 1993; Surdyk, 2002). Finally, the density at the depth where there is the best overall correlation between satellite observations and density time series is adopted for the RF experiment.

2.3.2. CHARACTERISATION OF FIRN TYPES USING TIME SERIES OF MICROWAVE OBSERVATIONS

In our study, the clustering of satellite observations is primarily carried out as a preparatory step aimed at ensuring that all the representative regions, i.e. the regions with distinctive satellite data patterns, are correctly accounted for in the RF model training procedure in Section 2.3.3. Moreover, we aim to rule out pixels where melt events can be observed, as the melt-induced liquid water and ice-lens formation complicate the satellite measurements (Stiles and Ulaby, 1980; Brucker et al., 2010; Trusel et al., 2012), rendering density estimations invalid in such cases. This step facilitates a comprehensive understanding of the spatio-temporal variations in firn properties based on the available satellite observations. We expect that clustering the time series of satellite observations will effectively differentiate pixels experiencing melting from those unaffected. By identifying and excluding melt-affected pixels, we can ensure the validity of density estimations using the RF regressor described in Section 2.3.3. Additionally, to enhance the ability of the RF regressor to capture the characteristics of various dry snow types, we choose training samples based on the identified dry snow types. This approach enables the representation of diverse snow types in the training dataset, improving the accuracy of the RF regressor in estimating density across different snow types.

To cluster and distinguish the different snow types, we propose to use the anomalies in T_B and σ^0_A described as follows. Since T_B is strongly dependent on seasonal variations in firn temperature, the average seasonal signal is removed in the clustering process to obtain time series anomalies that reflect the variations in temporary events such as melt–refreeze (Nicolas et al., 2017), and density or grain size variations (Picard et al., 2012; Champollion et al., 2013). We also derive the σ^0_A anomalies due to the impact from temperature seasonal cycles (Fraser et al., 2016). The time series anomalies are calculated by taking the 10-year average of T_B or σ^0_A for each day in a year, defined as $\overline{T}_B$ and $\overline{\sigma}^0_A$, and subtracting this averaged time series from the absolute observations for each year, leading to $T_{\mathrm{B}_\mathrm{anom}} = T_\mathrm{B} - \overline{T}_\mathrm{B}$ and $\sigma^0_{A_\mathrm{anom}} = \sigma^0_A - \overline{\sigma}^0_A$. The time series anomalies of $T_{\mathrm{B}_\mathrm{anom}}$ and $\sigma^0_{A_\mathrm{anom}}$ are then normalised and stacked for clustering.

The adopted clustering solution is a simple hierarchical algorithm (Ward, 1963) which uses the normalised and stacked $T_{\mathrm{B}_{\mathrm{anom}}}$ and $\sigma^0_{A_{\mathrm{anom}}}$ time series as input. For pre-processing, we remove outliers in the $T_{\mathrm{B}_{\mathrm{anom}}}$ and $\sigma^0_{A_{\mathrm{anom}}}$ time series per pixel by defining an interval of 3 standard deviations above and below average. Then, the temporal gaps are filled with a linear interpolation. The application of the clustering algorithm is illustrated with an example (Figure 2.2). The clustering process starts from all clusters, each containing one pixel, and the clusters are then hierarchically grouped together based on the similarity of features, which refers to the Euclidean distance between the normalised and stacked $T_{\mathrm{B}_{\mathrm{anom}}}$ and $\sigma^0_{A_{\mathrm{anom}}}$ time series of different pixels in our study (however, only $\sigma^0_{A_{\mathrm{anom}}}$ from January 14, 2016 is used in Figure 2.2 for illustration). The grouping process is typically represented by a dendrogram, as in Figure 2.2b. Finally, the number of clusters is determined empirically; different numbers of clusters result in different outcomes, as in Figure 2.2c–e. For our study where the normalised and stacked $T_{\mathrm{B}_{\mathrm{anom}}}$ and $\sigma^0_{A_{\mathrm{anom}}}$ time series between 2011 and 2020 are used, we select 7 clusters as the optimal number of clusters. To provide a brief overview of the clustering result, we visualise the time series of the mean, 20th percentile, and 80th percentile of different satellite parameters, together with an IMAU-FDM density for each cluster in Appendix 2.C. This allows a comparison of the changes in satellite parameters with density variations across the clusters and an assessment of the reliability of our study to distinguish melt zones from dry ones.

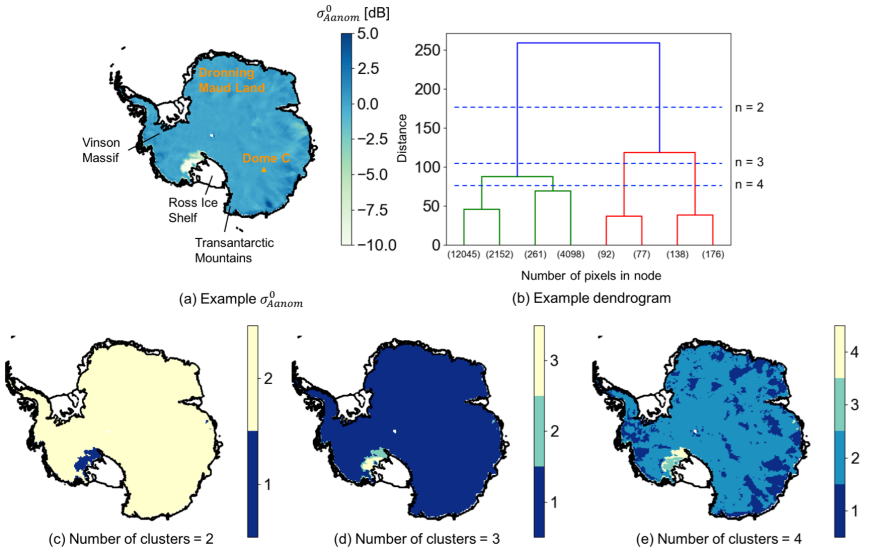

Figure 2.2: An example of the principle of hierarchical clustering. (a) Map of $\sigma^0_{A_{\mathrm{anom}}}$ acquired on January 14, 2016 following the melt event detected by Nicolas et al. (2017); (b) dendrogram obtained from panel (a), with low-hierarchy nodes simplified and n referring to the number of clusters; and (c)–(e) clustering results using different numbers of clusters. Several locations mentioned in this study are labelled in panel (a). The coastline is from Depoorter et al. (2013).

2.3.3. DERIVING FIRN DENSITIES USING SATELLITE PARAMETERS AND RANDOM FOREST REGRESSOR

Given the complex and often non-linear relationships between satellite observations and firn density (Fraser et al., 2016), a non-linear regression model based on machine learning is explored to relate the satellite time series to firn density. The method relies on a certain amount of known density measurements as the training dataset, and on the continuous satellite parameters as the trained features. We opt for a random forest regressor as machine learning model (RF regressor hereafter) due to the simplicity and usability (Vafakhah et al., 2022; Viallon-Galinier et al., 2023).

Ideally, in situ measurements should be used as the training dataset. However, in situ measurements are often single measurements that lack temporally continuous observations. As our goal is to relate the satellite time series to assess spatio-temporal variations in firn density, we adopt an alternative approach that uses the output of IMAU-FDM as training data instead of relying on in situ data. Although this approach has the disadvantage of training the RF regressor on a noisy IMAU-FDM dataset, which may exhibit spatial and temporal differences compared to actual in situ densities (e.g., biases between the model and in situ observations), we leverage the strengths of RF regression for pattern recognition in noisy datasets. The use of multiple decision trees and random feature selection can reduce the variance of the model and reduce overfitting, resulting in better generalisation performance on noisy data (Hastie et al., 2008). Therefore, we expect that the RF regressor generalises on the density estimations of IMAU-FDM, which is known to capture the spatial variation in in situ density measurements well and the temporal variations reasonably well (Veldhuijsen et al., 2023).

The training, testing, and implementation of the RF regressor involve three main steps:

- Training and hyperparameter tuning: a subset of IMAU-FDM densities (Subset I) is used as the training dataset in a 5-fold cross-validation procedure: in each fold, 20 % of the training set is used for validation and 80 % for training. The goal is to identify the configuration that achieves the best cross-validation score, indicating the optimal set of hyperparameters for the RF regressor. Multiple models are evaluated, representing different combinations of hyperparameters defined for the RF regressor (see Table 2.1).

- Testing and model evaluation: a different subset of temporally and spatially coregistered SSMIS and ASCAT measurements for the given pixels (Subset II) is used as input to the RF regressor, which has been trained on Subset I. The purpose of this step is to evaluate the performance of the model and assess the accuracy of the RF density estimations. Additionally, it helps to determine the importance of satellite parameters in the predictions of the regressor.

- Antarctica-wide implementation: the satellite time series covering the entire study area are fed into the RF regressor, which has been trained on Subset I. This step aims to estimate densities across the entire Antarctic dry-firn region. The output densities are then evaluated by comparing them to both the IMAU-FDM densities and the SUMup densities.

Table 2.1: Hyperparameter range and optimal values used to specify the random forest (RF) model.

Hyperparameter	Range	Optimal value
Number of trees	50, 100, 200	100
Maximum depth of the tree	12, 15, 18	12
The minimum number of samples at a leaf node	1, 3, 5, 7	5
The minimum number of samples to split an internal node	2, 3, 4, 5	4
The number of features to consider when searching for the best split	1, 3, 5	1

Both Subset I and Subset II consist of pixels randomly selected from the non-melting pixels clustered in Section 2.3.2. Subset I contains 10 % of the non-melting pixels, and Subset II contains 100 pixels in total. The selection ensures that the pixels from both subsets do not overlap. The time series of each feature ($\boldsymbol{X}$ in Eq. 2.2) in each pixel cover the period between January 1 2011, and December 31 2020 with a 10-day resolution. To ensure consistent temporal resolution between the input features and the target IMAU-FDM densities, the daily satellite parameters are also downsampled to the 10-day temporal resolution of the IMAU-FDM firn density by selecting satellite parameters that are acquired on the same dates as the available IMAU-FDM density, resulting in 366 samples in total for each feature in each pixel. Finally, Subset I consists of 1,748 pixels multiplied by 366 samples (639,768 samples in total), Subset II consists of 100 pixels multiplied by 366 samples (36,600 samples in total), and the Antarctica-wide dataset consists of 17,478 pixels multiplied by 366 samples (6,396,948 samples in total).

The RF regressor is implemented with the target variable, which is the IMAU-FDM density at the depth selected from the correlation analysis, and the input feature $\boldsymbol{X}$ initially defined as follows:

$$\boldsymbol{X} = (T_{\mathrm{B}}(19\mathrm{V}),\ T_{\mathrm{B}}(19\mathrm{H}),\ T_{\mathrm{B}}(37\mathrm{V}),\ T_{\mathrm{B}}(37\mathrm{H}),\ \sigma^0_A) \tag{2.2}$$

Within $\boldsymbol{X}$, we include T_{B} and σ^0_A, as they theoretically account for variations in temperature, precipitation, and other potential climate parameters that show a potentially strong seasonality (e.g. Champollion et al., 2013; Fraser et al., 2016).

In the testing and evaluation step, we assess the performance of the optimal RF regressor. This is achieved by comparing the RF and IMAU-FDM densities of Subset II using a scatterplot, the root-mean-square error (RMSE) and the correlation coefficient between the RF densities and the IMAU-FDM densities. The importance of satellite parameters in the RF regressor is computed by calculating the Gini importance, which is a measure of feature importance based on the Gini gain, i.e. impurity reduction (Strobl et al., 2007). For each feature used to split the data, the decrease in the Gini node impurity is recorded at each split, and the Gini importance is calculated as the average of all decreases in the Gini impurity in the forest where this feature forms the split (Archer and Kimes, 2008).

In the Antarctic-wide implementation, the optimal RF regressor is implemented to

Table 2.2: Average temporal correlation coefficient between satellite parameters and IMAU-FDM density from different depths.

Depth	T_B(19V)	T_B(19H)	T_B(37V)	T_B(37H)	σ^0_A
12 cm	0.19	0.18	0.20	0.20	-0.05
40 cm	0.24	0.23	0.20	0.19	-0.06
1 m	0.23	0.20	0.12	0.12	-0.06
2 m	0.18	0.12	0.03	0.02	-0.06
5 m	0.08	0.02	-0.07	-0.08	-0.04
10 m	0.05	0.01	-0.07	-0.07	-0.03

predict the spatial and temporal variations in firn density. These predictions are then compared with IMAU-FDM and the SUMup densities. The spatial agreement is assessed by comparing the temporal averages of the RF predictions, IMAU-FDM, and SUMup by using the mean difference and the RMSEs. The temporal agreement is assessed by the RMSE and by the correlation coefficient between the per-pixel time series of RF predictions and IMAU-FDM density. We also compare the spatial patterns of the RF-predicted densities with the ERA5 wind velocity as it is a potential driver for spatial variation in firn density, especially for the uncertainties in IMAU-FDM. Finally, we illustrate this temporal agreement by showing time series over four pixels that show representative differences between RF and IMAU-FDM densities (locations visualised in Figure 2.4).

In addition, since satellite parameters may exhibit a certain level of correlation with densities in the long term (Fraser et al., 2016), we also conduct a linear regression (LR) process, which fits a linear function between $\boldsymbol{X}$ and the target density. The RMSE and correlation coefficient between the LR-obtained density and the IMAU-FDM density are also used to assess the advantages and drawbacks of RF.

2.4. RESULTS

2.4.1. CORRELATION BETWEEN SATELLITE PARAMETERS AND FIRN DENSITY

The temporal correlation between satellite parameters and the average density from the upper x m depth (x refers to 12 cm, 40 cm, 1 m, 2 m, 5 m and 10 m) is calculated per pixel, and the spatial average of the correlation coefficient is summarised in Table 2.2. The results show that on average, the maximum absolute correlation coefficient can be obtained at 40 cm depth. The correlation between density and T_B at 19 GHz frequency drastically decreases at 5 m, and the correlation between density and T_B at 37 GHz frequency largely decreases at 2 m, similar to the penetration ability from Surdyk (2002). The correlation between densities and σ^0_A is constantly negative, and the absolute correlation coefficient is constantly low; however, it also demonstrates a slight decrease as the depth increases from 2 m to 10 m, showing a certain degree of sensitivity. Despite the low correlation, however, our study still includes σ^0_A due to the long-term correlation derived by Fraser et al. (2016).

The lack of spatial and temporal consistency between satellite and density is illustrated in Figure 2.3, which shows the pixel-wise temporal correlation of each satellite parameter with the 40 cm density in IMAU-FDM. All T_B channels generally show a pos-

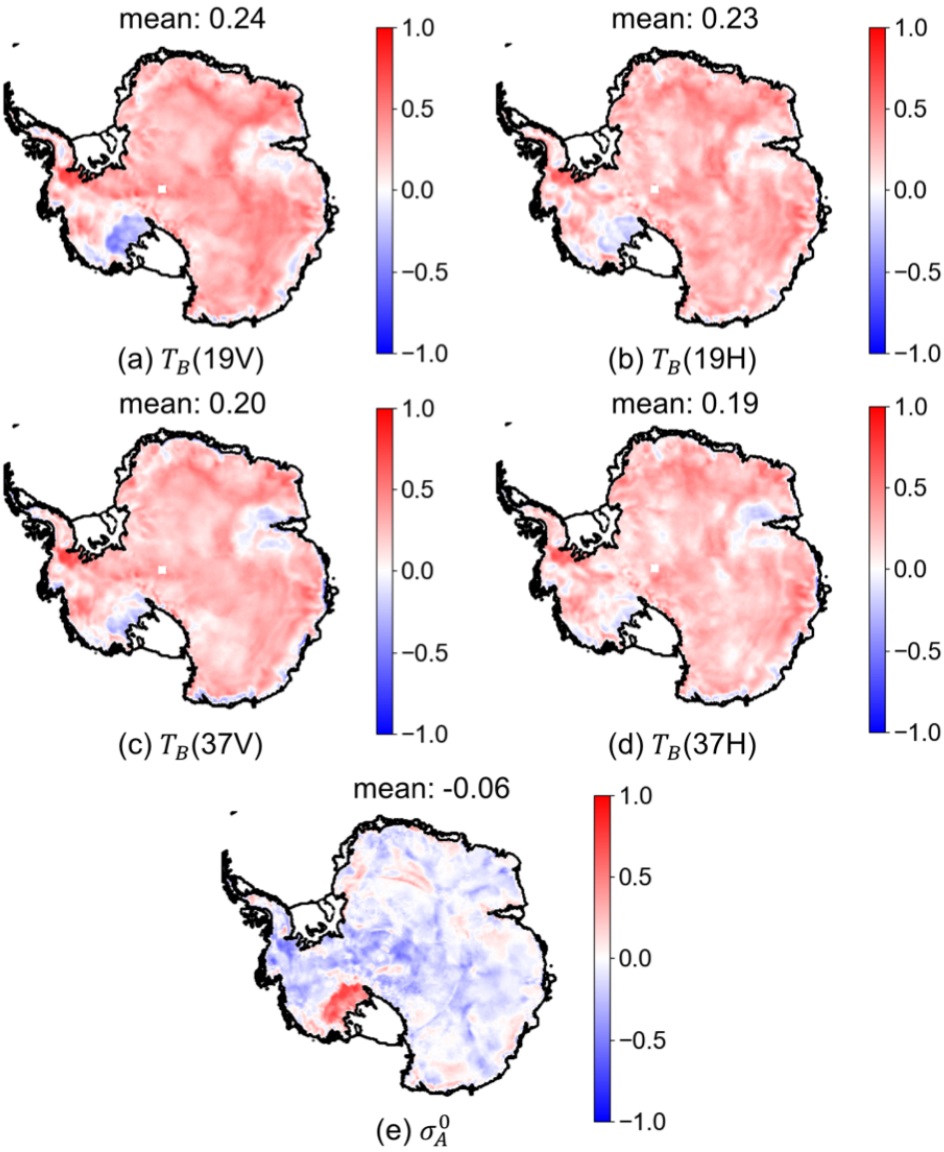

Figure 2.3: Map of temporal correlation calculated per pixel between 40 cm IMAU-FDM density and (a) brightness temperature (T_B) from 19 GHz vertical polarisation, (b) T_B from 19 GHz horizontal polarisation, (c) T_B from 37 GHz vertical polarisation, (d) T_B from 37 GHz horizontal polarisation, and (e) backscatter intensity (σ^0_A). The coastline is from Depoorter et al. (2013).

itive correlation with $\rho_{40\text{cm}}$ in East Antarctica but a negative correlation in parts of West Antarctica and many coastal regions. The negative correlation in coastal regions can be attributed to melt, as shown in the masked-out regions in Figure 4 of Picard et al. (2012). The correlation between $\rho_{40\text{cm}}$ and σ^0_A is generally low, except for the region next to the Ross Ice Shelf (location shown in Figure 2.2a), where the correlation coefficient can be up to 0.75.

Overall, this correlation analysis indicates that the relationship between satellite parameters and firn density is complex and that simple linear relationships may not adequately describe the IMAU-FDM density based on different satellite parameters. Therefore, non-linear approaches such as the RF regressor should be employed to assess the potential of relating the IMAU-FDM firn density to various satellite parameters (Vafakhah et al., 2022; Anilkumar et al., 2023).

2.4.2. FIRN-TYPE CLUSTERS

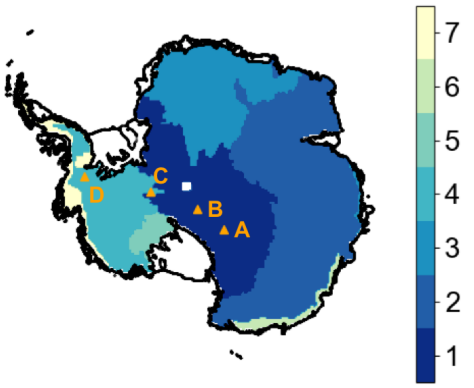

Figure 2.4: Clustering results from the combination of normalised T_B and σ^0_A after removing the seasonal trend. Triangles show the locations where temporal assessment per pixel is performed. The coastline is from Depoorter et al. (2013).

Figure 2.4 shows the map of clusters derived from time series of the combined satellite parameters, where each cluster represents a natural grouping of pixels with similar satellite time series behaviour. The map shows that four large clusters (referred to as firns 1–4) cover the dry-firn interior of Antarctica, with firns 1–3 in East Antarctica and firn 4 in West Antarctica. Firn 5 is a cluster in West Antarctica close to the Ross Sea which corresponds to the region that showed a strong melt event in January 2016 (Nicolas et al., 2017), while firn 6 and firn 7 show small regions near the coastline in East Antarctica and West Antarctica, respectively that also show clear melting signals (details shown in Appendix 2.C).

2.4.3. ASSESSMENT OF RF DENSITIES AT SAMPLE PIXELS

Figure 2.5a presents the results of the RF regressor for estimating firn densities based on satellite parameters. It demonstrates that the non-linear multivariate approach of

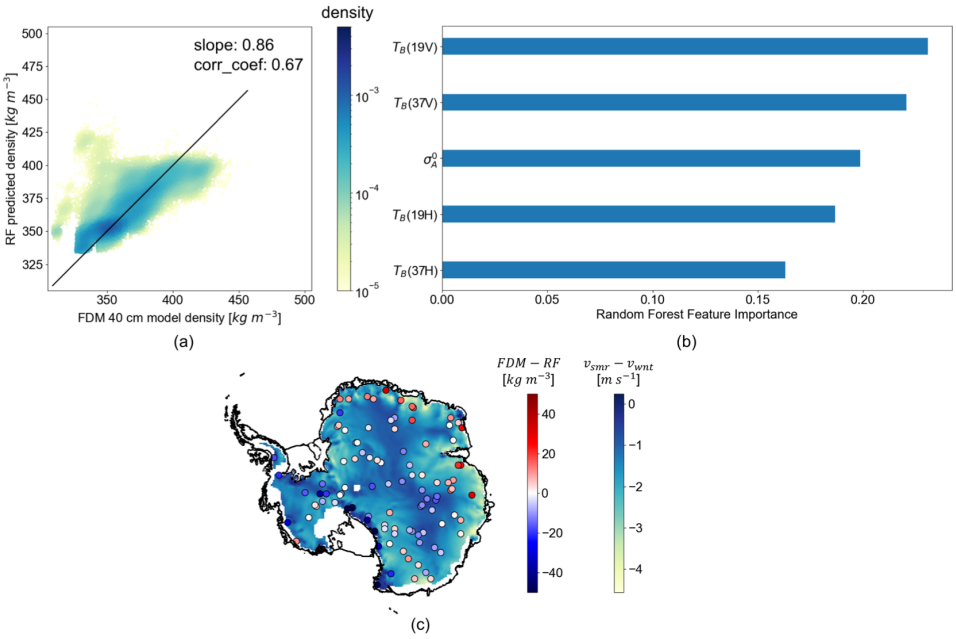

Figure 2.5: (a) Density comparison between RF densities and IMAU-FDM densities at sample pixels referred to as Subset II, with the colour of each point showing the density distribution of points; the colour bar is in logarithmic scale. (b) RF feature importance of different input satellite parameters. (c) The temporally averaged difference between IMAU-FDM and RF densities at the pixels, visualised on top of the map of the difference between the summer (v_{smr}) and winter wind velocity (v_{wnt}) from ERA5. The coastline is from Depoorter et al. (2013).

the RF regressor captures the spatial variations in IMAU-FDM density, exhibiting a linear relationship between IMAU-FDM and RF densities with a slope of 0.86. The RMSE is 19.23 kg m^{-3}, and the correlation coefficient between the estimated and training densities is 0.67. Moreover, the RF regressor performs most ideally between approximately 325 kg m^{-3} and 375 kg m^{-3}, whereas it fails to capture the large densities, as no RF estimate exceeds 410 kg m^{-3}, which can partially be due to a well-known extrapolation problem intrinsic to the RF regression (Hengl et al., 2018). The RF densities also exhibit an overestimation when the IMAU-FDM density is lower than 325 kg m^{-3}. The pixels with large overall underestimation (in dark red) and overestimation (in dark blue) of RF is also visible in Figure 2.5c. In general, the large underestimation of RF occurs in the coastal regions of East Antarctica, where the winter wind velocity largely exceeds the summer wind velocity (by approximately 3 m s^{-1}). The large overestimation of RF occurs along the Transantarctic Mountains, where the topography is more complex, introducing strong surface scattering instead of volume scattering. The feature importance provided by the Gini impurity index (Figure 2.5b) shows the ranked importance of satellite parameters in the predictive performance of the model, indicating that the vertical polarisation of T_B is dominant in predicting ρ_{40cm}. The higher importance of 19 GHz is also clearly visible in the temporal correlation coefficients in Figure 2.3. We attribute

the high importance of σ^0_A to the fact that it can be influenced by other parameters that have an impact on dry-snow scattering properties, such as wind and precipitation; the mechanism may not necessarily be linear, but rather complex (Fraser et al., 2016).

2

2.4.4. SPATIAL ASSESSMENT OF RF DENSITIES

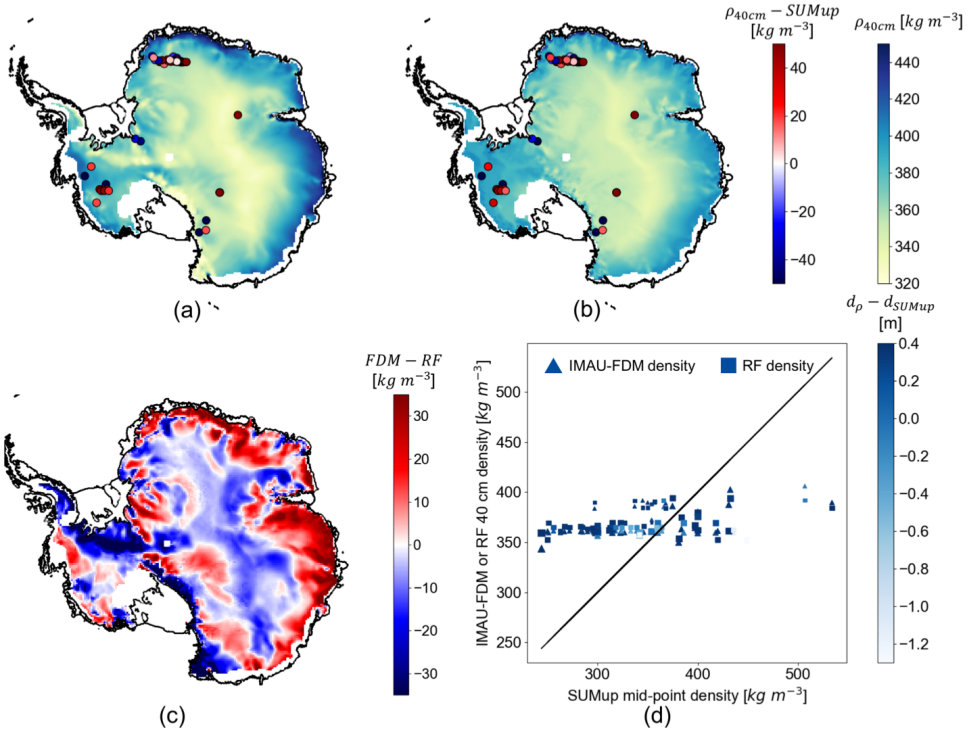

Figure 2.6: Maps of (a) temporally averaged IMAU-FDM 40 cm densities, (b) temporally averaged RF densities, and (c) the difference between averaged IMAU-FDM densities and RF densities ($FDM - RF$). Differences between the modelled or estimated densities and the SUMup densities are shown in scattered points in panels (a) and (b) as FDM-SUMup or RF-SUMup. Panels (a) and (b) share the same colour bar, in which blue–red shows the difference between the IMAU-FDM or RF densities and the SUMup densities ($\rho_{40\text{cm}} - SUMup$) and green–light blue shows the IMAU-FDM or RF densities ($\rho_{40\text{cm}}$). The coastline is from Depoorter et al. (2013). Panel (d) shows the relationship between IMAU-FDM or RF densities and SUMup densities. The sizes of the scattered points indicate the time difference between the SUMup measurements and the year 2020, and the colour shows the difference in depth between IMAU-FDM or RF measurements (both fixed at 40 cm) and SUMup measurements ($d_\rho - d_{\text{SUMup}}$).

In Fig 2.6, the temporally averaged RF density estimates and their differences relative to IMAU-FDM densities at the 40 cm depth and SUMup in situ densities are presented. The comparison in Figure 2.6c shows that temporally averaged RF density estimations are in general larger than temporally averaged IMAU-FDM density in interior regions of Antarctica except for megadune regions, whereas they are lower towards coastal regions. The RMSE between the IMAU-FDM and RF averages (referred to as FDM-RF) is 17.30 kg m^{-3} and the mean FDM-RF difference is −0.40 kg m^{-3}. An overestimation of

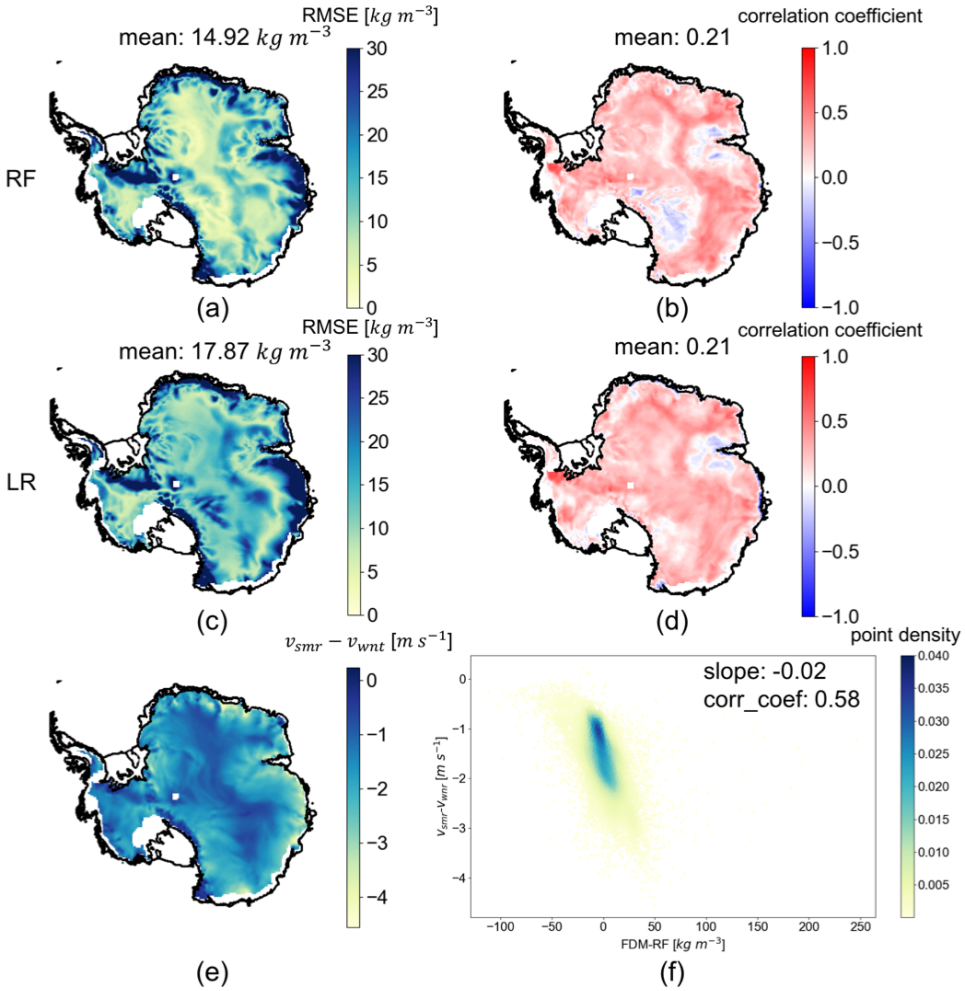

Figure 2.7: Maps of (a) the root-mean-square error (RMSE) between IMAU-FDM 40 cm densities and RF densities, (b) the correlation coefficient between IMAU-FDM 40 cm densities and RF densities, (c) root-mean-square error (RMSE) between IMAU-FDM 40 cm densities and LR densities, (d) the correlation coefficient between IMAU-FDM 40 cm densities and LR densities, and (e) the difference between the summer (v_{smr}) and winter (v_{wnt}) wind velocity from ERA5. (f) Scatterplot of the density difference between IMAU-FDM and RF versus the difference between summer and winter wind velocities, coloured by the density distribution of points. The coastline of the maps is from Depoorter et al. (2013).

RF is most pronounced in West Antarctica close to Vinson Massif (location shown in Figure 2.2a), which possibly corresponds to the overestimation in Figure 2.5a. Meanwhile, the comparison with the SUMup densities shows that RF and IMAU-FDM densities have comparable error patterns. The RMSE of FDM-SUMup is 59.17 kg m^{-3}, and the mean of FDM-SUMup bias is 23.92 kg m^{-3}; the RMSE of RF-SUMup is 62.22 kg m^{-3}, and the mean of RF-SUMup is 26.46 kg m^{-3}. This shows a general overestimation and a large bias of both the IMAU-FDM and the RF model when validated with the SUMup measurements. In Figure 2.6d, it can be observed that neither IMAU-FDM nor RF manages to follow the large SUMup dynamics. This difference between models and in situ measurements can be attributed to the temporal discrepancies between the measurements and the IMAU-FDM and satellite observations and to the IMAU-FDM model errors or uncertainties that can also be learned by the RF regressor.

Aided by Figure 2.7, we then analyse the temporal distribution of the offsets between the IMAU-FDM densities and the RF densities in more depth. Figure 2.7a generally shows a low RMSE between IMAU-FDM and RF densities in high-elevation regions of East Antarctica and part of West Antarctica. The errors increase towards the coastal regions. The low correlation coefficients in Figure 2.7b indicate a low temporal agreement between IMAU-FDM and RF densities. Furthermore, the correlation coefficients are generally positive: high correlation coefficients (≥ 0.5) can mainly be observed in high-elevation regions of East Antarctica (except for megadune regions; Fahnestock et al., 2000) and a part of West Antarctic Peninsula. The regions with high correlation coefficients also mainly correspond to regions with high correlation coefficients (≥ 0.5) in Figure 2.3a, with parts of West Antarctica as an exception, which generally matches the observation in Figure 2.5 where T_B(19V) has the highest importance. The temporal mismatch and low correlation between IMAU-FDM and RF may be in part due to the modelling errors of IMAU-FDM. The density changes that are not modelled by the IMAU-FDM but affect the satellite observations are expected to degrade the quality of the RF regressor. The satellite data might be affected by other climate parameters that are not included in the IMAU-FDM model. The comparison with LR density shows that RF largely outperforms LR in terms of RMSE, especially in the interior of the ice sheet. While the average correlation coefficient is comparable between RF and LR, RF outperforms LR in high-elevation regions of East Antarctica, and performs worse in the megadune regions. By assessing the temporal agreement (mainly correlation coefficients) with ERA5 wind velocity (Figure 2.7d and e), we can learn that a high temporal correspondence is spatially correlated with a small wind velocity difference (>-2.5 m s^{-1}) between Antarctic summer (October–March) and winter (April–September). However, despite the small wind velocity difference and a relatively high temporal correspondence, the RMSE between IMAU-FDM and RF is high in regions close to Vinson Massif and along the Transantarctic Mountains (locations shown in Figure 2.2a), indicating uncertainties potentially introduced by topography, and this has an impact on coarse-resolution satellite data. Finally, a potential usability of the RF regression at other depths persists; therefore a comparison between the performance of RF at different depths is provided in Appendix 2.D.

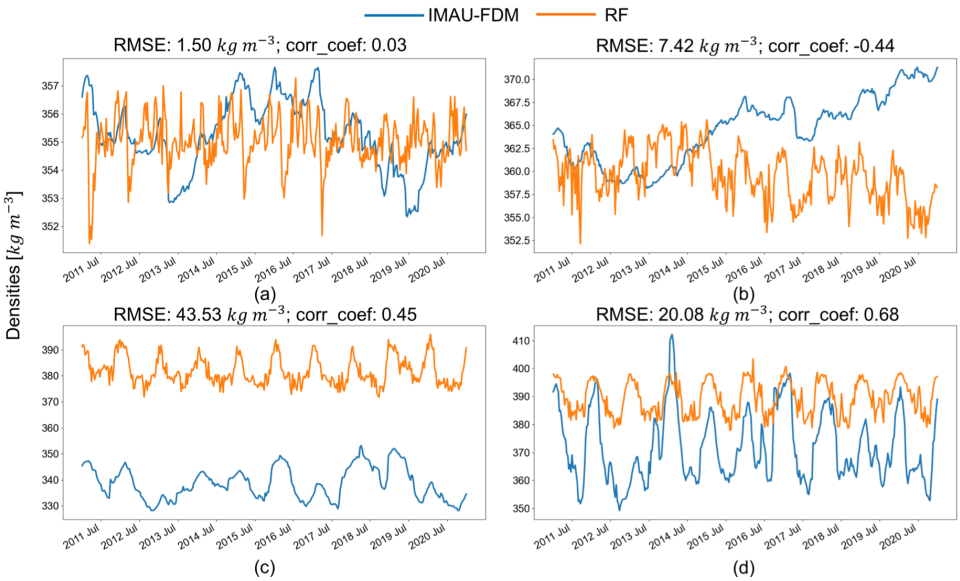

Figure 2.8: Comparison between time series of IMAU-FDM densities (in blue) and RF densities (in orange) at four representative sample points and Dome C. Panels (a)–(d) correspond to A–D labelled in Figure2.4. The RMSE and correlation coefficient (corr_coef) between the IMAU-FDM densities and the RF densities are shown above each figure.

2.4.5. TEMPORAL ASSESSMENT OF RF DENSITIES AT RANDOM PIXELS

In Figure 2.8, individual pixels are inspected to assess the temporal differences between IMAU-FDM and RF densities. Pixel A shows a low RMSE and a low correlation. Pixel B shows a relatively low RMSE but a negative correlation. Pixel C shows a reasonable correlation coefficient, but a large bias. Pixel D shows the overall most ideal RF performance. From the time series, it is apparent that the RF density estimations generally exhibit a stronger and more consistent seasonal cycle compared to the IMAU-FDM densities, which display a less consistent seasonal pattern with stronger inter-annual variations. This discrepancy explains the relatively low correlation coefficients, as only the pixels with similar seasonal cycles to the satellite observations (e.g., panels C and D) exhibit a higher correlation between the two datasets.

2.5. DISCUSSION

In this study, we developed an approach to estimate Antarctic firn densities using satellite radiometer and scatterometer observations using an RF regressor and IMAU-FDM density outputs as reference data. Our study is based on the complexity of the relationship between satellite observations and firn density: despite a theoretical impact of surface climate conditions, such as temperature, wind, and precipitation on both satellite parameters and firn density at a shallow depth (Fraser et al., 2016), the lack of a consistent linear relationship was evident in the examination of the individual satellite observations, as the highest mean temporal correlation between satellite observations and the

40 cm IMAU-FDM firn density is 0.24.

Our study first adopted an unsupervised machine learning method (hierarchical clustering) to distinguish dry-snow zones from zones that experienced melt as a preparation step to the density estimation using the random forest (RF) regressor. In contrast to Tran et al. (2008), our study could distinguish melt occurrences, possibly based on the abrupt rise in T_B during melt (Johnson et al., 2020) and the σ^0_A rise due to ice-layer formation following melt events (Trusel et al., 2012). However, in some coastal regions in East Antarctica, our clustering method may be less sensitive to melt compared to Brucker et al. (2010) and Picard et al. (2012), resulting in more dry-snow pixels. Among dry-snow zones, firn 1 consists of the most interior regions and is hence characterised by the smallest variations in satellite parameters and is overall the most stable, whilst firn 4 is located in West Antarctica and is hence the least stable with the largest variations in satellite parameters. The main difference between firn 2 and firn 3 is characterised by a larger $\sigma^0_{A_{\text{anom}}}$ variation in firn 2; the spatial separation between the two clusters resembles Figure 4 in Stokes et al. (2022), in which the region overlapping with firn 2 tends to lose mass, while the region overlapping with firn 3 tends to slightly gain mass. Therefore, we infer that this result might indicate that firn 2 has less stable conditions than firn 3.

To address the non-linear and complex nature of the relationship between satellite parameters and firn density, we employed an RF regressor model. This model allowed us to incorporate multiple input parameters and handle non-linear relationships effectively. The implementation of the RF regressor successfully reproduced the spatial pattern of the IMAU-FDM density, achieving a low RMSE of 14.92 kg m^{-3}, which outperforms the RMSE of a simple LR model (17.87 kg m^{-3}). This highlights the potential of using satellite parameters to create a map of long-term mean densities, matching the conclusion of Fraser et al. (2016), who managed to reconstruct one of the satellite observations (σ^0_A) using climate and firn parameters in the long term.

However, it is important to note some limitations and discrepancies in the RF density map. We observed a slight overestimation of densities in the interior of the Antarctic ice sheet, coupled with an underestimation towards the coastal regions, when compared to the IMAU-FDM densities. This discrepancy may arise from the inability of the RF regressor to extrapolate beyond the training data, leading to the restricted density range in the RF density map (maximum density of $\leq$ 450 kg m^{-3}). Furthermore, when comparing the RF and IMAU-FDM densities with the in situ SUMup measurements, we found comparable errors. Similar errors were reported by Keenan et al. (2021), who attributed them to local meteorological phenomena not captured by climate models and possible measurement uncertainties. These factors, which are not explicitly accounted for in the IMAU-FDM model or the RF regressor trained on that dataset, may contribute to the discrepancies observed. Finally, our combination of satellite parameters cannot be used to assess densities at depths deeper than approximately 80 cm. This limitation is first because of the theoretical penetration depth as shown in Appendix 2.A: a depth exceeding 80 cm is physically not meaningful for the 37 GHz microwave. Another reason for this limitation is that our study is based on the assumption that the surface climate conditions can affect both shallow-depth firn densities and satellite parameters simultaneously (Fraser et al., 2016). Firn densities at larger depth are not largely affected by surface conditions, hence our combination of satellite parameters is not applicable, even

if 19 GHz and C-band microwaves have a theoretical penetration depth larger than 5 m (as shown in Appendix 2.D). Finally, C-band microwaves are more sensitive to surface roughness than to densities at larger depths (as shown in Appendix 2.A).

While the RF regressor successfully captures the spatial variability in the long-term mean density, it falls short in accurately predicting the temporal variation in IMAU-FDM, particularly in coastal regions and megadune areas. Apart from the aforementioned potential underestimation of melt pixels of our clustering method in coastal regions, the temporal discrepancies between the RF regressor and IMAU-FDM can be attributed to the differences in seasonal patterns and the presence of complex climate conditions near the ice shelves. Coastal regions, characterised by large negative differences in wind velocity between summer and winter, exhibit larger temporal discrepancies. These findings suggest that IMAU-FDM may not capture the seasonal cycle of fresh snow density in these regions with high wind speeds during winter. The simplicity of how the density of freshly fallen snow is calculated within IMAU-FDM, assuming linear dependencies with wind speed and surface temperature (Veldhuijsen et al., 2023), fails to account for the intricate processes involving crystal size, shape, and riming, which are influenced by temperature and wind speed conditions (Judson and Doesken, 2000). The dependence of fresh snow density on wind speed may differ under various temperature conditions, which contributes to the discrepancies observed.

In summary, the RF regressor trained using IMAU-FDM and satellite parameters demonstrates promising results in capturing the spatial pattern of firn density. However, it may not fully capture the temporal fluctuations of IMAU-FDM, primarily due to the dominant influence of surface temperature (represented by T_B) in the RF estimation. The effects of precipitation (e.g. represented by changes in σ^0_A; Fraser et al., 2016), and wind velocity (e.g. documented by Champollion et al., 2013) are therefore potentially compromised in the RF model. Additionally, the discrepancy between the meteorological forcing in the IMAU-FDM model and the actual meteorological phenomena can also play a role. The meteorological phenomena can affect the satellite parameters, which in turn influence the RF results, but may not be reflected in the IMAU-FDM output. Our approach of training the RF regressor on IMAU-FDM, which may exhibit spatial and temporal differences compared to actual in situ densities, can therefore be considered a major shortcoming. This limitation should be taken into consideration when interpreting the RF density estimations. Future research could benefit from incorporating more in situ measurements for training the RF regressor, which would improve the accuracy of the temporal density estimates. Furthermore, care should also be taken when using the coarse-resolution IMAU-FDM and satellite data to represent the local firn densities. The firn property variation may be small in pixels with relatively flat topography such as Dome C (Picard et al., 2014). However, towards the coastal or mountainous regions, the ability of such coarse resolution to represent firn densities could be compromised, as a mismatch between the local meteorological phenomena, the satellite parameters and the modelled densities can be introduced. Indirect correlations between different layers of firn should also be considered when applying data fusion of multiple microwave frequencies. Additionally, exploring alternative machine learning algorithms, neural networks or ensemble approaches may further enhance the performance of density estimation and capture the complex relationships between satellite observations and firn

density, as assessed by Santi et al. (2012b) and Anilkumar et al. (2023). Finally, our study only demonstrated a simple approach in understanding the long-term correlation between firn density and satellite parameters, based on climate conditions that potentially affect them (Fraser et al., 2016). However, due to the different penetration abilities of different microwave frequencies (Surdyk, 2002) at different locations (Picard et al., 2009), future research can benefit from a more quantitative assessment regarding the extent to which the penetration depths and other climate parameters affect the results. Better parametrisation of satellite observations which can indicate the variation in firn depth (Santi et al., 2012a; Michel et al., 2014) and the formation and disappearance of surface and depth hoar-crystal (Champollion et al., 2013) can also be adopted.

Despite the limitations and discrepancies observed, the RF density map generated in this study can serve as an important intermediate step in translating satellite data into density estimations. It provides valuable insights into the discrepancy between firn models and satellite observations, shedding light on the complexities of the relationship between satellite parameters and firn density. The RF regressor captures the long-term mean density pattern, offering a useful tool for investigating spatial variations in firn density across Antarctica. However, it is essential to exercise caution when interpreting the temporal variations, particularly in coastal regions with complex climate conditions. Our study is also mainly limited to firn densities at shallow depths where the climate phenomena have a large impact; it cannot indicate the actual scattering of firn grains, as a more complicated mechanism persists (Picard et al., 2022).

Further improvements can be made to enhance the accuracy of the RF regressor in capturing the temporal variations in firn density. This could involve refining the training data and incorporating additional meteorological parameters that influence the satellite observations, as also suggested by Kar and Aksoy (2024). By better accounting for the effects of precipitation and wind velocity on the satellite parameters, the RF regressor could potentially capture a more accurate representation of the temporal dynamics of firn density. Furthermore, advancements in the parametrisation of fresh snow density within firn models, considering the complex processes driven by temperature and wind speed conditions, could help bridge the gap between model predictions and satellite observations. Finally, as the performance of the machine learning method varies based on different meteorological phenomena and topography, it can also be recommended for further studies to apply different parametrisations for different regions or test other machine learning methods.

2.6. CONCLUSION

In conclusion, this study demonstrates the potential of using multiple satellite observations to estimate Antarctic firn densities, with the IMAU-FDM densities serving as a reference. Our findings highlight several key points. Firstly, while satellite observations exhibit a certain level of spatial correlations with firn densities, a consistent linear relationship cannot be established. The correlations between $\rho_{40\text{cm}}$ and satellite parameters, particularly T_{B}, indicate the potential influence of firn density on variations in satellite observations.

Secondly, the impact of firn melt and refreeze on satellite observations is significant. Temporal anomalies in satellite parameters can be adopted to differentiate be-

tween wet- and dry-firn regions. Clustering of satellite observation time series helps to identify melt extents and assess the temporal correlation with densities at the cluster level. Notably, the scattering impact of refrozen melt layers is reflected in prolonged elevated σ_A^0 anomalies. However, in dry-snow clusters, the correlation between densities and satellite observations is not evident.

Based on these complexities, a non-linear model, such as the random forest (RF) regressor, is necessary to capture the relationship between firn densities and satellite observations. Our implementation of the RF regressor successfully reproduces the spatial pattern of firn densities, exhibiting good agreement with IMAU-FDM and even outperforming it in certain locations when compared with SUMup density measurements. However, the temporal simulation of densities by the RF regressor is compromised. Individual pixel analyses reveal that the RF densities tend to overlook the inter-annual variations in firn densities when the variations in satellite observations are not in phase with IMAU-FDM densities. In coastal regions, where satellite signals with strong variability dominate, the RF densities are not directly comparable to IMAU-FDM densities. These temporal discrepancies can be attributed to the simplifications in the IMAU-FDM model, particularly in capturing wind and temperature dependencies that strongly influence satellite observations. Furthermore, limitations of the RF regressor, including the inability to extrapolate from the training dataset and its strong dependence on brightness temperatures, result in a limited range of density estimation and primarily reflect surface temperatures.

APPENDICES

2.A. SENSITIVITY OF MICROWAVES TO CHANGES IN FIRN PROPERTIES AT DIFFERENT DEPTHS

Table 2.A.1: Firn properties adopted from Larue et al. (2021), including geographical coordinates, annual temperature, vertically averaged density, and vertically averaged specific surface area (SSA) at different locations.

Name	Latitude (°)	Longitude (°)	Temperature (°C)	SSA ($m^{-2}\,kg^{-1}$)	Density ($kg\,m^{-3}$)
charcot^A	-69.38	139.02	-37.9	12.0	433
ago5^E	-77.24	123.48	-54.4	7.4	361
paleo^E	-79.85	126.20	-50.5	7.7	392

For setting up the experiment, it is important to understand up to which depth different microwave frequencies can indicate firn properties. This appendix presents a simple sensitivity analysis using SMRT, where densities and grain sizes at different depths of the firn are varied, and the impact of changes in firn properties on σ^0_A and on T_B is presented. The initial state is a firn layer with a 20 m thickness, composed of small internal layers of 40 cm. The density and grain size are changed by 50 $kg\,m^{-3}$ and 0.5 mm, respectively. The changes are applied to one layer at a time. The sensitivity can also vary per location; therefore we adopt the field measurements in East Antarctica from Larue et al. (2021) to define the initial density, temperature, and grain size. The locations and parameters are summarised in Table 2.A.1. For the implementation of SMRT, we use a sticky hard spheres microstructure model represented by the grain radius and a stickiness parameter (Picard et al., 2018). The grain radius is derived from SSA with

$$r = \frac{3 \times 2.3}{SSA \rho_{ice}} \tag{2.3}$$

where $\rho_{ice} = 917\ kg\,m^{-3}$ (Larue et al., 2021). The stickiness is defined as 0.2 for all locations (Picard et al., 2018, 2022). For solving the radiative transfer equation, SMRT uses the discrete ordinate and eigenvalue (DORT) method, and the empirical electromagnetic theory we adopt is the improved Born approximation (IBA) (Mätzler, 1998). The simulated results are shown in Figure 2.A.1, where the changes in σ^0_A and T_B with respect to the original state are presented. In general, the sensitivity of both σ^0_A and T_B decreases with an increasing depth. Respectively, 19 GHz and 37 GHz are sensitive up to 6–10 m and 0.8–1 m. However, the variation in σ^0_A is below 1 dB (the radiometric uncertainty; Schmidt et al., 2018), indicating that the C-band may not be sufficiently sensitive to volume scattering. Therefore, we consider the effect of surface scattering, which can be modelled by SMRT using the Integral Equation Method (IEM) (Fung et al., 1992). Applying the IEM requires the snow surface to be defined by the surface roughness expressed

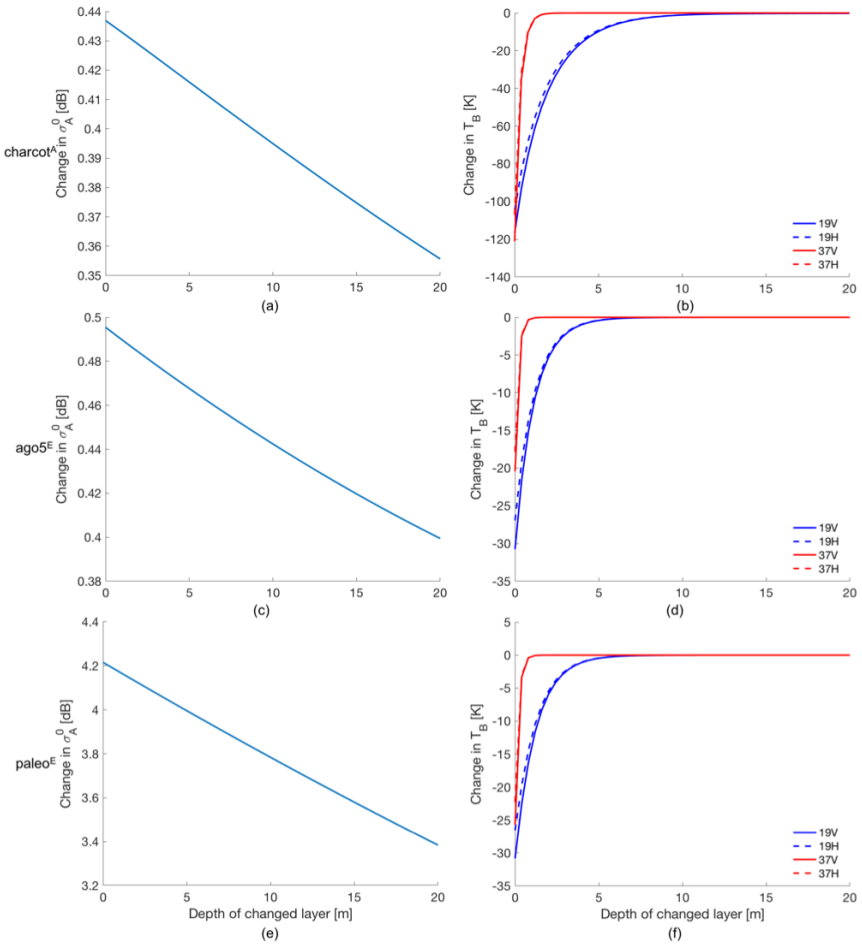

Figure 2.A.1: Change in σ^0_A and T_B as a function of the depth of the layer whose density and grain size are changed.

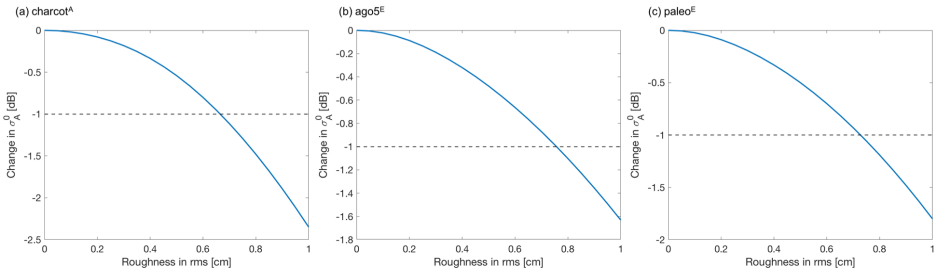

Figure 2.A.2: Change in C-band σ^0_A when the surface roughness (expressed as root-mean-square heights; rms) is changed. The dashed line indicates when the sensitivity exceeds 1 dB.

as root-mean-square (rms) heights and correlation length (Larue et al., 2021). In this experiment, we fix the correlation length to 0.1 cm and vary the surface roughness between 0 and 1 cm. The sensitivity of σ^0_A to surface roughness is shown in Fig. 2.A.2, where the change in σ^0_A indicates the difference between an increased surface roughness and a smooth surface. For all tested locations, σ^0_A shows a reduction that exceeds 1 dB when surface roughness increases by 0.7 cm, indicating a sufficient sensitivity to surface roughness. Typically, the changes in surface roughness are related to both wind patterns and surface firn density. Therefore, for the setting of our study, an optimal range to assess firn densities should be chosen between the surface and a depth of 80 cm.

2.B. TEMPORALLY AVERAGED SATELLITE PARAMETERS AND DENSITY FROM IMAU-FDM

Figure 2.B.1 displays the averaged maps of satellite parameters and $\rho_{40\text{cm}}$. This figure aims to demonstrate an overview of the spatial patterns of the data applied in this study. The figure shows that, although all satellite parameters reflect some of the spatial patterns of firn density, none of the parameters shows a spatially consistent relation with $\rho_{40\text{cm}}$. For example, in high-elevation regions of East Antarctica, firn densities show similar spatial patterns to T_B and reversed spatial patterns of σ^0_A. However, these patterns are not consistently observed in West Antarctica, along the Transantarctic Mountains (location shown in Figure 2.2a), and in firn 5 (Figure 2.4), where a significant melt event in 2016 affected the satellite observations (Nicolas et al., 2017).

2.C. TIME SERIES OF CLUSTERING RESULTS

This appendix presents the time series of different clusters following Sect. 2.3.2. Figure 2.C.1 presents the time series of the mean and 20th–80th percentiles of each parameter for each cluster, with panels (a)–(g) corresponding to clusters 1–7, respectively. Firns 1–4 exhibit small and short-term variations in T_{B_anom} and $\sigma^0_{A_\text{anom}}$; the extent of variations differs between different clusters. Firn 1 has the smallest variations in T_{B_anom} and $\sigma^0_{A_\text{anom}}$, which are within ±5 K and ±0.25 dB, respectively. Firn 2 and firn 3 have a T_{B_anom} between −5 K and 10 K; however, firn 2 has a $\sigma^0_{A_\text{anom}}$ within ±1 dB, while Firn 3 has a $\sigma^0_{A_\text{anom}}$ within ±0.5 dB. Firn 4 is characterised by a T_{B_anom} variation within ±10 K and a $\sigma^0_{A_\text{anom}}$ variation within ±0.5 dB.

On the contrary, firns 5–7 all show large and abrupt variations in T_{B_anom} and $\sigma^0_{A_\text{anom}}$, mainly as a result of melt events (e.g. Nicolas et al., 2017) that drastically change absorption, emission and scattering of microwave radiation and thus the T_{B_anom} and $\sigma^0_{A_\text{anom}}$. The effects of these melt events are also evident in the time series of the IMAU-FDM densities, as the abrupt changes in firn density are associated with the occurrence of melt events (Amory et al., 2024). For example, this can clearly be seen in the time series of firn 5, where the melt event of 2016 shows a prolonged effect on the $\sigma^0_{A_\text{anom}}$ time series due to the formation of a sub-surface refrozen high-density layer in IMAU-FDM. The high-density layer is detected by the scatterometer with stronger snow-penetrating capability. In IMAU-FDM, this high-density layer also appears in $\rho_{40\text{cm}}$, where it increases by approximately 100 kg m^{-3}. The comparison of all clusters highlights the dominant

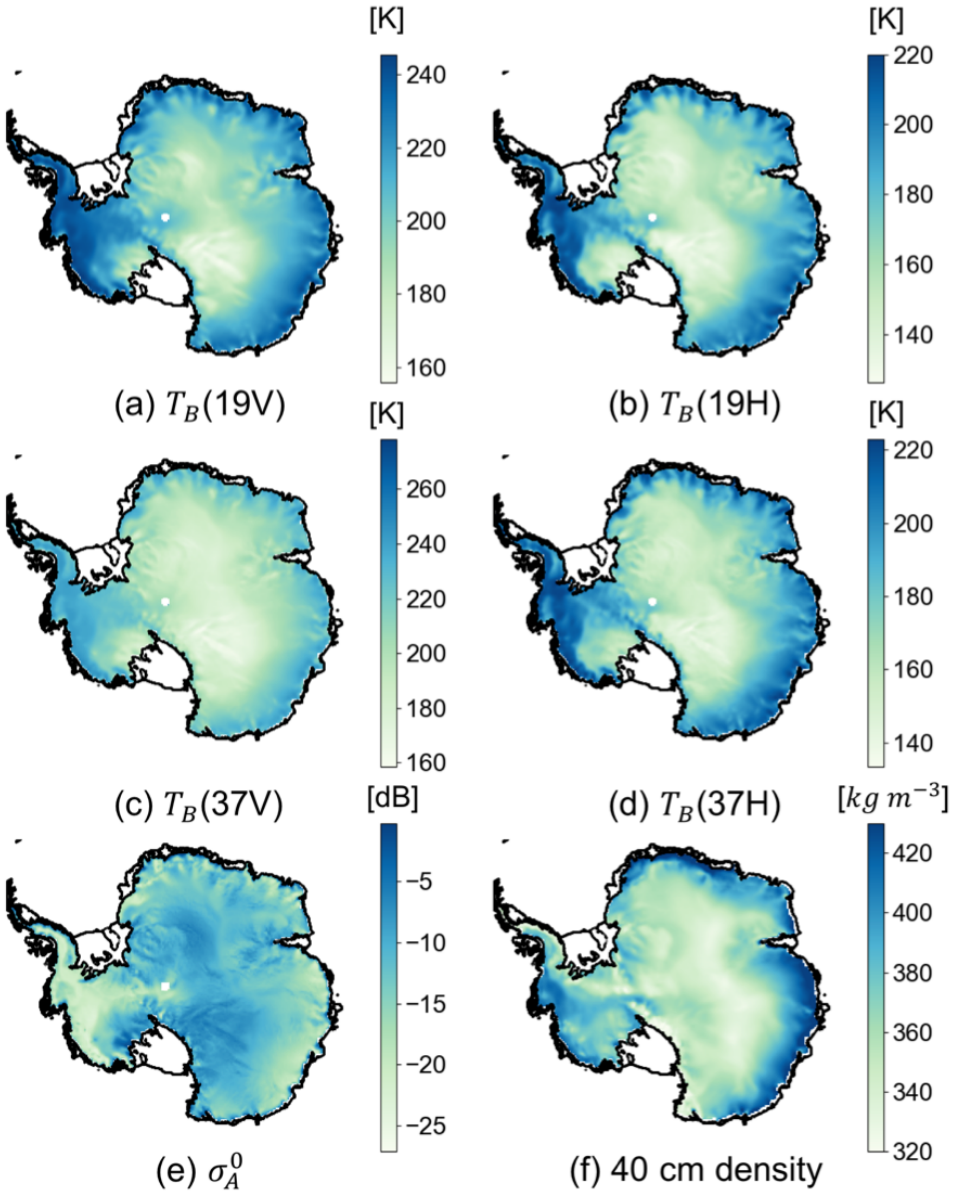

Figure 2.B.1: Temporally averaged map of (a) brightness temperature (T_B) from 19 GHz vertical polarisation, (b) T_B from 19 GHz horizontal polarisation, (c) T_B from 37 GHz vertical polarisation, (d) T_B from 37 GHz horizontal polarisation, (e) backscatter intensity (σ^0_A), and (f) 40 cm IMAU-FDM density ($\rho_{40\text{cm}}$). Panels (a)–(d) are acquired or derived parameters from SSMIS, and panel (e) is derived from ASCAT. The coastline is from Depoorter et al. (2013).

influence of melt events on $T_{\mathrm{B}_{\mathrm{anom}}}$ and $\sigma^0_{A_{\mathrm{anom}}}$ in the wet-firn pixels, whereas the dry-firn pixels exhibit a more pronounced seasonal variation in satellite parameters. It is important to note that the wet-firn clusters are not used in the following RF steps due to the complex impact of the melt–refreeze cycle on satellite observations.

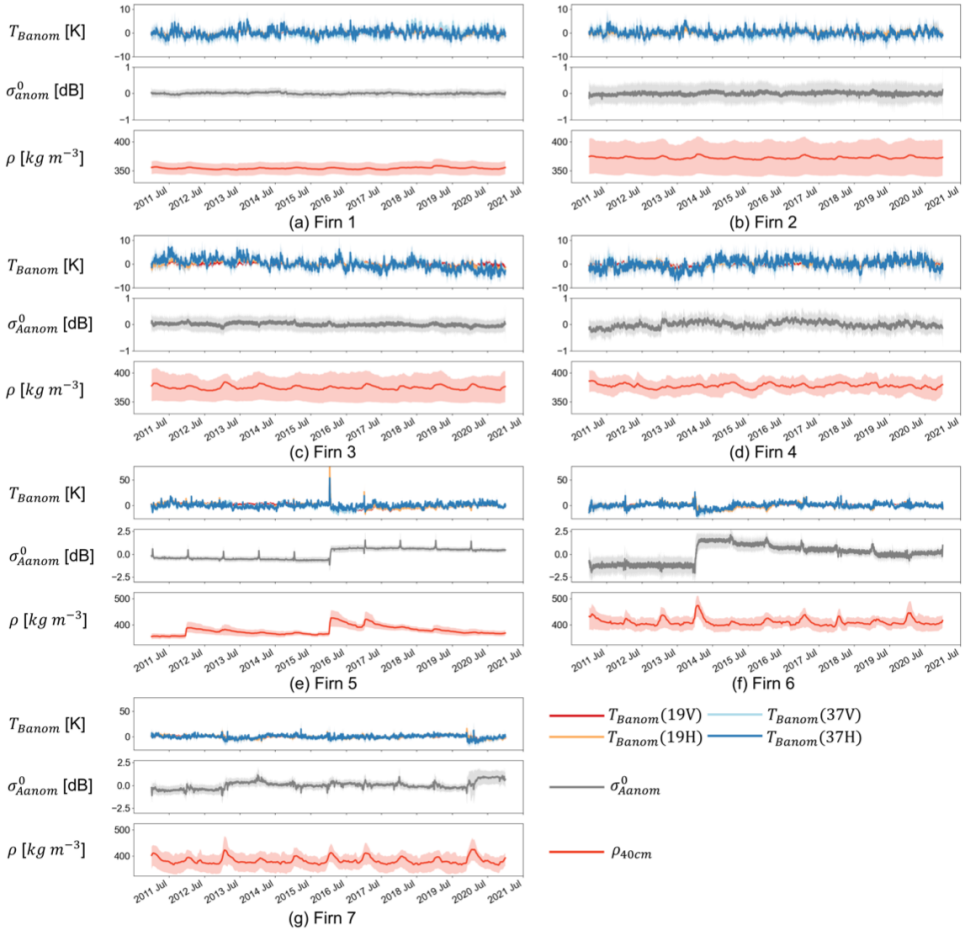

Figure 2.C.1: Time series of the mean (curves) and 20th–80th percentiles (shaded areas) of the clustering results in Figure 2.4, with panels (a)–(g) corresponding to firns 1–7. The visualised satellite observations are as follows: time series anomalies of brightness temperature (T_{B}) from 19 GHz and 37 GHz, both horizontal and vertical polarisation ($T_{\mathrm{B}_{\mathrm{anom}}}$(19V), $T_{\mathrm{B}_{\mathrm{anom}}}$(19H), $T_{\mathrm{B}_{\mathrm{anom}}}$(37V), and $T_{\mathrm{B}_{\mathrm{anom}}}$(37H), respectively), time series anomalies of backscatter intensity ($\sigma^0_{A_{\mathrm{anom}}}$), and IMAU-FDM density at 40 cm ($\rho_{40\mathrm{cm}}$) depth. The colours of the curves correspond to the legends in panel (g).

2.D. RF PERFORMANCE WITH VARYING DEPTH

In this section, we demonstrate the impact of the depth on the performance of RF. The result shows that, as the depth increases, the mean correlation coefficient decreases.

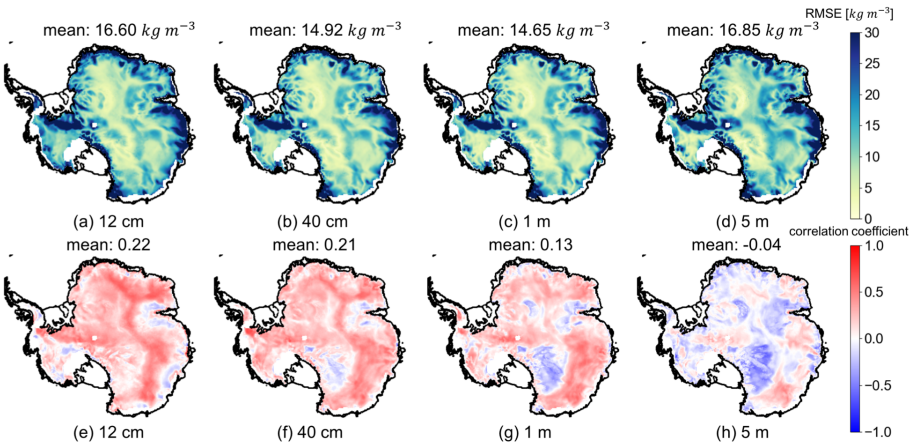

Figure 2.D.1: Maps of root-mean-square error (RMSE; upper panel) and correlation coefficients (lower panel) at different depths. The coastline is from Depoorter et al. (2013).

Table 2.D.1: Average temporal correlation coefficient between IMAU-FDM near-surface density (4 cm) and IMAU-FDM density at deeper depths.

Depth	12 cm	40 cm	1 m	5 m
4 cm	1.00	0.73	0.36	0.10

Moreover, the reduction in correlation coefficients first occurs in the megadune regions; this observation corresponds with e.g. Picard et al. (2009), who modelled and demonstrated that the penetration depth of 19 GHz is compromised in these regions. When we apply the RF regressor at 5 m density, the RMSE is the highest and the correlation is the lowest, showing most compromised performance. Since our study is based on the impact of surface climate conditions on firn depth, similar performances can be obtained at different depth due to similar impacts from surface climate conditions. We present in Table 2.D.1 the correlation coefficients between IMAU-FDM near-surface density (at 4 cm depth) and density at different depths, and we show that this correlation decreases with increasing depths. Therefore, the explanations for different performances in Figure 2.D.1 can be as follows: (i) the temporal variation in deeper firn layers is not as sensitive as the upper firn layers and the satellite parameters to climate conditions on the surface, (ii) the penetration ability of 37 GHz and 19 GHz largely decreases with firn depths, and (iii) there are biases in IMAU-FDM. This experiment depicts the limitation of our approach, as our combination of satellite parameters is mostly sensitive to surface temperature and potentially to wind patterns and precipitation on the surface; therefore, it is not indicative of properties of deeper firn layers, although they should be within the radar penetration depths (Rott et al., 1993; Surdyk, 2002). Further studies are therefore encouraged to incorporate better parametrisation of satellite data.

BIBLIOGRAPHY

Amory, C., Buizert, C., Buzzard, S., Case, E., Clerx, N., Culberg, R., Datta, R. T., Dey, R., Drews, R., Dunmire, D., Eayrs, C., Hansen, N., Humbert, A., Kaitheri, A., Keegan, K., Kuipers Munneke, P., Lenaerts, J. T. M., Lhermitte, S., Mair, D., McDowell, I., Mejia, J., Meyer, C. R., Morris, E., Moser, D., Oraschewski, F. M., Pearce, E., de Roda Husman, S., Schlegel, N.-J., Schultz, T., Simonsen, S. B., Stevens, C. M., Thomas, E. R., Thompson-Munson, M., Wever, N., and Wouters, B.: Firn on ice sheets, Nature Reviews Earth & Environment, https://doi.org/10.1038/s43017-023-00507-9, 2024.

Anilkumar, R., Bharti, R., Chutia, D., and Aggarwal, S. P.: Modelling point mass balance for the glaciers of the Central European Alps using machine learning techniques, The Cryosphere, 17, 2811–2828, https://doi.org/10.5194/tc-17-2811-2023, 2023.

Archer, K. J. and Kimes, R. V.: Empirical characterization of random forest variable importance measures, Computational Statistics & Data Analysis, 52, 2249–2260, https://doi.org/10.1016/j.csda.2007.08.015, 2008.

Arndt, S. and Haas, C.: Spatiotemporal variability and decadal trends of snowmelt processes on Antarctic sea ice observed by satellite scatterometers, The Cryosphere, 13, 1943–1958, https://doi.org/10.5194/tc-13-1943-2019, 2019.

Bingham, A. and Drinkwater, M.: Recent changes in the microwave scattering properties of the Antarctic ice sheet, Geoscience and Remote Sensing, IEEE Transactions on, 38, 1810 – 1820, https://doi.org/10.1109/36.851765, 2000.

Breiman, L.: Bagging predictors, Machine Learning, 24, 123–140, https://doi.org/10.1007/bf00058655, 1996.

Breiman, L.: Random Forests, Machine Learning, 45, 5–32, https://doi.org/10.1023/a:1010933404324, 2001.

Brigham Young University (BYU) Microwave Earth Remote Sensing (MERS) laboratory: Standard BYU ASCAT Land/Ice Image Products, URL `https://www.scp.byu.edu/data/Ascat/SIR/Ascat_sir.html`, (Date accessed: 6 February 2021), 2010.

Brucker, L., Picard, G., and Fily, M.: Snow grain-size profiles deduced from microwave snow emissivities in Antarctica, Journal of Glaciology, 56, 514–526, https://doi.org/10.3189/002214310792447806, 2010.

Brucker, L., Picard, G., Arnaud, L., Barnola, J.-M., Schneebeli, M., Brunjail, H., Lefebvre, E., and Fily, M.: Modeling time series of microwave brightness temperature at Dome C, Antarctica, using vertically resolved snow temperature and microstructure measurements, Journal of Glaciology, 57, 171–182, https://doi.org/10.3189/002214311795306736, 2011.

Brucker, L., Dinnat, E. P., Picard, G., and Champollion, N.: Effect of Snow Surface Metamorphism on Aquarius L-Band Radiometer Observations at Dome C, Antarctica, IEEE Transactions on Geoscience and Remote Sensing, 52, 7408–7417, https://doi.org/10.1109/tgrs.2014.2312102, 2014.

Cartwright, J., Fraser, A. D., and Porter-Smith, R.: Polar maps of C-band backscatter parameters from the Advanced Scatterometer, Earth System Science Data, 14, 479–490, https://doi.org/10.5194/essd-14-479-2022, 2022.

Champollion, N., Picard, G., Arnaud, L., Lefebvre, E., and Fily, M.: Hoar crystal development and disappearance at Dome C, Antarctica: observation by near-infrared photography and passive microwave satellite, The Cryosphere, 7, 1247–1262, https://doi.org/10.5194/tc-7-1247-2013, 2013.

Craven, M. and Allison, I.: Firnification and the effects of wind-packing on Antarctic snow, Annals of Glaciology, 27, 239–245, https://doi.org/10.3189/1998aog27-1-239-245, 1998.

de Roda Husman, S., Hu, Z., Wouters, B., Munneke, P. K., Veldhuijsen, S., and Lhermitte, S.: Remote Sensing of Surface Melt on Antarctica: Opportunities and Challenges, IEEE Journal of Selected Topics in Applied Earth Observations and Remote Sensing, pp. 1–20, https://doi.org/10.1109/jstars.2022.3216953, 2022.

Depoorter, M. A., Bamber, J. L., Griggs, J., Lenaerts, J. T. M., Ligtenberg, S. R. M., van den Broeke, M. R., and Moholdt, G.: Synthesized grounding line and ice shelf mask for Antarctica, https://doi.org/10.1594/PANGAEA.819151, supplement to: Depoorter, MA et al. (2013): Calving fluxes and basal melt rates of Antarctic ice shelves. Nature, 502, 89-92, https://doi.org/10.1038/nature12567, 2013.

Early, D. and Long, D.: Image reconstruction and enhanced resolution imaging from irregular samples, IEEE Transactions on Geoscience and Remote Sensing, 39, 291–302, https://doi.org/10.1109/36.905237, 2001.

Fahnestock, M., Bindschadler, R., Kwok, R., and Jezek, K.: Greenland Ice Sheet Surface Properties and Ice Dynamics from ERS-1 SAR Imagery, Science, 262, 1530–1534, https://doi.org/10.1126/science.262.5139.1530, 1993.

Fahnestock, M. A., Scambos, T. A., Shuman, C. A., Arthern, R. J., Winebrenner, D. P., and Kwok, R.: Snow megadune fields on the East Antarctic Plateau: Extreme atmosphere-ice interaction, Geophysical Research Letters, 27, 3719–3722, https://doi.org/10.1029/1999gl011248, 2000.

Figa-Saldaña, J., Wilson, J. J., Attema, E., Gelsthorpe, R., Drinkwater, M. R., and Stoffelen, A.: The advanced scatterometer (ASCAT) on the meteorological operational (MetOp) platform: A follow on for European wind scatterometers, Canadian Journal of Remote Sensing, 28, 404–412, https://doi.org/10.5589/m02-035, 2002.

Fraser, A. D., Nigro, M. A., Ligtenberg, S. R. M., Legrésy, B., Inoue, M., Cassano, J. J., Munneke, P. K., Lenaerts, J. T. M., Young, N. W., Treverrow, A., van den Broeke, M., and Enomoto, H.: Drivers of ASCAT C band backscatter variability in the dry snow zone of Antarctica, Journal of Glaciology, 62, 170–184, https://doi.org/10.1017/jog.2016.29, 2016.

Fujita, S., Goto-Azuma, K., Hirabayashi, M., Hori, A., Iizuka, Y., Motizuki, Y., Motoyama, H., and Takahashi, K.: Densification of layered firn in the ice sheet at Dome Fuji, Antarctica, Journal of Glaciology, 62, 103–123, https://doi.org/10.1017/jog.2016.16, 2016.

Fung, A., Li, Z., and Chen, K.: Backscattering from a randomly rough dielectric surface, IEEE Transactions on Geoscience and Remote Sensing, 30, 356–369, https://doi.org/10.1109/36.134085, 1992.

Hastie, T., Tibshirani, R., and Friedman, J.: Random Forests, pp. 587–604, Springer New York, https://doi.org/10.1007/978-0-387-84858-7_15, 2008.

Hengl, T., Nussbaum, M., Wright, M. N., Heuvelink, G. B., and Gräler, B.: Random forest as a generic framework for predictive modeling of spatial and spatio-temporal variables, PeerJ, 6, e5518, https://doi.org/10.7717/peerj.5518, 2018.

Johnson, A., Fahnestock, M., and Hock, R.: Evaluation of passive microwave melt detection methods on Antarctic Peninsula ice shelves using time series of Sentinel-1 SAR, Remote Sensing of Environment, 250, 112 044, https://doi.org/https://doi.org/10.1016/j.rse.2020.112044, 2020.

Judson, A. and Doesken, N.: Density of Freshly Fallen Snow in the Central Rocky Mountains, Bulletin of the American Meteorological Society, 81, 1577–1587, https://doi.org/10.1175/1520-0477(2000)081<1577:doffsi>2.3.co;2, 2000.

Kar, R. and Aksoy, M.: Passive Microwave Remote Sensing of the Antarctic Ice Sheet: Retrieval of Firn Properties Near the Concordia Station, IEEE Geoscience and Remote Sensing Letters, 21, 1–5, https://doi.org/10.1109/lgrs.2023.3343594, 2024.

Keenan, E., Wever, N., Dattler, M., Lenaerts, J. T. M., Medley, B., Munneke, P. K., and Reijmer, C.: Physics-based SNOWPACK model improves representation of near-surface Antarctic snow and firn density, The Cryosphere, 15, 1065–1085, https://doi.org/10.5194/tc-15-1065-2021, 2021.

Kingslake, J., Ely, J. C., Das, I., and Bell, R. E.: Widespread movement of meltwater onto and across Antarctic ice shelves, Nature, 544, 349–352, https://doi.org/10.1038/nature22049, 2017.

Koenig, L. and Montgomery, L.: Surface Mass Balance and Snow Depth on Sea Ice Working Group (SUMup) snow density subdataset, Greenland and Antartica, 1950-2018, https://doi.org/10.18739/A2JH3D23R, 2018.

Kuipers Munneke, P., Ligtenberg, S. R. M., Noël, B. P. Y., Howat, I. M., Box, J. E., Mosley-Thompson, E., McConnell, J. R., Steffen, K., Harper, J. T., Das, S. B., and van den Broeke, M. R.: Elevation change of the Greenland Ice Sheet due to surface mass balance and firn processes, 1960–2014, The Cryosphere, 9, 2009–2025, https://doi.org/10.5194/tc-9-2009-2015, 2015.

Kunkee, D. B., Poe, G. A., Boucher, D. J., Swadley, S. D., Hong, Y., Wessel, J. E., and Uliana, E. A.: Design and Evaluation of the First Special Sensor Microwave Imager/Sounder, IEEE Transactions on Geoscience and Remote Sensing, 46, 863–883, https://doi.org/10.1109/tgrs.2008.917980, 2008.

Larue, F., Picard, G., Aublanc, J., Arnaud, L., Robledano-Perez, A., Meur, E. L., Favier, V., Jourdain, B., Savarino, J., and Thibaut, P.: Radar altimeter waveform simulations in Antarctica with the Snow Microwave Radiative Transfer Model (SMRT), Remote Sensing of Environment, 263, 112 534, https://doi.org/10.1016/j.rse.2021.112534, 2021.

Leduc-Leballeur, M., Picard, G., Macelloni, G., Arnaud, L., Brogioni, M., Mialon, A., and Kerr, Y.: Influence of snow surface properties on L-band brightness temperature at Dome C, Antarctica, Remote Sensing of Environment, 199, 427–436, https://doi.org/https://doi.org/10.1016/j.rse.2017.07.035, 2017.

Lehning, M., Bartelt, P., Brown, B., Fierz, C., and Satyawali, P.: A physical SNOWPACK model for the Swiss avalanche warning: Part II. Snow microstructure, Cold Regions Science and Technology, 35, 147–167, https://doi.org/10.1016/s0165-232x(02)00073-3, 2002.

Lenaerts, J. T. M., Lhermitte, S., Drews, R., Ligtenberg, S. R. M., Berger, S., Helm, V., Smeets, C. J. P. P., van den Broeke, M. R., van de Berg, W. J., van Meijgaard, E., Eijkelboom, M., Eisen, O., and Pattyn, F.: Meltwater produced by wind–albedo interaction stored in an East Antarctic ice shelf, Nature Climate Change, 7, 58–62, https://doi.org/10.1038/nclimate3180, 2016.

Li, J. and Zwally, H. J.: Modeling the density variation in the shallow firn layer, Annals of Glaciology, 38, 309–313, https://doi.org/10.3189/172756404781814988, 2004.

Li, W., Lhermitte, S., and López-Dekker, P.: The potential of synthetic aperture radar interferometry for assessing meltwater lake dynamics on Antarctic ice shelves, The Cryosphere, 15, 5309–5322, https://doi.org/10.5194/tc-15-5309-2021, 2021.

Ligtenberg, S. R. M., Helsen, M. M., and van den Broeke, M. R.: An improved semi-empirical model for the densification of Antarctic firn, The Cryosphere, 5, 809–819, https://doi.org/10.5194/tc-5-809-2011, 2011.

Lindsley, R. D. and Long, D. G.: Standard BYU ASCAT Land/Ice Image Products, Tech. rep., Brigham Young University Microwave Earth Remote Sensing (MERS) Laboratory, URL `https://www.scp.byu.edu/docs/pdf/MERS1002.pdf`, (Date accessed: 20 June 2022), 2010.

Long, D. and Drinkwater, M.: Azimuth variation in microwave scatterometer and radiometer data over Antarctica, IEEE Transactions on Geoscience and Remote Sensing, 38, 1857–1870, https://doi.org/10.1109/36.851769, 2000.

Long, D., Hardin, P., and Whiting, P.: Resolution enhancement of spaceborne scatterometer data, IEEE Transactions on Geoscience and Remote Sensing, 31, 700–715, https://doi.org/10.1109/36.225536, 1993.

Macelloni, G., Brogioni, M., Pampaloni, P., and Cagnati, A.: Multifrequency Microwave Emission From the Dome-C Area on the East Antarctic Plateau: Temporal and Spatial Variability, IEEE Transactions on Geoscience and Remote Sensing, 45, 2029–2039, https://doi.org/10.1109/tgrs.2007.890805, 2007.

Meier, W. N., Stewart, J. S., Wilcox, H., Scott, D. J., and Hardman, M. A.: DMSP SSM/I-SSMIS Daily Polar Gridded Brightness Temperatures, Boulder, Colorado USA. NASA National Snow and Ice Data Center Distributed Active Archive Center, https://doi.org/10.5067/MXJL42WSXTS1, (Date Accessed: 15 March 2021), 2021.

Meredith, M., Sommerkorn, M., Cassotta, S., Derksen, C., Ekaykin, A., Hollowed, A., Kofinas, G., Mackintosh, A., Melbourne-Thomas, J., Muelbert, M., Ottersen, G., Pritchard, H., and Schuur, E.: Polar Regions, chap. 3, pp. 203–320, Cambridge University Press, Cambridge, UK and New York, NY, USA, https://doi.org/10.1017/9781009157964.005, 2019.

Michel, A., Flament, T., and Rémy, F.: Study of the Penetration Bias of ENVISAT Altimeter Observations over Antarctica in Comparison to ICESat Observations, Remote Sensing, 6, 9412–9434, https://doi.org/10.3390/rs6109412, 2014.

Montgomery, L., Koenig, L., and Alexander, P.: The SUMup dataset: compiled measurements of surface mass balance components over ice sheets and sea ice with analysis over Greenland, Earth System Science Data, 10, 1959–1985, https://doi.org/10.5194/essd-10-1959-2018, 2018.

Muñoz-Sabater, J.: ERA5-Land hourly data from 1950 to present, https://doi.org/10.24381/cds.e2161bac, 2019.

Muñoz-Sabater, J., Dutra, E., Agustí-Panareda, A., Albergel, C., Arduini, G., Balsamo, G., Boussetta, S., Choulga, M., Harrigan, S., Hersbach, H., Martens, B., Miralles, D. G., Piles, M., Rodríguez-Fernández, N. J., Zsoter, E., Buontempo, C., and Thépaut, J.-N.: ERA5-Land: a state-of-the-art global reanalysis dataset for land applications, Earth System Science Data, 13, 4349–4383, https://doi.org/10.5194/essd-13-4349-2021, 2021.

Mätzler, C.: Improved Born approximation for scattering of radiation in a granular medium, Journal of Applied Physics, 83, 6111–6117, https://doi.org/10.1063/1.367496, 1998.

Nicolas, J. P., Vogelmann, A. M., Scott, R. C., Wilson, A. B., Cadeddu, M. P., Bromwich, D. H., Verlinde, J., Lubin, D., Russell, L. M., Jenkinson, C., Powers, H. H., Ryczek, M., Stone, G., and Wille, J. D.: January 2016 extensive summer melt in West Antarctica favoured by strong El Niño, Nature Communications, 8, https://doi.org/10.1038/ncomms15799, 2017.

Pattyn, F. and Morlighem, M.: The uncertain future of the Antarctic Ice Sheet, Science, 367, 1331–1335, https://doi.org/10.1126/science.aaz5487, 2020.

Picard, G., Fily, M., and Gallee, H.: Surface melting derived from microwave radiometers: a climatic indicator in Antarctica, Annals of Glaciology, 46, 29–34, https://doi.org/10.3189/172756407782871684, 2007.

Picard, G., Brucker, L., Fily, M., Gallée, H., and Krinner, G.: Modeling time series of microwave brightness temperature in Antarctica, Journal of Glaciology, 55, 537–551, https://doi.org/10.3189/002214309788816678, 2009.

Picard, G., Domine, F., Krinner, G., Arnaud, L., and Lefebvre, E.: Inhibition of the positive snow-albedo feedback by precipitation in interior Antarctica, Nature Climate Change, 2, 795–798, https://doi.org/10.1038/nclimate1590, 2012.

Picard, G., Royer, A., Arnaud, L., and Fily, M.: Influence of meter-scale wind-formed features on the variability of the microwave brightness temperature around Dome C in Antarctica, The Cryosphere, 8, 1105–1119, https://doi.org/10.5194/tc-8-1105-2014, 2014.

Picard, G., Sandells, M., and Löwe, H.: SMRT: an active–passive microwave radiative transfer model for snow with multiple microstructure and scattering formulations (v1.0), Geoscientific Model Development, 11, 2763–2788, https://doi.org/10.5194/gmd-11-2763-2018, 2018.

Picard, G., Löwe, H., and Mätzler, C.: Brief communication: A continuous formulation of microwave scattering from fresh snow to bubbly ice from first principles, The Cryosphere, 16, 3861–3866, https://doi.org/10.5194/tc-16-3861-2022, 2022.

Rignot, E.: Mass balance of East Antarctic glaciers and ice shelves from satellite data, Annals of Glaciology, 34, 217–227, https://doi.org/10.3189/172756402781817419, 2002.

Rizzoli, P., Martone, M., Rott, H., and Moreira, A.: Characterization of Snow Facies on the Greenland Ice Sheet Observed by TanDEM-X Interferometric SAR Data, Remote Sensing, 9, https://doi.org/10.3390/rs9040315, 2017.

Rott, H., Sturm, K., and Miller, H.: Active and passive microwave signatures of Antarctic firn by means of field measurements and satellite data, Annals of Glaciology, 17, 337–343, https://doi.org/10.3189/S0260305500013070, 1993.

Santi, E., Brogioni, M., Paloscia, S., and Pampaloni, P.: Analysis of the frequency and polarization indexes over snow cover areas by means of experimental and theoretical data, in: 2012 12th Specialist Meeting on Microwave Radiometry and Remote Sensing of the Environment (MicroRad), IEEE, https://doi.org/10.1109/microrad.2012.6185250, 2012a.

Santi, E., Fontanelli, G., Pettinato, S., and Crepaz, A.: Monitoring of snow cover on Italian Alps using AMSR-E and Artificial Neural Networks, in: 2012 IEEE International Geoscience and Remote Sensing Symposium, IEEE, https://doi.org/10.1109/igarss.2012.6351095, 2012b.

Schmidt, K., Tous Ramon, N., and Schwerdt, M.: Radiometric accuracy and stability of sentinel-1A determined using point targets, International Journal of Microwave and Wireless Technologies, 10, 538–546, https://doi.org/10.1017/s1759078718000016, 2018.

Schröder, L., Horwath, M., Dietrich, R., Helm, V., van den Broeke, M. R., and Ligtenberg, S. R. M.: Four decades of Antarctic surface elevation changes from multi-mission satellite altimetry, The Cryosphere, 13, 427–449, https://doi.org/10.5194/tc-13-427-2019, 2019.

Spergel, J. J., Kingslake, J., Creyts, T., van Wessem, M., and Fricker, H. A.: Surface meltwater drainage and ponding on Amery Ice Shelf, East Antarctica, 1973–2019, Journal of Glaciology, p. 1–14, https://doi.org/10.1017/jog.2021.46, 2021.

Stiles, W. H. and Ulaby, F. T.: The active and passive microwave response to snow parameters: 1. Wetness, Journal of Geophysical Research: Oceans, 85, 1037–1044, https://doi.org/10.1029/jc085ic02p01037, 1980.

Stokes, C. R., Abram, N. J., Bentley, M. J., Edwards, T. L., England, M. H., Foppert, A., Jamieson, S. S. R., Jones, R. S., King, M. A., Lenaerts, J. T. M., Medley, B., Miles, B. W. J., Paxman, G. J. G., Ritz, C., van de Flierdt, T., and Whitehouse, P. L.: Response of the East Antarctic Ice Sheet to past and future climate change, Nature, 608, 275–286, https://doi.org/10.1038/s41586-022-04946-0, 2022.

Strobl, C., Boulesteix, A.-L., and Augustin, T.: Unbiased split selection for classification trees based on the Gini Index, Computational Statistics & Data Analysis, 52, 483–501, https://doi.org/10.1016/j.csda.2006.12.030, 2007.

Sugiyama, S., Enomoto, H., Fujita, S., Fukui, K., Nakazawa, F., Holmlund, P., and Surdyk, S.: Snow density along the route traversed by the Japanese-Swedish Antarctic Expedition 2007/08, Journal of Glaciology, 58, 529–539, https://doi.org/10.3189/2012jog11j201, 2012.

Surdyk, S.: Using microwave brightness temperature to detect short-term surface air temperature changes in Antarctica: An analytical approach, Remote Sensing of Environment, 80, 256–271, https://doi.org/10.1016/s0034-4257(01)00308-x, 2002.

Tedesco, M.: Snowmelt detection over the Greenland ice sheet from SSM/I brightness temperature daily variations, Geophysical Research Letters, 34, https://doi.org/10.1029/2006gl028466, 2007.

Tedesco, M.: Assessment and development of snowmelt retrieval algorithms over Antarctica from K-band spaceborne brightness temperature (1979–2008), Remote Sensing of Environment, 113, 979–997, https://doi.org/10.1016/j.rse.2009.01.009, 2009.

Tedesco, M. and Kim, E.: Intercomparison of Electromagnetic Models for Passive Microwave Remote Sensing of Snow, IEEE Transactions on Geoscience and Remote Sensing, 44, 2654–2666, https://doi.org/10.1109/tgrs.2006.873182, 2006.

Tran, N., Remy, F., Feng, H., and Femenias, P.: Snow Facies Over Ice Sheets Derived From Envisat Active and Passive Observations, IEEE Transactions on Geoscience and Remote Sensing, 46, 3694–3708, https://doi.org/10.1109/tgrs.2008.2000818, 2008.

Trusel, L. D., Frey, K. E., and Das, S. B.: Antarctic surface melting dynamics: Enhanced perspectives from radar scatterometer data, Journal of Geophysical Research: Earth Surface, 117, https://doi.org/10.1029/2011jf002126, 2012.

Ulaby, F., Siquera, P., Nashashibi, A., and Sarabandi, K.: Semi-empirical model for radar backscatter from snow at 35 and 95 GHz, IEEE Transactions on Geoscience and Remote Sensing, 34, 1059–1065, https://doi.org/10.1109/36.536521, 1996.

Vafakhah, M., Nasiri Khiavi, A., Janizadeh, S., and Ganjkhanlo, H.: Evaluating different machine learning algorithms for snow water equivalent prediction, Earth Science Informatics, 15, 2431–2445, https://doi.org/10.1007/s12145-022-00846-z, 2022.

van den Broeke, M.: Depth and Density of the Antarctic Firn Layer, Arctic, Antarctic, and Alpine Research, 40, 432–438, https://doi.org/10.1657/1523-0430(07-021)[broeke]2.0.co;2, 2008.

van den Broeke, M. R., Winther, J.-G., Isaksson, E., Pinglot, J. F., Karlöf, L., Eiken, T., and Conrads, L.: Climate variables along a traverse line in Dronning Maud Land, East Antarctica, Journal of Glaciology, 45, 295–302, https://doi.org/10.3189/s0022143000001799, 1999.

van Wessem, J. M., van de Berg, W. J., Noël, B. P. Y., van Meijgaard, E., Amory, C., Birnbaum, G., Jakobs, C. L., Krüger, K., Lenaerts, J. T. M., Lhermitte, S., Ligtenberg, S. R. M., Medley, B., Reijmer, C. H., van Tricht, K., Trusel, L. D., van Ulft, L. H., Wouters, B., Wuite, J., and van den Broeke, M. R.: Modelling the climate and surface mass balance of polar ice sheets using RACMO2 – Part 2: Antarctica (1979–2016), The Cryosphere, 12, 1479–1498, https://doi.org/10.5194/tc-12-1479-2018, 2018.

Veldhuijsen, S. B. M., van de Berg, W. J., Brils, M., Munneke, P. K., and van den Broeke, M. R.: Characteristics of the 1979–2020 Antarctic firn layer simulated with IMAU-FDM v1.2A, The Cryosphere, 17, 1675–1696, https://doi.org/10.5194/tc-17-1675-2023, 2023.

Verjans, V., Leeson, A. A., Nemeth, C., Stevens, C. M., Kuipers Munneke, P., Noël, B., and van Wessem, J. M.: Bayesian calibration of firn densification models, The Cryosphere, 14, 3017–3032, https://doi.org/10.5194/tc-14-3017-2020, 2020.

Viallon-Galinier, L., Hagenmuller, P., and Eckert, N.: Combining modelled snowpack stability with machine learning to predict avalanche activity, The Cryosphere, 17, 2245–2260, https://doi.org/10.5194/tc-17-2245-2023, 2023.

Ward, Jr., J. H.: Hierarchical Grouping to Optimize an Objective Function, Journal of the American Statistical Association, 58, 236–244, https://doi.org/10.1080/01621459.1963.10500845, 1963.

Zwally, H. J., Giovinetto, M. B., Li, J., Cornejo, H. G., Beckley, M. A., Brenner, A. C., Saba, J. L., and Yi, D.: Mass changes of the Greenland and Antarctic ice sheets and shelves and contributions to sea-level rise: 1992–2002, Journal of Glaciology, 51, 509–527, https://doi.org/10.3189/172756505781829007, 2005.

3

A LEADING-EDGE-BASED METHOD FOR CORRECTION OF SLOPE-INDUCED ERRORS IN ICE-SHEET HEIGHTS DERIVED FROM RADAR ALTIMETRY

Satellite radar altimetry has been an important tool for cryospheric applications such as measuring ice-sheet height or assessing anomalies in snow and ice properties (e.g. the extensive melt in Greenland in 2012). Although accurate height measurements are key for such applications, slope-induced errors due to undulating topography within the kilometre-wide beam-limited footprint can cause multi-metre errors. In this study, a leading edge point-based (LEPTA) method is presented that corrects for the slope-induced error by including the leading edge information of the radar waveform to determine the impact point. The principle of the method is that only the points on the ground that are within the range determined by the beginning and end of the leading edge are used to determine the impact point. The LEPTA method demonstrates a stable performance both in the flat, interior regions of Greenland and in regions with more complex topography. It also has good performance in both the median or the median absolute deviation when compared with existing methods. Based on that, we recommend considering LEPTA for obtaining accurate height measurements with radar altimetry data, especially towards the margins of the LRM coverage where the surface slopes increase; we also adopt LEPTA for further studies on assessing snow and ice properties.

3.1. INTRODUCTION

Satellite radar altimetry is a key tool for assessing the status and dynamics of the cryosphere as it allows constructing digital elevation models (DEMs) (Slater et al., 2018), deriving height change in ice sheets (Hurkmans et al., 2012; Helm et al., 2014a), understanding seasonal variations in snow (Adodo et al., 2018), and estimating snowpack properties

This chapter has been published as Li, W., Slobbe, C., and Lhermitte, S.: A leading-edge-based method for correction of slope-induced errors in ice-sheet heights derived from radar altimetry, The Cryosphere, 16, 2225–2243, https://doi.org/10.5194/tc-16-2225-2022, 2022. Minor changes have been made to correct for typographical errors and to improve consistency.

(Lacroix et al., 2008). To obtain accurate information on heights, altimetry processing involves correction for instrument errors, atmospheric effects, tidal effects, and slope-induced errors (Helm et al., 2014a; Hai et al., 2021). Of crucial importance is the correction for slope-induced errors as they can affect the obtained height measurements significantly. For example, according to the error propagation in Brenner et al. (1983), the CryoSat-2 satellite at an altitude of 717 km can give a vertical offset of approximately 39 m and a horizontal offset of 7.5 km when measuring heights of a terrain with a 0.6° slope.

To correct for the slope-induced errors, different methods have been developed (Brenner et al., 1983; Remy et al., 1989; Bamber, 1994; Roemer et al., 2007). The most widely used methods involve both a correction to the height and a relocation of the satellite measurement location from the nadir to the expected impact point (i.e. the radar reflection point) on the terrain. Two implementations of this so-called "relocation method" are known as the "slope" method and the "point-based" method (Bamber, 1994; Roemer et al., 2007). The slope method assumes constant surface slope parameters within the beam-limited altimeter footprint and calculates the relocated latitude, longitude, and height according to trigonometry (Levinsen et al., 2016). The point-based method uses a topographic model within the beam-limited satellite footprint and searches for minimum range between the satellite and a surface area in the size of the pulse-limited footprint (Roemer et al., 2007; Levinsen et al., 2016).

Although both methods have been refined and applied with reliable results, they both show methodological shortcomings. The slope method, for example, tends to ignore the local topography within the footprint and therefore may not be accurate enough in undulating areas (Levinsen et al., 2016). The point-based method of Roemer et al. (2007), on the other hand, is more accurate in the undulating regions (Roemer et al., 2007; Levinsen et al., 2016) as it considers the detailed topography, but by assuming a fixed footprint size, it neglects the actual footprint illuminated by the satellite on the terrain. For example, by taking the averaged range within the assumed footprint, this method may ignore part of the terrain that actually contributes to the return signal or assumes that part of the terrain not visible to the satellite could contribute to the return signal (Figure 1). The recent availability of high-resolution DEM products provides the opportunity to determine the part of the terrain contributing to the rise of the leading edge and therefore can determine the actual footprint of the radar altimeter. To overcome the shortcomings of both methods, we present a leading edge point-based (LEPTA) method that exploits high-resolution DEM information to correct for the slope-induced error by including the leading edge information of the radar waveform to determine the impact point. The principle of the method is that only the points on the ground that are actually within the range interval determined by the beginning and end of the leading edge are used to compute the impact point.

The chapter is organised as follows. Section 3.2 describes the data used for radar altimetric processing and assessment of the results. In Section 3.3, the different methods used for the correction of the slope-induced errors as well as the assessment workflow are introduced. To assess the performance of the LEPTA method, we apply it to all CryoSat-2 Low Resolution Mode (LRM) acquisitions over Greenland in 2019 and benchmark it to the slope and point-based methods by comparing it with laser altimeter ICESat-

2 height measurements. In Section 3.4 and Section 3.5 we present, analyse, and discuss the results. Finally, we conclude by emphasising the main findings.

3.2. DATA AND PRE-PROCESSING

3.2.1. CRYOSAT-2 OBSERVATIONS

In the interior of the Greenland ice sheet, data acquired by CryoSat-2 are in LRM. LRM is the conventional pulse-limited mode that requires correction for slope-induced errors. The pulse-limited LRM footprint is approximately 1.65 km in diameter, and the beam-limited footprint is approximately 14.39 km in diameter (Hai et al., 2021). Our evaluation employs all data acquired from 1 January to 31 December 2019, resulting in approximately 2.2×10^6 measurements. In particular, we use Level-1b (L1b) Baseline D data (European Space Agency, 2019a; Meloni et al., 2020).

To process the waveform information and obtain height estimations, the L1b waveforms are retracked using the offset centre of gravity (OCOG) method (Wingham et al., 1986) documented in Bamber (1994). We use OCOG because of its precision and robustness (Bamber, 1994; Schröder et al., 2019). According to Davis (1997), a 10 % threshold is ideal for detecting ice-sheet height change (or strong volume scattering; Aublanc et al., 2018), a 20 % threshold is the most appropriate for estimating the absolute or true ice-sheet height, and a 50 % threshold is the most appropriate for estimating the absolute height when the waveform is dominated by surface scattering (Davis, 1997; Aublanc et al., 2018). In this study, we follow the recommendation of Davis (1997) and use a 20 % threshold to obtain estimates of the true ice-sheet elevation. This allows a comparison with ICESat-2 data. Aublanc et al. (2018), who used a 25 % threshold, highlighted that this choice is a compromise between pure surface scattering (in which case the threshold should be around 50 %) and volume scattering (10 %). In the first case, one would underestimate the true elevation and in the other overestimate it. Hence, as pointed out by Davis (1997), "the 20 % retracking point provides a reasonable estimate of the true ice-sheet elevation in only an average sense". In addition, waveforms are removed if they meet one of the following empirically derived criteria: (i) the integrated normalised power exceeds 150; (ii) the normalised power in the first 10 range bins is larger than 0.2; or (iii) no peaks are identified in the waveform.

To benchmark our results, Level-2I (L2I) height data obtained with the OCOG retracker from the European Space Agency (2019b) are used. In the L2I products the slope-induced error is corrected with the Helm et al. (2014b) DEM, which has a resolution of 1 km × 1 km (Helm et al., 2014a). To enable a fair comparison with our in-house-processed L2I data, all L2I height measurements are removed for which the waveforms meet one of the criteria mentioned above.

3.2.2. ARCTICDEM

To compute a correction for the slope-induced errors, a DEM is needed. Here, the slope method uses a low-resolution DEM as it assumes a constant slope within the pulse-limited footprint (Levinsen et al., 2016). On the contrary, the point-based methods (i.e. LEPTA and the point-based method proposed by Roemer et al. (2007)) require DEMs with higher resolution to provide the full information of the local terrain.

In this study, ArcticDEM is used as reference DEM as it is constructed from recent stereo satellite imagery and is available in high resolution (2 m × 2 m) (Porter et al., 2018). The systematic error in ArcticDEM is less than 5 m (Noh and Howat, 2015), and the DEM has been updated since 2016. ArcticDEM is low-pass filtered to a 2 km resolution by applying a block-mean filter for the slope-based method and to a 100 m resolution for the point-based and LEPTA methods. The use of a 100 m resolution instead of 2 m is a compromise for computational efficiency. To assess the impact of DEM resolution on the correction methods, we vary the resolutions from 100 m (200 m for the slope method, for computational efficiency) to 900 m with a 100 m interval and from 1 to 8 km with a 1 km interval.

3.2.3. ICESAT-2 OBSERVATIONS

For validation of the different slope correction methods, the ICESat-2 L3A Land Ice Height (ATL06) product (Smith et al., 2020a) is used. ICESat-2 uses the Advanced Topographic Laser Altimeter System (ATLAS), which emits green light pulses and counts the received photons (Abdalati et al., 2010) The laser beams are configured in a 2 × 3 array. The distance between and within beam pairs is ~ 3.3 km and ~ 90 m, respectively (Smith et al., 2019). The along-track resolution of the land ice height product is ~ 20 m (Smith et al., 2020b). The ATL06 products have a known geolocation accuracy (or bias) of less than 10 m (National Snow and Ice Data Center (NSIDC), 2021). A comparison between ICESat-2 and ArcticDEM is shown in Appendix 3.A. The results show that the median ICESat-2 height for the different beam pairs is up to 0.21 m higher than ArcticDEM. The median absolute deviation of the differences is 0.72 m for all beam pairs.

3.3. METHODOLOGY

3.3.1. METHODS TO CORRECT FOR SLOPE-INDUCED ERRORS

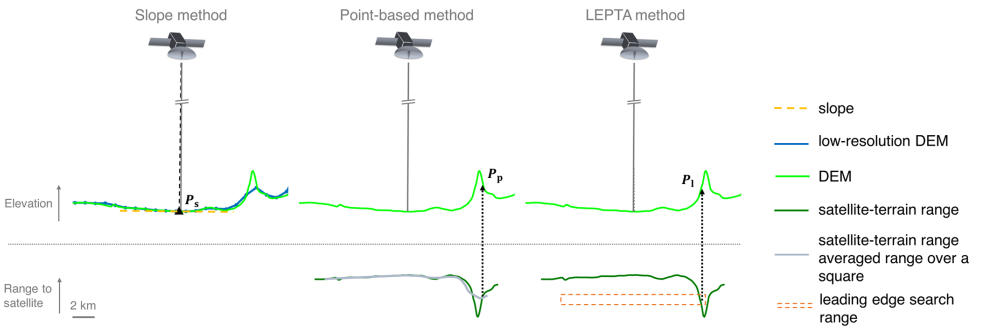

Figure 1: Conceptual illustration of different slope-induced error correction methods. The impact points estimated from the slope method, the point-based method, and LEPTA are represented by P_s, P_p and P_l. The slope method computes a correction based on the surface slopes obtained from a DEM, whereas the point-based method and LEPTA are based on the range between the satellite and the terrain.

The different slope-induced error correction methods are conceptually illustrated in Figure 1. The impact points estimated from the slope method, the point-based method, and LEPTA are represented by P_s, P_p and P_l. The "low-resolution DEM" (2 km) is only

used by the slope method, whereas the point-based method and LEPTA use a "high-resolution DEM" (100 m). The slope method computes a correction based on the surface slopes obtained from a DEM, whereas the point-based method and LEPTA are based on the range between the satellite and the terrain.

SLOPE CORRECTION METHOD

The slope method uses the slope of the low-resolution DEM at the nadir point to compute the impact point. It assumes that the slope within the CryoSat-2 pulse-limited footprint is constant and is defined by direction θ and magnitude Φ (Cooper, 1989; Bamber, 1994). In our implementation, θ and Φ are computed in the same map projection and grid as ArcticDEM. The gridded θ and Φ are then interpolated to the satellite nadir point. The corrected height (h_C), corresponding to the height of the impact point P_s, can then be obtained by (Bamber, 1994)

$$h_C = \frac{R_s \sin(\Phi - \Gamma)}{\sin \Phi} - R_\alpha, \tag{3.1}$$

where

$$\Gamma = \sin^{-1}\left(\frac{R \sin \Phi}{R_s}\right), \tag{3.2}$$

$$R_s = R_\alpha + h_S, \tag{3.3}$$

$$R_\alpha = \frac{\rho \nu}{\nu \cos^2\theta + \rho \sin^2\theta}, \tag{3.4}$$

$$\nu = \frac{a}{\sqrt{1 - e^2 \sin^2 \phi}}, \tag{3.5}$$

$$\rho = \frac{a(1-e^2)}{\sqrt{(1 - e^2 \sin^2 \phi)^3}}, \tag{3.6}$$

R represents the retracked range, a and e the semi-major axis and eccentricity of the reference ellipsoid being used, and ϕ the latitude of the satellite. The corrected location of the impact point in latitude ϕ_c and longitude λ_c (in radians) is computed as

$$\phi_c = \frac{\pi}{2} - 2\sin^{-1}\left(\frac{X + \Delta x}{2R_\alpha \cos \lambda_c}\right), \tag{3.7}$$

$$\lambda_c = \tan^{-1}\left(\frac{Y + \Delta y}{X + \Delta x}\right), \tag{3.8}$$

where X and Y define the position of the satellite in Cartesian coordinates,

$$\Delta x = R_\alpha \Gamma \cos\theta, \tag{3.9}$$

and

$$\Delta y = R_\alpha \Gamma \sin\theta. \tag{3.10}$$

Application of the slope method in Figure 1 shows that the impact point will be assumed at the position P_s. Inaccuracies usually occur when this method is applied to complex terrains due to the simplification of the complex topography to a constant slope (Levinsen et al., 2016).

POINT-BASED CORRECTION METHOD

The point-based method directly uses the topographic information from the a priori DEM to find the impact point (P_p). It does so by minimising the mean distance $\bar{R}_P$ to the satellite over a pre-defined fixed-size rectangular footprint area (e.g. 1.65 km × 1.65 km in Hai et al., 2021). Assuming the pre-defined rectangular footprint with area A consists of n DEM grid cells, $\bar{R}_P$ is computed by (Roemer et al., 2007)

$$\bar{R}_P = \frac{1}{A} \sum_{j=1}^{n} A_{Pj} \bar{R}_{Pj}, \tag{3.11}$$

where A_{Pj} and $\bar{R}_{Pj}$ are the area of and range to each grid cell j. The point for which $\bar{R}_P$ is minimal is referred to as P_p with latitude ϕ_c and longitude λ_c. The range between the satellite and P_p is referred to as r_p. In line with Roemer et al. (2007), we use the 100 m DEM to find an approximate position. The final point is obtained by a second search in the vicinity of the approximate position for which we use an up-sampled DEM of 10 m × 10 m. The corrected height h_C is computed as (Roemer et al., 2007)

$$h_C = h_N + r_p - (h_S - h_I), \tag{3.12}$$

where h_N is the surface height of the nadir point relative to the reference ellipsoid (i.e. the ellipsoidal height of the satellite h_S minus the retracked range R), and h_I is the DEM height of P_p. Equation (3.11) also shows, however, that this approach can take DEM points into account that actually do not contribute to the rise of the leading edge (i.e. points that fall outside the pulse-limited footprint).

LEADING EDGE POINT-BASED (LEPTA) CORRECTION METHOD

The LEPTA method is similar to the point-based method as it also uses the topographic information from the a priori DEM to find the impact point (P_l) but differs in the search method of the impact point. Instead of pre-defining a fixed pulse-limited footprint size, the LEPTA method identifies the parts of the terrain within the beam-limited satellite footprint that contribute to the rise of the leading edge. To identify these points, we use a beam-limited satellite footprint of 14.39 km × 14.39 km (Hai et al., 2021) centred around the nadir point and a search range bounded by r_{begin} and r_{end}:

$$r_{\text{begin}} = \max(r_{1\%}, r_{20\%} - \Delta r), \tag{3.13}$$

$$r_{\text{end}} = \min(r_{90\%}, r_{20\%} + \Delta r), \tag{3.14}$$

where $r_{1\%}$ and $r_{90\%}$ refer to the retracked ranges obtained using a 1% and 90% threshold retracker (Davis, 1997), respectively; $r_{20\%}$ is the OCOG retracked range using a 20% threshold to obtain the firn–air interface; and Δr is a user-defined threshold. Δr is used to avoid the search range ($r_{\text{end}} - r_{\text{begin}}$) becoming unrealistically large. For all experiments, we use a value of 1.25 m based on an empirical optimisation of Δr. If no DEM grid points are identified within the search range, we compute the difference between the distance from the satellite to the closest DEM grid point and the retracked range. Then, we added this difference to r_{begin} and r_{end}.

The location of P_l is computed as the average of all identified DEM grid points K. Finally, the corrected height h_C is computed by

$$h_C = h_N + \frac{1}{K}\sum_{i=1}^{K}(r^i_{\text{DEM}} - (h_S - h^i_{\text{DEM}})), \tag{3.15}$$

where h^i_{DEM} is the ellipsoidal height of the ith identified DEM grid point and r^i_{DEM} the range between the satellite and the ith identified DEM grid point. By using averaging to compute P_l, it is theoretically possible that the average location is outside the actual pulse-limited footprint (e.g. when the impact points form a doughnut shape or two equally large but disjointed sets of points). These occurrences can be easily identified.

One of the advantages of the LEPTA method compared to the point-based method is that it includes points that contribute to the rise of the leading edge signal but are outside the fixed (square) pulse-limited footprint and rejects points that do not contribute to the rise of the leading edge signal but are inside the pre-defined pulse-limited footprint. An additional advantage of LEPTA is that it does not apply the recursive computation process as the point-based method; therefore it speeds up the processing.

3.3.2. PERFORMANCE ASSESSMENT

To assess the performance of the LEPTA method, we benchmark the different methods by comparing their accuracy relative to reference data. First, we directly compare the corrected heights (h_C) for each method with the reference height from the 100 m ArcticDEM. To compare h_C with the DEM, we bi-linearly interpolate the DEM heights to the CryoSat-2 locations (h_{DEMC}). Then, the CryoSat-2 measurements are grouped in 25 km × 25 km tiles. For each tile, we compute the median and median absolute deviation of the $h_C - h_{\text{DEMC}}$ values. This assessment cannot be considered as a validation as ArcticDEM is not an independent dataset. However, it is insightful especially when the CryoSat-2 points do not have an ICESat-2 point nearby.

Second, we compare the corrected height measurements with the ICESat-2 heights for each method. This comparison is carried out per month; i.e. we compare the CryoSat-2 heights acquired in a particular month to the ICESat-2 heights acquired in the same month. For each point, we first identify all ICESat-2 points within 50 m of the CryoSat-2 point. If ICESat-2 points are available in each quadrant surrounding the CryoSat-2 point, the ICESat-2 heights are interpolated to the CryoSat-2 point using a natural-neighbour interpolation (h_{ICE2}). Otherwise a nearest neighbour interpolation is applied. A natural neighbour interpolation provides a smoother solution (Bobach, 2009) yet requires weighting functions based on the surrounding points. To correct for the height difference between the locations of the CryoSat-2 and ICESat-2 points over a potentially sloping terrain, we apply a correction computed as the height difference between the 100 m ArcticDEM evaluated at the CryoSat-2 (h_{DEMC}) and ICESat-2 (h_{DEMI}) locations. Hence, the differences between the CryoSat-2 and ICESat-2 heights (Δh) become

$$\Delta h = h_C - h_{\text{ICE2}} - (h_{\text{DEMC}} - h_{\text{DEMI}}) \tag{3.16}$$

Similarly to the comparison with ArcticDEM, we compute the median and median absolute deviation of Δh for each 25 km × 25 km tile.

When benchmarking the methods, two aspects of accuracy are assessed. First, we determine the difference between the slope-corrected CryoSat-2 measurements and the reference heights (h_{DEMC} or h_{ICE2}) using standard statistical parameters (median, median absolute deviation, mean, and standard deviation). Second, we assess the variability in the statistics for the different methods. The statistical parameters are computed with and without outliers. Cumulative functions are provided mainly to visualise the percentiles that indicate the distribution of the results and determine the outliers. Here, we consider $h_C - h_{\text{DEM}}$ or Δh outside the 10th–90th percentile range as an outlier. Probability distribution functions are provided to visualise the overall distribution of results. The skewness parameter is provided as long tails of the probability distribution are not completely visualised. In addition, tiles including less than 10 measurements are rejected for visualisation and interpretation as the statistics of these tiles do not represent sufficient data and cannot be informative.

3.3.3. SENSITIVITY ANALYSIS

The LEPTA method is potentially sensitive to i) the definition of r_{end} and r_{begin} and hence Δr (Equations. 3.13 and 3.14), ii) a potential bias in the DEM, and iii) the resolution of the DEM. Another aspect that may impact the height estimates of all methods is the adopted OCOG threshold. To assess how our choices impact the results, we conduct a number of sensitivity analyses in which we:

- vary Δr (Equations. 3.13 and 3.14) from 0.5 to 5 m in steps of 0.5 m to define an optimal choice;
- vary the adopted OCOG threshold to determine R and hence h_N (Equation 3.16) from 10% to 90% in steps of 20%, using an optimal choice of Δr for LEPTA;
- add a bias to the DEM from −7.5 to 2.5 m in steps of 2.5 m, using a 20% OCOG threshold and an optimal choice of Δr for LEPTA;
- vary the DEM resolution from 200 to 900 m in steps of 100 m, and from 1 to 8 km in steps of 1 km, using a 20% OCOG threshold and an optimal choice of Δr for LEPTA.

3.4. RESULTS

3.4.1. COMPARISON WITH ARCTICDEM

The cumulative distribution of $h_C - h_{\text{DEMC}}$ for all methods (Figure 2a) shows that most values are within the [-1.0, 3.0] m interval (as shown by 10th and 90th percentiles), although outliers have an impact on the interpretation of the results. These outliers have most impact on the overall standard deviation and skewness of $h_C - h_{\text{DEMC}}$, as shown in Table 1 and Figure 3. Although the distribution curves show a positive bias, the skewness is negative for all methods, showing more or larger negative outliers, as also shown in Figure 3.B.1. Comparison of the methods, however, shows that LEPTA is least affected by such negative outliers.

Removing the outliers significantly reduces the standard deviation of $h_C - h_{\text{DEMC}}$ and skewness for all methods and brings the mean closer to the median. Comparison of the

Table 1: Statistics of the height difference between slope-corrected CryoSat-2 measurements and ArcticDEM and ICESat-2 ($h_C - h_{\mathrm{DEM_C}}$ or Δh as computed by Equation 3.16). Height statistics are in unit of metres. The parameters are shown with and without outliers (referred to as w/ outlier and w/o outlier) using 10th and 90th percentiles. E, S, P and L represent ESA L2I, slope method, point-based method and LEPTA, respectively.

CryoSat-2		vs. ArcticDEM				vs. ICESat-2			
		E	S	P	L	E	S	P	L
No. of data	w/ outlier	2.2e6	2.2e6	2.2e6	2.2e6	8.2e4	8.3e4	8.3e4	8.2e4
	w/o outlier	1.8e6	1.8e6	1.8e6	1.8e6	6.6e4	6.6e4	6.6e4	6.6e4
median	w/ outlier	0.43	0.69	0.71	0.24	0.01	0.21	0.48	0.00
	w/o outlier	0.43	0.69	0.71	0.24	0.01	0.21	0.48	0.00
median absolute deviation	w/ outlier	0.58	0.66	0.45	0.45	0.18	0.24	0.14	0.12
	w/o outlier	0.44	0.50	0.35	0.34	0.14	0.19	0.10	0.09
mean	w/ outlier	0.58	1.27	0.47	0.22	0.39	1.14	0.39	0.06
	w/o outlier	0.51	0.87	0.70	0.22	0.13	0.51	0.50	0.00
standard deviation	w/ outlier	2.87	3.11	2.75	1.72	2.73	3.27	1.78	1.64
	w/o outlier	0.64	0.82	0.46	0.46	0.35	0.70	0.15	0.13
skewness	w/ outlier	-14.29	-2.87	-22.03	-1.93	-2.58	2.86	-21.13	-15.60
	w/o outlier	0.49	0.90	-0.11	-0.17	1.77	1.93	0.50	-0.15

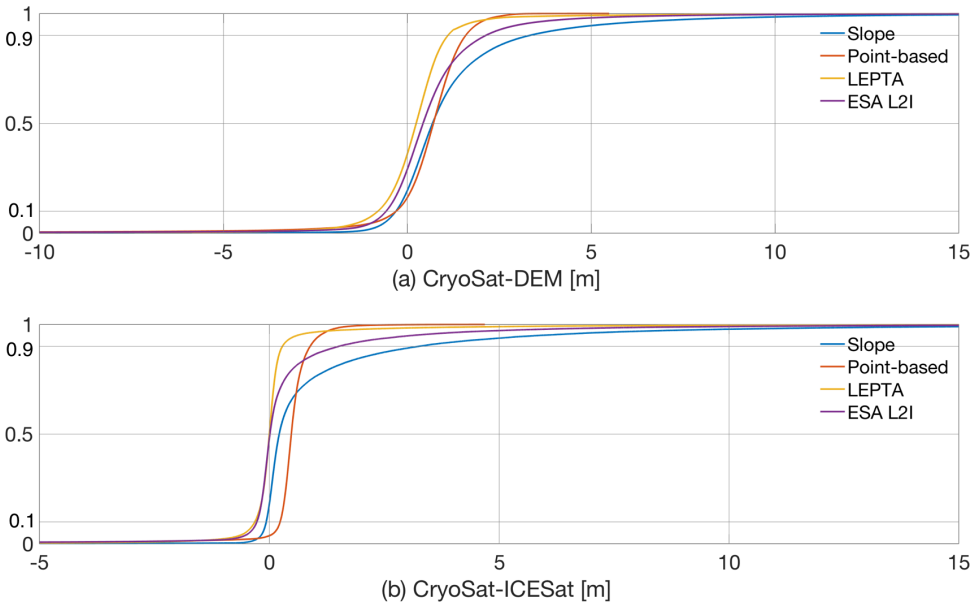

Figure 2: Cumulative distribution figures of (**a**) the difference between CryoSat-2 and ArcticDEM ($h_C - h_{\text{DEM}}$) and (**b**) the difference between CryoSat-2 and ICESat-2 (Δh), including outliers. The 10th and 90th percentiles are shown in the figures for outlier removal. For visualisation, the x-axis is restricted to [-10, 15] m for figure (**a**) and to [-5, 15] m for (**b**).

mean and median values (Table 1) and probability distribution (Fig. 3a) moreover indicates that LEPTA performs better than other methods when compared with ArcticDEM, with a mean height difference of 0.22 m and a median difference of 0.24 m. The slope method results in the largest mean difference of 0.87 m, while the point-based method gives the largest median of 0.71 m. The standard deviation (0.46 m) and median absolute deviation (0.34 m) from LEPTA are also the smallest, the same as those obtained from the point-based method. The largest $h_C - h_{\text{DEMC}}$ deviation values after outlier removal are given by the slope method, with the standard deviation being 0.82 m and median absolute deviation being 0.50 m. An additional note is that the mean and median from all methods are positive, which implies that the heights obtained by these methods are generally higher than ArcticDEM heights.

Comparison of the spatial patterns of median and median absolute deviation (Figure 3) shows large spatial differences in both pattern and magnitude among the different methods. In general, the largest median and median absolute deviation values occur near the margins of the LRM coverage, where the terrain is steeper. For the point-based method and LEPTA, the median values on the western side are generally lower than on the eastern side. This spatial pattern is similar to that of the differences between ICESat-2 and ArcticDEM (shown in Figure 3.A.1). For ESA L2I products and the slope method, the largest median values occur on both the eastern and the western sides of Greenland, and those from the slope method largely exceed those of the ESA L2I products, the point-based method, and LEPTA. So far, we lack a conclusive explanation for the spa-

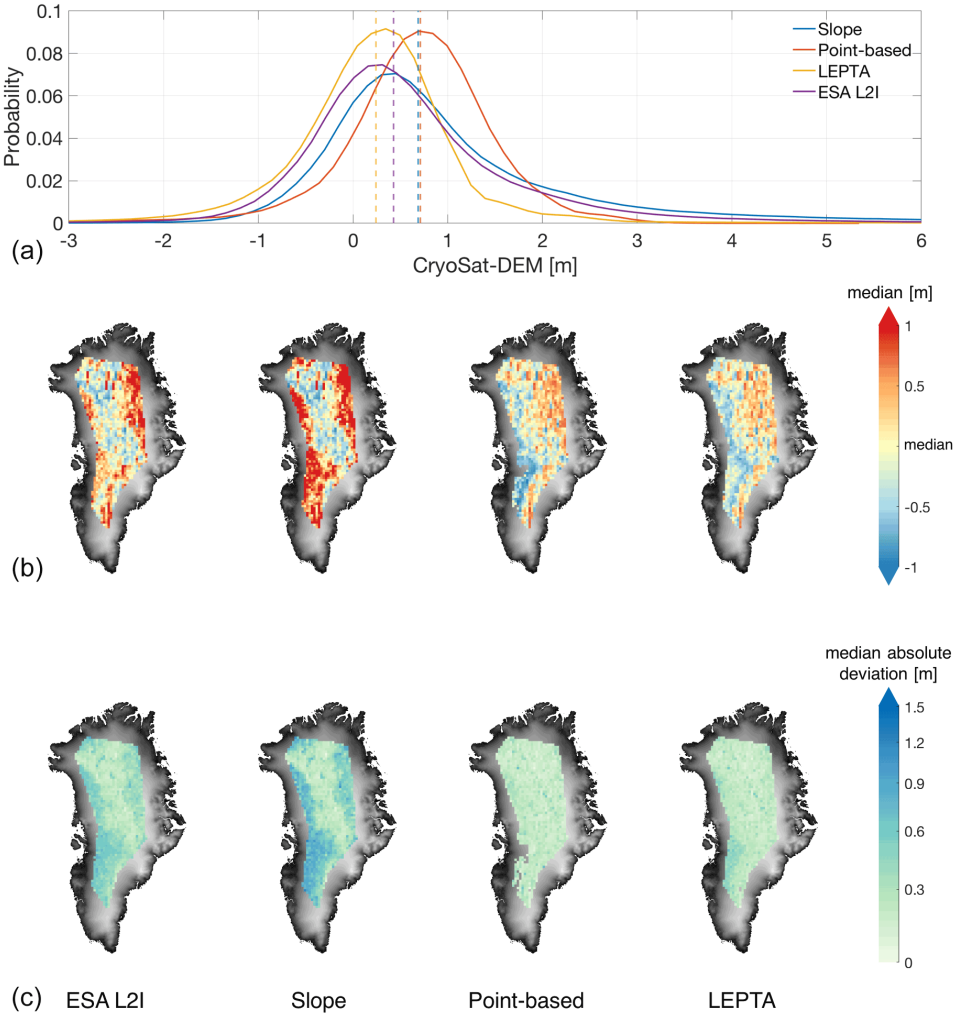

Figure 3: (**a**)) Probability distribution of height difference between CryoSat-2 and the ArcticDEM, before removing the outliers with 10th and 90th percentiles. The probability distribution is plotted with all data samples but restricted to [-3, 6] m for visualisation (for better illustration of the skewness and large outliers, please refer to Appendix 3.B). Vertical lines show the median value per method. (**b**, **c**) Spatial distribution of median and median absolute deviation of the height difference per tile of 25 km × 25 km, after removing the outliers. To enhance the visibility of the maps, the median value of each method is subtracted in (**b**). The colours of the median absolute deviation plots are on a logarithmic scale to enhance contrast. The spatial distribution results from left to right are obtained by ESA L2I products, the slope method, the point-based method and LEPTA, with the 1 km × 1 km DEM covering Greenland (Helm et al., 2014a,b) as background.

tial differences between the methods. Regarding the median absolute deviation values, we observe in general higher values on the western side of the ice sheet than in the interior. For the ESA L2I products and the slope method, the median absolute deviation values are also high on the eastern side. These median absolute deviation values show that topography affects the different performances of the methods, and the point-based method and LEPTA are less affected on the eastern side. In addition, for the point-based method, removing the outliers results in the most missing data close to Jakobshavn Isbræ. Combining the statistics in Table 1 and the spatial distribution of median and median absolute deviation in Figure 3, it can be concluded that LEPTA performs best when compared with ArcticDEM.

Using averaging in Equation 3.15 to compute P_l results in 5.2% of the impact points being outside the actual footprint. Removing these points as "unreliable data" minimally affects the median and mean (0.26 m and 0.25 m), but improves the median absolute deviation (0.32 m) and standard deviation (0.40 m).

3.4.2. VALIDATION WITH ICESAT-2 OBSERVATIONS

Comparison of CryoSat-2 and ICESat-2 heights (Figure 2b) shows again the impact of outliers on the results, although the outliers are generally lower than for the ArcticDEM comparison. ESA L2I products, the point-based method, and LEPTA have more impacts from negative outliers, while the slope method results in more positive outliers.

With the outliers removed, the standard deviation of Δh values from all methods is greatly reduced, especially for the ESA L2I and slope method, which show the largest outliers (Figure 2b). The lowest median (0.00 m), mean (0.00 m), median absolute deviation (0.09 m), and standard deviation (0.13 m) of Δh are obtained by LEPTA, showing that the LEPTA method again outperforms the other methods. The largest median (0.48 m) is obtained by the point-based method, and the largest mean (0.51 m), median absolute deviation (0.19 m), and standard deviation (0.70 m) are from the slope method.

The comparison of the height differences between CryoSat-2 vs. ArcticDEM and CryoSat-2 vs. ICESat-2 shows moreover that the height differences with ICESat-2 are smaller, probably due to the better quality of ICESat-2 data compared to ArcticDEM and the longer time gap between CryoSat-2 and ArcticDEM, as satellite imagery data for generating ArcticDEM have been gathered since 2007 (Noh and Howat, 2017; Howat et al., 2019) and co-registered to ICESat since before 2009, whereas ICESat-2 measurements were obtained in the same month as CryoSat-2 data. The comparison between CryoSat-2 and ICESat-2 also results in fewer data points as not all CryoSat-2 measurements have corresponding nearby ICESat-2 measurements within the 50 m criterion.

The spatial distribution of the median and median absolute deviation of Δh (Figure 4) shows clear spatial patterns. For the ESA L2I products, the slope method, and the point-based method, the median differences with respect to the overall median difference are generally negative (positive) in the central part (margins of the LRM zone). For LEPTA, the variability in negative or positive differences is smaller (especially vs. ESA L2I and the slope method) but with a slightly reversed pattern. This reversed pattern can be explained by LEPTA's definition of r_{begin} and r_{end} that may result in an asymmetry around $r_{20\%}$ that can spatially vary. Figure 4 also shows that LEPTA has the lowest spatial variability in the median absolute deviation, whereas the slope method shows the largest

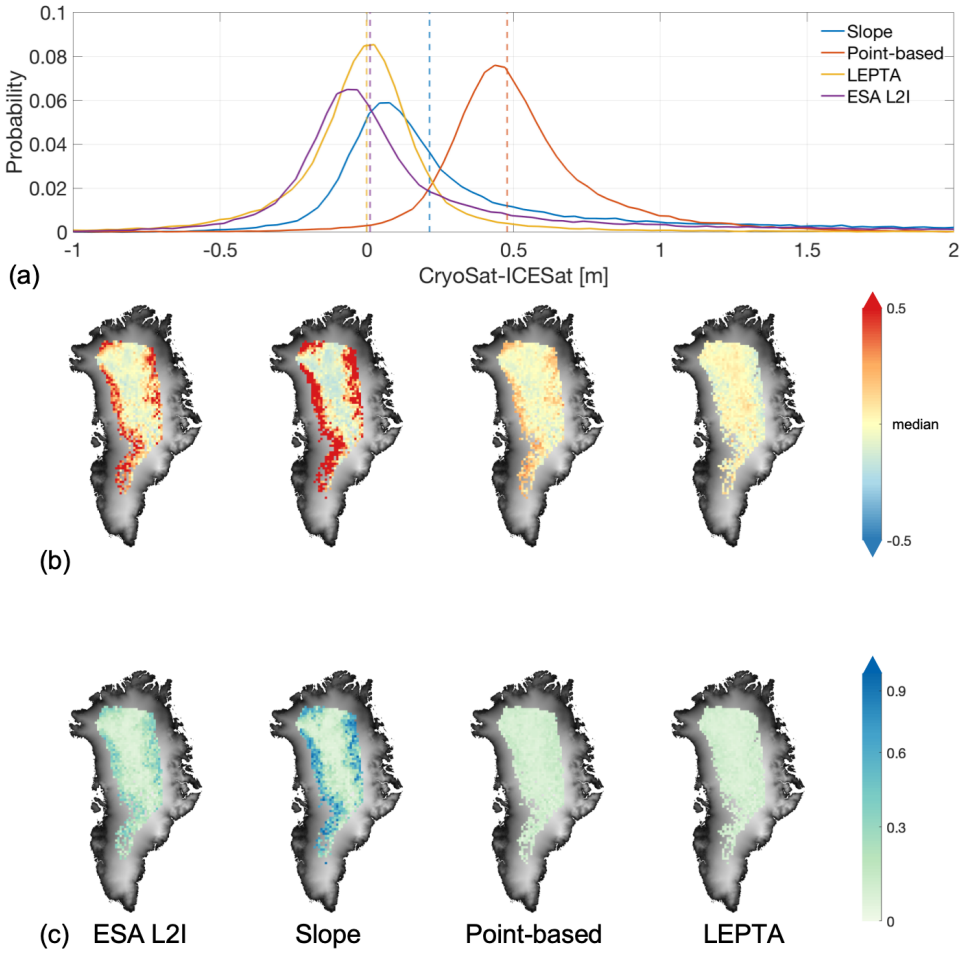

Figure 4: (**a**)) Probability distribution of height difference between CryoSat-2 and ICESat-2, before removing the outliers. The probability distribution is plotted with all data samples but restricted to [-1, 2] m for visualisation (for better illustration of the skewness and large outliers, please refer to Appendix 3.B). Vertical lines show the median value per method. (**b**, **c**) Spatial distribution of median and median absolute deviation of the height difference per tile of 25 km × 25 km, after removing the outliers. To enhance the visibility of the maps, the median value of each method is subtracted in (**b**). The colours of the median absolute deviation plots are on a logarithmic scale. The spatial distribution results from left to right are obtained by ESA L2I products, the slope method, the point-based method and LEPTA, with the 1 km × 1 km DEM covering Greenland (Helm et al., 2014a,b) as background.

contrast between the interior and the margins of the LRM zone.

3.4.3. SENSITIVITY TO THE DEFINITION OF THE SEARCH RANGE

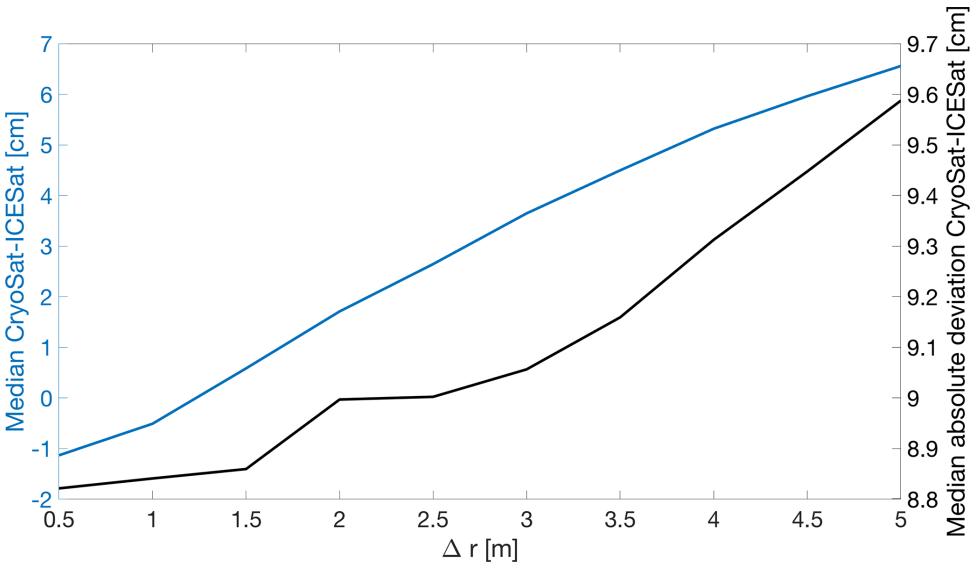

Figure 5: Median (left axis) and median absolute deviation (right axis) of the height differences between CryoSat-2 and ICESat-2 (Δh calculated with Equation 3.16) as a function of Δr. Outliers are removed using 10th and 90th percentiles.

The performance of the LEPTA method relies on the definition of r_{begin} and r_{end} and hence Δr. To assess the sensitivity of LEPTA to the choice of Δr, we repeat the performance assessment by varying Δr, as introduced in Section 3.3. The results of this Δr sensitivity assessment are summarised in Figure 5. This shows that while Δr changes at the metre level, the median and the median absolute deviation values of Δh only change at the centimetre level. More specifically, the median and median absolute deviation increase with increasing Δr. From Figure 5, we can also conclude that $\Delta r = 1.25$ m results in a near-zero median difference compared to ICESat-2. Hence $\Delta r = 1.25$ m is used for all experiments.

However, it is not sufficient to conclude that LEPTA is robust to the choice of Δr by merely assessing Δh. The reason for this is that different Δr's might result in different horizontal locations, which are then compared to potentially different ICESat-2 measurements. Therefore, Figure 6 shows the differences in the ellipsoidal height and horizontal position of the impact points obtained using $\Delta r = 2$ m (Δr_2) and $\Delta r = 1$ m (Δr_1). This comparison shows whether a Δr change of 1 m can result in large horizontal and vertical offsets. In the interior of the ice sheet this effect is small as the vertical and horizontal offsets resulting from Δr_2 vs. Δr_1 are close to 0. In the margin regions of LRM coverage, however, increasing Δr results in lower elevation of impact points and horizontal offsets with mean values up to 20 m and standard deviations up to 250 m.

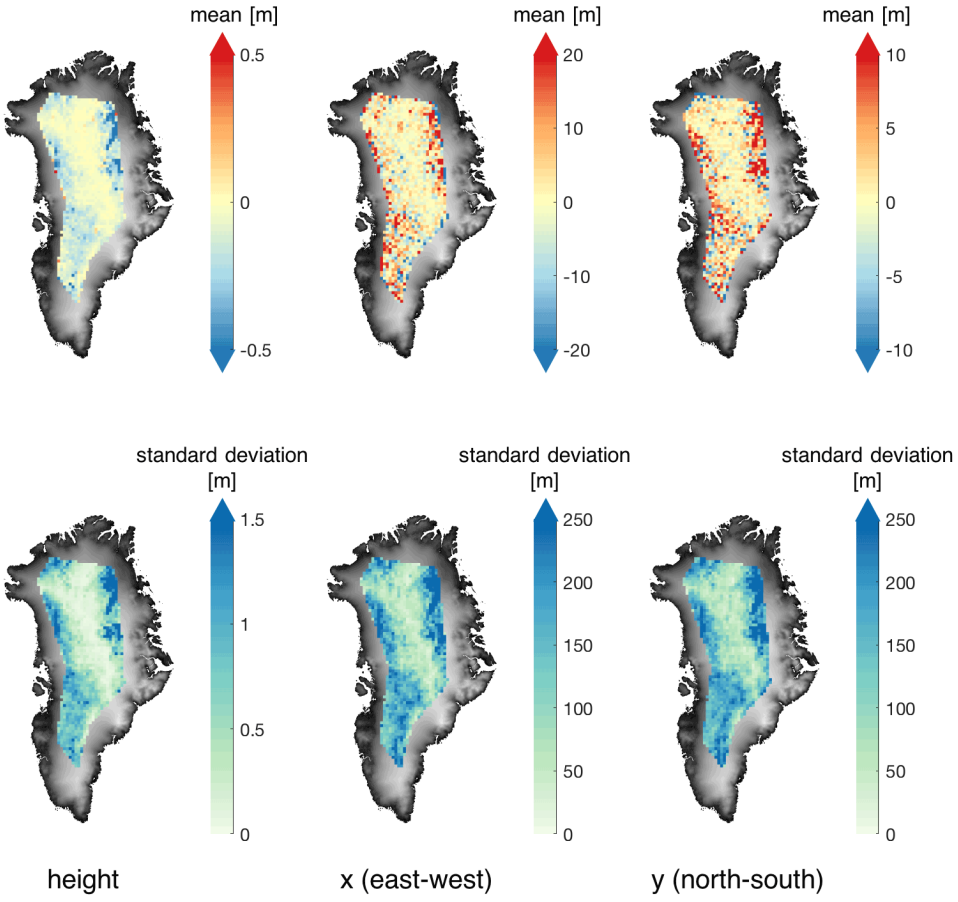

Figure 6: Mean and standard deviation of the differences between the height and horizontal location of the impact point obtained using Δr = 2 m (Δr_2) and Δr = 1 m (Δr_1). The mapped locations are based on the horizontal locations (x and y) derived from Δr_1, tiled by the 25 km × 25 km grid as in Figure 4.

3.4.4. ASSESSMENT OF OCOG RETRACKER THRESHOLD DEPENDENCE

Changing the OCOG retracker threshold from 10 % to 90 % results in retracked points further away from the satellite and hence lower height estimates (Figure 7). For all methods, this behaviour is apparent as the median of Δh is reduced by approximately 1.2 m when the threshold increases from 10 % to 90 %. Changing the OCOG retracker threshold in LEPTA results only in a change in the height of P_l and does not affect the selection of the DEM points that contribute to P_l. This means that increasing the OCOG retracker threshold actually corresponds to increasing the depth of the radar return within the snowpack or firn. Moreover, Figure 7 highlights that the adopted OCOG retracker threshold of 20 % for LEPTA results in a near-zero median difference compared to ICESat-2, indicating that on average it effectively detects the absolute ice-sheet height.

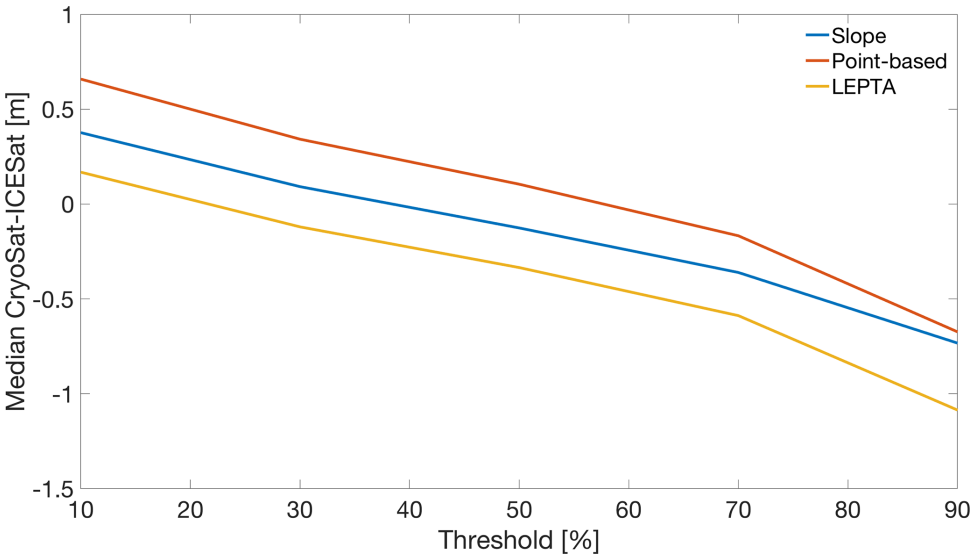

Figure 7: Median of height differences between CryoSat-2 and ICESat-2 (Δh calculated with Equation 3.16) as a function of the OCOG retracker threshold. Outliers are removed using 10th and 90th percentiles.

3.4.5. SENSITIVITY TO POTENTIAL BIASES IN THE DEM

To assess the sensitivity of the methods to potential constant ice-sheet elevation changes, we perform a sensitivity analysis in which we add biases to the DEM. Figure 8 shows that the slope and the point-based methods are not affected by these DEM biases, while they do affect LEPTA. The impact, though, depends on the sign of the bias. Adding a bias between -7.5 m and -2.5 m (which corresponds to ice-sheet lowering) only changes the median Δh by approximately 2.3 cm, while adding a bias of 2.5 m (which corresponds to an increase in ice-sheet elevation) results in a median Δh that is 8.8 cm higher. A similar observation holds for the median absolute deviation of Δh. This dependency on the sign of the bias can be easily understood. The impact point is typically in the area where the range between the satellite and the terrain is smallest. Lowering the DEM and thereby increasing the range to the satellite hence result in a reduced number of DEM grid points within the search range ($r_{\text{end}} - r_{\text{begin}}$). If no points are found, the search range is adjusted. Applying a positive bias, on the other hand, will result in other parts of the terrain being within the search range.

Despite LEPTA's sensitivity to a potential bias in the DEM, however, the median and median absolute deviation of Δh remain lower than the other methods for negative biases up to -7.5 m. With a positive bias of 2.5 m, the median absolute deviation of Δh from LEPTA is approximately 8 mm higher than that from the point-based method. In Appendix 3.C, we present the results of a similar analysis to that shown in Figure 6. This shows that the impact of a potential bias in the DEM is largest on the western side of the LRM zone, resulting in vertical and horizontal offsets with mean values of up to 2 and 50 m and standard deviations of up to 3.5 and 700 m, respectively.

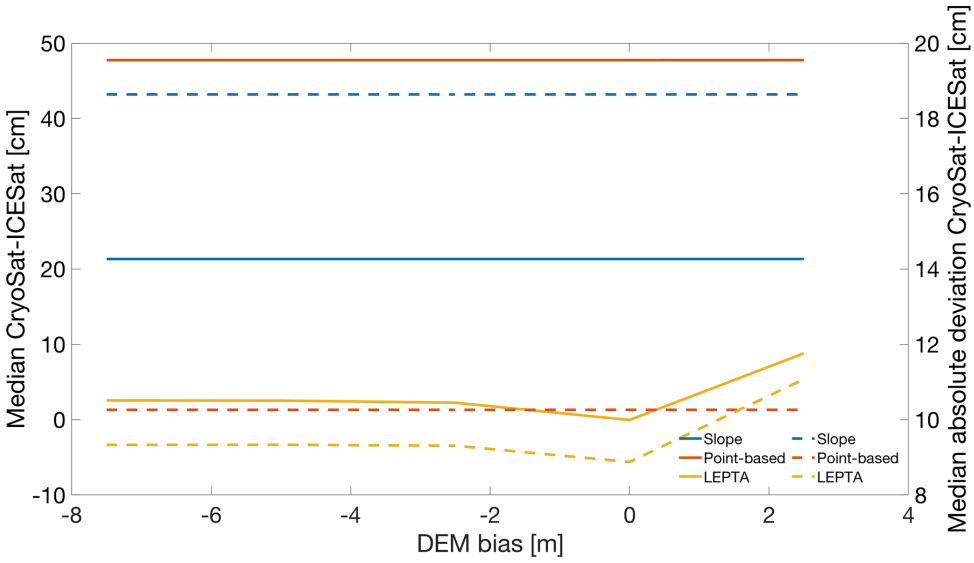

Figure 8: Median (left axis, solid curves) and median absolute deviation (right axis, dashed curves) of height differences between CryoSat-2 and ICESat-2 (Δh calculated with Equation 3.16) as a function of a bias in the DEM. Outliers are removed using 10th and 90th percentiles.

3.4.6. SENSITIVITY TO THE RESOLUTION OF THE DEM

Figure 9 shows the effect of changing the DEM resolution on the median and median absolute deviation of Δh for different slope correction methods. For both the slope and the point-based method, the smallest median Δh is obtained at a 2 km resolution. For the slope method, the median Δh increases from 0.21 to 0.30 m when the DEM resolution increases from 2 to 8 km. For the point-based method, the variation in median Δh for DEM resolutions between 100 m and 2 km is within the millimetre level. Lowering the resolution down to 8 km increases the median to 0.62 m. For LEPTA, the variation in the median Δh for DEM resolutions between 100 m and 1 km is within the millimetre level. For lower resolutions, the median Δh increases to 0.23 m (8 km resolution). The smallest median absolute deviations for the slope method (0.19 m) and the point-based method (0.09 m) are obtained at a 2 km resolution. For LEPTA, the smallest median absolute deviation is obtained when using a 1 km resolution, though the values between resolutions of 100 m and 2 km vary at the millimetre level. For resolutions lower than 2 km, the median absolute deviation for both the point-based method and LEPTA increases by approximately 10 cm. For the slope method, the increase is 6 cm.

3.5. DISCUSSION

The comparison with ArcticDEM and validation based on ICESat-2 shows that the presented LEPTA method outperforms the slope and point-based methods as well as the ESA L2I product in accuracy with lower median, mean, and median absolute deviations. Especially in the margin regions of the LRM zone, heights derived from LEPTA corre-

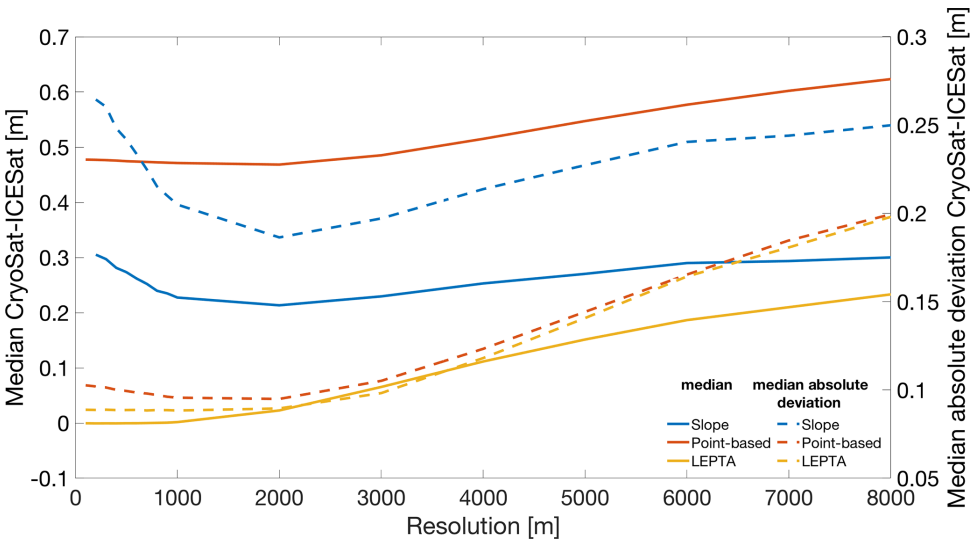

Figure 9: Median (left axis, solid curves) and median absolute deviation (right axis, dashed curves) of height differences between CryoSat-2 and ICESat-2 (Δh calculated with Equation 3.16) as a function of DEM resolution. Outliers are removed using 10th and 90th percentiles.

spond more closely to ICESat-2 height measurements compared to the slope method being used by ESA. This indicates that including leading edge information to determine the impact point results in an important improvement in the accuracy of CryoSat-2 LRM height estimations. By showing the importance of accurately determining the impact points over steeper margin areas, our results confirm earlier work of Levinsen et al. (2016) in the margin regions, where they also showed that the point-based method outperforms the slope method in median absolute deviation values. The improved performance of the point-based method and LEPTA method can be explained by the assumption of a constant slope within the footprint in the slope-based method, which results in a biased impact point further away from the satellite than the optimal location (Levinsen et al., 2016). An explanation for the improved performance of LEPTA over the point-based method can be found in the design of the method, which only takes into account areas that contribute to the rise of the CryoSat-2 LRM waveform leading edge (Figure 1).

Our results also show that the ESA L2I product outperforms our self-implemented slope correction method. This agrees with Levinsen et al. (2016), who attributed the different performance between ESA's Envisat Radar Altimeter 2 products and their self-implementation of the slope correction method to the Doppler slope correction step implemented in ESA L2I products (Blarel and Legresy, 2012) and differences in the DEM used. We must admit that at this stage an explanation for the difference we obtained is lacking. Detailed analysis (not shown in this paper) shows that the differences cannot be explained by the fact that in our study we use another DEM.

The first sensitivity analysis shows that in terms of bulk statistics, LEPTA is quite robust to the definition of the search range. Compared to ICESat-2, the change in the median is < 0.1 m for the interval over which we changed Δr, while the change in the me-

dian absolute deviation is at the millimetre level. Regionally, the impact may be larger. In particular, we observe changes of up to 1.46 m in the vertical and 231 m in the horizontal position of the impact points towards the margins of the LRM zone. In these areas, the mean and standard deviation of the leading edge width are larger. This, in turn, suggests using a larger Δr locally. The use of a spatially varying Δr is hence considered a potential further improvement of the method.

Increasing the OCOG retracker threshold lowers the height estimates for all methods. For both LEPTA and the point-based method, the horizontal position of the impact points does not change. This means that increasing the OCOG retracker threshold actually corresponds to increasing the depth of the radar return within the snowpack or firn. That is, the adopted threshold controls the observed penetration. Our results confirm that using a 20 % threshold gives on average comparable height estimates to ICESat-2. It is meanwhile worth noting that the probable scattering of ICESat-2 photons within the snowpack cannot be neglected (Smith et al., 2021).

Differently from the slope and point-based methods, LEPTA shows sensitivity to a bias in the DEM. The presence of a bias in the DEM does not affect the slope or the relative differences between the DEM points, which are key to the slope method and the point-based method, respectively. However, in the case of LEPTA, when the DEM heights are biased and the search range determined by the waveform leading edge is unchanged, the DEM points used to calculate the impact point of LEPTA are changed. According to Appendix 3.C, this bias mainly affects the margins of the LRM coverage. Overall these bias effects indicate that it is key to have up-to-date, time-varying DEMs when applying LEPTA to correct for slope-induced errors. Changes in the elevation over time will affect the applied correction as well as the location of the impact point. However, in the case of non-homogeneous elevation changes (which will result in slope changes) this also holds for the other methods.

Sensitivity to DEM resolution shows that the slope and point-based methods perform best with an intermediate DEM resolution (2 km), which is consistent with Levinsen et al. (2016). However, differently from Levinsen et al. (2016), who obtained stable performance for the point-based method between a 2 and 4 km DEM resolution, our results show that the performance of the point-based method is stable when the DEM resolution is finer than 2 km. This can be attributed to differences in (i) the study area, (ii) the altimeter data used, (iii) the used DEM to compute the corrections, and (iv) the reference data and methods for validation. In principle, the point-based method should perform better with a finer DEM resolution because it has the advantage of using full topography rather than assuming a constant slope, as used by the slope method. While Levinsen et al. (2016) attributed the optimal 2 km resolution of other methods to the radar altimetry's ability to resolve small-scale surface features, our results show that Δr used by LEPTA to define the pulse-limited footprint may have a different impact (e.g. asymmetry around $r_{20\%}$). Therefore, for future studies, fine-tuning the impact of Δr is still of high importance.

Moreover, our experiment focuses on the performance of LEPTA in the CryoSat-2 LRM-covered regions over the Greenland ice sheet; therefore it remains to be studied how it performs over more complex terrains and Antarctica. Since the topography and DEM quality in other regions of the Earth are different from those in Greenland, we ex-

pect LEPTA to perform differently, and the impact of Δr can also vary. This phenomenon provides more aspects for future works.

Finally, while we use CryoSat-2 Baseline D data, Baseline E is available. However, we do not expect changes that significantly affect the conclusions of this study as the main changes in Baseline E are associated with the sea ice products (European Space Agency, 2021).

3.6. CONCLUSION

Reducing slope-induced errors is a key correction algorithm when processing LRM data over ice sheets. To correct for this error, different methods have been developed to determine the impact point, which all rely on footprint assumptions: e.g. the slope method, which assumes a constant slope within the footprint, or the point-based method, which assumes a fixed footprint size to determine the impact point by minimising the mean distance. Each of these methods has shortcomings as they neglect either the actual topography or the actual footprint that can be estimated by a combination of the leading edge and topography. To overcome these shortcomings, we present a leading edge point-based (LEPTA) method that corrects for the slope-induced error by including the leading edge information of the radar waveform to determine the impact point. The principle of the method is that only the points on the ground that are within the range determined by a specific search range that contributes to the rise of the waveform leading edge are used to determine the impact point.

Different methods for correcting the slope-induced errors are used in this study using CryoSat-2 measurements over the Greenland ice sheet. Statistics show that the LEPTA method outperforms all other methods with the smallest median and variability in errors. The median difference between ICESat-2 heights and CryoSat-2 heights derived by LEPTA using a 20 % OCOG threshold and Δr = 1.25 m search range is 0.00 m. Spatially, LEPTA has a good improvement compared to the traditional slope method on the margins of the LRM-covered regions of the ice sheet as it derives heights generally more than 2 m closer to ICESat-2 measurements. LEPTA is sensitive to the definition of the search range and the bias in the DEM used to correct for the slope-induced error, mainly in the horizontal location of the impact points. However, comparison with ICESat-2 measurements generally shows centimetre-level sensitivity. Therefore, LEPTA is a method worth considering to obtain accurate height measurements with radar altimetry, especially in regions with complex topography.

APPENDICES

3.A. COMPARISON BETWEEN ICESAT-2 MEASUREMENTS AND ARCTICDEM

ICESat-2 ALT06 Land Ice Height data include a large amount of measurements between 1 January and 31 December 2019. Therefore, we compute the statistics of the differences between ICESat-2 heights (h_{ICE2}) and ArcticDEM interpolated to the corresponding locations (h_{DEMI}) per beam pair. In this process, data outside the CryoSat-2 LRM zone have been excluded. The statistics are summarised in Table 3.A.1. All differences are computed as $h_{\text{ICE2}} - h_{\text{DEMI}}$. The median difference between ICESat-2 and ArcticDEM for all beam pairs is 0.21 m, showing good agreement. The mean differences are around 5 cm.

Table 3.A.1: Difference between ICESat-2 measurements and ArcticDEM values interpolated to ICESat-2 locations.

Beam pair of measurements	vs. ArcticDEM [m]			
	mean	standard deviation	median	median absolute deviation
pair one	0.05	1.13	0.21	0.72
pair two	0.06	1.13	0.21	0.72
pair three	0.05	1.13	0.21	0.72

3.B. PROBABILITY DISTRIBUTION FUNCTIONS OF THE HEIGHT DIFFERENCES SHOWING SKEWNESS

Probability distribution functions of all methods are provided in Figures 3.B.1 and 3.B.2 to illustrate the underlying skewness in Table 1 and Figures 3 and 4 within the [-10, 10] m range. However, the skewness can also be affected by large outliers, as also shown in the figures. For the slope method, the DEM resolution is 2 km. For LEPTA, Δr is 1.25 m. For the slope method, point-based method, and LEPTA, the retracker is the OCOG retracker with a 20 % threshold.

3.C. IMPACT OF A BIAS IN THE ARCTICDEM ON THE 3D LOCATION OF THE LEPTA IMPACT POINTS

Figures 3.C.1 and 3.C.2 show the three-dimensional difference between using the original ArcticDEM and the vertically displaced DEM to correct for the slope-induced error. The vertical and horizontal differences are calculated using the difference between the location of impact points P_l of the biased DEM minus the location of the impact points

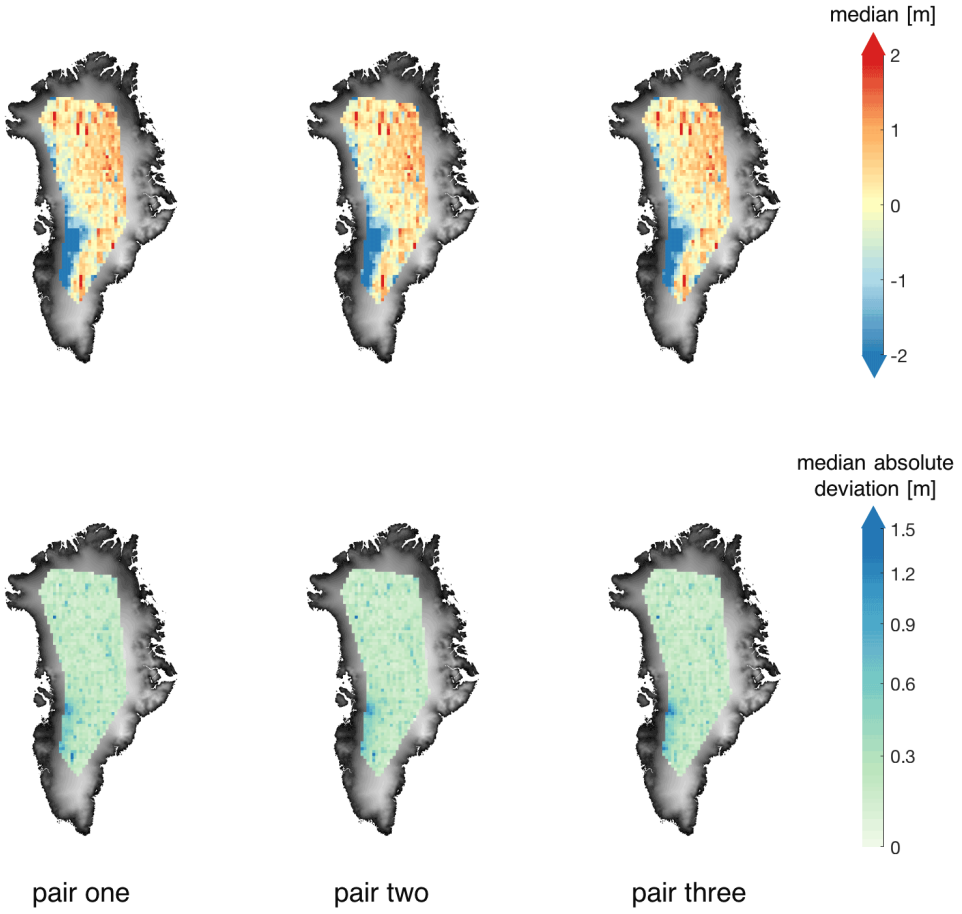

Figure 3.A.1: Spatial distribution of median and median absolute deviation of the height difference between each pair of ICESat-2 beams and ArcticDEM (tiled in 25 km × 25 km). The colours of the median absolute deviation plots are on a logarithmic scale.

of the original ArcticDEM. Figure 3.C.1 shows that when the DEM used has a negative bias, the corrected heights are higher, the horizontal locations on the western side of the ice sheet are in general biased towards the northeast, and the horizontal locations on the northeast side of the ice sheet are biased towards the southwest. Figure 3.C.2 shows an inverse pattern when the DEM shows a positive bias. On the interior of the ice sheet, however, the effects of the DEM biases are small.

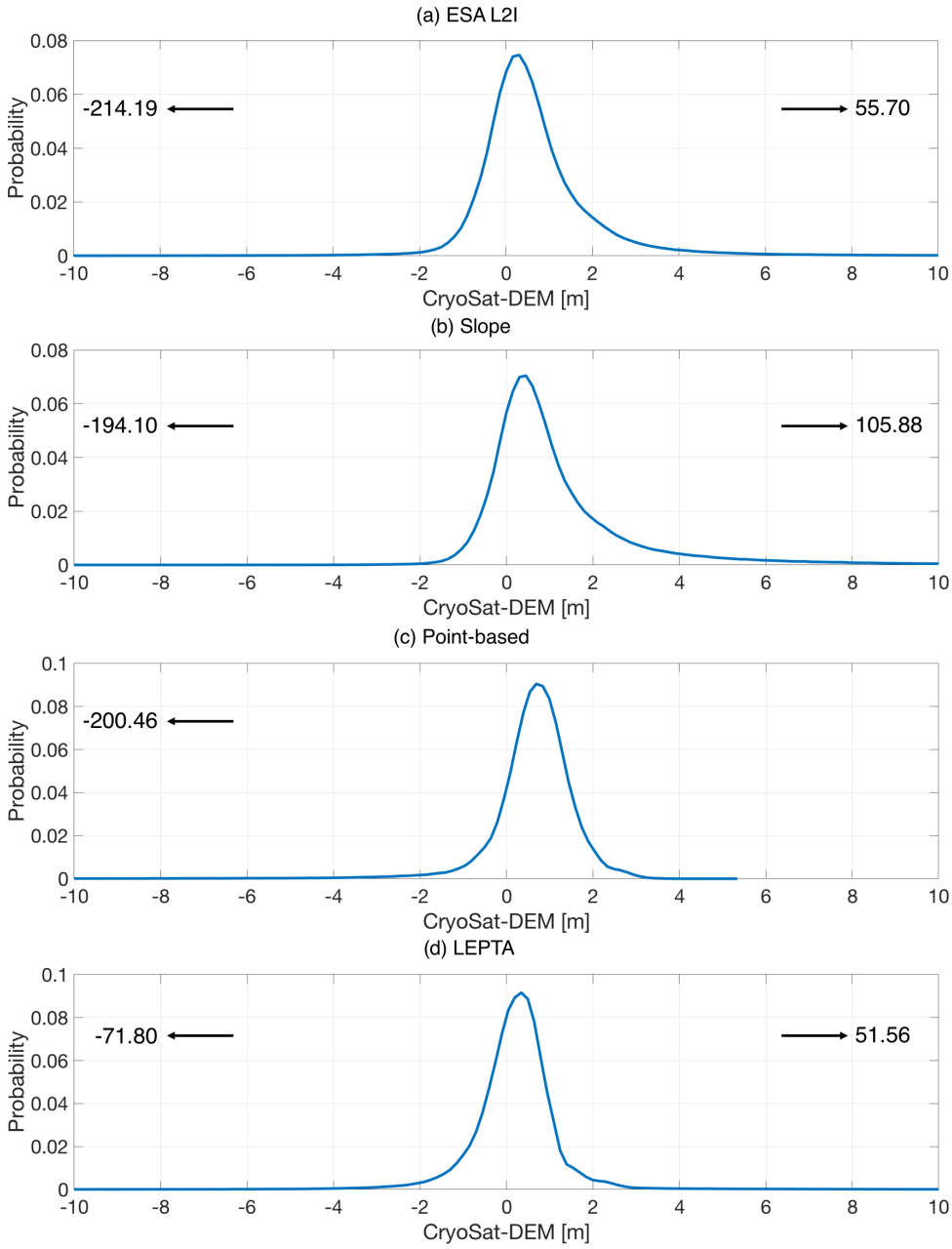

Figure 3.B.1: Probability distribution functions of heights between CryoSat-2 and ArcticDEM derived from (**a**) ESA L2I, (**b**) the slope method, (**c**) the point-based method, and (**d**) LEPTA centred between −10 m and 10 m. To clearly show minimum and maximum values (values displayed with arrows), the curves are not displayed in the same panel.

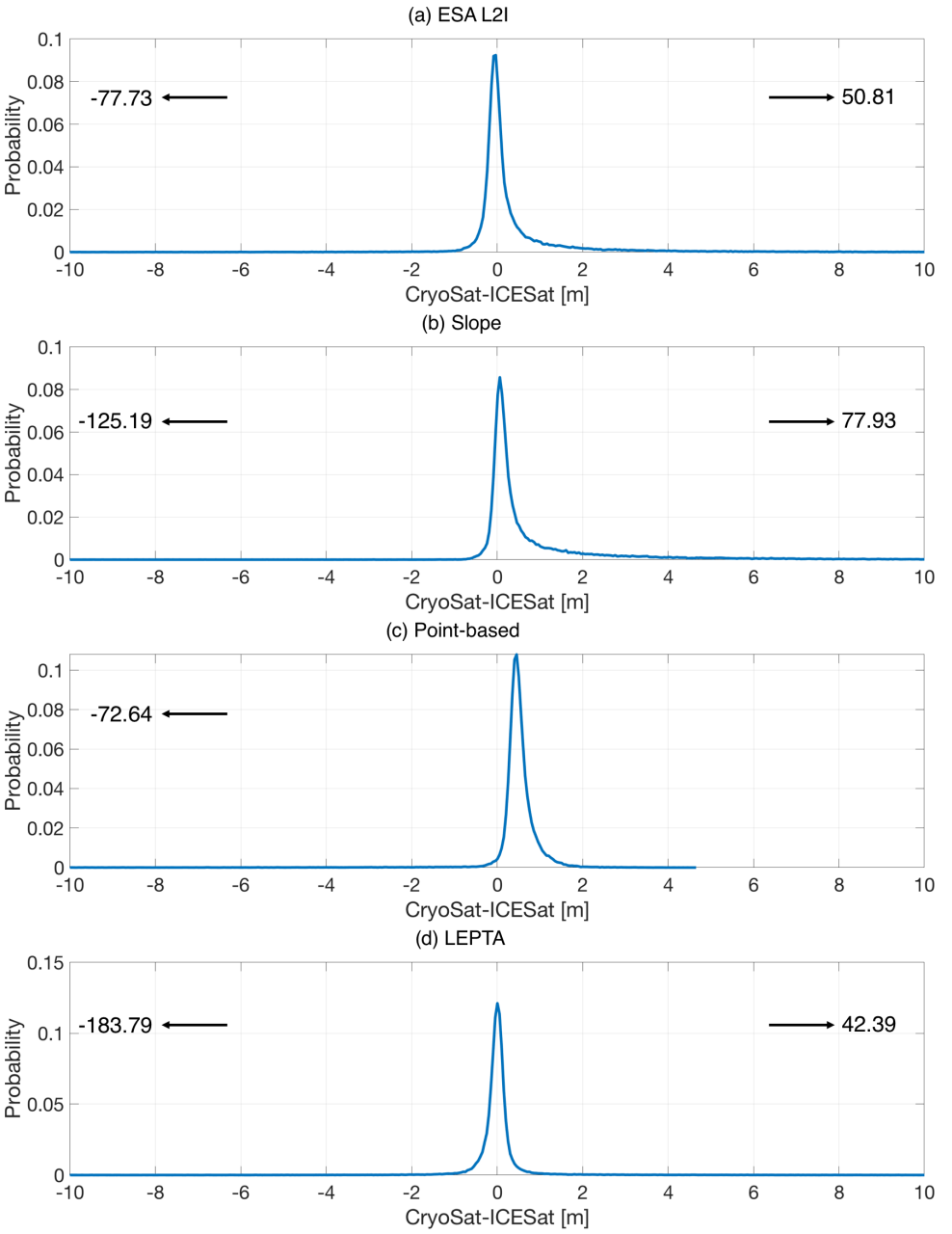

Figure 3.B.2: Probability distribution functions of heights between CryoSat-2 and ICESat-2 derived from (**a**) ESA L2I, (**b**) the slope method, (**c**) the point-based method, and (**d**) LEPTA centred between −10 m and 10 m. To clearly show minimum and maximum values (values displayed with arrows), the curves are not displayed in the same panel.

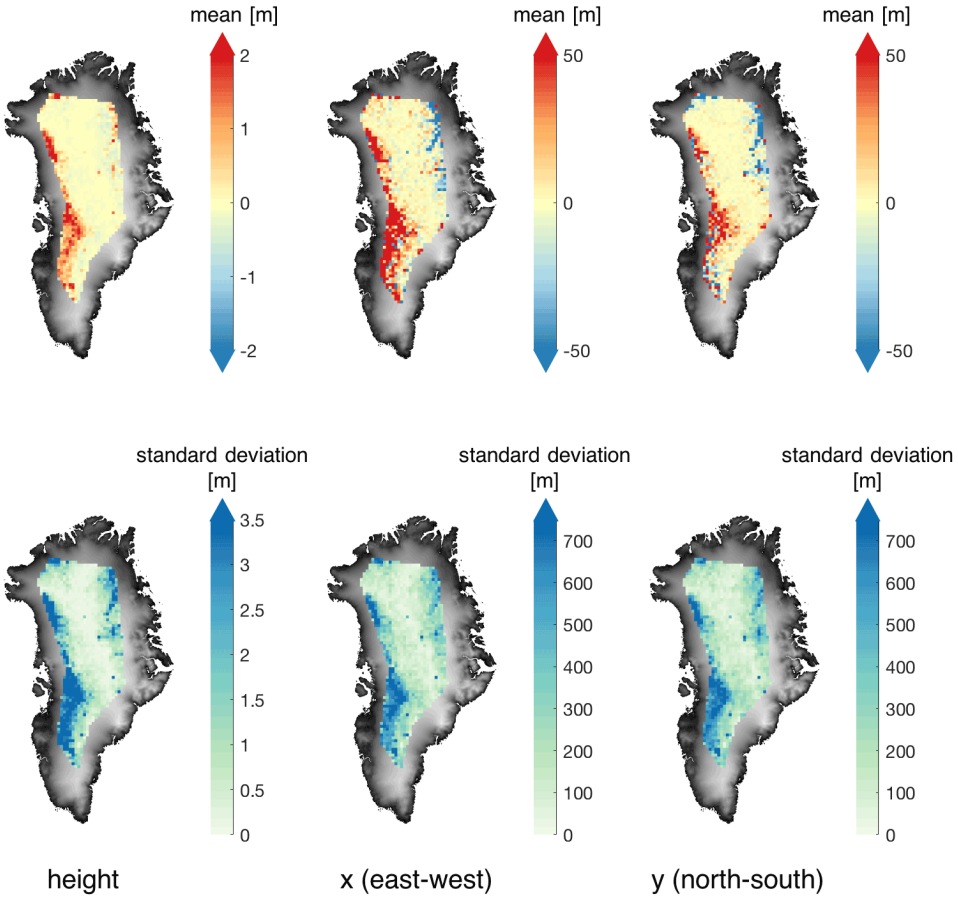

Figure 3.C.1: Mean and standard deviation of vertical and horizontal difference in derived impact point P_I between (i) using the DEM with a homogeneous vertical displacement $\Delta h_{\mathrm{DEM}} = -2.5$ m (Δh_{DEM1}) and (ii) using the original ArcticDEM ($\mathrm{DEM_{orig}}$). The mapped locations are based on the horizontal locations (x and y) derived from $\mathrm{DEM_{orig}}$, tiled by the 25 km × 25 km grid same as in Fig. 6.

BIBLIOGRAPHY

Abdalati, W., Zwally, H. J., Bindschadler, R., Csatho, B., Farrell, S. L., Fricker, H. A., Harding, D., Kwok, R., Lefsky, M., Markus, T., Marshak, A., Neumann, T., Palm, S., Schutz, B., Smith, B., Spinhirne, J., and Webb, C.: The ICESat-2 Laser Altimetry Mission, Proceedings of the IEEE, 98, 735–751, https://doi.org/10.1109/jproc.2009.2034765, 2010.

Adodo, F. I., Remy, F., and Picard, G.: Seasonal variations of the backscattering coefficient measured by radar altimeters over the Antarctic Ice Sheet, The Cryosphere, 12, 1767–1778, https://doi.org/10.5194/tc-12-1767-2018, 2018.

Aublanc, J., Moreau, T., Thibaut, P., Boy, F., Rémy, F., and Picot, N.: Evaluation of SAR

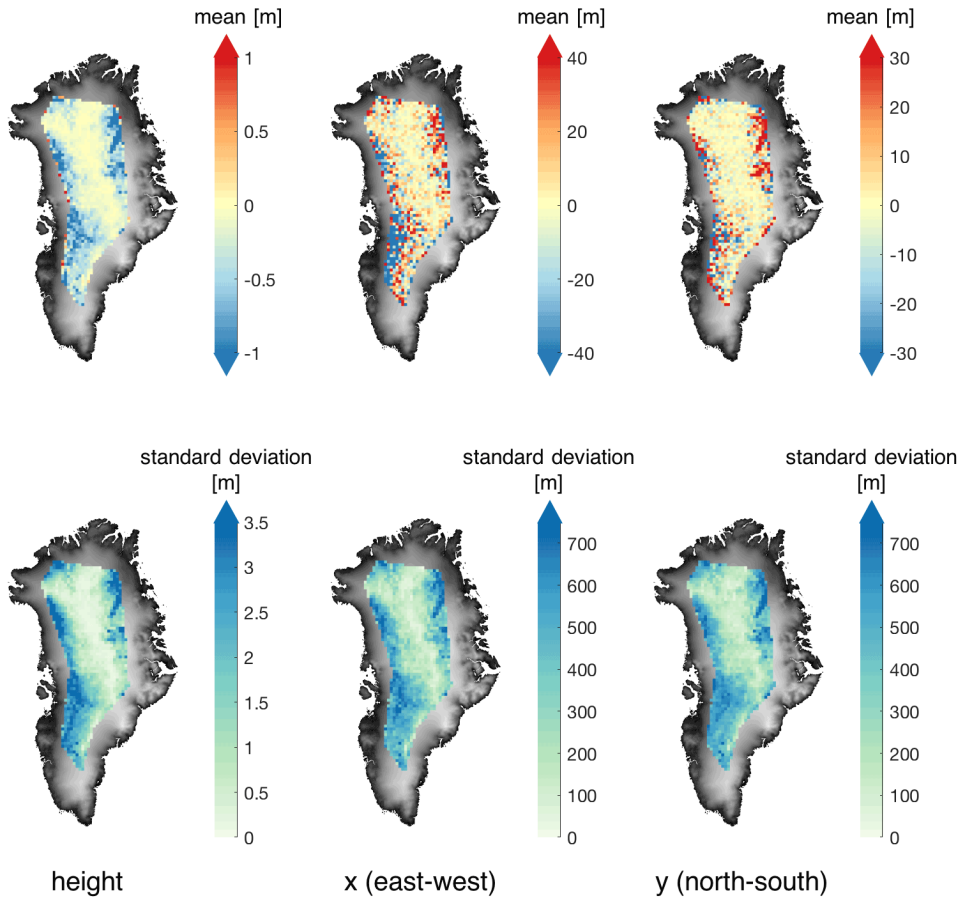

Figure 3.C.2: Mean and standard deviation of vertical and horizontal difference in derived impact point P_l between (i) using the DEM with a homogeneous vertical displacement $\Delta h_{\mathrm{DEM}} = 2.5$ m (Δh_{DEM1}) and (ii) using the original ArcticDEM ($\mathrm{DEM}_{\mathrm{orig}}$). The mapped locations are based on the horizontal locations (x and y) derived from $\mathrm{DEM}_{\mathrm{orig}}$, tiled by the 25 km × 25 km grid same as in Fig. 6.

altimetry over the antarctic ice sheet from CryoSat-2 acquisitions, Advances in Space Research, 62, 1307–1323, https://doi.org/10.1016/j.asr.2018.06.043, 2018.

Bamber, J. L.: Ice sheet altimeter processing scheme, International Journal of Remote Sensing, 15, 925–938, https://doi.org/10.1080/01431169408954125, 1994.

Blarel, F. and Legresy, B.: Investigations on the Envisat RA2 Doppler slope correction for ice sheets, in: European Space Agency-CNES Symp., Venice, Italy, 2012.

Bobach, T. A.: Natural Neighbor Interpolation - Critical Assessment and New Contributions, Ph.D. thesis, Technische Universität Kaiserslautern, URL `https://kluedo.ub.rptu.de/frontdoor/deliver/index/docId/2104/file/diss.bobach.natural.neighbor.20090615.pdf`, (Date Accessed: 23 August 2023), 2009.

Brenner, A. C., Bindschadler, R. A., Thomas, R. H., and Zwally, H. J.: Slope-induced errors in radar altimetry over continental ice sheets, Journal of Geophysical Research, 88, 1617, https://doi.org/10.1029/jc088ic03p01617, 1983.

Cooper, A.: Slope Correction By Relocation For Satellite Radar Altimetry, in: 12th Canadian Symposium on Remote Sensing Geoscience and Remote Sensing Symposium, IEEE, https://doi.org/10.1109/igarss.1989.577978, 1989.

Davis, C.: A robust threshold retracking algorithm for measuring ice-sheet surface elevation change from satellite radar altimeters, IEEE Transactions on Geoscience and Remote Sensing, 35, 974–979, https://doi.org/10.1109/36.602540, 1997.

European Space Agency: L1b LRM Precise Orbit. Baseline D, URL https://doi.org/10.5270/CR2-cbow23i, (Date Accessed: 25 February 2021), 2019a.

European Space Agency: L2 LRM Precise Orbit. Baseline D, URL https://doi.org/10.5270/CR2-k1o4pyh, (Date Accessed: 25 February 2021), 2019b.

European Space Agency: New Ice Baseline E and Near Real Time Processors, URL https://earth.esa.int/eogateway/news/new-ice-baseline-e-and-near-real-time-processors, (Date accessed: 18 April 2022), 2021.

Hai, G., Xie, H., Du, W., Xia, M., Tong, X., and Li, R.: Characterizing slope correction methods applied to satellite radar altimetry data: A case study around Dome Argus in East Antarctica, Advances in Space Research, 67, 2120–2139, https://doi.org/10.1016/j.asr.2021.01.016, 2021.

Helm, V., Humbert, A., and Miller, H.: Elevation and elevation change of Greenland and Antarctica derived from CryoSat-2, The Cryosphere, 8, 1539–1559, https://doi.org/10.5194/tc-8-1539-2014, 2014a.

Helm, V., Humbert, A., and Miller, H.: Elevation Model of Greenland derived from CryoSat-2 in the period 2011 to 2013, links to DEM and uncertainty map as GeoTIFF, https://doi.org/10.1594/PANGAEA.831393, 2014b.

Howat, I. M., Porter, C., Smith, B. E., Noh, M.-J., and Morin, P.: The Reference Elevation Model of Antarctica, The Cryosphere, 13, 665–674, https://doi.org/10.5194/tc-13-665-2019, 2019.

Hurkmans, R. T. W. L., Bamber, J. L., and Griggs, J. A.: Brief communication "Importance of slope-induced error correction in volume change estimates from radar altimetry", The Cryosphere, 6, 447–451, https://doi.org/10.5194/tc-6-447-2012, 2012.

Lacroix, P., Dechambre, M., Legrésy, B., Blarel, F., and Rémy, F.: On the use of the dual-frequency ENVISAT altimeter to determine snowpack properties of the Antarctic ice sheet, Remote Sensing of Environment, 112, 1712–1729, https://doi.org/10.1016/j.rse.2007.08.022, 2008.

Levinsen, J. F., Simonsen, S. B., Sorensen, L. S., and Forsberg, R.: The Impact of DEM Resolution on Relocating Radar Altimetry Data Over Ice Sheets, IEEE Journal of Selected Topics in Applied Earth Observations and Remote Sensing, 9, 3158–3163, https://doi.org/10.1109/jstars.2016.2587684, 2016.

Meloni, M., Bouffard, J., Parrinello, T., Dawson, G., Garnier, F., Helm, V., Bella, A. D., Hendricks, S., Ricker, R., Webb, E., Wright, B., Nielsen, K., Lee, S., Passaro, M., Scagliola, M., Simonsen, S. B., Sørensen, L. S., Brockley, D., Baker, S., Fleury, S., Bamber, J., Maestri, L., Skourup, H., Forsberg, R., and Mizzi, L.: CryoSat Ice Baseline-D validation and evolutions, The Cryosphere, 14, 1889–1907, https://doi.org/10.5194/tc-14-1889-2020, 2020.

National Snow and Ice Data Center (NSIDC): ATL06 release 005 known issues, URL https://nsidc.org/sites/nsidc.org/files/technical-references/ICESat2_ATL06_Known_Issues_v005.pdf, (Date accessed: 18 April 2022), 2021.

Noh, M.-J. and Howat, I. M.: Automated stereo-photogrammetric DEM generation at high latitudes: Surface Extraction with TIN-based Search-space Minimization (SETSM) validation and demonstration over glaciated regions, GIScience & Remote Sensing, 52, 198–217, https://doi.org/10.1080/15481603.2015.1008621, 2015.

Noh, M.-J. and Howat, I. M.: The Surface Extraction from TIN based Search-space Minimization (SETSM) algorithm, ISPRS Journal of Photogrammetry and Remote Sensing, 129, 55–76, https://doi.org/10.1016/j.isprsjprs.2017.04.019, 2017.

Porter, C., Morin, P., Howat, I., Noh, M.-J., Bates, B., Peterman, K., Keesey, S., Schlenk, M., Gardiner, J., Tomko, K., Willis, M., Kelleher, C., Cloutier, M., Husby, E., Foga, S., Nakamura, H., Platson, M., Wethington, Michael, J., Williamson, C., Bauer, G., Enos, J., Arnold, G., Kramer, W., Becker, P., Doshi, A., D'Souza, C., Cummens, P., Laurier, F., and Bojesen, M.: ArcticDEM, https://doi.org/10.7910/DVN/OHHUKH, 2018.

Remy, F., Mazzega, P., Houry, S., Brossier, C., and Minster, J.: Mapping of the Topography of Continental Ice by Inversion of Satellite-altimeter Data, Journal of Glaciology, 35, 98–107, https://doi.org/10.3189/002214389793701419, 1989.

Roemer, S., Legrésy, B., Horwath, M., and Dietrich, R.: Refined analysis of radar altimetry data applied to the region of the subglacial Lake Vostok/Antarctica, Remote Sensing of Environment, 106, 269–284, https://doi.org/10.1016/j.rse.2006.02.026, 2007.

Schröder, L., Horwath, M., Dietrich, R., Helm, V., van den Broeke, M. R., and Ligtenberg, S. R. M.: Four decades of Antarctic surface elevation changes from multi-mission satellite altimetry, The Cryosphere, 13, 427–449, https://doi.org/10.5194/tc-13-427-2019, 2019.

Slater, T., Shepherd, A., McMillan, M., Muir, A., Gilbert, L., Hogg, A. E., Konrad, H., and Parrinello, T.: A new digital elevation model of Antarctica derived from CryoSat-2 altimetry, The Cryosphere, 12, 1551–1562, https://doi.org/10.5194/tc-12-1551-2018, 2018.

Smith, B., Fricker, H. A., Holschuh, N., Gardner, A. S., Adusumilli, S., Brunt, K. M., Csatho, B., Harbeck, K., Huth, A., Neumann, T., Nilsson, J., and Siegfried, M. R.: Land ice height-retrieval algorithm for NASA's ICESat-2 photon-counting laser altimeter, Remote Sensing of Environment, 233, 111 352, https://doi.org/10.1016/j.rse.2019.111352, 2019.

Smith, B., Fricker, H. A., Gardner, A., Siegfried, M. R., Adusumilli, S., Csathó, B. M., Holschuh, N., Nilsson, J., Paolo, F. S., and the ICESat-2 Science Team: ATLAS/ICESat-2 L3A Land Ice Height, Version 4, https://doi.org/10.5067/ATLAS/ATL06.004, (Date Accessed: 8 July 2021), 2020a.

Smith, B., Hancock, D., Harbeck, K., Roberts, L., Neumann, T., Brunt, K., Fricker, H., Gardner, A., Siegfried, M., Adusumilli, S., Csathó, B., Holschuh, N., Nilsson, J., and Paolo, F.: Algorithm Theoretical Basis Document (ATBD) for Land Ice Along-Track Height Product (ATL06), Tech. rep., ICESat-2 Project Science Office, URL https://nsidc.org/sites/nsidc.org/files/technical-references/ICESat2_ATL06_ATBD_r004.pdf, 2020b.

Smith, B., Hancock, D., Harbeck, K., Roberts, L., Neumann, T., Brunt, K., Fricker, H., Gardner, A., Siegfried, M., Adusumilli, S., Csathó, B., Holschuh, N., Nilsson, J., and Paolo, F.: ICESat-2 Algorithm Theoretical Basis Document for Land Ice Height (ATL06) Release 005, URL https://nsidc.org/sites/nsidc.org/files/technical-references/ICESat2_ATL06_ATBD_r005.pdf, (Date accessed: 18 April 2022), 2021.

Wingham, D., Rapley, C., and D, G.: New Techniques in Satellite Altimeter Tracking Systems, in: Digest - International Geoscience and Remote Sensing Symposium (IGARSS), vol. ESA SP-254, pp. 1339–1344, Zurich, 1986.

4

ASSESSING SPATIO-TEMPORAL CHANGES IN GREENLAND FIRN PROPERTIES WITH SATELLITE ALTIMETERS

In recent decades, satellite radar altimetry has been widely used to assess volume changes over the Greenland Ice Sheet. Especially, melt events result in drastic changes in volume scattering of firn, which induces a pronounced change in parameters derived from radar altimetry. Due to the recent and increasingly frequent melt events over Greenland, the impacts of these events on the firn condition i.e. formation of ice lenses and reduction of firn air content, need to be better understood. This study therefore exploits the ability of long-term CryoSat-2 data in indicating changes in firn volume scattering, in order to assess the spatio-temporal firn condition variations in Greenland. More specifically, this study utilises the leading edge width (LeW) parameter derived from CryoSat-2 Low Resolution Mode (LRM), which has been proven to be the parameter most sensitive to changes in volume scattering, and assesses its variation between September 2010 and September 2024. With a combined analysis of remote sensing observations, in situ observations and outputs from regional climate models, our study demonstrates that the LeW drop induced by extreme melt events in the interior of Greenland experiences a gradual recovery, which can potentially be explained by new snow deposition. However, in many high-elevation regions of Greenland where firn layers were originally dry, due to the recently recurring extensive melt, the firn volume scattering does not fully recover to the original state before the 2012 melt, indicating the response of the Greenland ice sheet to a changing climate. Finally, our study also confirms the capability of using radar altimeter data to monitor changes in volume scattering properties of firn in the long-term.

4.1. INTRODUCTION

Over the recent decades, the Greenland Ice Sheet has experienced a notable increase in the frequency and intensity of melt events (Tedesco et al., 2011, 2013; Nilsson et al., 2015;

This chapter is under review in The Cryosphere. The preprint is available as: Li, W., Lhermitte, S., Wouters, B., Slobbe, C., Brils, M., and Fettweis, X.: Assessing spatio-temporal variability of firn volume scattering over Greenland with satellite altimeters, EGUsphere [preprint], https://doi.org/10.5194/egusphere-2024-3251, 2024.

Tedesco et al., 2016; Tedesco and Fettweis, 2020). These events are particularly prevalent in low-elevation regions, where they contribute to runoff towards the ocean. This runoff negatively impacts the surface mass balance (SMB) of the ice sheet and may lead to irreversible ice loss and sea-level rise (Lenton et al., 2008; Sasgen et al., 2012). In contrast, at higher elevations, meltwater can infiltrate and refreeze within the porous firn (Harper et al., 2012). This refreezing process releases latent heat, which accelerates firn compaction and diminishes the firn's capacity to store additional meltwater, consequently speeding up runoff from the ice sheet's interior (van den Broeke et al., 2016; Machguth et al., 2016; Vandecrux et al., 2019). Surface meltwater also drains towards the bedrock through crevasses and moulins, altering basal frictions and ice velocities (Zwally et al., 2002; Sundal et al., 2011; Meierbachtol et al., 2013). Furthermore, studies suggest that the runoff and melt will continue to increase (Vizcaíno et al., 2009; Huybrechts et al., 2011), making the determination of melt and refreezing in the firn layer over Greenland of utmost importance for understanding the ice sheet's overall stability and response to climate change (Heilig et al., 2018).

Remote sensing techniques are essential for long-term, spatio-temporally continuous monitoring of melt and refreezing events over the Greenland ice sheet, as in situ data are sparse in both space and time (Hall et al., 2008; Koenig et al., 2016; Castelao and Medeiros, 2022). Radar altimetry sensors, primarily used to measure surface height (changes) (Helm et al., 2014; Slater et al., 2018), can provide information on melt and refreezing events with much greater coverage. They do this indirectly, as refreezing impacts firn density, firn air content (FAC) and grain size (Vandecrux et al., 2019; Brils et al., 2022), which further influences the altimetry signals through changes in volume and surface scattering (Fahnestock et al., 1993; Adodo et al., 2018; Alley et al., 2018; Larue et al., 2021). The mechanism of surface and volume scattering in radar altimetry is illustrated in Ridley and Partington (1988): the satellite altimeter measures the time of a radar pulse travelling to the measured surface and back again, and records the returned echoes into a waveform (Davis and Moore, 1993). When the radar pulse intersects the surface, a circular region is illuminated. The area of the illuminated region and the corresponding returned power increases during the intersection. After the back of the pulse intersects the surface, the returned power attenuates. The part of the waveform with an increasing returned pulse is referred to as the leading edge, and the attenuating part is referred to as the trailing slope. With the presence of a rough surface or a certain volume within the penetration depth of the radar, the number of scatterers increases, hence the width of the leading edge increases (Ridley and Partington, 1988; Davis and Moore, 1993). Over the Greenland ice sheet, the high-elevation zone is typically the dry-snow zone, characterised by snow and firn with low density, small grain size and uniform crystals, whereas the low-elevation area consists of the percolation zone and the ablation zone, characterised by high-density, large-grain ice layers formed from melt and refreezing (Benson, 1960). Due to such distinctions between firn properties, the radar waveform leading edge widths (LeWs) in the high-elevation dry zone are dominated by volume scattering, and those in the low-elevation zones are dominated by surface scattering (Partington et al., 1989). Due to the difference in penetration abilities in firn between radar and laser altimeters, height measurements from laser altimeters can often be used as a reference surface to derive the penetration bias in radar altimeter height estimates, which in

turn indicates firn volume changes (Michel et al., 2014; Simonsen and Sørensen, 2017; Rutishauser et al., 2024).

Various studies have focused on deriving firn properties from the radar altimeter waveform. For example, the European Space Agency (ESA) CryoSat-2 satellite, equipped with a radar altimeter operating at Ku-band (13.575 GHz) frequency, has been employed to track the formation of ice lenses following melt events (Nilsson et al., 2015), to understand the impact of volume scattering properties on height estimations (Simonsen and Sørensen, 2017), and to derive surface snow properties such as roughness and density (Scanlan et al., 2023). Nilsson et al. (2015) and Simonsen and Sørensen (2017) showed that LeW is an indicator of volume scattering, while Nilsson et al. (2015) in particular observed the impact of the 2012 Greenland melt event and its subsequent refreezing on the parameters derived from radar waveforms, including LeW, trailing edge slope (TeS) and peakiness, backscatter intensity and height. The Simonsen and Sørensen (2017) study indicated that within the Low Resolution Mode (LRM) coverage, LeW could be effectively used to correct for height biases caused by volume scattering. Furthermore, Scanlan et al. (2023) developed a model using CryoSat-2 waveforms to derive surface roughness and density of snow in Greenland between 2013 and 2019. In addition, although the study was conducted over Antarctica, Michel et al. (2014) analysed the height differences between radar (ENVISAT) and laser (ICESat) altimeters to derive Ku-band radar penetration depths into firn and compared these height differences with LeW, providing insights into opportunities for similar approaches to study Greenland's firn.

Despite the advances in using altimetry to monitor Greenland's firn, the evaluation of firn properties has been limited to either periods without extensive melt (e.g. January 2013 to January 2019; Scanlan et al., 2023) or a short period right after the 2012 melt (e.g., up to 2014; Nilsson et al., 2015). The firn condition in a longer term, especially following the 2019 melt (Tedesco and Fettweis, 2020), needs to be better monitored. The availability of over a decade of CryoSat-2 data, offers an opportunity for long-term studies of Greenland's firn scattering properties. Following previous studies, we focus on the spatio-temporal variation in the LeW, which will be used to provide insights into the volume scattering of Greenland firn. Modelling results have shown that the LeW is sensitive to the volume scattering in the dry-snow zone of Greenland (Partington et al., 1989) as it decreases with an increasing density (Lacroix et al., 2008). However, within the coverage of CryoSat-2 data over Greenland, both dry-snow zone and percolation zone are present. It is important to distinguish the regions where volume scattering dominates from the regions where surface scattering dominates. For this purpose, we employ the surface roughness dataset derived by Scanlan et al. (2023) and assess the topography with ArcticDEM (Porter et al., 2018) as indications of surface scattering. As an indicator of volume scattering, we derive the height difference between ICESat-2 and CryoSat-2 referred to as laser-radar height offsets, due to a larger penetration depth of Ku-band radar than ICESat-2 green light (Michel et al., 2014; Smith et al., 2018). The penetration bias is typically 1–4 m over the Greenland Ice Sheet (Slater et al., 2018) depending on the firn status (e.g. dry, wet, refrozen) and the retracker (Chapter 3; Michel et al., 2014; Simonsen and Sørensen, 2017).

After determining the region with dominating volume scattering, we need validation datasets to demonstrate that the density increase within the Greenland firn result-

ing from melt–refreezing event can be associated with LeW decreases, in order to monitor the long-term firn-property variations with LeW variations. Three different types of datasets are adopted for this purpose. Recent developments in climate and firn models, such as the Modèle Atmosphérique Régionale (MAR) (Fettweis et al., 2011, 2017; Lambin et al., 2022) and the Firn Densification Model from the Institute for Marine and Atmospheric research Utrecht (IMAU-FDM v1.2G; Brils et al., 2022), provide spatially and temporally continuous firn property data. By comparing long-term LeW measurements with firn properties from climate and firn models, we analyse how spatial and temporal variations in firn properties affect LeW and to improve the interpretation of radar altimeter scattering properties. With the collaborative and continuously updating Surface Mass Balance and Snow on Sea Ice Working Group (SUMup) dataset (Montgomery et al., 2018; Vandecrux et al., 2024), in situ density measurements can be used to indicate the high-density ice formation at multiple locations. Finally, using data from NASA's Operation IceBridge (OIB) mission, i.e. data from the Multichannel Coherent Radar Depth Sounder (MCoRDS) and Airborne Topographic Mapper (ATM) laser altimeter, Rutishauser et al. (2024) assessed the relation between vertical offsets in the radar surface reflection and the vertical heterogeneity caused by melt events. This dataset can be used to provide the evidence of ice-lens formation from a different perspective, while supporting our analysis of advantages and disadvantages of our LeW approach.

The objective of this chapter is to assess long-term subsurface changes over the Greenland Ice Sheet. For this purpose, we present the spatio-temporal variations of LeW between 2010 and 2024 and of the difference between ICESat-2 and CryoSat-2 height estimations between 2019 and 2024 over the interior of Greenland. Subsequently, we assess whether such variations can reflect the variations in firn properties by comparing them with variations in modelled firn density and FAC provided by MAR and IMAU-FDM. The details of data and coverage are described in Section 4.2. The derivation of LeWs and height differences between ICESat-2 and CryoSat-2 will be detailed in Section 4.3. Sections 4.4 and 4.5 present, analyse and discuss the results. Finally, our main findings and outlook are presented in Section 4.6.

4.2. DATA

This section introduces the datasets used to assess how the CryoSat-2 time series can indicate the impact of recurrent melt–refreezing on Greenland's firn, with a focus on time series of LeW derived from CryoSat-2, and height difference between ICESat-2 and CryoSat-2. The time series of satellite data are complemented by reference datasets for a comprehensive interpretation of volume and surface scattering variations.

4.2.1. REFERENCE DIGITAL ELEVATION MODEL

We use a digital elevation model (DEM) to (i) correct the CryoSat-2 LRM height estimates for slope-induced errors with the LEPTA correction method (Chapter 3), (ii) compute the topography within each investigated grid cell, and (iii) divide the Greenland ice sheet into different elevation groups for the spatio-temporal analysis. In our study, we use the ArcticDEM, which is constructed from recent stereo satellite imagery (Porter et al., 2023) with a systematic error below 5 m (Noh and Howat, 2015). The ArcticDEM is available in

different resolution, ranging from 2 m to 1 km (Porter et al., 2023). Due to the limitation of the computational power of our processing programme, we use the 100 m resolution ArcticDEM to correct for slope-induced errors in deriving CryoSat-2 height estimates (Chapter 3). For the further spatio-temporal analysis, the interior of Greenland is horizontally divided into a 10 km ×10 km grid, consistent with the resolution of the reference firn model outputs. To conduct a Greenland-wide analysis of CryoSat-2 data time series, we divide the interior of Greenland into 10 elevation groups: 1 group below the elevation of 1500 m, 8 groups between 1500 m and 3000 m, and 1 group above 3000 m. As an indicator of the topography, the standard deviation of ArcticDEM elevations within each 10 km ×10 km grid cell is computed. This computation is performed using a 1 km × 1 km ArcticDEM. This choice is again a compromise between the limitation of the computational power and a sufficient number of data (100 points per grid cell) for computing the standard deviation and in turn for representing the topography.

4.2.2. CRYOSAT-2 OBSERVATIONS

CryoSat-2 operates in different modes: Low Resolution Mode (LRM), which is the typical pulse-limited radar altimeter used in the interior of ice sheets; Synthetic Aperture Radar (SAR) mode, which estimates the freeboard of ice flows in sea ice by enhancing along-track resolution using SAR technology; and SAR Interferometric (SARIn) mode, applied in coastal zones, where a second antenna is used to correct for cross-track slope (Kleinherenbrink et al., 2014). To study the interior of Greenland, we process CryoSat-2 LRM data acquired over the interior of the Greenland ice sheet in order to obtain LeW and height estimates (Nilsson et al., 2015; European Space Agency, 2023; Meloni et al., 2020). The acquisition period of the CryoSat-2 LRM Baseline E data we use in this study is between September 1, 2010 and September 30, 2024. We derive both LeW and height estimates of CryoSat-2 (h_C) from the waveforms using the Offset Centre of Gravity (OCOG) retracker (Wingham et al., 1986; Bamber, 1994; Gommenginger et al., 2010). To apply the retracker, the waveforms are normalised based on their peak power. The amplitude of each waveform is then calculated as

$$\text{amplitude} = \sqrt{\sum_{n=1+\text{aln}_1}^{n=128-\text{aln}_2} y^4(n) \Big/ \sum_{n=1+\text{aln}_1}^{n=128-\text{aln}_2} y^2(n)} \tag{4.1}$$

where aln_1 and aln_2 are the number of aliased bins at the beginning and the end of the waveform, respectively. y is the value at bin n. The LeW in metres is computed from the normalised waveform as

$$\text{LeW} = \frac{1}{2} c \Delta t (b_{0.95} - b_{0.05}) \tag{4.2}$$

where $b_{0.95}$ and $b_{0.05}$ are the range biases corresponding to the bins where the normalised waveform power equals 0.95 and 0.05 times the OCOG amplitude, respectively (found with linear interpolation), c is the speed of light, and Δt is the waveform sampling interval (3.125 ns) of CryoSat-2 LRM.

The CryoSat-2 height estimates h_C are derived with a 50 % threshold. Such a high (50 %) threshold corresponds to the radar return within the firn and is expected to indicate the volume scattering of Ku-band radar in the firn layer (Chapter 3). To correct for

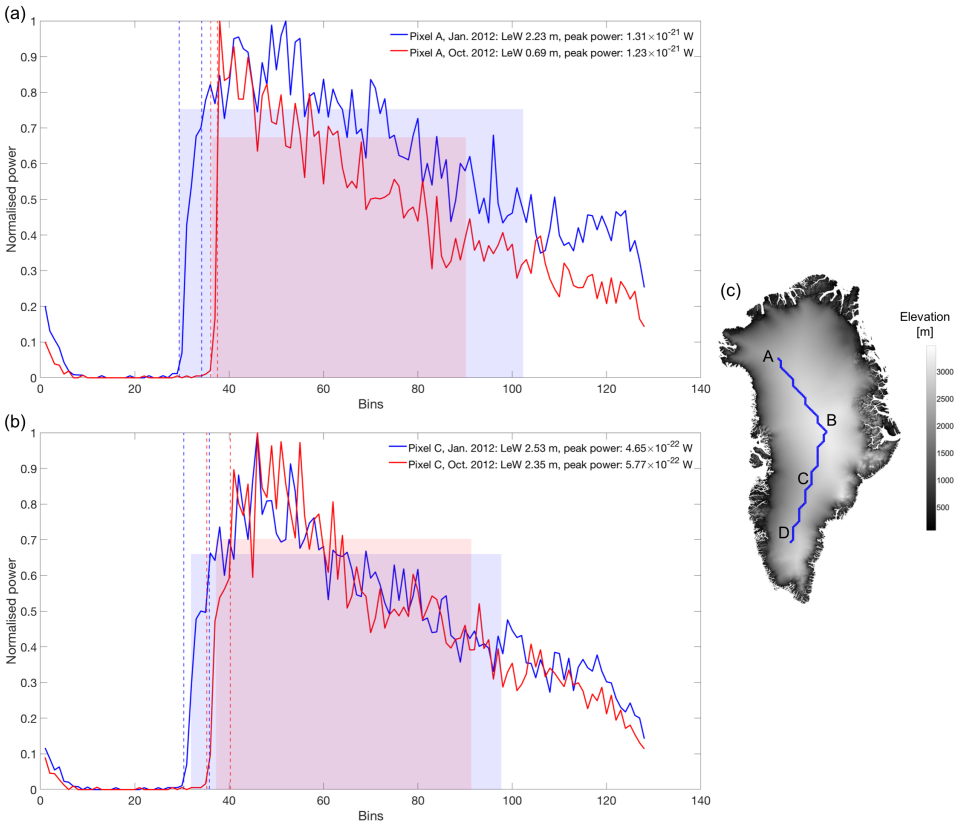

Figure 1: Normalised waveform examples ((a) and (b)) from different regions of interest in different periods. The shaded areas represent the amplitude and width of the OCOG box. The dashed lines corresponding to the waveform colours indicate $b_{0.95}$ and $b_{0.05}$ of each waveform. The computed LeW and the peak power of the original waveform are indicated in the legends. Pixel A (a) and pixel C (b) refer to the highlighted pixels in (c), along an investigated transect introduced in Section 4.3.

slope-induced errors in the h_C height estimation, we use the leading edge point-based (LEPTA) method from Chapter 3, as it utilises a high-resolution DEM (100 m ArcticDEM) and has the advantage to account for impacts of complex terrains.

To demonstrate the typical waveforms under different conditions and the corresponding LeWs, we provide examples of waveforms before (January) and after (October) the extensive 2012 melt event (Tedesco et al., 2013) in different regions of interest in Fig. 1: pixel A corresponds to the vicinity of the NEEM site as studied by Nilsson et al. (2015), where the difference between January and July 2012 shows reduced volume scattering due to the 2012 melt event. Pixel C corresponds to the region with constantly high surface roughness as derived by Scanlan et al. (2023), where a rougher surface typically corresponds to a higher LeW and less pronounced differences before and after the melt, potentially due to the dominant role of surface scattering from a constantly rough surface.

The derived LeWs are grouped into grids with the aforementioned (Section 4.2.1) 10 km×10 km resolution. The grid is used to observe the LeW variations along a north-south transect as well as to perform a Greenland-wide analysis of LeW variations, based on 10 different elevation groups.

4.2.3. ICESAT-2 OBSERVATIONS

To assess the volume scattering variation of CryoSat-2, we derive the height variation of CryoSat-2 with respect to a reference surface height as a measure for volume scattering properties; the ICESat-2 L3A Land Ice Height (ATL06) product Version 6 (Smith et al., 2023a) is hence used as the reference surface. ICESat-2 uses the Advanced Topographic Laser Altimeter System (ATLAS) with laser at a 532 nm wavelength (Abdalati et al., 2010). The along-track resolution of ATL06 product is ~ 40 m (Smith et al., 2023b), and the geolocation bias is less than 10 m (National Snow and Ice Data Center (NSIDC), 2021). In this study, we use ATL06 between January 1, 2019 and September 30, 2024 to obtain ICESat-2 heights (h_{ICE2}) for each CryoSat-2 point (h_C). The ATL06 data do not have a fixed or regularly gridded resolution, therefore we use a natural-neighbour interpolation to obtain ICESat-2 heights (h_{ICE2}) at each CryoSat-2 point (h_C). For each CryoSat-2 point, the ICESat-2 points within 50 m and acquired within the same month are selected for this interpolation. The selection of the 50 m search range aims to search for the ICESat-2 points that best correspond to the height at the CryoSat-2 impact point (Chapter 3), which is also similar to the crossover principle from Michel et al. (2014), while preserving sufficient amount of corresponding data pairs. Over a sloping terrain, extra height differences between h_C and h_{ICE2} can be caused by potential topography differences within the 50 m distance. To correct for this topography-induced difference, we bi-linearly interpolate (due to the regular resolution) the reference DEM (100 m ArcticDEM) to both the CryoSat-2 (h_{DEMC}) and ICESat-2 (h_{DEMI}) locations; hence, the differences between the ICESat-2 and CryoSat-2 heights (Δh) is calculated as

$$\Delta h = h_{\text{ICE2}} - h_C - (h_{\text{DEMI}} - h_{\text{DEMC}}) \tag{4.3}$$

Within the investigated time period, there are approximately 1.87×10^7 h_C points in total. The concurrent search of ICESat-2 point within 50 m radius per CryoSat-2 measurements results in approximately 4.53×10^5 Δh values in total (Section 4.4.1).

4.2.4. FIRN MODELS

To support the interpretation of the altimeter-derived parameters (LeW and Δh), we use firn density, melt water content (MWC) and firn air content (FAC) from two different regional climate and firn models, the Modèle Atmosphérique Régional (MAR, Section 4.2.4) and IMAU Firn Densification Model (IMAU-FDM, Section 4.2.4) respectively.

MODÈLE ATMOSPHÉRIQUE RÉGIONAL (MAR)

Layered firn densities and melt water content (MWC) over the study period are obtained from the version 3.14 Modèle Atmosphérique Régional (MAR) forced by the ERA5 reanalysis (Fettweis et al., 2017; Lambin et al., 2022; Grailet et al., 2024). The MAR outputs have a spatial (horizontal) resolution of 10 km and a daily temporal resolution, whereas the vertical resolution of the snowpack varies in time between 10 cm close to the surface

to 5 m at the bottom of the snowpack. The MAR model resolves here the 20 first metres of snow only and the weighted average density of the top layers (a threshold based on Fig. 3) is calculated where the weight is the thickness of each firn layer (due to the uneven vertical resolution). The firn density profile can be used to infer the amount of volume scattering. For example, the presence of a refrozen layer (i.e. a layer with high density; Nilsson et al., 2015; Otosaka et al., 2020) prevents the penetration of the radar signal, hence reduces the volume scattering.

The MWC is used to restrict our analysis to non-melt conditions, in order to reduce the impact of meltwater production on Ku-band radar and 532 nm laser. When MWC> 0, meltwater is present in the firn layer, hence the altimeter-derived parameters. A nearest-neighbour interpolation is performed to identify the MWC values at each CryoSat-2 location.

To assess the timing and extent of melt–refreeze patterns, the meltwater production and refreezing outputs of MAR (in the unit of mmWE day^{-1}) are used as reference. To provide insights into volume scattering variations, the total snow height change (i.e. the snowfall accumulation) from MAR is adopted. We calculate the accumulated total snow height change as the sum of daily total snow height change from the time of the intensive melt (July, 2012; Nghiem et al., 2012) to September, 2024. The time series of these outputs are visualised in Appendix 4.A. To be consistent with CryoSat-2 time series, the monthly average density, melt and refreezing are computed from the daily data, and the monthly integration of snow height change is computed from the daily snow height change.

FIRN DENSIFICATION MODEL (IMAU-FDM)

Alternatively, firn density, MWC and FAC with a 10-day temporal resolution are obtained from the firn density model IMAU-FDM v1.2G (Brils et al., 2022). It is a Lagrangian 1D firn model which computes the evolution of the firn thickness, density, temperature and water balance. It uses a “bucket method" for computing meltwater percolation into the firn. Its ability to accurately model firn properties has been validated in Brils et al. (2022). At its surface, IMAU-FDM is forced by the output of the polar version of the Regional Atmospheric Climate Model (RACMO2; Noël et al., 2018). Results from the model are available between October 1957 and December 2020. Similarly to the MAR data, we averaged the density over the layers (the depth is determined based on Fig. 3).

The FAC is the vertically integrated porosity in the firn (Kuipers Munneke et al., 2015), which is in the unit of metres. While density is calculated over the top layers, the FAC is calculated for the entire firn column. FAC is the total porosity of firn, indicating the capability of the firn layer to retain meltwater (Vandecrux et al., 2019). Although the CryoSat-2 signals are restricted to observing only the top firn layers, we leverage the modelled FAC time series to assess whether the observed melt–refreeze patterns notably influence the broader firn conditions. The application of this dataset is two-fold. First, to understand whether the firn conditions greatly altered in the recent decades when CryoSat-2 data are available, we use IMAU-FDM firn density and FAC as a reference dataset to compare with both LeW and MAR density monthly time series between January 2011 and December 2020. Second, to learn about the most recent changes of the Greenland ice sheet with respect to previous decades, we derive a long-term time series (between 1961 and 2020) by computing the yearly average of the IMAU-FDM density and FAC. While FAC

increases with elevation and can have a large spatial variation, i.e. approximately 0 towards the margins and more than 20 m in the interior of the ice sheet, the juxtaposed FAC over the entire studied area shows pronounced spatial variation and little temporal variation. Therefore, the temporal variation needs to be enhanced with respect to the spatial variation in FAC. For this purpose, we remove the long-term mean of each pixel (using the same grids as the resampled CryoSat-2 LeW) from the time series. The monthly mean density and FAC are also computed to match the CryoSat-2 time series.

4.2.5. IN SITU DENSITY ACQUISITIONS

Besides the firn model data, we also use various available in situ density profiles from Vandecrux et al. (2024) at different locations to show the impact of melt events on firn layers. In situ measurements are helpful in providing insights into whether and where refrozen layers persist within the Greenland firn and hence support the interpretation of the LeW variations. We use available and published in situ densities in our analysis if: (i) the acquisition site is within the CryoSat-2 LRM coverage; (ii) the acquisition contains the 2012 or more melt layers to provide information on the existence and depth of refrozen ice layers, (iii) the acquisition is vertically continuous, instead of one measurement at a single depth. The adopted in situ measurements include the ones collected along a trajectory between NEEM and East Greenland Ice-core Project (EGRIP) (Schaller et al., 2016a), along the Expédition Glaciologique Internationale Au Groenland (EGIG) line (Otosaka et al., 2020), from Summit and Saddle stations (MacFerrin et al., 2022), from Greenland Traverse for Accumulation and Climate Studies (GreenTrACS; Lewis et al., 2019), ice cores from central west Greenland (CWG; Trusel et al., 2018) and from Vandecrux et al. (2023). The locations and corresponding densities are shown in Fig. 2.

4.2.6. STRATIGRAPHY AND ROUGHNESS DATA

In addition to the modelled firn properties and in situ densities, we use the vertical stratigraphy derived from Rutishauser et al. (2024) to understand the formation of melt-induced ice layers. We can also analyse the performance and sensitivity of the derived LeW to the melt events by comparing the LeW with the stratigraphy dataset. The stratigraphy is represented by the vertical offsets between the ice surface height obtained by the OIB ATM laser altimeter, and the 195 MHz OIB MCoRDS, acquired simultaneously between 2011 and 2019, computed as

$$dz = h_{laser} - h_{radar} \tag{4.4}$$

where h_{radar} is the height derived by picking the optimal peaks in MCoRDS surface returns, and h_{laser} is the mean height of all laser observations within MCoRDS' pulse-limited footprint. The obtained dz values correspond with firn stratigraphy (a low dz corresponds to a homogeneous vertical structure). Since dz increases with the vertical heterogeneity of the firn, an increase in dz indicates the formation of refrozen layers (Rutishauser et al., 2024). The dz dataset contains 15.5 million data points with an annual temporal resolution (Rutishauser et al., 2024).

We use the surface roughness dataset derived by Scanlan et al. (2023) to analyse under which circumstances the LeW variation is dominated by surface scattering, since LeW can also be affected by topography and surface roughness (Chapter 3; Legrésy and

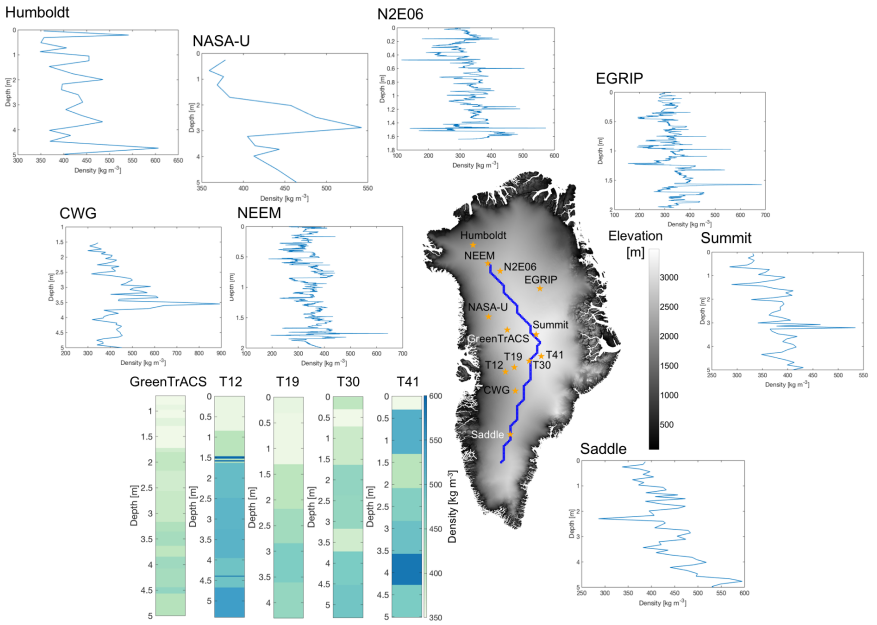

Figure 2: In situ densities and locations of measurements acquired from Schaller et al. (2016b); Otosaka (2020); Vandecrux et al. (2024). The background is the 1 km ×1 km ArcticDEM. Blue rectangles represent the transect of interest used in Section 4.3.

Rémy, 1997). The dataset was created by adopting the Radar Statistical Reconnaissance (RSR) technique in combination with a backscattering model. The temporal coverage of the dataset is between 2013 and 2019 with a monthly resolution.

4.3. METHODS

Since LeW variations are driven by both surface and volume scattering, especially melt and subsequent refreezing, we present a qualitative study of the relationship between LeW variations and melt–refreezing events.

4.3.1. ASSESSMENT OF LEW'S ABILITY TO INDICATE SCATTERING VARIATIONS

Since LeW variations can be affected by variations in both volume and surface scattering, we first perform a comparison with the available remote sensing data of stratigraphy and roughness (see Section 4.2.6).

First, to assess the potential of LeW in indicating the spatio-temporal variability in volume scattering, we compare LeWs with dz values derived by Rutishauser et al. (2024). Due to the large amount of dz points, we compute the mean dz values per OIB campaign over the 10 km ×10 km grid consistent to the resampled resolution of LeW. Finally, we mask out grid cells where either dz values or LeWs are not available.

Second, we compare the LeW data with the available roughness and topography data

as spatio-temporal LeW variations can also be affected by surface scattering, which is composed of surface roughness and topography (Chapter 3; Michel et al., 2014). On the one hand, we use the Scanlan et al. (2023) roughness data to represent the wavelength-scale surface roughness. We first resample the Scanlan et al. (2023) data to the 10 km×10 km grid same as the LeW. The time series analysis of LeW and roughness data is two-fold, where we juxtapose LeW and roughness data both (i) along a geographical transect connecting the NEEM site (Nilsson et al., 2015; Schaller et al., 2016a), Summit Camp and South Greenland and (ii) along 10 different averaged elevation bands between below 1500 m and above 3000 m (Section 4.2.1). On the other hand, we also compare the LeW data with the ArcticDEM standard deviation in order to assess the impact of macro-scale roughness due to topographic variation on LeW.

4.3.2. CORRELATION ANALYSIS BETWEEN LEW AND Δh

Since Δh is a typical indicator of radar altimeter penetration ability (Michel et al., 2014), we compute the correlation between all LeW and Δh estimates to assess to what extent the LeW variation is dominated by the penetration bias hence volume scattering. For this purpose, we adopt the 10 km×10 km grid introduced in Section 4.2.2. Within each grid cell, the Pearson correlation coefficients are computed between LeW and Δh for all valid Δh estimations throughout the entire studied period. To assess the reliability of the derived correlation between parameters, a p-value representing the significance of the correlation is computed for each correlation coefficient; the correlation coefficient is insignificant when the p-value exceeds 0.05 (Bermudez-Edo et al., 2018).

4.3.3. INTERPRETATION OF LEW'S SPATIO-TEMPORAL VARIATION

After the monthly gridded LeWs are obtained, we compute the average LeW between every non-melt season (October every year to April of the following year), and assess the difference in the averaged LeW between (i) every year and its previous year, and (ii) every year and 2010, respectively. With the first comparison, we asses the annual changes in volume scattering as melt events typically occur within summer season (June to August) (Tedesco and Fettweis, 2020). With the second comparison, we assess the LeW recovery since the extreme 2012 melt event (Tedesco et al., 2013).

To analyse the LeW variation with respect to the modelled firn properties, we perform the same two-fold time series analysis as proposed in Section 4.3.1, where the spatio-temporal variations of LeW, FAC, MAR densities and IMAU-FDM densities are juxtaposed and compared. The comparison is performed over two different time periods. The first one is between 2010 and 2024, when the CryoSat-2 Baseline E data are available. This comparison is purely to assess the capability of LeW to indicate firn processes. The second comparison is performed between 1960 and 2020, when IMAU-FDM data are available. This comparison is a supportive assessment to understand whether the firn processes are recent, and to provide insight and indications for future studies.

4.4. RESULTS

4.4.1. HEIGHT DIFFERENCE BETWEEN ICESAT-2 AND CRYOSAT-2

The spatial distribution as well as the overall probability distribution of Δh between January 2019 and September 2024 are visualised in Fig. 3. It can be observed that when the radar altimeter waveform is dominated by surface scattering, a 50 % threshold retracker can result in an underestimated or negative laser-radar offset (Davis, 1997). For the analysis where we compare and interpret the spatio-temporal variations with firn properties, we can observe from Fig. 3 that Δh is generally between 0 and 1.5 m on the interior of the ice sheet, therefore this range is used to select valid Δh that can be used as an indicator of volume scattering. Following Chapter 3, large Δh outliers below the 10^{th} and above the 90^{th} percentiles will be excluded for further analyses.

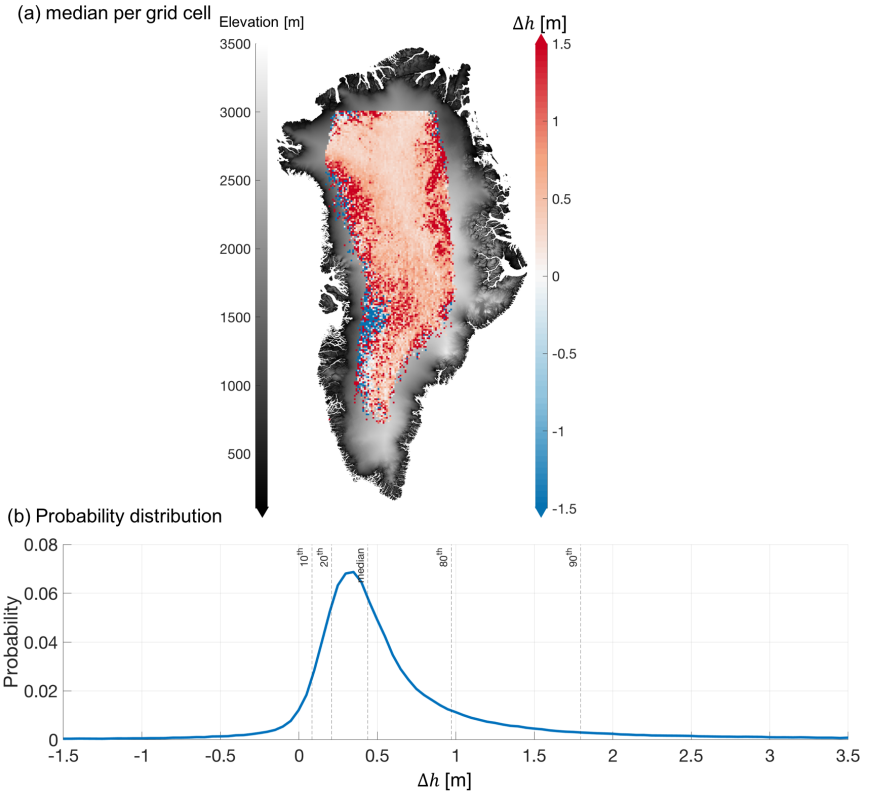

Figure 3: Statistics of height difference between ICESat-2 and CryoSat-2 (Δh). (a) is the median Δh per grid cell in a 10 km ×10 km grid; the background is the 1 km ×1 km ArcticDEM. (b) is the probability distribution function of Δh with percentiles labelled in vertical lines.

4.4.2. LEW TIME SERIES COMPARED WITH VERTICAL STRATIGRAPHY

Figure 4 presents the time series of vertical stratigraphy dz, alongside the time series of LeW. Both dz and LeW are generally high near the western margins, reaching up to

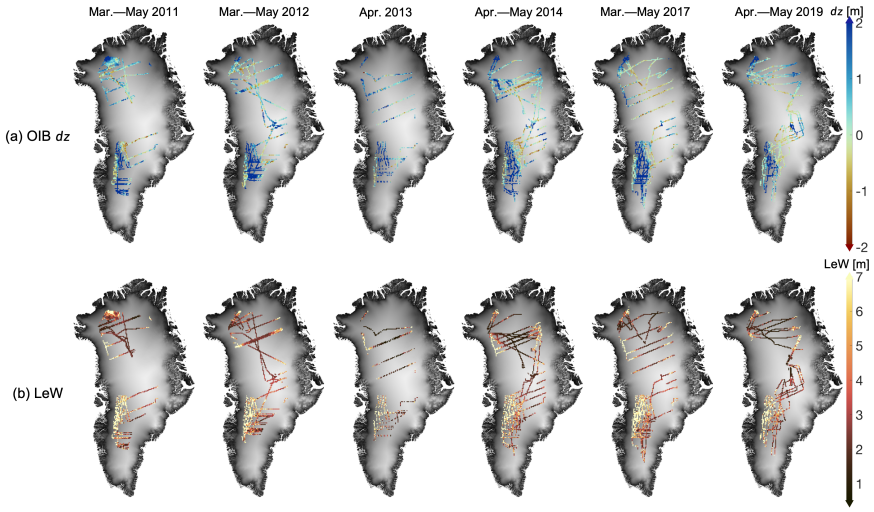

Figure 4: Upper: dz computed by Rutishauser et al. (2024); lower: LeW in the corresponding time of acquisition (indicated at the top of each column) as dz. The background is the 1 km ×1 km ArcticDEM.

around 2 m and 10 m, respectively. In contrast, both values are low in the high-elevation interior of the ice sheet, with dz ranging from −0.2 m to 0.1 m and LeW between 1 m and 4 m. However, in the southwest ablation zone, a low dz of around 0.1 m is observed, while LeW remains high at approximately 10 m.

Within the coverage of CryoSat-2 LRM data, dz is approximately 0.5 m higher in 2013 than in the earlier years, but decreases to lower values between 2014 and 2019. In contrast, the reduction in LeW persists over a longer period. During the period from 2013 to 2019, LeW values from CryoSat-2 are 1 m to 2 m lower compared to the period between 2011 and 2012.

According to Rutishauser et al. (2024), increases in dz are linked to the formation of ice slabs. The recovery of dz after 2013 suggests that the deposition of new snow between 2014 and 2019 covered the ice slabs beyond the MCoRDS' penetration depth. In our LeW time series, a reduction in LeW can be observed in 2013 within the high-elevation area, following the 2012 melt event. This phenomenon indicates that LeW reduces due to subsurface high-density layers that cause a reduced volume scattering (Partington et al., 1989). On the contrary to dz that recovered after 2014, our LeW time series does not show an immediate recovery. This observation is consistent with the layers with elevated firn densities shown in Fig. 2. At locations such as N2E06, EGRIP and T12, thin (approximately 0.1 m) high-density (more than 500 kg m^{-3}) layers persist at around 1.5 m depth in 2015 or 2017.

4.4.3. ASSESSMENT OF THE CONTRIBUTION OF SURFACE SCATTERING TO LEW VARIATIONS

The comparison of the LeW and surface roughness time series between 2013 and 2019, shown in Figures 5a and c, reveals a clear correspondence between these two variables.

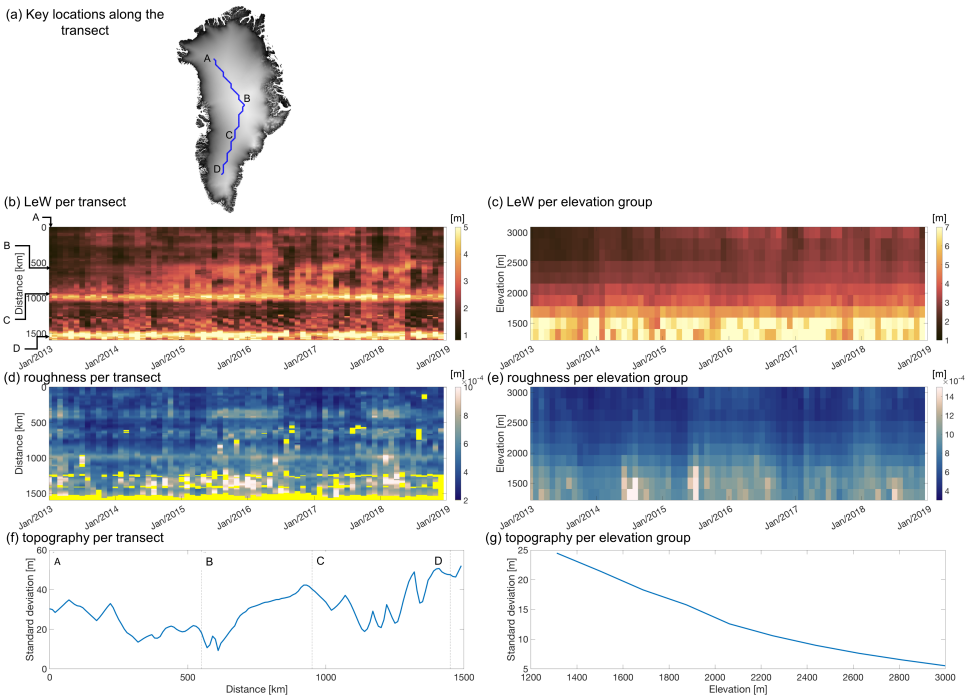

Figure 5: (a),(c),(e) LeW, surface roughness (represented by surface root mean square (RMS) height in unit of metres) and variability of the topography (represented by the standard deviation of ArcticDEM per 10 km pixel) along the north–south transect, respectively. A–D correspond to the inspected pixels highlighted in Fig. 2. (b),(d),(f) LeW, surface roughness and topography grouped by the 10 elevation bands, respectively. Orange colour indicates that the data are not available.

Zones of high surface roughness (greater than 6×10^{-4} m) coincide with elevated LeW values (greater than 6 m) around pixels C and D. The region south of pixel C corresponds to Fig. 4 of van den Broeke et al. (2023), where the modelled melt extent exceeds 10 kg m^{-2} yr^{-1}. Similarly, in Figures 5b and d, regions with high LeW (greater than 7 m) are associated with increased surface roughness (greater than 8×10^{-4} m) at elevations below 1800 m.

Figure 5e demonstrates that the spatial variation in topography follows a similar pattern to the LeW (Fig. 5a), with a high standard deviation of elevation per grid cell (greater than 50 m) around pixel D, where the roughness data is not available. Figure 5f shows that the complexity of the topography decreases with increasing elevation, a trend that mirrors the LeW pattern in Figure 5b, where LeW generally increases as elevation decreases.

This combined analysis of surface roughness and topography indicates that LeW tends to increase in areas where surface roughness is high and the topography is complex.

4.4.4. ASSESSMENT OF CORRELATION BETWEEN LEW AND Δh

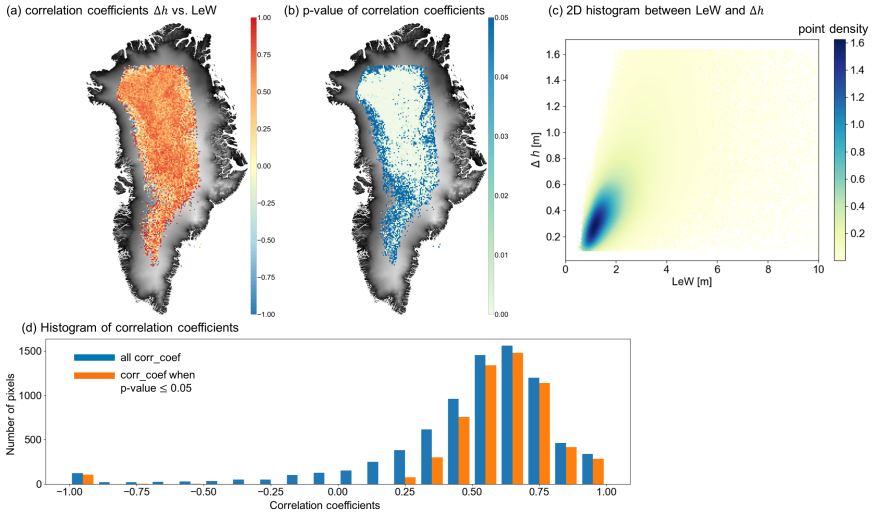

Figure 6: (a) Map of correlation coefficients between Δh and LeW, and (b) map of p-values of correlation coefficients between Δh and LeW. The background is the 1 km ×1 km ArcticDEM. (c) 2D histogram showing the relationship between all LeW and Δh points. The point density is calculated using Gaussian kernel estimation (Węglarczyk, 2018). (d) Histogram of correlation coefficients when all correlation coefficients are considered in blue, and when only significant correlation coefficients are considered (p-value≤ 0.05) in orange.

Figure 6 presents the correlation coefficients between the Δh and LeW time series for each 10 km×10 km grid cell. Overall, within the CryoSat-2 LRM coverage, LeW and Δh exhibit a generally positive correlation, with a median value of approximately 0.6. The histogram in Figure 6d further highlights that the correlation between LeW and Δh tends to be positive over the study areas.

The significance of these correlations, as indicated by the p-values, shows that the correlation coefficients are generally more significant in the interior of the ice sheet compared to the margins. When applying a threshold (0.05) on the p-value to focus on pixels with significance, the median correlation coefficient remains at around 0.6. The lower correlation and significance towards the margins can likely be attributed to higher surface scattering, which is caused by surface roughness and topographic variation (Legrésy and Rémy, 1997; Nilsson et al., 2015), as demonstrated earlier in Section 4.4.3. We interpret this observation as follows. When surface scattering dominates the variation of LeW, the effect of volume scattering cannot be reflected by LeW time series. The performance of ICESat-2 may be compromised due to the large slopes and rough surfaces (Smith et al., 2023c). Although LEPTA used for deriving height estimates from CryoSat-2 has been optimised based on topography, the performance towards the margins is still less ideal than the interior (Chapter 3).

The positive correlation between LeW and Δh suggests that within the interior of Greenland, as LeW increases, the laser-radar height offset also increases, indicating a rise in volume scattering. However, the correlation coefficients do not exceed 0.9 overall. This aligns with the findings of Nilsson et al. (2015), which showed that LeW was more

sensitive to ice-lens formation and volume scattering variations than Δh. Nevertheless, LeW was used as an indirect parameter to assess volume scattering, particularly when ICESat-2 data were not available.

4.4.5. ASSESSMENT OF INTER-ANNUAL LEW VARIATIONS

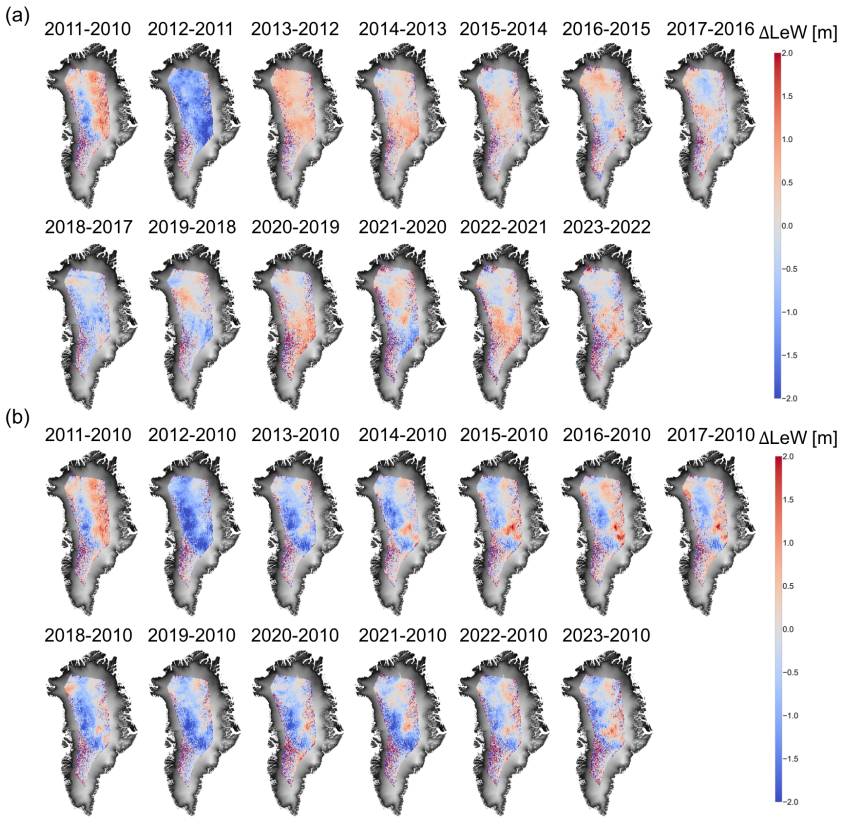

Figure 7: (a) Difference between the average LeW over the period of October to the following April of every year and the average LeW over the period of October to the following April of the previous year, and (b) difference between the average LeW over the period of October to the following April of every year and the average LeW over the period of October 2010 to April 2011.

Figure 7a presents the differences in averaged autumn—spring LeW between consecutive years. The indicated years are the years in which October occurs. It shows a notable reduction (greater than 2 m) in LeW over the interior of the ice sheet between 2011 and 2012, followed by a recovery between 2013 and 2015, with an increase of approximately 0.5 m. This initial reduction in 2011—2012 indicates a decrease in volume scattering, corresponding to the extreme melt event and subsequent ice-lens formation in 2012 (Tedesco et al., 2013; Nilsson et al., 2015). The recovery between 2013 and 2015 suggests a return to stronger volume scattering, likely due to new snow deposition hence the downward movement of ice lenses (Rennermalm et al., 2021).

Similarly, between 2018 and 2019, LeW experiences another minor drop of about 1 m, which coincides with the early melt observed in April and May 2019 (Tedesco and Fettweis, 2020) and the strong melt events between June and December 2018 that reduced volume scattering. Between 2019 and 2023, LeW increases and decreases alternately occur over the northern and southern parts of the interior of Greenland.

Figure 7b compares the average LeW (from October to the following April) of each year with the average LeW between October 2010 and April 2011, highlighting long-term variations relative to the extreme melt year of 2012. All years show a negative difference in the interior to western side of the ice sheet, except for the difference between 2010 and 2011, indicating that after the 2012 melt, LeW does not fully recover. It remains approximately 1.5 m below 2010 levels in the centre-west of the ice sheet. The area with negative values (i.e., no LeW recovery since 2012) shrinks between 2013 and 2018, expands again in 2019, remains stable until 2021, and recovers again until 2023.

When combining Figs. 7a and b, a notable recovery in LeW since 2012 is evident. This recovery can be attributed to new snow deposition on top of the ice lenses, although it was interrupted by the melt event in 2019.

4.4.6. ASSESSMENT OF LEW TIME SERIES IN RELATION TO FIRN PROPERTY VARIATIONS

Figure 8 shows the monthly mean LeW, MAR density, IMAU-FDM density, and detrended FAC time series along the transect highlighted in Fig. 2. The most significant reduction in LeW in Fig. 8a aligns with the sharp decrease in 2012, also shown in Fig. 7.

In the pixels north of pixel C, the monthly mean LeW is generally high (above 3 m) before the 2012 melt event, after which it abruptly drops below 1.5 m and gradually recovers until 2018. Along with the LeW reduction in 2012, both the MAR and IMAU-FDM models show increased average densities in the upper 1.5 m due to refreezing (Fig. 4.A.1c). Since 2018, LeW has fluctuated around 2 m, with annual drops occurring each summer from 2018 to 2023. Although these yearly declines are not as prolonged as in 2012, they occur more frequently than before 2018. In 2019, the detrended FAC in these regions drops by approximately 0.2 m and remains lower than pre-2019 levels. The density also increases, remaining higher than pre-2012 levels. These observations align with Fig. 7, which shows that LeW in the interior of the ice sheet dropped after the 2012 melt event, gradually recovered between 2014 and 2019, and stabilised between 2019 and 2023, remaining about 1.5 m below 2010 levels.

In the pixels south of pixel C, the monthly mean LeW since 2010 does not show remarkable anomalies related to melt events (Fig. 4.A.1b). These pixels experience recurrent melting each year, as indicated by the density time series, which increase every summer. Densities in the southern pixels are also 10 kg m^{-3} to 100 kg m^{-3} higher than those in the north, and the drop-and-recovery pattern of FAC is more pronounced in the south. The regions around pixel C and pixel D exhibit consistently higher LeW values (greater than 6 m) than those between pixels C and D (2 m to 4 m).

Our interpretation of the LeW patterns suggests that in the region between pixels A and C, the snow was initially dry before the 2012 melt, resulting in LeW patterns dominated by large volume scattering. The 2012 melt and the subsequent refreezing reduced volume scattering, causing a drop in LeW. LeW gradually recovered as the refrozen layer

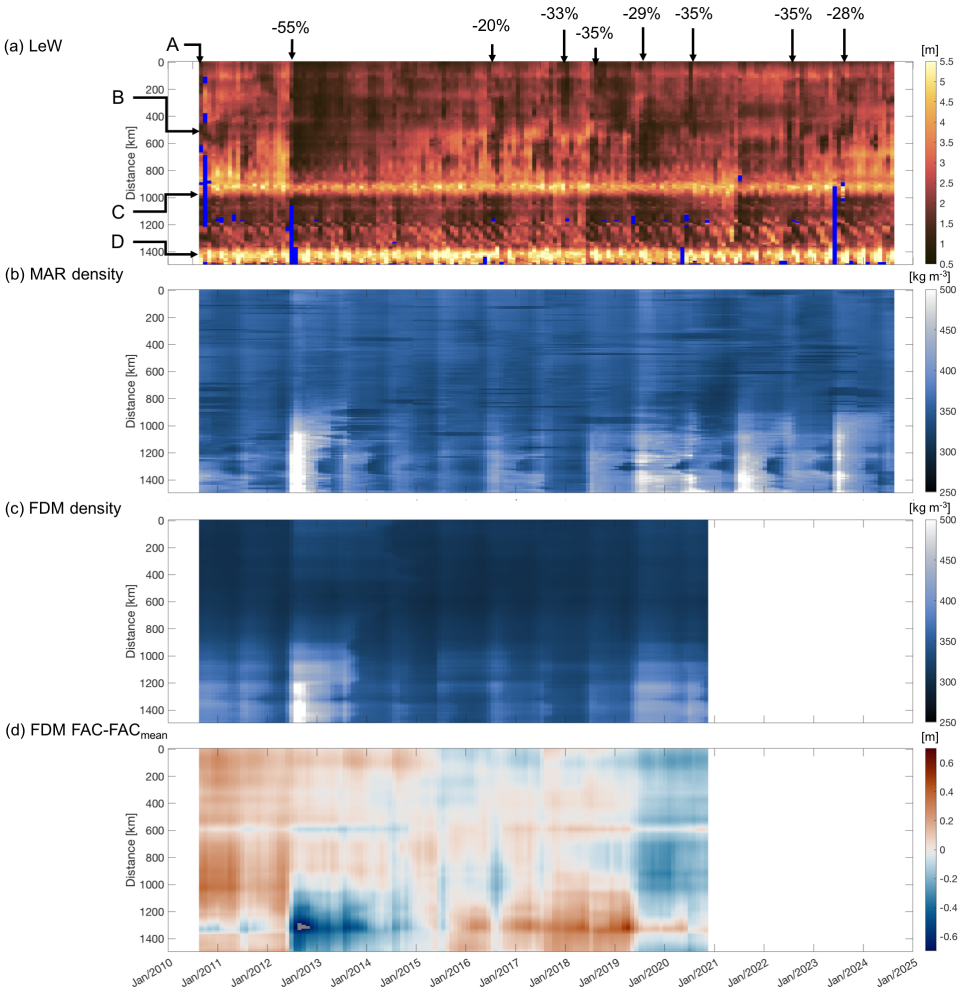

Figure 8: Monthly mean LeW, MAR density of the top 1.5 m of snow, IMAU-FDM density, and IMAU-FDM firn air content (FAC) time series per pixel along the transect visualised in Fig. 2. The FAC time series are processed subtracting the long-term mean of each pixel. The y-axes refer to the distance from the northernmost pixel. Arrows indicate the inspected pixels A–D. Large LeW decreases with respect to the previous month for pixels north of pixel C are labelled. Blue (a) or grey (b–d) colour indicates the values that are not available.

was buried, leading to the restoration of volume scattering. However, this recovery was interrupted by more recent and frequent melt events. In contrast, the regions south of pixel C show relatively stable LeW throughout the time series, as the melt–refreeze cycle occurs annually and the snow deposition rate is higher (shown in Fig. 4.A.1), causing less dramatic changes in volume scattering. Finally, the high LeW around pixels C and D is likely due to increased surface scattering caused by surface roughness and topography (Legrésy and Rémy, 1997), as discussed earlier in Section 4.4.3.

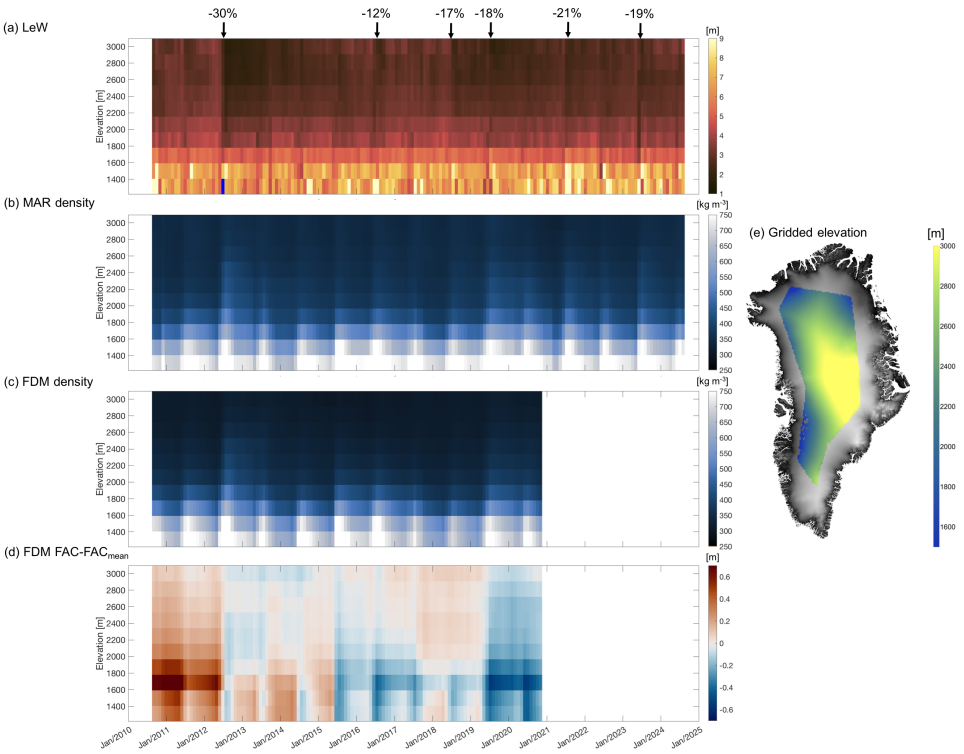

Figure 9: Time series of monthly mean LeW, density from MAR, density from IMAU-FDM, and detrended FAC from IMAU-FDM, grouped by a down-sampled (gridded) DEM. Blue (a) or grey (b–d) colour indicates that the data are not available. A map of the gridded DEM is provided on the right (e), with the original 1 km ×1 km ArcticDEM as background.

Figure 9 shows the variations in LeW, MAR density, IMAU-FDM density, and IMAU-FDM FAC (detrended by subtracting the long-term mean) between September 2010 and September 2024 for different elevation groups. In the low-elevation regions (below 1800 m), the LeW remains consistently high (around 9 m), with seasonal fluctuations of approximately 2 m during several years. For example, LeW decreases by about 2 m between June and August in 2013, in 2014, and in 2019. The density in these low-elevation areas also remains higher than in other parts of Greenland, with noticeable seasonal variations (densities increase in June). These density increases coincide with annual decreases in detrended FAC between June and August which correspond to the melt season.

Above the 1800 m elevation, a reduction in LeW is observed across all elevation groups following the 2012 melt event. The reduction is approximately 2 m in regions above 1800 m. This LeW reduction in mid-2012 corresponds to the widespread melting, increased densities in both MAR and IMAU-FDM models, and a decline in detrended FAC. Smaller increases in density and decreases in FAC were also observed in mid-2015, mid-2016, and mid-2019 above 1800 m, with a slight decline in LeW during mid-2016 and mid-2018.

From the time series, we also observe that in the 1800 m–2200 m range, the LeW recovery rate is faster than in regions above 2200 m (approximately 0.6 $m\ yr^{-1}$ versus 0.2 $m\ yr^{-1}$). By spring 2018, in areas above 1800 m, the LeW had nearly returned to pre-2012 levels (about 1 m lower). However, it temporarily dropped in mid-2018 by about 0.5 m and has since fluctuated around that level. This trend is consistent with the observations in Fig. 7b. Notably, our time series indicates that aside from the well-documented 2019 melt event (Tedesco and Fettweis, 2020) (characterised by density increases and FAC decreases), a change in volume scattering already occurred in mid-2018. This led to a slight decrease in LeW above 2200 m, suggesting reduced volume scattering. However, unlike other events, the LeW decrease in mid-2018 does not correspond to a density increase or FAC decrease in the models.

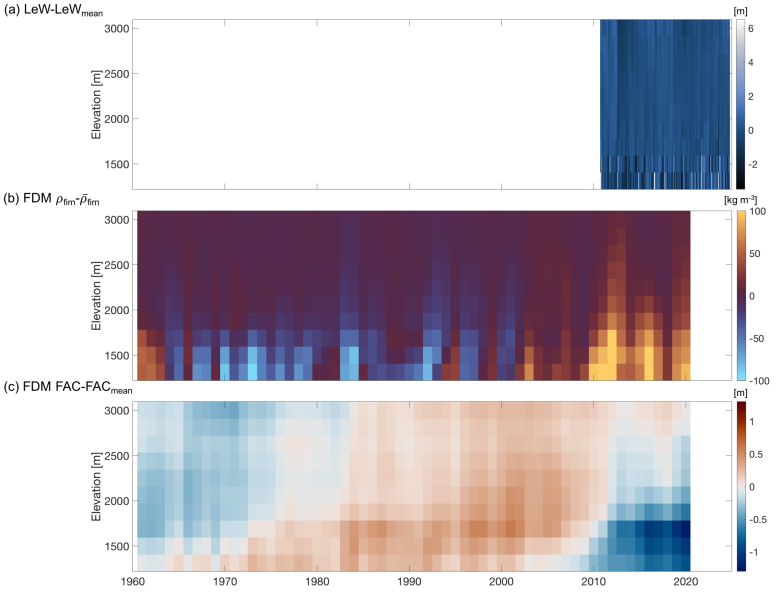

Figure 10: (a) Monthly mean LeW between Sept. 2010 and Sept. 2024 with long-term mean removed, grouped by gridded DEM. (b) Annual mean density between 1961 and 2020 from IMAU-FDM with long-term mean removed, grouped by gridded DEM. (c) Annual mean FAC between 1961 and 2020 from IMAU-FDM with long-term mean removed.

Finally, Fig. 10 displays the monthly mean LeW between 2010 and 2024, and the annually mean IMAU-FDM density and FAC time series from 1961 to 2020 for different elevation groups, where the long-term mean values are removed from each parameter to

visualise the contrast. This comparison aims to determine whether the changes in volume scattering observed in CryoSat-2 LeW show a recent instability in Greenland's firn. Above 2000 m, densities have increased by approximately 20 kg m^{-3} since 2012. In the past decade, FAC below 2000 m dropped considerably compared to earlier periods. In contrast, FAC values above 2200 m in the past decade are similar to those observed between 1975 and 1985, although they are lower than FAC values between 1985 and 2010. Between 2012 and 2020, FAC experienced slight drops and recoveries that correspond to the LeW pattern between 2012 and 2018, followed by another decline between 2018 and 2020, which also aligns with LeW trends. The comparison shows that, although LeW and the top 1.5 m density indicate large variations within the recent decade, the FAC does not indicate essential firn condition changes.

4.5. DISCUSSION

This study explores the capability of using LeW derived from CryoSat-2 waveforms to assess the spatial and temporal variations of the volume scattering properties of firn in Greenland. By comparing the LeW time series with the vertical stratigraphy from Rutishauser et al. (2024), we observed a slower recovery of firn following the 2012 melt event in the interior dry snow zone of Greenland compared to their findings. We explain the discrepancy as follows. CryoSat-2 LRM operates in a different manner from the OIB MCoRDS radar. While we used Δh and LeW to indicate the terrain topography, roughness and part of the firn layer that have an impact on radar altimeter's waveforms, the Rutishauser et al. (2024) study tracks the peak of the the reflected radar signal. Therefore, in the Rutishauser et al. (2024) study, a perfectly dry-snow condition results in $dz = 0$, indicating the radar reflection from the air-firn interface, while in our study, dry snow results in $\Delta h > 0$, indicating the height offset between laser and radar due to radar penetration. With the formation of an ice lens, dz from the Rutishauser et al. (2024) study increases, as another strong subsurface reflector is detected, while in our study, Δh and LeW immediately drop due to the reduction of Ku-band penetration ability. This distinction shows LeW's focus on volume scattering, which contrasts with the limitations of dz in accounting for topography, roughness, and timing corrections of the MCoRDS signal, as noted by Rutishauser et al. (2024). Our findings suggest that CryoSat-2 LeW, with its greater sensitivity to volume scattering, provides a more reliable tool for assessing firn recovery in the dry-snow zone, where surface scattering is minimal. The spatial and temporal continuity offered by CryoSat-2 is another advantage over OIB data, which is more spatially limited. CryoSat-2's Greenland-wide coverage enables a more comprehensive tracking of firn evolution, particularly in remote regions where OIB data may not be available, providing a more detailed overview of post-melt firn processes.

However, outside of the central dry snow zones, LeW is less effective in tracking melt–refreeze processes, as surface features such as roughness and topography begin to dominate its variability. This was confirmed through comparisons with ArcticDEM, firn models, and the data from Scanlan et al. (2023). To further validate LeW as a measure of firn changes, we compared it with laser-radar height offsets (calculated as the height difference between ICESat-2 and CryoSat-2). Overall, the relationship is similar to the conclusion of Michel et al. (2014), who proposed a linear function between LeW and penetration depth in flat regions of Antarctica. Our study, although not explicitly defin-

ing a “flat" region, delineated the interior of Greenland where the correlation between LeW and laser-radar height offsets is positive (around 0.6) and is significant ($p \leq 0.05$). By distinguishing areas where LeW is dominated by volume scattering from those dominated by surface scattering, our study provides a valuable framework for understanding firn response to melt events across different regions of Greenland.

This study is the first known demonstration of a Greenland-wide (within the CryoSat-2 LRM data coverage) LeW time series analysis, supported by two different firn models. The time series between 2010 and 2024 show that the 2012 melt event had a more prolonged impact than any other following melt events, resulting in a reduction in LeW that persisted until 2018, especially over the central-west Greenland. Recurrent melt events since 2018 have interrupted the firn recovery that was expected by Nilsson et al. (2015), underscoring the importance of monitoring these processes over long timescales. These findings highlight the value of CryoSat-2 LeW in assessing post-melt firn evolution, particularly at higher elevations.

When observed over a longer time scale (between 1960 and 2020), firn models indicate that the most pronounced firn changes, such as increases in density and decreases in FAC, occur below 1800 m elevation. At these lower elevations, LeW changes are less pronounced, showing a less than 1 m reduction compared to the long-term mean. In contrast, at elevations above 2250 m, LeW is comparably sensitive to the long-term effect of refreezing layer as FAC and density, while exhibiting higher sensitivity in 2018. This sensitivity suggests that LeW data could play a crucial role in refining firn models, especially for higher elevations, where existing models may underestimate the impacts of melt events on volume scattering.

Our findings indicate that in southern and low-elevation regions of Greenland, where surface scattering dominates and melt events are more frequent, LeW is less effective in capturing firn changes. Future studies could address these limitations by incorporating additional altimeter-derived parameters such as trailing edge slope (TeS), waveform peakiness, and backscatter coefficients, which are more sensitive to surface scattering processes (Nilsson et al., 2015). These parameters, combined with LeW, would offer a more complete picture of surface and volume scattering interactions.

To better simulate the complex contributions of surface and volume scattering, radiative transfer models (Adodo et al., 2018; Larue et al., 2021) can be employed. These models, when taking into account the varying viewing geometry of the satellite, can enable more accurate representations of how melt–refreeze processes (characterised by varying temperature, firn density, microstructure and grain size) impact firn properties.

The ongoing ICESat-2 mission should also continue to provide the opportunity to indicate Ku-band radar penetration abilities, which also allows to continuously monitor changes in subsurface firn due to melt–refreeze processes. This could complement CryoSat-2 data, offering a higher-resolution view of firn structure over time. Combining radar altimeter data from different frequencies can also help derive volume scattering information from different subsurface layers. According to Lacroix et al. (2008) who compared waveform parameters from S-band and Ku-band radar altimeters, the impact of surface scattering as well as from snow grain size decreases with an increasing radar frequency. According to Scanlan et al. (2023) who derived firn properties using both Ku-band and Ka-band radar altimeters, radar altimeters operating in a lower frequency

are sensitive to firn densities at a larger depth. For future dual-frequency radar altimeters, e.g. the Copernicus Polar Ice and Snow Topography Altimeter (CRISTAL) mission which operates in both Ku- and Ka-bands (Kern et al., 2020), the different penetration abilities and sensitivities to firn properties offer the potential of a multi-layered analysis approach. For a higher frequency such as Ka-band, the penetration depth is smaller, hence we expect a quicker recovery of LeW after a melt event than that of Ku-band. This different recovery rate can help future studies to locate the subsurface refrozen layers and derive accumulation rate. Such a multi-layered approach can be particularly useful in regions where surface and volume scattering overlap, offering more nuanced insights into firn changes.

To enhance future firn studies, LeW data can be integrated into firn models to improve predictions of melt impacts on volume scattering, particularly at higher elevations. Although not presented in this study, the up-to-date Goddard Space Flight Center (GSFC) firn model (Medley et al., 2022) and Glacier Energy and Mass Balance (GEMB) firn model (Gardner et al., 2023) can also be incorporated in the satellite time series analysis by both qualitatively indicating the presence of subsurface ice lenses and by quantitatively deriving firn properties with radiative transfer models. By using interdisciplinary approaches, we can deepen our understanding of how melt events affect firn properties over the long term, improving our ability to predict future ice sheet dynamics.

4.6. CONCLUSIONS

This study explored and demonstrated the possibility for using the LeW derived from CryoSat-2 to assess spatio-temporal changes in Greenland firn status caused by melt–refreezing events. While previous studies indicated a recovery pattern in LeW when new snow is deposited on top of the refrozen layers, our study further investigated whether this snow deposition can be observed with the help of LeW time series over the long-term. Our analysis showed that the recovery speed can be related to the elevation and new snow deposition. However, the recovery is hampered by more recent melt events (although not as severe as the 2012 event). In central-west Greenland, the LeW never recovered to the pre-2012 level; in regions where LeW managed to recover, new melt events resulted in new LeW reductions, which indicates a reduction in volume scattering hence a reduction in its capacity to store meltwater. Such alternation can also be confirmed using the long-term time series, which showed a decreasing LeW, an elevated density and a decreasing FAC in recent decades.

Finally, this study has demonstrated the reliability and limitations for using LeW from radar altimeter to understand the volume scattering variations and associated firn processes, paving the way for the study of subsurface firn processes in a changing climate. The use of a combination of CryoSat-2 and ICESat-2 height measurements can also contribute to the study of Ku-band penetration ability hence volume scattering.

APPENDICES

4.A. LEW AND MAR MELT, REFREEZE AND TOTAL SNOW HEIGHT CHANGE TIME SERIES

Figure 4.A.1 illustrates the time series of monthly mean LeW, MAR meltwater production, meltwater refreezing and accumulated total snow height change along the transect highlighted in Figure 2. The meltwater production and refreezing correspond to the density increases in Figure 8b. Figure 4.A.1a indicates that the overall decrease in LeW in 2012 corresponds to both the extensive meltwater production as well as refreezing. Furthermore, a slight LeW decrease in mid-2019 between pixels A and C also corresponds with the melt–refreezing event. By comparing Figure 4.A.1a and Figure 4.A.1d, we notice that north of pixel B shows a slower LeW recovery than between pixels B and C, which corresponds to a lower cumulative total snow height change (i.e snowfall accumulation) from the July 2012.

Similarly, we present the time series per elevation group in Figure 4.A.2. The melt–refreeze patterns correspond with the density increases in Figure 9b. However, differently from Figure 4.A.1a and Figure 4.A.1d, Figure 4.A.2a and Figure 4.A.2d do not show a high correspondence between LeW recovery and total accumulated snow: the total accumulated snow height from July 2012 shows the highest increase between 2014 and 2024 at around 2400 m elevation, while the fastest LeW recovery occurs between 1800 m and 2200 m. This discrepancy could be attributed to the significantly larger snow accumulation in the South of Greenland than the North, despite being at the same elevation.

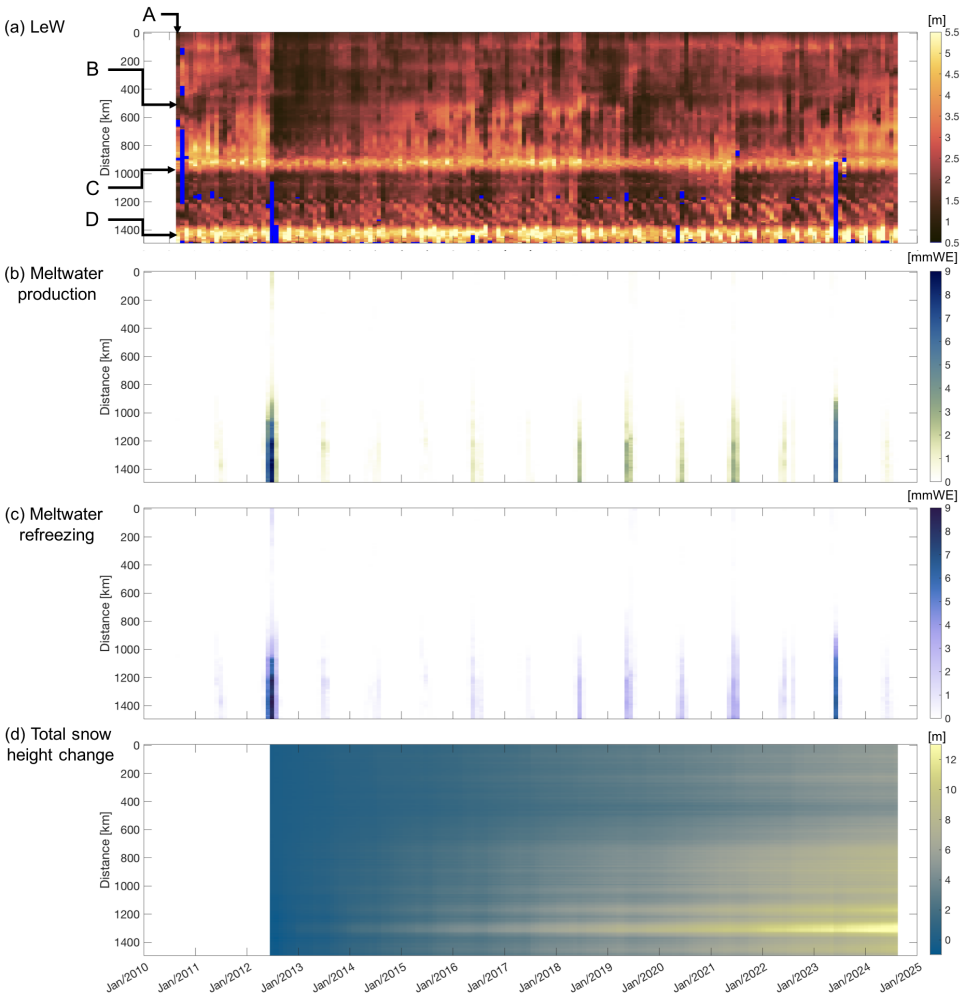

Figure 4.A.1: Monthly mean LeW, daily MAR surface meltwater production, daily MAR meltwater refreezing, and daily accumulated total snow height change (i.e. snow accumulation) from 12 July 2012 time series per pixel along the transect visualised in Figure 2. The LeW and MAR total snow height change time series adopt a diverging colour bar to enhance the contrast. The y-axes refer to the distance from the northernmost pixel. White colour indicates the values that are not available. Arrows indicate the inspected pixels A—D.

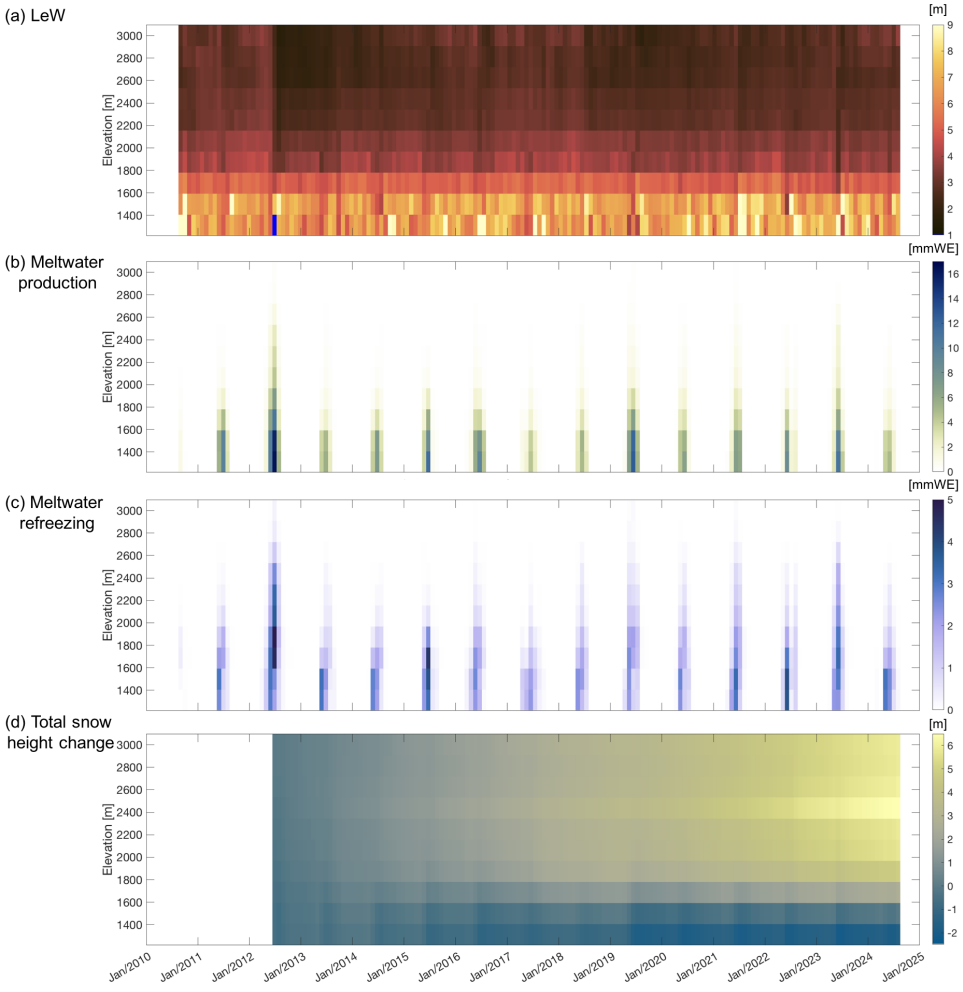

Figure 4.A.2: Monthly mean LeW, daily MAR surface meltwater production, daily meltwater refreezing, and daily accumulated total snow height change (i.e. snow accumulation) from July 2012 time series grouped by a down-sampled (gridded) DEM. The LeW and MAR total snow height change time series adopt a diverging colour bar to enhance the contrast. White colour indicates that the data are not available. A map of the gridded DEM is provided on the right, with the 1 km ×1 km Helm et al. (2014) DEM as background.

BIBLIOGRAPHY

Abdalati, W., Zwally, H. J., Bindschadler, R., Csatho, B., Farrell, S. L., Fricker, H. A., Harding, D., Kwok, R., Lefsky, M., Markus, T., Marshak, A., Neumann, T., Palm, S., Schutz, B., Smith, B., Spinhirne, J., and Webb, C.: The ICESat-2 Laser Altimetry Mission, Proceedings of the IEEE, 98, 735–751, https://doi.org/10.1109/jproc.2009.2034765, 2010.

Adodo, F. I., Remy, F., and Picard, G.: Seasonal variations of the backscattering coefficient measured by radar altimeters over the Antarctic Ice Sheet, The Cryosphere, 12, 1767–1778, https://doi.org/10.5194/tc-12-1767-2018, 2018.

Alley, K., Scambos, T., Miller, J., Long, D., and MacFerrin, M.: Quantifying vulnerability of Antarctic ice shelves to hydrofracture using microwave scattering properties, Remote Sensing of Environment, 210, 297–306, https://doi.org/10.1016/j.rse.2018.03.025, 2018.

Bamber, J. L.: Ice sheet altimeter processing scheme, International Journal of Remote Sensing, 15, 925–938, https://doi.org/10.1080/01431169408954125, 1994.

Benson, C. S.: Stratigraphic studies in the snow and firn of the Greenland ice sheet, Ph.D. thesis, California Institute of Technology, https://doi.org/10.7907/G7V2-0T57, 1960.

Bermudez-Edo, M., Barnaghi, P., and Moessner, K.: Analysing real world data streams with spatio-temporal correlations: Entropy vs. Pearson correlation, Automation in Construction, 88, 87–100, https://doi.org/10.1016/j.autcon.2017.12.036, 2018.

Brils, M., Kuipers Munneke, P., van de Berg, W. J., and van den Broeke, M.: Improved representation of the contemporary Greenland ice sheet firn layer by IMAU-FDM v1.2G, Geoscientific Model Development, 15, 7121–7138, https://doi.org/10.5194/gmd-15-7121-2022, 2022.

Castelao, R. M. and Medeiros, P. M.: Coastal Summer Freshening and Meltwater Input off West Greenland from Satellite Observations, Remote Sensing, 14, 6069, https://doi.org/10.3390/rs14236069, 2022.

Davis, C.: A robust threshold retracking algorithm for measuring ice-sheet surface elevation change from satellite radar altimeters, IEEE Transactions on Geoscience and Remote Sensing, 35, 974–979, https://doi.org/10.1109/36.602540, 1997.

Davis, C. H. and Moore, R. K.: A combined surface-and volume-scattering model for ice-sheet radar altimetry, Journal of Glaciology, 39, 675–686, https://doi.org/10.3189/002214300001657 9, 1993.

European Space Agency: L1b LRM Precise Orbit. Baseline E, URL `https://doi.org/10.5270/CR2-614f341`, (Date Accessed: 7 February 2025), 2023.

Fahnestock, M., Bindschadler, R., Kwok, R., and Jezek, K.: Greenland Ice Sheet Surface Properties and Ice Dynamics from ERS-1 SAR Imagery, Science, 262, 1530–1534, https://doi.org/10.1126/science.262.5139.1530, 1993.

Fettweis, X., Tedesco, M., van den Broeke, M., and Ettema, J.: Melting trends over the Greenland ice sheet (1958–2009) from spaceborne microwave data and regional climate models, The Cryosphere, 5, 359–375, https://doi.org/10.5194/tc-5-359-2011, 2011.

Fettweis, X., Box, J. E., Agosta, C., Amory, C., Kittel, C., Lang, C., van As, D., Machguth, H., and Gallée, H.: Reconstructions of the 1900–2015 Greenland ice sheet surface mass balance using the regional climate MAR model, The Cryosphere, 11, 1015–1033, https://doi.org/10.5194/tc-11-1015-2017, 2017.

Gardner, A. S., Schlegel, N.-J., and Larour, E.: Glacier Energy and Mass Balance (GEMB): a model of firn processes for cryosphere research, Geoscientific Model Development, 16, 2277–2302, https://doi.org/10.5194/gmd-16-2277-2023, 2023.

Gommenginger, C., Thibaut, P., Fenoglio-Marc, L., Quartly, G., Deng, X., Gómez-Enri, J., Challenor, P., and Gao, Y.: Retracking Altimeter Waveforms Near the Coasts, in: Coastal Altimetry, pp. 61–101, Springer Berlin Heidelberg, https://doi.org/10.1007/978-3-642-12796-0_4, 2010.

Grailet, J.-F., Hogan, R. J., Ghilain, N., Fettweis, X., and Grégoire, M.: Inclusion of the ECMWF ecRad radiation scheme (v1.5.0) in the MAR model (v3.14), regional evaluation for Belgium and assessment of surface shortwave spectral fluxes at Uccle observatory, EGUsphere [preprint], https://doi.org/10.5194/egusphere-2024-1858, 2024.

Hall, D., Box, J., Casey, K., Hook, S., Shuman, C., and Steffen, K.: Comparison of satellite-derived and in-situ observations of ice and snow surface temperatures over Greenland, Remote Sensing of Environment, 112, 3739–3749, https://doi.org/10.1016/j.rse.2008.05.007, 2008.

Harper, J., Humphrey, N., Pfeffer, W. T., Brown, J., and Fettweis, X.: Greenland ice-sheet contribution to sea-level rise buffered by meltwater storage in firn, Nature, 491, 240–243, https://doi.org/10.1038/nature11566, 2012.

Heilig, A., Eisen, O., MacFerrin, M., Tedesco, M., and Fettweis, X.: Seasonal monitoring of melt and accumulation within the deep percolation zone of the Greenland Ice Sheet and comparison with simulations of regional climate modeling, The Cryosphere, 12, 1851–1866, https://doi.org/10.5194/tc-12-1851-2018, 2018.

Helm, V., Humbert, A., and Miller, H.: Elevation Model of Greenland derived from CryoSat-2 in the period 2011 to 2013, links to DEM and uncertainty map as GeoTIFF, https://doi.org/10.1594/PANGAEA.831393, 2014.

Huybrechts, P., Goelzer, H., Janssens, I., Driesschaert, E., Fichefet, T., Goosse, H., and Loutre, M.-F.: Response of the Greenland and Antarctic Ice Sheets to Multi-Millennial Greenhouse Warming in the Earth System Model of Intermediate Complexity LOVECLIM, Surveys in Geophysics, 32, 397–416, https://doi.org/10.1007/s10712-011-9131-5, 2011.

Kern, M., Cullen, R., Berruti, B., Bouffard, J., Casal, T., Drinkwater, M. R., Gabriele, A., Lecuyot, A., Ludwig, M., Midthassel, R., Navas Traver, I., Parrinello, T., Ressler, G., Andersson, E., Martin-Puig, C., Andersen, O., Bartsch, A., Farrell, S., Fleury, S., Gascoin, S., Guillot, A., Humbert, A., Rinne, E., Shepherd, A., van den Broeke, M. R., and Yackel, J.: The Copernicus Polar Ice and Snow Topography Altimeter (CRISTAL) high-priority candidate mission, The Cryosphere, 14, 2235–2251, https://doi.org/10.5194/tc-14-2235-2020, 2020.

Kleinherenbrink, M., Ditmar, P., and Lindenbergh, R.: Retracking Cryosat data in the SARIn mode and robust lake level extraction, Remote Sensing of Environment, 152, 38–50, https://doi.org/10.1016/j.rse.2014.05.014, 2014.

Koenig, L. S., Ivanoff, A., Alexander, P. M., MacGregor, J. A., Fettweis, X., Panzer, B., Paden, J. D., Forster, R. R., Das, I., McConnell, J. R., Tedesco, M., Leuschen, C., and Gogineni, P.: Annual Greenland accumulation rates (2009–2012) from airborne snow radar, The Cryosphere, 10, 1739–1752, https://doi.org/10.5194/tc-10-1739-2016, 2016.

Kuipers Munneke, P., Ligtenberg, S. R., Suder, E. A., and Van den Broeke, M. R.: A model study of the response of dry and wet firn to climate change, Annals of Glaciology, 56, 1–8, https://doi.org/10.3189/2015aog70a994, 2015.

Lacroix, P., Dechambre, M., Legrésy, B., Blarel, F., and Rémy, F.: On the use of the dual-frequency ENVISAT altimeter to determine snowpack properties of the Antarctic ice sheet, Remote Sensing of Environment, 112, 1712–1729, https://doi.org/10.1016/j.rse.2007.08.022, 2008.

Lambin, C., Fettweis, X., Kittel, C., Fonder, M., and Ernst, D.: Assessment of future wind speed and wind power changes over South Greenland using the Modèle Atmosphérique Régional regional climate model, International Journal of Climatology, 43, 558–574, https://doi.org/10.1002/joc.7795, 2022.

Larue, F., Picard, G., Aublanc, J., Arnaud, L., Robledano-Perez, A., Meur, E. L., Favier, V., Jourdain, B., Savarino, J., and Thibaut, P.: Radar altimeter waveform simulations in Antarctica with the Snow Microwave Radiative Transfer Model (SMRT), Remote Sensing of Environment, 263, 112 534, https://doi.org/10.1016/j.rse.2021.112534, 2021.

Legrésy, B. and Rémy, F.: Altimetric observations of surface characteristics of the Antarctic ice sheet, Journal of Glaciology, 43, 265–275, https://doi.org/10.3189/s002214300000321x, 1997.

Lenton, T. M., Held, H., Kriegler, E., Hall, J. W., Lucht, W., Rahmstorf, S., and Schellnhuber, H. J.: Tipping elements in the Earth's climate system, Proceedings of the National Academy of Sciences, 105, 1786–1793, https://doi.org/10.1073/pnas.0705414105, 2008.

Lewis, G., Osterberg, E., Hawley, R., Marshall, H. P., Meehan, T., Graeter, K., McCarthy, F., Overly, T., Thundercloud, Z., and Ferris, D.: Recent precipitation decrease across the western Greenland ice sheet percolation zone, The Cryosphere, 13, 2797–2815, https://doi.org/10.5194/tc-13-2797-2019, 2019.

MacFerrin, M. J., Stevens, C. M., Vandecrux, B., Waddington, E. D., and Abdalati, W.: The Greenland Firn Compaction Verification and Reconnaissance (FirnCover) dataset, 2013–2019, Earth System Science Data, 14, 955–971, https://doi.org/10.5194/essd-14-955-2022, 2022.

Machguth, H., MacFerrin, M., van As, D., Box, J. E., Charalampidis, C., Colgan, W., Fausto, R. S., Meijer, H. A. J., Mosley-Thompson, E., and van de Wal, R. S. W.: Greenland meltwater storage in firn limited by near-surface ice formation, Nature Climate Change, 6, 390–393, https://doi.org/10.1038/nclimate2899, 2016.

Medley, B., Neumann, T. A., Zwally, H. J., Smith, B. E., and Stevens, C. M.: Simulations of firn processes over the Greenland and Antarctic ice sheets: 1980–2021, The Cryosphere, 16, 3971–4011, https://doi.org/10.5194/tc-16-3971-2022, 2022.

Meierbachtol, T., Harper, J., and Humphrey, N.: Basal Drainage System Response to Increasing Surface Melt on the Greenland Ice Sheet, Science, 341, 777–779, https://doi.org/10.1126/science.1235905, 2013.

Meloni, M., Bouffard, J., Parrinello, T., Dawson, G., Garnier, F., Helm, V., Bella, A. D., Hendricks, S., Ricker, R., Webb, E., Wright, B., Nielsen, K., Lee, S., Passaro, M., Scagliola, M., Simonsen, S. B., Sørensen, L. S., Brockley, D., Baker, S., Fleury, S., Bamber, J., Maestri, L., Skourup, H., Forsberg, R., and Mizzi, L.: CryoSat Ice Baseline-D validation and evolutions, The Cryosphere, 14, 1889–1907, https://doi.org/10.5194/tc-14-1889-2020, 2020.

Michel, A., Flament, T., and Rémy, F.: Study of the Penetration Bias of ENVISAT Altimeter Observations over Antarctica in Comparison to ICESat Observations, Remote Sensing, 6, 9412–9434, https://doi.org/10.3390/rs6109412, 2014.

Montgomery, L., Koenig, L., and Alexander, P.: The SUMup dataset: compiled measurements of surface mass balance components over ice sheets and sea ice with analysis over Greenland, Earth System Science Data, 10, 1959–1985, https://doi.org/10.5194/essd-10-1959-2018, 2018.

National Snow and Ice Data Center (NSIDC): ATL06 release 005 known issues, URL `https://nsidc.org/sites/nsidc.org/files/technical-references/ICESat2_ATL06_Known_Issues_v005.pdf`, (Date accessed: 18 April 2022), 2021.

Nghiem, S. V., Hall, D. K., Mote, T. L., Tedesco, M., Albert, M. R., Keegan, K., Shuman, C. A., DiGirolamo, N. E., and Neumann, G.: The extreme melt across the Greenland ice sheet in 2012, Geophysical Research Letters, 39, https://doi.org/10.1029/2012gl053611, 2012.

Nilsson, J., Vallelonga, P., Simonsen, S. B., Sørensen, L. S., Forsberg, R., Dahl-Jensen, D., Hirabayashi, M., Goto-Azuma, K., Hvidberg, C. S., Kjaer, H. A., and Satow, K.: Greenland 2012 melt event effects on CryoSat-2 radar altimetry, Geophysical Research Letters, 42, 3919–3926, https://doi.org/10.1002/2015gl063296, 2015.

Noh, M.-J. and Howat, I. M.: Automated stereo-photogrammetric DEM generation at high latitudes: Surface Extraction with TIN-based Search-space Minimization (SETSM) validation and demonstration over glaciated regions, GIScience & Remote Sensing, 52, 198–217, https://doi.org/10.1080/15481603.2015.1008621, 2015.

Noël, B., van de Berg, W. J., van Wessem, J. M., van Meijgaard, E., van As, D., Lenaerts, J. T. M., Lhermitte, S., Kuipers Munneke, P., Smeets, C. J. P. P., van Ulft, L. H., van de Wal, R. S. W., and van den Broeke, M. R.: Modelling the climate and surface mass balance of polar ice sheets using RACMO2 – Part 1: Greenland (1958–2016), The Cryosphere, 12, 811–831, https://doi.org/10.5194/tc-12-811-2018, 2018.

Otosaka, I. N.: Firn density profiles in West Central Greenland (ESA CryoVEx 2017), https://doi.org/10.1594/PANGAEA.921672, (Date accessed: 27 October 2023), 2020.

Otosaka, I. N., Shepherd, A., Casal, T. G. D., Coccia, A., Davidson, M., Di Bella, A., Fettweis, X., Forsberg, R., Helm, V., Hogg, A. E., Hvidegaard, S. M., Lemos, A., Macedo, K., Kuipers Munneke, P., Parrinello, T., Simonsen, S. B., Skourup, H., and Sørensen, L. S.: Surface Melting Drives Fluctuations in Airborne Radar Penetration in West Central Greenland, Geophysical Research Letters, 47, https://doi.org/10.1029/2020gl088293, 2020.

Partington, K., Ridley, J., Rapley, C., and Zwally, H.: Observations of the Surface Properties of the Ice Sheets by Satellite Radar Altimetry, Journal of Glaciology, 35, 267–275, https://doi.org/10.3189/s0022143000004603, 1989.

Porter, C., Morin, P., Howat, I., Noh, M.-J., Bates, B., Peterman, K., Keesey, S., Schlenk, M., Gardiner, J., Tomko, K., Willis, M., Kelleher, C., Cloutier, M., Husby, E., Foga, S., Nakamura, H., Platson, M., Wethington, Michael, J., Williamson, C., Bauer, G., Enos, J., Arnold, G., Kramer, W., Becker, P., Doshi, A., D'Souza, C., Cummens, P., Laurier, F., and Bojesen, M.: ArcticDEM, https://doi.org/10.7910/DVN/OHHUKH, 2018.

Porter, C., Howat, I., Noh, M.-J., Husby, E., Khuvis, S., Danish, E., Tomko, K., Gardiner, J., Negrete, A., Yadav, B., Klassen, J., Kelleher, C., Cloutier, M., Bakker, J., Enos, J., Arnold, G., Bauer, G., and Morin, P.: ArcticDEM - Mosaics, Version 4.1, https://doi.org/10.7910/DVN/3VDC4W, 2023.

Rennermalm, Å. K., Hock, R., Covi, F., Xiao, J., Corti, G., Kingslake, J., Leidman, S. Z., Miège, C., Macferrin, M., Machguth, H., Osterberg, E., Kameda, T., and McConnell, J. R.: Shallow firn cores 1989–2019 in southwest Greenland's percolation zone reveal decreasing density and ice layer thickness after 2012, Journal of Glaciology, 68, 431–442, https://doi.org/10.1017/jog.2021.102, 2021.

Ridley, J. K. and Partington, K. C.: A model of satellite radar altimeter return from ice sheets, International Journal of Remote Sensing, 9, 601–624, https://doi.org/10.1080/01431168808954881, 1988.

Rutishauser, A., Scanlan, K. M., Vandecrux, B., Karlsson, N. B., Jullien, N., Ahlstrøm, A. P., Fausto, R. S., and How, P.: Mapping the vertical heterogeneity of Greenland's firn from

2011–2019 using airborne radar and laser altimetry, The Cryosphere, 18, 2455–2472, https://doi.org/10.5194/tc-18-2455-2024, 2024.

Sasgen, I., van den Broeke, M., Bamber, J. L., Rignot, E., Sørensen, L. S., Wouters, B., Martinec, Z., Velicogna, I., and Simonsen, S. B.: Timing and origin of recent regional ice-mass loss in Greenland, Earth and Planetary Science Letters, 333-334, 293–303, https://doi.org/10.1016/j.epsl.2012.03.033, 2012.

Scanlan, K. M., Rutishauser, A., and Simonsen, S. B.: Observing the Near-Surface Properties of the Greenland Ice Sheet, Geophysical Research Letters, 50, https://doi.org/10.1029/2022gl101702, 2023.

Schaller, C. F., Freitag, J., Kipfstuhl, S., Laepple, T., Steen-Larsen, H. C., and Eisen, O.: A representative density profile of the North Greenland snowpack, The Cryosphere, 10, 1991–2002, https://doi.org/10.5194/tc-10-1991-2016, 2016a.

Schaller, C. F., Freitag, J., Kipfstuhl, S., Laepple, T., Steen-Larsen, H. C., and Eisen, O.: NEEM to EGRIP traverse - density and δ^{18}O of the surface snow (2 m profiles), https://doi.org/10.1594/PANGAEA.867875, (Date accessed: 13 December 2023), 2016b.

Simonsen, S. B. and Sørensen, L. S.: Implications of changing scattering properties on Greenland ice sheet volume change from Cryosat-2 altimetry, Remote Sensing of Environment, 190, 207–216, https://doi.org/10.1016/j.rse.2016.12.012, 2017.

Slater, T., Shepherd, A., McMillan, M., Muir, A., Gilbert, L., Hogg, A. E., Konrad, H., and Parrinello, T.: A new digital elevation model of Antarctica derived from CryoSat-2 altimetry, The Cryosphere, 12, 1551–1562, https://doi.org/10.5194/tc-12-1551-2018, 2018.

Smith, B., H. A. Fricker, A. Gardner, M. R. Siegfried, S. Adusumilli, B. M. Csathó, N. Holschuh, J. Nilsson, F. S. Paolo, and Team, T. I.-. S.: ATLAS/ICESat-2 L3A Land Ice Height, Version 6, https://doi.org/10.5067/ATLAS/ATL06.006, (Date Accessed: 7 February 2025), 2023a.

Smith, B., Hancock, D., Harbeck, K., Roberts, L., Neumann, T., Brunt, K., Fricker, H., Gardner, A., Siegfried, M., Adusumilli, S., Csatho, B., Holschuh, N., Nilsson, J., Paolo, F., and Felikson, D.: Ice, Cloud, and Land Elevation Satellite (ICESat-2) Project Algorithm Theoretical Basis Document (ATBD) for Land Ice Along-Track Height Product (ATL06), version 6, https://doi.org/10.5067/VWOKQDYJ7ODB, 2023b.

Smith, B. E., Gardner, A., Schneider, A., and Flanner, M.: Modeling biases in laser-altimetry measurements caused by scattering of green light in snow, Remote Sensing of Environment, 215, 398–410, https://doi.org/10.1016/j.rse.2018.06.012, 2018.

Smith, B. E., Medley, B., Fettweis, X., Sutterley, T., Alexander, P., Porter, D., and Tedesco, M.: Evaluating Greenland surface-mass-balance and firn-densification data using ICESat-2 altimetry, The Cryosphere, 17, 789–808, https://doi.org/10.5194/tc-17-789-2023, 2023c.

Sundal, A. V., Shepherd, A., Nienow, P., Hanna, E., Palmer, S., and Huybrechts, P.: Melt-induced speed-up of Greenland ice sheet offset by efficient subglacial drainage, Nature, 469, 521–524, https://doi.org/10.1038/nature09740, 2011.

Tedesco, M. and Fettweis, X.: Unprecedented atmospheric conditions (1948–2019) drive the 2019 exceptional melting season over the Greenland ice sheet, The Cryosphere, 14, 1209–1223, https://doi.org/10.5194/tc-14-1209-2020, 2020.

Tedesco, M., Fettweis, X., van den Broeke, M. R., van de Wal, R. S. W., Smeets, C. J. P. P., van de Berg, W. J., Serreze, M. C., and Box, J. E.: The role of albedo and accumulation in the 2010 melting record in Greenland, Environmental Research Letters, 6, 014 005, https://doi.org/10.1088/1748-9326/6/1/014005, 2011.

Tedesco, M., Fettweis, X., Mote, T., Wahr, J., Alexander, P., Box, J. E., and Wouters, B.: Evidence and analysis of 2012 Greenland records from spaceborne observations, a regional climate model and reanalysis data, The Cryosphere, 7, 615–630, https://doi.org/10.5194/tc-7-615-2013, 2013.

Tedesco, M., Mote, T., Fettweis, X., Hanna, E., Jeyaratnam, J., Booth, J. F., Datta, R., and Briggs, K.: Arctic cut-off high drives the poleward shift of a new Greenland melting record, Nature Communications, 7, https://doi.org/10.1038/ncomms11723, 2016.

Trusel, L. D., Das, S. B., Osman, M. B., Evans, M. J., Smith, B. E., Fettweis, X., McConnell, J. R., Noël, B. P. Y., and van den Broeke, M. R.: Nonlinear rise in Greenland runoff in response to post-industrial Arctic warming, Nature, 564, 104–108, https://doi.org/10.1038/s41586-018-0752-4, 2018.

van den Broeke, M. R., Enderlin, E. M., Howat, I. M., Munneke, P. K., Noël, B. P. Y., van de Berg, W. J., van Meijgaard, E., and Wouters, B.: On the recent contribution of the Greenland ice sheet to sea level change, The Cryosphere, 10, 1933–1946, https://doi.org/10.5194/tc-10-1933-2016, 2016.

van den Broeke, M. R., Kuipers Munneke, P., Noël, B., Reijmer, C., Smeets, P., van de Berg, W. J., and van Wessem, J. M.: Contrasting current and future surface melt rates on the ice sheets of Greenland and Antarctica: Lessons from in situ observations and climate models, PLOS Climate, 2, e0000 203, https://doi.org/10.1371/journal.pclm.0000203, 2023.

Vandecrux, B., MacFerrin, M., Machguth, H., Colgan, W. T., van As, D., Heilig, A., Stevens, C. M., Charalampidis, C., Fausto, R. S., Morris, E. M., Mosley-Thompson, E., Koenig, L., Montgomery, L. N., Miège, C., Simonsen, S. B., Ingeman-Nielsen, T., and Box, J. E.: Firn data compilation reveals widespread decrease of firn air content in western Greenland, The Cryosphere, 13, 845–859, https://doi.org/10.5194/tc-13-845-2019, 2019.

Vandecrux, B., Box, J., Ahlstrøm, A., Fausto, R., Karlsson, N., Rutishauser, A., Citterio, M., Larsen, S., Heuer, J., Solgaard, A., How, P., Colgan, W., and Fahrner, D.: GEUS snow and firn data in Greenland, https://doi.org/10.22008/FK2/9QEOWZ, 2023.

Vandecrux, B., Amory, C., Ahlstrøm, A. P., Akers, P. D., Albert, M., Alley, R. B., Alves De Castro, M., Arnaud, L., Baker, I., Bales, R., Benson, C., Box, J. E., Brucker, L., Buizert, C., Chandler, D., Charalampidis, C., Cherblanc, C., Clerx, N., Colgan, W., Covi, F., Dattler, M., Denis, G., Derksen, C., Dibb, J. E., Ding, M., Dixon, D., Eisen, O., Fahrner, D., Fausto, R., Favier, V., Fernandoy, F., Freitag, J., Gerland, S., Harper, J., Hawley, R. L., Heuer, J., Hock, R., Hou, S., How, P., Humphrey, N., Hubbard, B., Iizuka, Y., Isaksson, E., Kameda, T., Karlsson, N. B., Kawakami, K., Kjær, H. A., Kreutz, K., Kuipers Munneke, P., Lazzara, M., Lemeur, E., Lenaerts, J. T. M., Lewis, G., Lindau, F. G. L., Lindsey-Clark, J., MacFerrin, M., Machguth, H., Magand, O., Mankoff, K. D., Marquetto, L., Martinerie, P., McConnell, J. R., Medley, B., Miège, C., Miles, K. E., Miller, O., Miller, H., Montgomery, L., Morris, E., Mosley-Thompson, E., Mulvaney, R., Niwano, M., Oerter, H., Osterberg, E., Otosaka, I., Picard, G., Polashenski, C., Reijmer, C., Rennermalm, A., Rutishauser, A., Scanlan, K., Simoes, J. C., Simonsen, S. B., Smeets, P. C., Smith, A., Solgaard, A., Spencer, M., Steen-Larsen, H. C., Stevens, C. M., Sugiyama, S., Svensson, J., Tedesco, M., Thomas, E., Thompson-Munson, M., Tsutaki, S., Van As, D., Van Den Broeke, M. R., Van Tiggelen, M., Wang, Y., Wilhelms, F., Winstrup, M., Xiao, J., and Xiao, C.: The SUMup collaborative database: Surface mass balance, subsurface temperature and density measurements from the Greenland and Antarctic ice sheets (2024 release), https://doi.org/10.18739/A2M61BR5M, 2024.

Vizcaíno, M., Mikolajewicz, U., Jungclaus, J., and Schurgers, G.: Climate modification by future ice sheet changes and consequences for ice sheet mass balance, Climate Dynamics, 34, 301–324, https://doi.org/10.1007/s00382-009-0591-y, 2009.

Wingham, D., Rapley, C., and D, G.: New Techniques in Satellite Altimeter Tracking Systems, in: Digest - International Geoscience and Remote Sensing Symposium (IGARSS), vol. ESA SP-254, pp. 1339–1344, Zurich, 1986.

Węglarczyk, S.: Kernel density estimation and its application, ITM Web of Conferences, 23, 00 037, https://doi.org/10.1051/itmconf/20182300037, 2018.

Zwally, H. J., Abdalati, W., Herring, T., Larson, K., Saba, J., and Steffen, K.: Surface Melt-Induced Acceleration of Greenland Ice-Sheet Flow, Science, 297, 218–222, https://doi.org/10.1126/science.1072708, 2002.

5

CONCLUSION

The goal of this thesis was to propose and assess the applications of various satellite data in observing firn processes on GrIS and AIS. This chapter, therefore, summarises the main conclusions of this thesis in Sect. 5.1, where research questions posed in Sect. 1.4 are answered, and the framing of our study into the state-of-art is discussed. Section 5.2 discusses the implications of our work for cryosphere studies, and provides recommendations for future works.

5.1. CONCLUSIONS

- **What is the added value of combining radiometer and scatterometer data in estimating firn density in the Antarctic dry-snow zone?**

  To address this research question, Chapter 2 explored the information from a combination of 10-year time series from passive (SSMIS) and active (ASCAT) satellite microwave instruments. Starting from a correlation analysis between satellite time series from each acquisition channel of both satellite missions and IMAU-FDM firn density time series at different depths, this study demonstrated the complexity of relating firn density with observations from a single satellite, in turn stressing the need of a non-linear model to estimate firn densities using satellite data. Furthermore, this analysis provided indications on the optimal depth where firn densities can be effectively estimated with satellite data. The firn density at the depth of 40 cm was selected as the optimal target to assess our estimation method.

  An unsupervised machine learning approach (hierarchical clustering method) was subsequently applied to a combination of satellite time series, where the long-term mean was removed from the time series of each satellite data, in order to mitigate the effect of high-density ice lenses formed through a melt–refreezing event (Nicolas et al., 2017). This analysis successfully distinguished the timing and coverage of the melt event in West Antarctica in January 2016 (Nicolas et al., 2017) by detecting an abrupt rise in σ^0_A time series, which indicated the presence of a subsurface, high-density scatterer (Joughin et al., 2008). A sharp, instantaneous rise in T_B was also observed, indicating meltwater production (Johnson et al., 2020). Similarly, other regions that potentially underwent melt in January 2014 and 2019 were identified. However, in regions where ice-lens formation was not pronounced, this

method could underestimate the amount of melt pixels, identifying more dry-firn pixels compared to previous studies (Trusel et al., 2012; Fraser et al., 2016). Finally, the dry-firn regions identified in our result showed a similar spatial pattern to the 2003–2019 ice sheet mass changes in East Antarctica, shown as Fig. 4 in Stokes et al. (2022). Our classification provided a different aspect from the study of Tran et al. (2008), who attributed their classification outcome to topography. Therefore, from our clustering experiment, different snow types could be identified and proven useful in the following experiment, where pixels used as the training dataset well represented different types and regions of the AIS.

Using the dry-firn pixels defined by the previous step, the RF regression method was used to estimate firn densities at 40 cm depth. 10 % of IMAU-FDM densities were used as the training dataset, while the total IMAU-FDM densities were used as a validation dataset. The densities obtained by the RF approach, when averaged over time, demonstrated similar spatial patterns as the IMAU-FDM densities, with larger biases in coastal and mountainous regions. Such similar spatial patterns between IMAU-FDM and RF-derived densities were similar to the observation of Fraser et al. (2016), who demonstrated that both densities and ASCAT observations were largely influenced by temperature in the long-term.

However, the temporal correspondence between RF-derived densities and IMAU-FDM densities, indicated by temporal correlation coefficient and the RMSE between the two sets of densities, was compromised. On the one hand, Chapter 2 was primarily based on the assumptions from Champollion et al. (2013), where the difference between V- and H-polarised T_B increased as a result of hoar-crystal disappearance and the associated density increase, and from Fraser et al. (2016), where σ^0_A was indirectly correlated with firn density through precipitation (a low density is the result of a high precipitation). This is still an over-simplified assumption compared to the realistic physical process, where the grain size and microstructure of firn have a non-negligible impact on dielectric properties and hence affect T_B and σ^0_A (Picard et al., 2018). Surface roughness and layering are other major influential factors for σ^0_A variations (Picard et al., 2018). As grain size, microstructure, surface roughness and layering are not represented in the RF parametrisation, the method proposed in Chapter 2 only reproduces the IMAU-FDM density over the areas where the surface is flat and the grain size does not undergo a drastic temporal variation due to the lack of wind compaction (Veldhuijsen et al., 2023): in these areas, grain size and density often exhibit strong correlations (Mätzler, 2002), while other factors such as surface roughness and temperature gradient are less impactful. This mechanism allows the RF to capture the general density variations effectively, as T_B and σ^0_A can reflect trends in both grain size and density. In contrast, in regions with pronounced temporal variations, e.g. wind compaction, melt and temperature gradient, capturing general patterns of firn density and grain size is insufficient. In these regions, it is crucial to understand the effect of density, grain size and roughness on satellite signals separately, in order to effectively perform a data-driven density estimation. On the other hand, as the RF regressor largely relies on the training data, i.e. IMAU-FDM density, wherever IMAU-FDM does not sufficiently represent the density, the errors are propagated

to the RF-estimated density.

Chapter 2, compared to the typical radiative transfer approach to derive firn properties (Kar and Aksoy, 2024), fell short in providing a quantitative relationship between different properties and the satellite observations. The amount of firn properties that could be retrieved is therefore also limited. However, the machine learning approach has shown the advantage of being data-driven and computationally efficient when implemented over a large terrain. Overall, both the radiative transfer modelling approach (Kar and Aksoy, 2024) and our approach showed biases that should be corrected for by including ancillary data that provide more insights into accurate meteorological phenomena and firn densification processes.

In summary, the combination of radiometer and scatterometer data used in Chapter 2 could provide a long-term overview of firn density in flat and dry regions of AIS, especially when seasonal variations in wind velocity and direction are not dominant. On the contrary, the requirement for the RF model to account for other influencing factors such as grain size, grain shape and roughness highlights the limitations of the model in detecting firn-property anomalies. Future research should focus on enhancing the sensitivity of satellite signals to individual firn properties and on improving the robustness of machine-learning models in dynamic environments.

- **How can radar altimeter waveform information be used to improve the correction for slope-induced errors in height estimation?**

  To answer this search question, Chapter 3 proposed a method (LEPTA) to correct for slope-induced errors in height estimation using CryoSat-2 LRM L1b data. The method defined a search range based on the leading edge of a radar altimetry waveform, and searched for points on the measured terrain that are located within the defined range using a high-resolution (100 m) DEM. The location of the impact point, i.e. the radar reflection point, was calculated as the averaged DEM points. The height estimates using LEPTA were validated against the height measurements provided by concurrent ICESat-2 L3A Land Ice Height (ATL06) products as a performance assessment. The performance of LEPTA is simultaneously compared with previously existing methods, namely the "slope" method and the "point-based method" (Levinsen et al., 2016).

  Statistics of difference between heights estimated by CryoSat-2 and heights measured by ICESat-2 showed that LEPTA outperformed the slope and point-based methods, as well as the CryoSat-2 LRM L2 products. The improvements are most notable compared to the slope method towards the margins of GrIS, showing the reliability of LEPTA for incorporating the leading edge information into the height-estimation process.

  Furthermore, LEPTA demonstrated sensitivity to several factors, including the definition of search range on the leading edge, retracker threshold, systematic DEM bias, and DEM resolution. In addition, the sensitivity of height to the retracker threshold showed that when the threshold is lower than 70 %, the derived heights typically indicated the depth of the radar return within the firn layer. This indica-

tion provided a theoretical basis when determining the proper threshold used to assess penetration depth for the next research question. All comparisons demonstrated that LEPTA is a promising method that can be recommended to obtain more accurate height measurements with pulse-limited radar altimetry, especially in regions with complex topography.

Finally, the LEPTA method has provided indications for processing multi-peak waveforms acquired from SAR altimeters, which operate in non-interferometric delay-Doppler mode (Huang et al., 2024). Such an improvement enables the analysis of the margin regions of both AIS and GrIS, which will provide more opportunity for a more ice-sheet-wide, comprehensive firn property analysis.

- **To what extent can a long-term analysis of radar altimeter data improve the understanding of firn processes over Greenland?**

  To investigate this research question, Chapter 4 focused on the impact of firn processes on the volume scattering properties of the satellite radar altimeter. The study was based on the assumption that when melt occurs, the penetration depth of microwave is reduced: following the melt, a high-density ice layer forms as a results of refreezing, which acts as a near-surface reflector, reducing the penetration depth hence volume scattering. Finally, as new snow is deposited on top of the ice layer, the penetration depth of microwave recovers (Nilsson et al., 2015).

  Due to the increasingly frequent melt over GrIS in recent decades, Chapter 4 better verified and monitored such an assumption in a more continuous manner. We exploited the long-term variation (between September 2010 and September 2024) of the leading edge width (LeW) information from the CryoSat-2 waveforms. The study was conducted over the regions covered by CryoSat-2 LRM data in the GrIS. Although the LeW was mainly influenced by volume scattering, the impact of surface scattering could not be neglected (Legrésy et al., 2005; Nilsson et al., 2015). Therefore, Chapter 4 explored the relationship between LeW and surface roughness data from Scanlan et al. (2023), the topography derived from ArcticDEM (Porter et al., 2018), and a height difference between ICESat-2 and CryoSat-2 derived from Chapter 4. This study showed capability of delineating the regions over the interior of GrIS where volume scattering is dominant in LeW variations: the regions where surface scattering is dominant correspond to the study of van den Broeke et al. (2023), where the modelled melt extent exceeds 10 kg m^{-2} yr^{-1}.

  Using firn densities from two different models, MAR and IMAU-FDM, the LeW time series anslysis proposed in Chapter 4 could identify the melt and ice-lens formation due to the consequential increase of densities. Using FAC data from IMAU-FDM, Chapter 4 also provided an assessment of the potential depletion of Greenland firn. We juxtaposed the long-term time series of LeW and firn densities to provide a spatio-temporal analysis of how the melt–refreezing processes impact the firn condition in the long run, and observed that while LeW drops generally corresponded with the melt–refreezing events shown in firn densities and FAC time series, the overall LeW trend was more sensitive than the models to the prolonged impact of ice-lens formation on the volume scattering properties of the Greenland firn.

Although the theoretical scenario is that the LeW gradually recovers after the melt, indicating a recovering volume scattering hence a recovering firn condition (Nilsson et al., 2015), our observations indicated otherwise. The extent of drops and recovery of LeW time series depended on the extent of melt and also varied between regions. The drop-recovery pattern in LeW time series has been increasingly frequent in the recent decade. In regions such as the central-west Greenland, the LeW could not recover to the pre-2012 level, whilst in the central-east, the LeW recovered and dropped again following the recent melt events since 2018. Regions in the south of GrIS already demonstrated a relatively stable LeW compared to the north, as these regions are already dominated by annually recurring melting as well as large surface scattering.

Finally, we also compared our LeW time series with the stratigraphy derived by Rutishauser et al. (2024). The comparison showed that LeW was more sensitive to the long-term persistence of the sub-surface ice layers than the Rutishauser et al. (2024) study. In addition, the satellite-derived products have the advantage than the airborne-derived products due to higher spatio-temporal coverage and continuity.

Overall, this PhD focused on ice-sheet-wide, long-term variations of satellite parameters, and demonstrated the indications of such variations in relation to firn processes. Novel methods of analysing satellite parameters have been proposed and assessed, with the limitation discussed. From this PhD, we also demonstrated the discrepancies between satellite parameters and firn models, indicating how satellite parameters can be integrated in further studies to improve firn models (Veldhuijsen et al., 2023).

5.2. RECOMMENDATIONS

While this PhD has proposed methods to utilise and analyse the long-term, ice-sheet-wide satellite observations in relation to assessing firn processes, including a data-driven approach to estimate Antarctic dry-firn density and analysing spatio-temporal melt–refreezing patterns over Greenland, potential improvements and indications should be considered for future studies.

In Chapter 2, where the objective was to estimate firn densities over the AIS through a data-driven approach, two major assumptions were adopted. One assumption was that the IMAU-FDM density could be regarded as “true" data, despite its apparent discrepancy with in situ density measurements provided by the SUMup database. The other assumption was that the T_B properly reflected the temperature variations, while σ^0_A variation is influenced by firn density (as a result of varying precipitation and temperature) (Fraser et al., 2016). However, both assumptions were over-simplified. With the continuously updating SUMup database (Vandecrux et al., 2024), we encourage to add more in situ density measurements to the training dataset. Meanwhile, as the SUMup database continues to provide in situ temperature and SMB data, these data can also be utilised for a better parametrisation that takes into account the actual climate factors within the machine learning model. The incorporation of the in situ density data and of the measured parameters that drive density variations could improve the training quality of machine-learning models.

Currently, the RF approach based on T_B and σ^0_A only works well in reproducing the IMAU-FDM density where the seasonal wind variation is not pronounced, hence the firn density and grain size are stable. Since the T_B and σ^0_A are affected by firn density, grain size, grain shape and layering in a more complex manner than assumed in Chapter 2, future studies could benefit from establishing a more sophisticated relationship between satellite parameters and firn parameters using snow radiative transfer models. The machine learning model could also be applied in a localised manner: a wind parameter can be introduced in the model in the regions where wind compaction dominates the seasonal variations in firn density.

The RF regressor used in Chapter 2 mainly considers the absolute values of the satellite parameters and IMAU-FDM density, while neglecting the spatial or temporal correlation of the density patterns. Future works are encouraged to explore alternative machine learning and deep learning models, such as Recurrent Neural Networks (RNNs) and Long Short-Term Memory (LSTM), which account for the spatial or temporal patterns of firn density (Sherstinsky, 2020).

In Chapter 3, we proposed a method based on the leading-edge information of the radar altimeter waveform to correct for slope-induced errors in order to derive more accurate height estimates using radar altimeters. However, due to the varying firn conditions over ice sheets, further studies can benefit from exploring different Δr values in different regions to define the search range of the leading edge, which is currently homogeneously applied within the entire LRM coverage in our study. This improvement is expected to account for the spatial variability in penetration depths of CryoSat-2 signals and the variability in the localised topography. It can be done through a more localised statistical analysis of the CryoSat-2 versus ICESat-2 biases. Furthermore, over the terrains with high variations in topography, multiple peaks of the signal can occur, making it difficult to derive a single and proper range on the LeW to determine the height. In these cases, the analysis on waveforms with multiple peaks should be performed. This improvement has now been proposed by Huang et al. (2024). With the help of the improved method, the analysis of radar penetration in the southwest of Greenland, the north of Antarctica, as well as the margin regions of both ice sheets where SAR or SARIn altimetry data are available, can be better performed for future studies.

Using time series of LeW and Ku-band penetration depth derived from radar altimeter data, Chapter 4 was able to delineate the regions where volume scattering is dominant. However, in the regions where surface scattering is dominant, the melt–refreezing processes are more frequent, which was not sufficiently captured in our study. With the recently available laser altimeter data, we recommend further studies to continue monitoring the changes in volume scattering using the combination of radar and laser altimeter height estimations. Using multiple frequencies of radar altimeter to obtain firn status over different depths is also beneficial (Adodo et al., 2018). Furthermore, to distinguish volume scattering from surface scattering, additional waveform parameters and radiative transfer modelling are expected to be beneficial for further studies of variations in firn properties (Nilsson et al., 2015; Larue et al., 2021). Finally, to facilitate a more comprehensive detection of melt–refreezing, and to understand whether the snow deposition following the extensive melt events is sufficient to reconstruct a healthy firn layer, we encourage future studies to develop a time series analysis, where the moment

of LeW drops and the rate of recovery over the Greenland and Antarctic ice sheets can be automatically estimated.

This PhD has made notable progress in combining data from radiometers and scatterometers, as well as exploring the use of altimeter data to study firn properties. However, a comprehensive integration of all three types of satellite data has not yet been achieved, due to the differences in spatial and temporal resolution between the altimeters and the other two instruments. The different viewing geometry and frequency of radar altimeters add to the complexity of interpreting the spatio-temporal variation of altimetric parameters, especially over the dry-firn regions over Antarctica (Adodo et al., 2018). Future studies are encouraged to employ a multivariate data analysis approach to effectively combine the parameters from radiometers, scatterometers and altimeters in a time series analysis or a machine learning model, in order to study the firn density variation and melt–refreezing events over the ice sheets.

While this PhD has focused on 19 GHz and 37 GHz frequency from SSMIS, C-band frequency from ASCAT, Ku-band frequency from CryoSat-2 and laser photons from ICESat-2, future studies are encouraged to explore the application of a wider variety of frequencies, such as the Copernicus Imaging Microwave Radiometer (CIMR; Donlon et al., 2023) which operates in multiple low-frequency bands, the Radar Observing System for Europe operating in L-band (ROSE-L; Davidson et al., 2023), and the Copernicus Polar Ice and Snow Topography Altimeter (CRISTAL; Kern et al., 2020) which operates in dual-frequency (Ku-band and Ka-band). The different frequencies have different penetrating abilities within the firn layer, potentially facilitating a multi-layer analysis of firn processes.

This PhD has focused primarily on two key aspects: spatio-temporal density estimations in Antarctic dry zones and melt-refreezing patterns in Greenland. Both of these aspects essentially examine variations in firn densities, and involve the analysis of firn temperature and meltwater production. In reality, however, firn processes largely involve the changes in firn grain size, grain shape, and impurity, which are typically observed with satellite optical imagers (Jin et al., 2008; Palm et al., 2011; Huovinen et al., 2018; Gray et al., 2020). Over the polar regions, the optical imagers are limited by cloud and polar nights. Therefore, to comprehensively assess the firn processes, including variations in firn density, temperature, meltwater content, grain size, grain shape and impurity, future studies are encouraged to develop a data-fusion technique to effectively combine satellite radar data and optical images while accounting for the varying data resolution and availability.

This PhD limits the estimation of firn density to the dry regions of Antarctica; it also only observes the melt–refreezing patterns over Greenland. The motivation for investigating different processes lies in the different climate conditions between the two ice sheets: the abrupt and frequent melt events mainly occur in Greenland (Tedesco and Fettweis, 2020) and Antarctic ice shelves (Kingslake et al., 2017). The melt events cause an anomalous increase in firn density, which does not follow the firn compaction theory that increases with time and temperature (Arthern et al., 2010). Therefore, to explore the applicability of the density estimation and melt–refreezing assessment in this PhD in Greenland, Antarctica, and potentially smaller ice caps worldwide, future studies could investigate the inclusion of melt–refreezing patterns into a spatio-temporal sequence

analysis framework. Such a framework can be supported by the aforementioned radiative transfer modelling (Weng, 2007), multi-sensor data fusion, and multi-frequency, multi-layer analysis.

Finally, the currently adopted firn models in this PhD mainly use the climate forcings and focus on the theoretic relationships between firn density and temperature, wind and accumulation rate. Specifically, the semi-empirical models, such as IMAU-FDM, utilise the in situ firn density measurements for model calibration. Under this circumstance, integrating satellite data into climate models could potentially improve predictions and the understanding of firn dynamics, as satellite data are sensitive to firn properties at different depths depending on a variety of frequencies and have a higher spatial and temporal availability. Satellite data also have the potential of indicating the variations in firn parameters, such as grain size and grain shape, which are currently difficult to simulate using firn models. Through data assimilation methods, such as Optimal Interpolation, Kalman filter, three-dimensional variational assimilation (3D-Var), and 4D-Var (Reichle, 2008), satellite data could be effectively used to calibrate the existing firn models.

BIBLIOGRAPHY

Adodo, F. I., Remy, F., and Picard, G.: Seasonal variations of the backscattering coefficient measured by radar altimeters over the Antarctic Ice Sheet, The Cryosphere, 12, 1767–1778, https://doi.org/10.5194/tc-12-1767-2018, 2018.

Arthern, R. J., Vaughan, D. G., Rankin, A. M., Mulvaney, R., and Thomas, E. R.: In situ measurements of Antarctic snow compaction compared with predictions of models, Journal of Geophysical Research: Earth Surface, 115, https://doi.org/10.1029/2009jf001306, 2010.

Champollion, N., Picard, G., Arnaud, L., Lefebvre, E., and Fily, M.: Hoar crystal development and disappearance at Dome C, Antarctica: observation by near-infrared photography and passive microwave satellite, The Cryosphere, 7, 1247–1262, https://doi.org/10.5194/tc-7-1247-2013, 2013.

Davidson, M., Kubanek, J., Iannini, L., Furnell, R., Di Cosimo, G., Gebert, N., Petrolati, D., Geudtner, D., and Osborne, S.: Rose-L – The Copernicus L-Band Synthetic Aperture Radar Imaging Mission, in: IGARSS 2023 - 2023 IEEE International Geoscience and Remote Sensing Symposium, IEEE, https://doi.org/10.1109/igarss52108.2023.10281640, 2023.

Donlon, C., Galeazzi, C., Midthassel, R., Sallusti, M., Triggianese, M., Fiorelli, B., De Paris, G., Kornienko, A., and Khlystova, I.: The Copernicus Imaging Microwave Radiometer (CIMR): Mission Overview and Status, in: IGARSS 2023 - 2023 IEEE International Geoscience and Remote Sensing Symposium, pp. 989–992, IEEE, https://doi.org/10.1109/igarss52108.2023.10281934, 2023.

Fraser, A. D., Nigro, M. A., Ligtenberg, S. R. M., Legrésy, B., Inoue, M., Cassano, J. J., Munneke, P. K., Lenaerts, J. T. M., Young, N. W., Treverrow, A., van den Broeke, M., and Enomoto, H.: Drivers of ASCAT C band backscatter variability in the dry snow zone of Antarctica, Journal of Glaciology, 62, 170–184, https://doi.org/10.1017/jog.2016.29, 2016.

Gray, A., Krolikowski, M., Fretwell, P., Convey, P., Peck, L. S., Mendelova, M., Smith, A. G., and Davey, M. P.: Remote sensing reveals Antarctic green snow algae as important terrestrial carbon sink, Nature Communications, 11, https://doi.org/10.1038/s41467-020-16018-w, 2020.

Huang, Q., McMillan, M., Muir, A., Phillips, J., and Slater, T.: Multipeak retracking of radar altimetry waveforms over ice sheets, Remote Sensing of Environment, 303, 114 020, https://doi.org/10.1016/j.rse.2024.114020, 2024.

Huovinen, P., Ramírez, J., and Gómez, I.: Remote sensing of albedo-reducing snow algae and impurities in the Maritime Antarctica, ISPRS Journal of Photogrammetry and Remote Sensing, 146, 507–517, https://doi.org/10.1016/j.isprsjprs.2018.10.015, 2018.

Jin, Z., Charlock, T. P., Yang, P., Xie, Y., and Miller, W.: Snow optical properties for different particle shapes with application to snow grain size retrieval and MODIS/CERES radiance comparison over Antarctica, Remote Sensing of Environment, 112, 3563–3581, https://doi.org/10.1016/j.rse.2008.04.011, 2008.

Johnson, A., Fahnestock, M., and Hock, R.: Evaluation of passive microwave melt detection methods on Antarctic Peninsula ice shelves using time series of Sentinel-1 SAR, Remote Sensing of Environment, 250, 112 044, https://doi.org/https://doi.org/10.1016/j.rse.2020.112044, 2020.

Joughin, I., Das, S. B., King, M. A., Smith, B. E., Howat, I. M., and Moon, T.: Seasonal Speedup Along the Western Flank of the Greenland Ice Sheet, Science, 320, 781–783, https://doi.org/10.1126/science.1153288, 2008.

Kar, R. and Aksoy, M.: Passive Microwave Remote Sensing of the Antarctic Ice Sheet: Retrieval of Firn Properties Near the Concordia Station, IEEE Geoscience and Remote Sensing Letters, 21, 1–5, https://doi.org/10.1109/lgrs.2023.3343594, 2024.

Kern, M., Cullen, R., Berruti, B., Bouffard, J., Casal, T., Drinkwater, M. R., Gabriele, A., Lecuyot, A., Ludwig, M., Midthassel, R., Navas Traver, I., Parrinello, T., Ressler, G., Andersson, E., Martin-Puig, C., Andersen, O., Bartsch, A., Farrell, S., Fleury, S., Gascoin, S., Guillot, A., Humbert, A., Rinne, E., Shepherd, A., van den Broeke, M. R., and Yackel, J.: The Copernicus Polar Ice and Snow Topography Altimeter (CRISTAL) high-priority candidate mission, The Cryosphere, 14, 2235–2251, https://doi.org/10.5194/tc-14-2235-2020, 2020.

Kingslake, J., Ely, J. C., Das, I., and Bell, R. E.: Widespread movement of meltwater onto and across Antarctic ice shelves, Nature, 544, 349–352, https://doi.org/10.1038/nature22049, 2017.

Larue, F., Picard, G., Aublanc, J., Arnaud, L., Robledano-Perez, A., Meur, E. L., Favier, V., Jourdain, B., Savarino, J., and Thibaut, P.: Radar altimeter waveform simulations in Antarctica with the Snow Microwave Radiative Transfer Model (SMRT), Remote Sensing of Environment, 263, 112 534, https://doi.org/10.1016/j.rse.2021.112534, 2021.

Legrésy, B., Papa, F., Rémy, F., Vinay, G., van den Bosch, M., and Zanife, O.-Z.: ENVISAT radar altimeter measurements over continental surfaces and ice caps using the ICE-2 retracking algorithm, Remote Sensing of Environment, 95, 150–163, https://doi.org/10.1016/j.rse.2004.11.018, 2005.

Levinsen, J. F., Simonsen, S. B., Sorensen, L. S., and Forsberg, R.: The Impact of DEM Resolution on Relocating Radar Altimetry Data Over Ice Sheets, IEEE Journal of Selected Topics in Applied Earth Observations and Remote Sensing, 9, 3158–3163, https://doi.org/10.1109/jstars.2016.2587684, 2016.

Mätzler, C.: Relation between grain-size and correlation length of snow, Journal of Glaciology, 48, 461–466, https://doi.org/10.3189/172756502781831287, 2002.

Nicolas, J. P., Vogelmann, A. M., Scott, R. C., Wilson, A. B., Cadeddu, M. P., Bromwich, D. H., Verlinde, J., Lubin, D., Russell, L. M., Jenkinson, C., Powers, H. H., Ryczek, M., Stone, G., and Wille, J. D.: January 2016 extensive summer melt in West Antarctica favoured by strong El Niño, Nature Communications, 8, https://doi.org/10.1038/ncomms15799, 2017.

Nilsson, J., Vallelonga, P., Simonsen, S. B., Sørensen, L. S., Forsberg, R., Dahl-Jensen, D., Hirabayashi, M., Goto-Azuma, K., Hvidberg, C. S., Kjaer, H. A., and Satow, K.: Greenland 2012 melt event effects on CryoSat-2 radar altimetry, Geophysical Research Letters, 42, 3919–3926, https://doi.org/10.1002/2015gl063296, 2015.

Palm, S. P., Yang, Y., Spinhirne, J. D., and Marshak, A.: Satellite remote sensing of blowing snow properties over Antarctica, Journal of Geophysical Research, 116, https://doi.org/10.1029/2011jd015828, 2011.

Picard, G., Sandells, M., and Löwe, H.: SMRT: an active–passive microwave radiative transfer model for snow with multiple microstructure and scattering formulations (v1.0), Geoscientific Model Development, 11, 2763–2788, https://doi.org/10.5194/gmd-11-2763-2018, 2018.

Porter, C., Morin, P., Howat, I., Noh, M.-J., Bates, B., Peterman, K., Keesey, S., Schlenk, M., Gardiner, J., Tomko, K., Willis, M., Kelleher, C., Cloutier, M., Husby, E., Foga, S., Nakamura, H., Platson, M., Wethington, Michael, J., Williamson, C., Bauer, G., Enos, J., Arnold, G., Kramer, W., Becker, P., Doshi, A., D'Souza, C., Cummens, P., Laurier, F., and Bojesen, M.: ArcticDEM, https://doi.org/10.7910/DVN/OHHUKH, 2018.

Reichle, R. H.: Data assimilation methods in the Earth sciences, Advances in Water Resources, 31, 1411–1418, https://doi.org/10.1016/j.advwatres.2008.01.001, 2008.

Rutishauser, A., Scanlan, K. M., Vandecrux, B., Karlsson, N. B., Jullien, N., Ahlstrøm, A. P., Fausto, R. S., and How, P.: Mapping the vertical heterogeneity of Greenland's firn from 2011–2019 using airborne radar and laser altimetry, The Cryosphere, 18, 2455–2472, https://doi.org/10.5194/tc-18-2455-2024, 2024.

Scanlan, K. M., Rutishauser, A., and Simonsen, S. B.: Observing the Near-Surface Properties of the Greenland Ice Sheet, Geophysical Research Letters, 50, https://doi.org/10.1029/2022gl101702, 2023.

Sherstinsky, A.: Fundamentals of Recurrent Neural Network (RNN) and Long Short-Term Memory (LSTM) network, Physica D: Nonlinear Phenomena, 404, 132 306, https://doi.org/10.1016/j.physd.2019.132306, 2020.

Stokes, C. R., Abram, N. J., Bentley, M. J., Edwards, T. L., England, M. H., Foppert, A., Jamieson, S. S. R., Jones, R. S., King, M. A., Lenaerts, J. T. M., Medley, B., Miles, B. W. J., Paxman, G. J. G., Ritz, C., van de Flierdt, T., and Whitehouse, P. L.: Response of the East Antarctic Ice Sheet to past and future climate change, Nature, 608, 275–286, https://doi.org/10.1038/s41586-022-04946-0, 2022.

Tedesco, M. and Fettweis, X.: Unprecedented atmospheric conditions (1948–2019) drive the 2019 exceptional melting season over the Greenland ice sheet, The Cryosphere, 14, 1209–1223, https://doi.org/10.5194/tc-14-1209-2020, 2020.

Tran, N., Remy, F., Feng, H., and Femenias, P.: Snow Facies Over Ice Sheets Derived From Envisat Active and Passive Observations, IEEE Transactions on Geoscience and Remote Sensing, 46, 3694–3708, https://doi.org/10.1109/tgrs.2008.2000818, 2008.

Trusel, L. D., Frey, K. E., and Das, S. B.: Antarctic surface melting dynamics: Enhanced perspectives from radar scatterometer data, Journal of Geophysical Research: Earth Surface, 117, https://doi.org/10.1029/2011jf002126, 2012.

van den Broeke, M. R., Kuipers Munneke, P., Noël, B., Reijmer, C., Smeets, P., van de Berg, W. J., and van Wessem, J. M.: Contrasting current and future surface melt rates on the ice sheets of Greenland and Antarctica: Lessons from in situ observations and climate models, PLOS Climate, 2, e0000 203, https://doi.org/10.1371/journal.pclm.0000203, 2023.

Vandecrux, B., Amory, C., Ahlstrøm, A. P., Akers, P. D., Albert, M., Alley, R. B., Alves De Castro, M., Arnaud, L., Baker, I., Bales, R., Benson, C., Box, J. E., Brucker, L., Buizert, C., Chandler, D., Charalampidis, C., Cherblanc, C., Clerx, N., Colgan, W., Covi, F., Dattler, M., Denis, G., Derksen, C., Dibb, J. E., Ding, M., Dixon, D., Eisen, O., Fahrner, D., Fausto, R., Favier, V., Fernandoy, F., Freitag, J., Gerland, S., Harper, J., Hawley, R. L., Heuer, J., Hock, R., Hou, S., How, P., Humphrey, N., Hubbard, B., Iizuka, Y., Isaksson, E., Kameda, T., Karlsson, N. B., Kawakami, K., Kjær, H. A., Kreutz, K., Kuipers Munneke, P., Lazzara, M., Lemeur, E., Lenaerts, J. T. M., Lewis, G., Lindau, F. G. L., Lindsey-Clark, J., MacFerrin, M., Machguth, H., Magand, O., Mankoff, K. D., Marquetto, L., Martinerie, P., McConnell, J. R., Medley, B., Miège, C., Miles, K. E., Miller, O., Miller, H., Montgomery, L., Morris, E., Mosley-Thompson, E., Mulvaney, R., Niwano, M., Oerter, H., Osterberg, E., Otosaka, I., Picard, G., Polashenski, C., Reijmer, C., Rennermalm, A., Rutishauser, A., Scanlan, K., Simoes, J. C., Simonsen, S. B., Smeets, P. C., Smith, A., Solgaard, A., Spencer, M., Steen-Larsen, H. C., Stevens, C. M., Sugiyama, S., Svensson, J., Tedesco, M., Thomas, E., Thompson-Munson, M., Tsutaki, S., Van As, D., Van Den Broeke, M. R., Van Tiggelen, M., Wang, Y., Wilhelms, F., Winstrup, M., Xiao, J., and Xiao, C.: The SUMup collaborative database: Surface mass balance, subsurface temperature and density measurements from the Greenland and Antarctic ice sheets (2024 release), https://doi.org/10.18739/A2M61BR5M, 2024.

Veldhuijsen, S. B. M., van de Berg, W. J., Brils, M., Munneke, P. K., and van den Broeke, M. R.: Characteristics of the 1979–2020 Antarctic firn layer simulated with IMAU-FDM v1.2A, The Cryosphere, 17, 1675–1696, https://doi.org/10.5194/tc-17-1675-2023, 2023.

Weng, F.: Advances in Radiative Transfer Modeling in Support of Satellite Data Assimilation, Journal of the Atmospheric Sciences, 64, 3799–3807, https://doi.org/10.1175/2007jas2112.1, 2007.

ACKNOWLEDGEMENTS

Let us keep this section simple, because I am not very good at expressing emotions — most of the times I find it cheesy. If anything, I prefer to tell people in person.

I would like to express my utmost gratitude to everyone who has provided me with support and engaged in discussions technically: Stef, Cornelis, Bert, Sanne, Xavier, Max, Ghislain, Lorenzo, Pavel, Freek, Shashwat, Jan, Thore, Ann-Sofie, Sophie, Marcel, and Frithjof. I have learned a lot throughout my work thanks to all of you. I would like to thank my PhD committee members Roland, Ramon, Sebastian, Paco, and Roderik for spending time to review my thesis; and the journal editors and reviewers for helping me improve my manuscripts.

Then, I would like to thank all my friends who have been emotionally supporting me and tolerating my craziness and complaints. Because some of you may prefer to stay anonymous, and I am also afraid of missing out anyone by mistake, I would not list the name of everyone here. Thanks to my family who supported me to study and work here to explore the other side of the world.

I also appreciate Stef, Paco, Pavel, Roland and Bert for allowing me to join the polar research. It has been a special and cool experience.

Thanks to everyone who has provided me with delicious food, the influencers who created interesting contents, the authors who wrote insightful books, and the professors who provided nice open-source online courses. But I will not turn my thesis into an advertisement here.

Finally, the research is supported by the Dutch Research Council (NWO). Special acknowledgements are also dedicated to the sources of the important datasets that have been used in this thesis, as my thesis is greatly dependent on the data:

- **ArcticDEM** provided by the Polar Geospatial Center under NSF-OPP awards 1043681, 1559691, and 1542736.
  Authors: Porter, C., Morin, P., Howat, I., Noh, M.-J., Bates, B., Peterman, K., Keesey, S., Schlenk, M., Gardiner, J., Tomko, K., Willis, M., Kelleher, C., Cloutier, M., Husby, E., Foga, S., Nakamura, H., Platson, M., Wethington Jr., M., Williamson, C., Bauer, G., Enos, J., Arnold, G., Kramer, W., Becker, P., Doshi, A., D'Souza, C., Cummens, P., Laurier, F., and Bojesen, M.
  Describing literature: doi: 10.1080/15481603.2015.1008621.
  Link to data: doi: 10.7910/DVN/OHHUKH.
- **ASCAT incidence-angle-normalised backscatter intensity** provided by Brigham Young University (BYU) Microwave Earth Remote Sensing (MERS) laboratory.
  Authors: Lindsley, R. D. and Long, D. G.
  Describing literature: `https://www.scp.byu.edu/docs/pdf/MERS1002.pdf`.
  Link to data: `https://www.scp.byu.edu/`.
- **CryoSat-2 L1b and L2 data** provided by ESA.

Describing literature: https://earth.esa.int/eogateway/documents/20142/37627/CryoSat-Baseline-D-Product-Handbook.pdf.
Link to data: ftp://science-pds.cryosat.esa.int/.

- **ERA5 wind and temperature data** provided by Copernicus Climate Change Service (C3S) Climate Data Store (CDS).
  Author: Muñoz Sabater, J.
  Describing literature: doi: 10.5194/essd-13-4349-2021.
  Link to data: doi: 10.24381/cds.e2161bac.
- **ICESat-2 Land Ice Height data**
  ATLAS/ICESat-2 L3A Land Ice Height, Version 6 provided by NSIDC.
  Authors: Smith, B., Fricker, H. A., Gardner, A., Siegfried, M. R., Adusumilli, S., Csathò, B. M., Holschuh, N., Nilsson, J., Paolo, F. S., and The ICESat-2 Science Team.
  Describing literature: https://nsidc.org/sites/default/files/documents/user-guide/atl06-v006-userguide.pdf.
  Link to data: doi: 10.5067/ATLAS/ATL06.006.
- **IMAU-FDM density profile over Antarctica**
  Authors: Veldhuijsen, S. B. M., van de Berg, W. J., Brils, M., Kuipers Munneke, P., and van den Broeke, M. R.
  Describing literature: doi: 10.5194/tc-17-1675-2023.
- **IMAU-FDM density profile, melt and FAC over Greenland**
  Authors: Brils, M., Kuipers Munneke, P., van de Berg, W. J., and van den Broeke, M.
  Describing literature: doi: 10.5194/gmd-15-7121-2022.
- **MAR density profile, melt and refreezing, and snow height change over Greenland**
  Author: Fettweis, X.
  Describing literature: doi: 10.5194/tc-7-469-2013.
- **SSMIS brightness temperature** provided by NSIDC.
  Authors: Meier, W. N., Stewart, J. S., Wilcox, H., Scott, D. J., and Hardman, M. A.
  Describing literature: https://nsidc.org/sites/default/files/documents/user-guide/nsidc-0001-v006-userguide_1.pdf.
  Link to data: doi: 10.5067/MXJL42WSXTS1.
- **Stratigraphy of Greenland firn**
  Author: Rutishauser, A.
  Describing literature: doi: 10.5194/tc-18-2455-2024.
  Link to data: doi: 10.22008/FK2/OLVPFG.
- **SUMup firn density**
  Authors: Koenig, L. and Montgomery, L.
  Describing literature: doi: 10.5194/essd-10-1959-2018.
  Link to data: doi: 10.18739/A2JH3D23R.
- **Surface roughness data of Greenland firn**
  Authors: Scanlan, K. M., Simonsen, S. B., and Rutishauser, A.
  Describing literature: doi: 10.1029/2022gl101702.
  Link to data: doi: 10.11583/DTU.21333291.V1.

ChatGPT is used for language check in parts of the thesis.

CURRICULUM VITÆ

Li WEIRAN

Oct. 1994 Born in Beijing, China.

EDUCATION

2006–2012 High School Affiliated to Beijing Institute of Technology (BIT)

2012–2016 Bachelor of Science in Opto-Electronic Engineering
Beihang University

2016–2018 Master of Science in Geomatics
Delft University of Technology

2018 PhD candidate in Geoscience and Remote Sensing
Delft University of Technology

LIST OF PUBLICATIONS

- **Li, W.**, Lhermitte, S., and López-Dekker, P.: The potential of synthetic aperture radar interferometry for assessing meltwater lake dynamics on Antarctic ice shelves, The Cryosphere, 15, 5309–5322, https://doi.org/10.5194/tc-15-5309-2021, 2021.
- **Li, W.**, Slobbe, C., and Lhermitte, S.: A leading-edge-based method for correction of slope-induced errors in ice-sheet heights derived from radar altimetry, The Cryosphere, 16, 2225–2243, https://doi.org/10.5194/tc-16-2225-2022, 2022.
- **Li, W.**, Veldhuijsen, S. B. M., and Lhermitte, S.: Machine learning of Antarctic firn density by combining radiometer and scatterometer remote-sensing data, The Cryosphere, 19, 37–61, https://doi.org/10.5194/tc-19-37-2025, 2025.
- **Li, W.**, Lhermitte, S., Wouters, B., Slobbe, C., Brils, M., and Fettweis, X.: Assessing spatio-temporal variability of firn volume scattering over Greenland with satellite altimeters, EGUsphere [preprint], https://doi.org/10.5194/egusphere-2024-3251, 2024.